TOPOGRAPHICALLY INDUCED BAROCLINIC EDDIES ALONG A COASTLINE

by

GORDON EDWIN SWATERS

B.Math.(Honours), University Of Waterloo, 1980

A THESIS SUBMITTED IN PARTIAL FULFILMENT OF

THE REQUIREMENTS FOR THE DEGREE OF

MASTER OF SCIENCE

in

THE FACULTY OF GRADUATE STUDIES

Department Of Mathematics
Institute Of Applied Mathematics And Statistics
Department Of Oceanography

We accept this thesis as conforming

to the required standard

THE UNIVERSITY OF BRITISH COLUMBIA

August 1983

In presenting this thesis in partial fulfilment of the requirements for an advanced degree at the University of British Columbia, I agree that the Library shall make it freely available for reference and study. I further agree that permission for extensive copying of this thesis for scholarly purposes may be granted by the Head of my Department or by his or her representatives. It is understood that copying or publication of this thesis for financial gain shall not be allowed without my written permission.

Department of Mathematics

The University of British Columbia
2075 Wesbrook Place
Vancouver, Canada
V6T 1W5

Date: August 1, 1983

Abstract

A mathematical model is formulated which describes the interaction between a baroclinic current and order Rossby number topography along a coastline. The lead term solution, in an asymptotic expansion in the Rossby number, is obtained for the pressure, density, velocity and mass transport fields. The lead term solution is found using a normal mode analysis and a Green's function technique. The solution is applied to the possible topographic generation of the Sitka eddy in the north east Pacific Ocean. The numerical calculations of the model and the observed location, dimensions, velocities and transports of the Sitka eddy are in very good agreement.

Table of Contents

List of Figures

Acknowledgement

It is a pleasure to thank my advisor Professor Lawrence A. Mysak for suggesting this research topic and for his guidance during the preparation of this thesis. Professor Paul H. LeBlond deserves special thanks for the many discussions we had about physical oceanography and this thesis during the 1982-83 academic year when Professor Mysak was on sabbatical leave.

I would like to express my gratitude to Professor Mysak for the generous financial support provided me from a grant awarded him by the United States Department of Naval Research. I would also like to thank the Department of Mathematics for the Teaching Assistantships awarded me from 1981 through to 1983, and the Department of Oceanography for use of their computing facilities.

I. INTRODUCTION

In the upper north east of the Pacific Ocean, a few hundred kilometres offshore from Sitka, Alaska, there exists a mesoscale baroclinic anticyclonic eddy (Tabata; 1982). This eddy, with radius about 150 km and extending about 1000 metres into the water column, seems to occur annually during the Northern Hemisphere summer. The eddy seems to dissipate during the winter months. Tabata(1982) has definitely documented its existence during 1958, 1960 and 1961, and has provided compelling evidence for its existence in other years. This eddy, referred to as the Sitka eddy, reoccurs in the same geographic location during the years it has been observed.

Analysis of the wind stress data for this region showed that the spectral energy of the annual frequency was an order of magnitude larger than all other frequencies bands (Bakun; 1978). This fact, coupled to the observation that the curl of the wind stress should generate anticyclonic motions in the region, naturally lead to the attempt to correlate the Sitka eddy to atmospheric forcing. However, it was not possible to correlate the occurance of the Sitka eddy with the annual change in the curl of the wind stress (Tabata; 1982).

Willmott and Mysak(1980) showed that a six year periodic atmospheric forcing of the north east Pacific Ocean will generate eddies situated, more or less, along the Alaskan panhandle. These eddies were the result of reflections of baroclinic Rossby waves, created by the atmospheric forcing of

the ocean, off the Alaskan-British Columbian coastline.

The Willmott and Mysak(1980) treatment was unable to resolve two key features of the Sitka eddy. First, the Sitka eddy occurs along that part of the Alaskan coastline which is adjacent to British Columbia and not along the panhandle. Second, their treatment produced many eddies whereas the available data suggested there were few. Therefore even supposing that the Sitka eddy is atmospherically induced some other forcing mechanism is operating to select out the observed eddy. One obvious candidate is an interaction process between the regional topography and the local mean flow.

This thesis examines the possibility that the local mean summertime current field can interact with the prominent regional topography to produce mesoscale anticyclonic baroclinic eddies. In order to investigate this conjecture a mathematical model is developed for the topographic forcing of a baroclinic current along a coastline.

The model is formulated in Chapter II. Prior to discussing the details of the mathematical derivation, a brief description of the oceanographic and bathymetric data for the north east Pacific Ocean is given. The structure and origins of the region's currents is described as are the principle topographic features. A qualitative description of the Sitka eddy is also given.

Based on this examination of the avialible data the inviscid, stratified, steady, incompressible, Boussinesq and f-plane equations of motion are scaled via geostrophy to ascertain

the qualitative nature of the fluid dynamics. The relevant parameter is the Rossby number. The smallness of the Rossby number is exploited by constructing the lead order solutions for the pressure, density, velocity and mass transport fields in an asymptotic expansion in the Rossby number. The order one pressure field, which acts as a stream function, must conserve potential vorticity. Chapter II concludes with the formulation of the appropiate boundary conditions which the solution of the potential vorticity equation must satisfy.

Chapter III contains the analytical solution of the problem. A solution is sought in which the order one pressure field is given as the sum of the upstream stream function and a pressure field representing the topographic mean flow interaction. This interaction pressure field is obtained by using a normal mode analysis described by Chao et al.; (1980). The normal modes are found to be given by Bessel functions of order one, with the solution found via a method described in Bryan and Ripa(1978). The horizontal amplitude functions are found using a Green's function techinque. Chapter III concludes with the explicit formulae given for the order one pressure, velocity, density and mass transport fields.

Chapter IV has two functions. The solution is described when evaluated for the set of parameters that were obtained as estimates from the data for the north east Pacific Ocean. The results of varying the parameters is also described. In addition to describing the numerical changes resulting from parameter variations, physical explanations are also given,

based on vorticity arguments.

Chapter V discusses the application of the model to generation of the Sitka eddy. Chapter VI summarizes the work contained in this thesis.

II. FORMULATION OF THE MATHEMATICAL MODEL

2.1 Currents And Geometry Of The North East Pacific Ocean

The motivation for creating a mathematical model for topographically induced eddies along a coastline is the possible application of the model in understanding the dynamics of the Sitka eddy. It is therefore essential to have at least a qualitative appreciation of the oceanography and bathymetry of this region. In this section a brief survey of the physical oceanography and geometry of the north east Pacific Ocean is presented. Specifically, that region which is bounded by the lines of longitude 130°W and 145°W, and the lines of latitude 53°N and 59°N. In the subsequent discussion this is the geographical area referred to as 'the region'. This summary is largely drawn from the work of Tabata(1982) and Bennett(1959).

Figure 1 is a bathymetric map of the north east Pacific Ocean. In the region of interest, the ocean floor can be described as a slightly sloping abyssal plain with several irregularly spaced seamounts. Of particular note is the collection of seamounts in the immediate vicinity of the Pratt seamount, located at 142°W 56°N. These seamounts have heights on the order of 2500 metres in about 3500+ metres of water. Toward the southeast the bottom profile becomes highly irregular with many topographic protrusions. Their sizes however are somewhat smaller than the collection near the Pratt seamount.

The Alaskan-British Columbian coastline, in the above region, is more or less straight, inclined about 45° to the west of a line of constant longitude. Northward of the region the

Alaskan coastline turns 90° to the west, giving the impression of forming a boundary of a quarter plane region. Southeastward of the region, the gross features of the British Columbian coastline remain qualitatively straight.

The continental slope in this area has an interesting characterization. In the north the shelf break occurs within 50 km and parallel to the coast. However near the location of the Sitka eddy the slope region broadens giving the impression of a horizontal protrusion of the shelf out into the deeper ocean. Southeast of the continental slope bump, the shelf break resumes its northern pattern. This 'bump' along the shelf break is roughly symmetric about the normal to the coastline taken at latitude 56°N and longitude 135°W. In Figure 1 the 1600 fathom (3000 metre) contour is marked, providing a bench mark for the extent of the continental slope bump, out to about 140°W 55°N.

Thus in the region in which the Sitka eddy occurs the topography forms the following idealized picture. First the coastline is more or less straight falling off quickly to an abyssal plain of about 3500 metres depth. Near Sitka, Alaska there is a limited protrusion of the continental slope which falls off somewhat more slowly to the abyssal plain below than the surrounding continental shelf. If the 3000 metre contour is taken as the extent of the horizontal protrusion then the maximum extent of this topographic feature is nearly out to the Pratt seamont. The second pronounced topographic feature is the collection of seamounts in the immediate area of the Pratt seamount with the surrounding terrain in comparison appearing

relatively flat.

The circulation along the British Columbian and Alaskan coast near the south of the above region consists of a broad weak poleward current with a speed on the order of 10 cm s^{-1}. This current has its origins in the eastward flowing Sub-Arctic Polar current of the Pacific Ocean situated on about the 50°N line of latitude. Upon reaching the continental shelf of North America this current bifurcates into a poleward and equatorward component. The poleward flowing current being the coastal current mentioned above.

This northward flow continues until it is directed southwestward by the Alaskan shelf where it forms itself into a narrow coastal jet known as the Alaskan Stream. Thomson(1972) has shown that this streaming is dynamically similiar to the intensification of western boundary currents.

The vertical structure of the northward flowing coastal current varies as the distance from the coastline increases. Bennett(1959) classified the velocity profiles into four categories. Figure 2, taken from Bennett's paper, shows that the near coastal current (group 4) is strongly attenuated by depth, with a maximum surface speed of about 10 cm s^{-1}. Group 2 currents, situated to the immediate west of the group 4 currents also montonically decay with depth although the attenuation is not as severe as with the group 4 currents. Typically, group 2 currents have speeds on the order of 5 cm s^{-1}.

Group 3 currents, located more or less westward of the group 2 currents have smaller speeds than either group 4 or

group 3 currents. Typically they have magnitudes on the order of 3 cm s^{-1}. One interesting feature of the contour between group 2 and group 3 currents is the suggestion of a tongue of group 2 currents which protrudes northward into a nominally group 3 regime. This protrusion lies precisely over the Pratt seamount, a significant orographic feature of the regional bathymetry.

Figure 2 also gives the qualitative impression that most of the transport occurs in the upper layers of the ocean. Calculations by Tabata(1982) confirm this by reporting that about 75 percent of the transport occurs in the first 500 metres of ocean.

Tabata's(1982) analysis of geopotential anomaly data for this region for the years 1954 to 1967 has shown the existence of a mesoscale baroclinic anticyclonic eddy, situated at about 57°N 138°W, referred to as the Sitka eddy. This location would place the Sitka eddy slightly to the east and north of the Pratt seamount, and slightly to the west and north of the continental shelf bump. This location is shown in Figure 1.

The Sitka eddy is observed to have a typical radius of between 200 and 300 km. Obseved surface speeds range from 15 cm s^{-1} to 37 cm s^{-1} at 50 km from the centre of the eddy. Estimates of the surface speed, based on drifting-buoy trajectories, go as high as 110 cm s^{-1} 70 km from the eddy centre. The depth to which the eddy occurs is typically about 1000 metres, although evidence supports estimates up to 2000 metres.

The Sitka eddy seems to be most detectable during the Northern Hemisphere summer and less so in the winter. Tabata(1982) has identified it during the late spring through late summer of the years 1958, 1960 and 1961. In other years, during the same season, Tabata's analysis has shown that there is some ambiguity in attempting to resolve the Sitka eddy. However, within some of these years, Tabata's maps of the geopotential anomaly show a marked clockwise flow at the location of the Sitka eddy. Even still, significant variability has been observed in the region's currents. Interestingly, Bennett(1959) has a figure of the transport for 1955 which clearly indicates a strong cyclonic eddy in the region where the Sitka eddy normally occurs. On balance, the evidence indicates that the Sitka eddy is a more or less annual event occuring in the late spring through to late summer.

The relatively stable geographical location of the Sitka eddy naturally suggests that topography may be an important forcing mechanism in its generation and maintainance. With this possibility in mind this thesis examines the following conjecture: that the mean flow typically observed in this region during the spring and summer can interact with the prominent regional topography to produce mesoscale anticyclonic eddies.

2.2 The Basic Equations Of Motion And Mass

This section is concerned with formulating the appropriate mathematical model for topographically induced baroclinic eddies. The basic equations for momentum and mass are nondimensionalized with macro scales in order to ascertain the

qualitative nature of the fluid dynamics.

The subsequent analysis occurs on a f-plane. In other words a right-handed uniformly rotating cartesian coordinate system. If the ordered triple (x*,y*,z*) is a point in this space, then positive x* points northward, positive y* points westward and positive z* points upward. The location of the origin of this coordinate sytem is motivated by the geometry of the problem discussed in the last section. The plane y* = 0 is taken to be the coastline. The plane z* = 0 is taken as the abyssal plain described last section. The origin is taken as the point on the intersection of the above two planes corresponding to latitude 55°N. The angular velocity of the f-plane is given by (0,0,f/2) where $f=2|\Omega|\sin(\theta)$ is the Coriolos parameter, $|\Omega|$ the magnitude of the angular velocity of the Earth's rotation and θ the latitude.

Let (u*,v*,w*), p*, ρ* be the velocity, pressure and density fields respectively. The steady, inviscid, incompressible, stratified, Boussinesq and f-plane dimensionalized equations of motion can be written (LeBlond and Mysak; 1978) as:

$$u^*\partial^*_1 u^* + v^*\partial^*_2 u^* + w^*\partial^*_3 u^* - fv^* = -\rho_0^{-1}\partial^*_1 p^*$$

$$u^*\partial^*_1 v^* + v^*\partial^*_2 v^* + w^*\partial^*_3 v^* + fu^* = -\rho_0^{-1}\partial^*_2 p^*$$

$$\rho_0(u^*\partial^*_1 w^* + v^*\partial^*_2 w^* + w^*\partial^*_3 v^*) + g\rho^* = -\partial^*_3 p^*$$

$$\partial^*_1 u^* + \partial^*_2 v^* + \partial^*_3 w^* = 0$$

$$u^*\partial^*_1\rho^* + v^*\partial^*_2\rho^* + w^*\partial^*_3\rho^* = 0.$$

The above equations have been written with the following conventions. The superscript '*' implies that the variable immediately preceeding it is dimensional. The quantities ∂^*_1, ∂^*_2 and ∂^*_3 are the first partial derivatives with respect to the dimensionalized variables x*, y* and z* respectively. The Boussinesq approximation has been implemented through defining ρ_0 as a constant reference density. However ρ^* is defined as a dimensionalized variable density.

The first three equations are the momentum equations in the x*, y* and z* directions respectively. The fourth and fifth equations express the fact the flow is incompressible. Since the flow is inhomogeneous but incompressible the usual requirement that the velocity field is solenoidal (the fourth equation) is supplemented by the fifth equation which expresses the fact that the density of a fluid particle remains constant following its motion.

In order to assess the importance of each term in the above equations it is appropriate to nondimensionalize each variable utilizing qualitative geophysical fluid dynamic balances. For example, the ocean to lowest order is at rest and in hydrostatic balance. Therefore the mean pressure and density fields are in hydrostatic equilibrium, which suggests an appropriate scaling for them. Large scale motions, such as baroclinic eddies, are

primarily in geostrophic balance. It follows that the dynamic pressure field associated with fluid motion should be nondimensionalized using geostrophic scaling. Associated with the dynamic pressure field is a dynamic density field which is scaled so that these two fields are in hydrostatic balance.

The horizontal coordinates x* and y* are scaled by L, a characteristic length obtained from geometrical considerations, discussed later in this section. The vertical coordinate z* is scaled by the mean ocean depth, say H. The horizontal velocity field u* and v* is scaled with a characteristic speed U which is obtained from upstream flow conditions.

The scaling for the vertical velocity is deduced from the fact that the velocity field is nondivergent. Suppose for the moment that all three terms in $\nabla^*\cdot(u^*,v^*,w^*)=0$ are the same order of magnitude. (Here ∇^* is the dimensionalized Laplacian.) It follows that w* should be scaled with UHL^{-1}. However it turns out that this is an over estimate of the order of magnitude of the vertical velocity. Since the horizontal velocity field is scaled via geostrophy the resulting flow is essentially horizontally nondivergent. This implies to a first approximation that there is no vertical shear in the vertical velocity. So that if ever w*=0 then throughout the water column w*=0. For quasi-geostrophic dynamics a better estimate of w* is $U^2H(fL^2)^{-1}$.

The nondimensional (unasterisked) variables are defined as follows:

$$(x^*,y^*) = L(x,y),\ z^* = Hz$$

$$(u^*,v^*) = U(u,v),\ w^* = \epsilon UHL^{-1}w$$

$$\rho^* = \rho_0[\bar{\rho}(z) + \epsilon F\rho(x,y,z)]$$

$$p^* = \rho_0 gH\bar{p}(z) + \rho_0 fULp(x,y,z)\ ,$$

with ϵ defined as the Rossby number $U(fL)^{-1}$ and F the squared ratio of the length scale to the external Rossby deformation radius, ie. $L^2f^2/(gH)$. The terms $\bar{\rho}(z)$ and $\bar{p}(z)$ are the mean density and pressure fields respectively, which depend only the vertical coordinate. These two fields are in hydrostatic balance, are flow independent and must be obtained from observation. When the above scaled variables are substituted into the equations of motion, they result in:

$$\epsilon(u\partial_1 u + v\partial_2 u + \epsilon w\partial_3 u) - v + \partial_1 p = 0$$

$$\epsilon(u\partial_1 v + v\partial_2 v + \epsilon w\partial_3 v) + u + \partial_2 p = 0$$

$$\epsilon^2\delta^2(u\partial_1 w + v\partial_2 w + \epsilon w\partial_3 w) + \rho + \partial_3 p = 0$$

$$\partial_1 u + \partial_2 v + \epsilon\partial_3 w = 0$$

$$u\partial_1\rho + v\partial_2\rho + \epsilon w\partial_3\rho = S(z)w\ ,$$

with the quantities ∂_1, ∂_2 and ∂_3 defined as the first partials with respect to x, y and z respectively.

The parameter δ is the aspect ratio defined as HL^{-1}. The aspect ratio is thought of as estimating the ratio of the length scale associated with vertical motions to the length scale associated with horizontal motions. If the aspect ratio is

small compared to unity then the flow is primarily horizontal.

The Rossby number ϵ measures the degree to which the nonlinearity in the equations of motion force a departure from strict geostrophy. The hydrostatic approximation requires that $\epsilon\delta << O(1)$. Later in this section it is shown that $\delta \simeq O(\epsilon)$ with $\epsilon << O(1)$.

The parameter F has the physical interpetation of measuring the contribution to the total potential vorticity of the vorticity associated with barotropic isobaric deflections compared to the relative vorticity $\partial_1 v - \partial_2 u$. Thus if $F << O(1)$, then the sea surface can be approximated as a rigid lid. However if $F \simeq O(1)$ then the vorticity associated with sea surface deformation is not a negligible aspect of the potential vorticity. Later in this section it shown that $F \simeq O(\epsilon)$.

The quantity S(z) is defined

$$S(z) = -F^{-1}D_3\overline{\rho}$$

with D_3 the ordinary derivative with respect to z. Willmott and Mysak(1980) calculated a least squares fit of a Brunt-Vaisala frequency typically observed in the north east Pacific Ocean, with an exponential of the form,

$$[N^*(z^*)]^2 = N_0^2 \exp[\gamma^*(z^*-H)] \ .$$

This expression has been written in dimensional form, with $z^*=0$ corresponding to the ocean floor in the absence of topography

and $z^*=H$ to the ocean surface. The least squares procedure resulted in $N_0 = .011045\ s^{-1}$ and $\gamma^* = (254.51)^{-1}\ m^{-1}$.

Since the definition of the Boussinesq Brunt-Vaisala frequency is

$$[N^*(z^*)]^2 = -g(H\rho_0)^{-1}D_3[\rho_0\bar{\rho}(z)]$$

it follows that

$$D_3\bar{\rho}(z) = -N_0^2Hg^{-1}\exp[\gamma(z-1)]$$

where $\gamma = \gamma^*H$, and consequently that

$$S(z) = [(N_0H)/(fL)]^2\exp[\gamma(z-1)] \ .$$

It is clear that $S(z)$ can be interpeted as a nondimensional Brunt-Vaisala frequency. The parameter $(N_0H)/(fL)$ is a stratification or Burger number. It measures the ratio of the internal Rossby radius to the geometric length scale L. In the situation where $S << O(1)$ the motion is barotropic implying that the effects of stratification are negligible. On the other hand when $S >> O(1)$ baroclinicity is a dominant feature of the fluid dynamics.

In section one of this chapter a general discussion of the bathymetric and oceanographic data in this region was presented. Based on this discussion it is now possible to make a reasonable

qualitative estimate of the parameters ϵ, δ, F and $s_0 = [(N_0H)/(fL)]^2$.

The depth of the abssyal plain is on the order of 3500 metres. This is chosen to be H. The distance between the coastline and the Pratt seamount is on the order of 400 km. This chosen to be L. The magnitude of Earth's rotation vector is $7.292 \cdot 10^{-5}$ s^{-1}, so that at 55°N the Coriolos parameter is $1.2 \cdot 10^{-4}$ s^{-1}. Tabata(1982) reported currents as high as 1 ms^{-1}, so we take $U = 1$ ms^{-1}. The value for N_0 is taken to be that calculated by Willmott and Mysak(1980).

With this scaling the nondimensional parameters are: F=0.07, ϵ=0.02, δ=0.01 and s_0=0.65. Consequently it is expected that the dynamics of the region is governed by $s_0 \simeq O(1)$, $\delta \simeq O(\epsilon)$, $F \simeq O(\epsilon)$ and that $\epsilon << O(1)$.

This parameter regime implies that the effects of vortex tube stretching is an important source of vorticity in the water column. However, the barotropic response of the ocean, which is manifested in a sea surface slope is negligible. Therefore the ocean surface can be approximated as a rigid lid. The aspect ratio appears to be at most the same order of magnitude as the Rossby number. Consequently a hydrostatic balance between the pressure and density fields holds to a remarkably good approximation.

Figure 3 is a graph of the nondimensional Brunt-Vaisala frequency S(z) vs. z. The largest gradient in S(z) occurs in the top 25% of ocean, implying that in the upper regions of the water column the rest state density varies rapidly. In the

interior of the water column ($z = 0$ to $z \simeq .5$) $S(z) \simeq 0$, so that the density is approximately uniform.

Figure 4 is a graph of the nondimensional density field $\bar{\rho}$ vs. z. The scale density ρ_0 is chosen to be an average surface density, resulting in $\bar{\rho}(0) = 1$. Typical values for the surface density in the north east Pacific Ocean (Tabata; 1982) place $\rho_0 \simeq 1025$ kg m^{-3}.

The density profile in Figure 4 increases about .3% in the top 25% of ocean, consistent with the observations contained in Tabata(1982) and Bennett(1959). Below $z \simeq .75$ (900 metres) the density is uniform with a value of about 1.0032 times its surface value.

2.3 Quasi-Geostrophic Potential Vorticity Equation

The relative estimates of the parameters F, δ, s_0 and ϵ suggests that the significant parameter is the Rossby number. The smallness of ϵ is exploited by constructing the lead terms of a naive asymptotic expansion for u, v, w, p and ρ in the Rossby number.

Consider a solution of the form:

$$u = u^{(0)} + \epsilon u^{(1)} + \epsilon^2 u^{(2)} \ldots$$

$$v = v^{(0)} + \epsilon v^{(1)} + \epsilon^2 v^{(2)} \ldots$$

$$w = w^{(0)} + \epsilon w^{(1)} + \epsilon^2 w^{(2)} \ldots$$

$$p = p^{(0)} + \epsilon p^{(1)} + \epsilon^2 p^{(2)} \ldots$$

$$\rho = \rho^{(0)} + \epsilon \rho^{(1)} + \epsilon^2 \rho^{(2)} \ldots \quad .$$

Substitution of the above expansions in to the scaled equations of motion implies that the O(1) field equations are:

$$\partial_1 p^{(0)} - v^{(0)} = 0 \qquad 2.1$$

$$u^{(0)} + \partial_2 p^{(0)} = 0 \qquad 2.2$$

$$\rho^{(0)} + \partial_3 p^{(0)} = 0 \qquad 2.3$$

$$\partial_1 u^{(0)} + \partial_2 v^{(0)} = 0 \qquad 2.4$$

$$u^{(0)}\partial_1 \rho^{(0)} + v^{(0)}\partial_2 \rho^{(0)} = S(z)w^{(0)} \ . \qquad 2.5$$

The $u^{(0)}$ and $v^{(0)}$ are in geostrophic balance with the $p^{(0)}$ pressure field. However since the O(1) pressure field trivially satisfies $(\partial_1,\partial_2)\cdot(u^{(0)},v^{(0)}) = 0$, the above system of equations is underdetermined, referred to as geostrophic degeneracy. The field equations are closed by constructing the quasi-geostrophic potential vorticity equation.

To begin with, the relevant $O(\epsilon)$ equations are:

$$u^{(0)}\partial_1 u^{(0)} + v^{(0)}\partial_2 u^{(0)} - v^{(1)} = -\partial_1 p^{(1)} \qquad 2.6$$

$$u^{(0)}\partial_1 v^{(0)} + v^{(0)}\partial_2 v^{(0)} + u^{(1)} = -\partial_2 p^{(1)} \qquad 2.7$$

$$\partial_1 u^{(1)} + \partial_2 v^{(1)} + \partial_3 w^{(0)} = 0. \qquad 2.8$$

Taking $\partial_1(2.7) - \partial_2(2.6)$ and using 2.8 and 2.4 it follows that,

$$u^{(0)}\nabla^2 v^{(0)} - v^{(0)}\nabla^2 u^{(0)} = \partial_3 w^{(0)}, \qquad 2.9$$

where ∇^2 is the horizontal Laplacian given by $\partial_{11} + \partial_{22}$. Rewriting 2.9 in terms of the pressure field yields

$$J[p^{(0)}, \nabla^2 p^{(0)} + \partial_3(S^{-1}\partial_3 p^{(0)})] = 0 ,$$

where J[A,B] is the Jacobian of A and B ie. $\partial_1 A \partial_2 B - \partial_2 A \partial_1 B$.

The terms on the right in the Jacobian formalism form the potential vorticity. The first of these is the vorticity associated with the angular momentum of the fluid and the second is the vorticity associated with the stretching of vortex tubes. Since the Jacobian between the stream function and the potential vorticity is zero, the potential vorticity can be written in terms of the pressure field. In other words the potential vorticity is conserved along streamlines. This implies that the essential physical feature incorporated into the mathematical model is that the conservation of angular momentum is primarily a balance between the relative vorticity (ie. the z-component of the curl of the velocity field) and the angular momentum induced by baroclinic vortex tube stretching.

In view of the above remarks the quasi-geostrophic potential vorticity equation can be written as:

$$\nabla^2 p^{(0)} + \partial_3[S^{-1}\partial_3 p^{(0)}] = \text{func}[p^{(0)}] ,$$

where 'func' means function. Generally speaking the precise functional form of func[$p^{(0)}$] is determined by the upstream flow conditions. This thesis considers a function of the form $-\kappa p^{(0)}$, with κ a real number. It will become obvious that even a linear function as this will give rise to a nontrivial upstream vertical current shear. The real advantage of the linearity is, of course, that it permits analytical solutions. Therefore the conservation of potential vorticity reduces to finding the stream function which satisfies

$$[\nabla^2 + \partial_3(S^{-1}\partial_3) + \kappa]p^{(0)} = 0 \qquad 2.10$$

subject to appropriate boundary conditions.

Ideally the domain in which the above equation should be solved is the semi-infinite domain which is bounded below by the bottom, above by the surface and to one side by the coastline. However assuming that the topography has compact support and that any topographic mean flow interaction must decay with increasing distance from the source topography it follows that a suitably large channel parallel to the coastline can mimick the ideal domain. Mathematically this assumption allows the cross stream current structure to be solved in terms of cross stream orthogonal basis functions.

Suppose that the bottom of the ocean is given by z=h(x,y). When there is no topography h(x,y)=0. The potential vorticity equation 2.10 is solved in the domain given by:

$$\{ (x,y,z): -\infty<x<+\infty,\ 0<y<2,\ h(x,y)<z<1 \}.$$

The seaward channel wall has been chosen as y=2. Numerical calculations, presented in chapter IV, confirm this choice as suitable.

The boundary conditions which the pressure field must satisfy are now considered. Let the upstream or far field current be given by

$$u_0 = \exp(-\alpha y)Z(z)$$
$$v_0 = 0,$$

where Z(z) represents the vertical structure of the upstream flow field. Since the far field current is assumed O(1) then as $|x| \to \infty$, $u^{(0)} \to u_0$ and $v^{(0)} \to 0$. In terms of the pressure field the O(1) far field boundary condition is:

$$p^{(0)} \to \alpha^{-1}(\exp[-\alpha y] - 1)Z(z) \text{ as } |x| \to \infty .$$

The upstream flow condition corresponds to a horizontally and vertically sheared current. The horizontal shear is exponential with an e-folding length of α^{-1}. In dimensional notation this would be α^{-1}L metres. The vertical shear must be chosen so that the potential vorticity associated with this flow is consistent with linearization done to the quasi-geostrophic potential vorticity equation. Taking $-\partial_2$(2.10) it follows that:

$$D_3(S^{-1}D_3Z) + (a^2 + \kappa)Z = 0 \ .$$

Along the boundaries of the channel the normal component of the velocity field must vanish. On y=0 and y=2 this means that $v^{(0)}$ must be identically zero. On z=1, the sea surface, $w^{(0)} = 0$. In terms of the pressure field:

$$\partial_1 p^{(0)} = 0 \text{ on } y=0 \text{ and } y=2$$
$$J[p^{(0)}, S^{-1}\partial_3 p^{(0)}] = 0 \quad \text{on } z=1. \qquad 2.11$$

The boundary conditions at z = 1 and z = 0 are cast into the form suggested by Hogg(1980). The surface boundary condition implies that $\partial_3 p^{(0)}$ is conserved along streamlines on z=1. For those streamlines which originate upstream 2.11 integrates to

$$Z\partial_3 p^{(0)} - p^{(0)} D_3 Z = 0 \text{ on } z=1.$$

The upstream vertical current structure function trivially satisfies this boundary condition. Consequently the boundary value of Z at z=1 is a free parameter, chosen from observation.

Along the bottom of the channel the normal component of the velocity field must vanish. In dimensional variables this can be written:

$$w^* = (u^*, v^*) \cdot \nabla^* h^*(x^*, y^*) \text{ on } z^* = h^*(x^*, y^*).$$

Defining $h^*(x^*,y^*) = \epsilon H h(x,y)$, results in the nondimensional bottom boundary condition:

$$w = (u,v)\cdot\nabla h(x,y) \text{ on } z = \epsilon h(x,y).$$

Let the maximum height of $h^*(x^*,y^*)$ be h_0. For $h(x,y) \simeq O(1)$ it is required that $\epsilon^{-1}(h_0/H) \simeq O(1)$. This implies that the height of the topography is at most $O(\epsilon)$ with respect to the mean depth of the ocean. This provides formal justification for expanding the bottom boundary condition in a Taylor series about $z=0$ as follows:

$$(w^{(0)} + \ldots) + \epsilon h\partial_3(w^{(0)} + \ldots) + \ldots = [(u^{(0)} + \ldots ,v^{(0)} + \ldots) + \epsilon h\partial_3(u^{(0)} + \ldots , v^{(0)} + \ldots) + \ldots]\cdot\nabla h \text{ on } z=0.$$

The $O(1)$ bottom boundary condition is therefore given by:

$$w^{(0)} = (u^{(0)},v^{(0)})\cdot\nabla h \text{ on } z=0,$$

which in terms of the pressure field is written,

$$J[p^{(0)}, \partial_3 p^{(0)} + S(0)h(x,y)] = 0 \text{ on } z = 0.$$

This can be integrated upstream to yield

$$Z\partial_3 p^{(0)} - p^{(0)}D_3 Z = -Z(z)S(z)h(x,y) \text{ on } z=0.$$

Since h(x,y) has compact support, as $|x| \to \infty$; h(x,y)=0 implying Z(z) trivially satisfies this boundary condition. Therefore the boundary value of Z(z) for z=0 is a free parameter obtained from observation.

The idealized topography h(x,y) has the form,

$$h(x,y) = h_1\cos(\pi x)\cos(\pi y) \quad \text{for } |x|<.5 \quad 0<y<.5 \qquad 2.12$$

$$= h_2\cos[4\pi(x-.6)]\cos[4\pi(y-.75)]$$

$$\text{for } |x-.6|<.125 \text{ and } |y-.75|<.125 \qquad 2.13$$

$$= 0 \quad \text{for all other x and y,} \qquad 2.14$$

where h_1 and h_2 are the maximum heights of the continental slope protrusion and the Pratt seamount respectively, scaled by the quantity ϵH. Figure 5 is a contour map of the idealized topography, with contouring intervals of 5 units ($5\epsilon H$ metres). The support of h(x,y) was obtained by examing Figure 1 and estimating the relevant coordinate lengths.

The form of h(x,y) given by 2.12 corresponds to the continental slope protrusion. The form of h(x,y) given by 2.13 models the the collection of seamounts in the immediate vincinty of the Pratt seamount as a smooth orographic feature with the nondimensional height of the Pratt seamount. The form for h(x,y) given by 2.14 corresponds to the abyssal plain.

Finally, the problem for the O(1) flow field reduces to

finding the solution of the following inhomogeneous Helmoltz boundary value problem:

$$[\nabla^2 + \partial_3(S^{-1}\partial_3) + \kappa]p^{(0)} = 0 \qquad 2.15$$

subject to the boundary conditions

$$\partial_1 p^{(0)} = 0 \quad \text{on } y=0 \text{ and } y=2 \qquad 2.16$$

$$Z\partial_3 p^{(0)} - p^{(0)}D_3 Z = 0 \quad \text{on } z=1 \qquad 2.17$$

$$Z\partial_3 p^{(0)} - p^{(0)}D_3 Z = -ZSh \quad \text{on } z=0 \qquad 2.18$$

$$p^{(0)} \to a^{-1}(\exp[-ay] - 1)Z(z) \quad \text{as } |x| \to \infty \qquad 2.19$$

with $Z(z)$ the solution of

$$D_3(S^{-1}D_3 Z) + (\kappa + a^2)Z = 0 \qquad 2.20$$

subject to the boundary conditions

$$Z(0) = b \quad \text{and} \quad Z(1) = a. \qquad 2.21$$

Figure 1 - Bathymetry of the north east Pacific Ocean

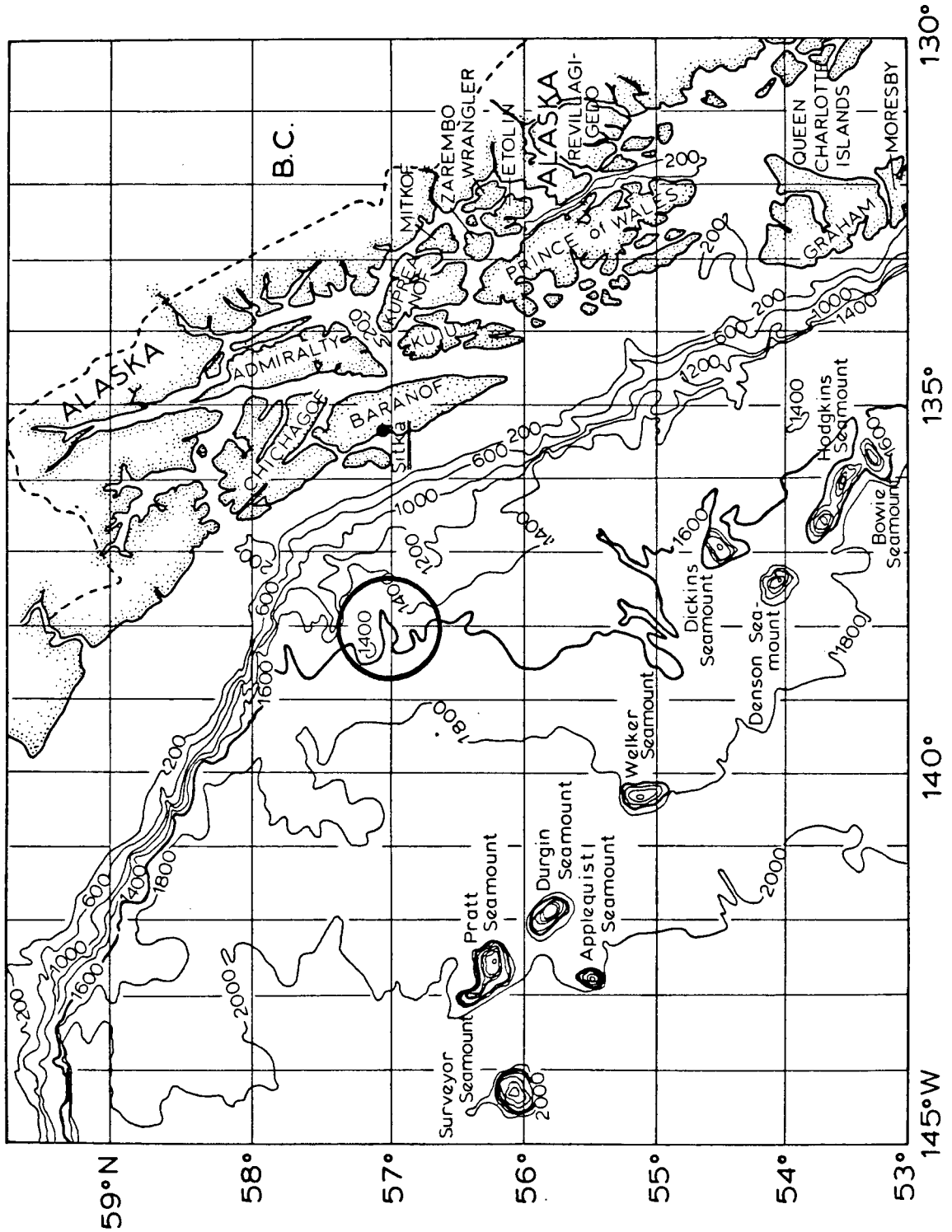

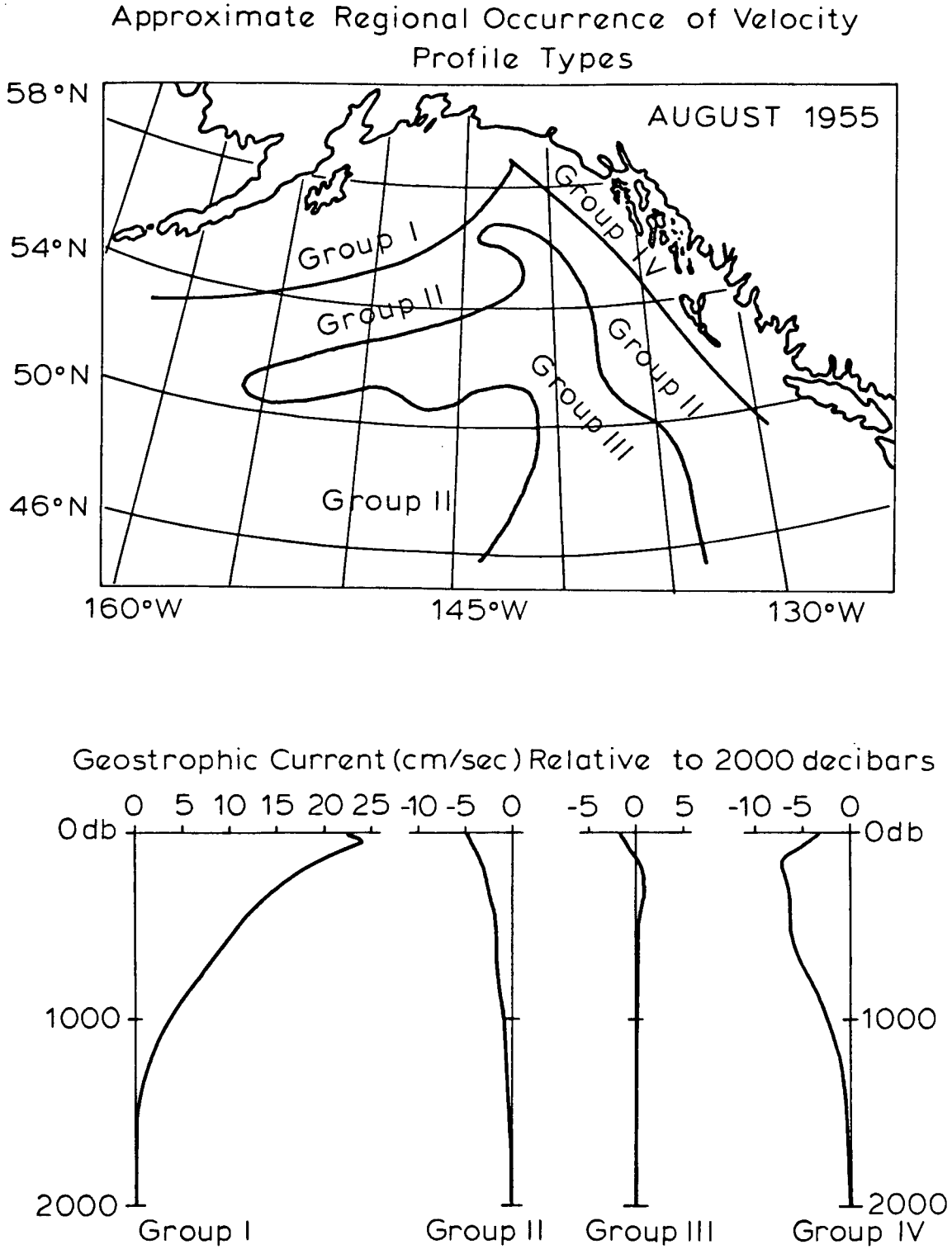

Figure 2 - Horizontal and vertical current structure in the north east Pacific Ocean

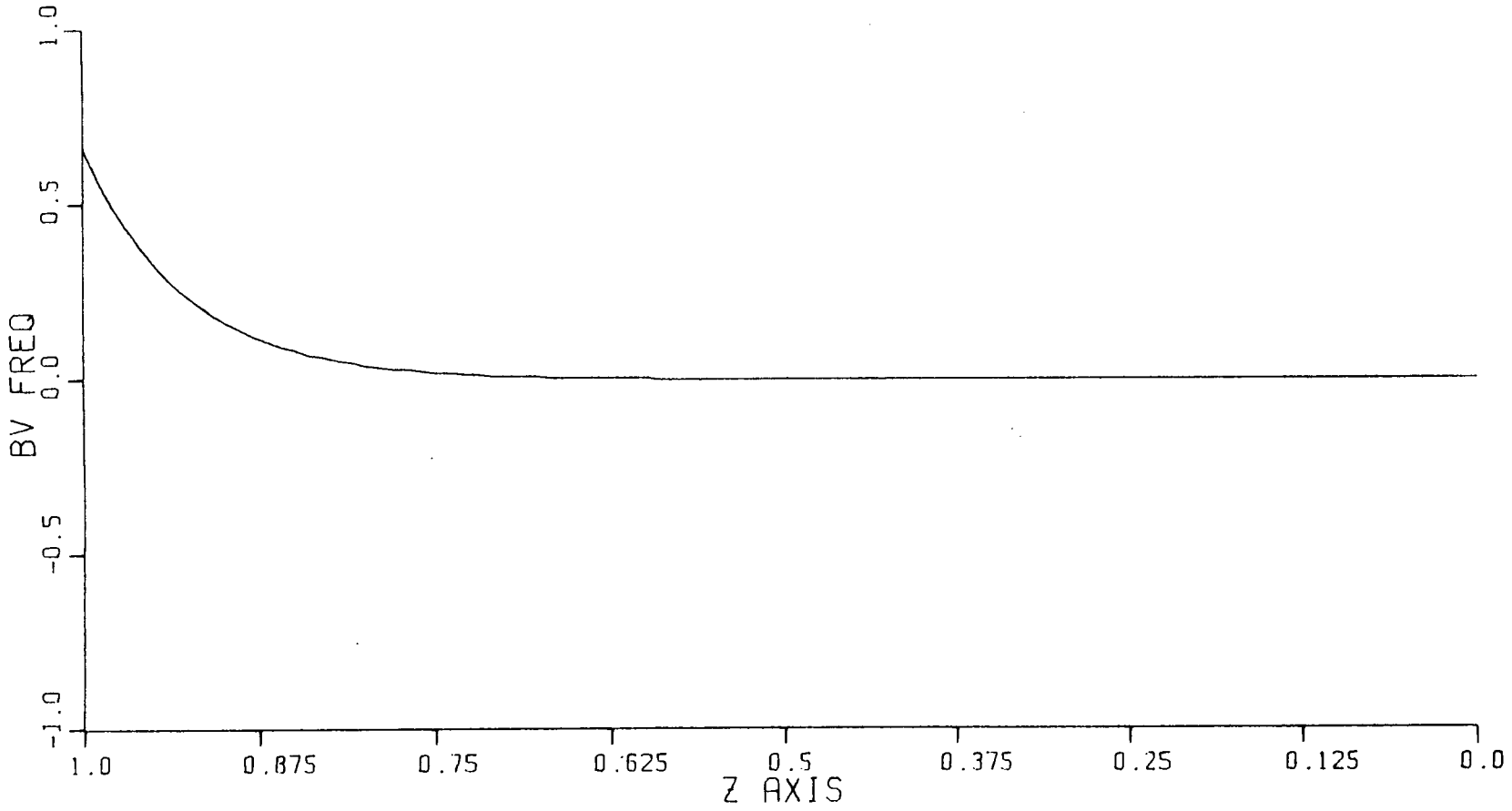

Figure 3 - Brunt-Vaisala frequency

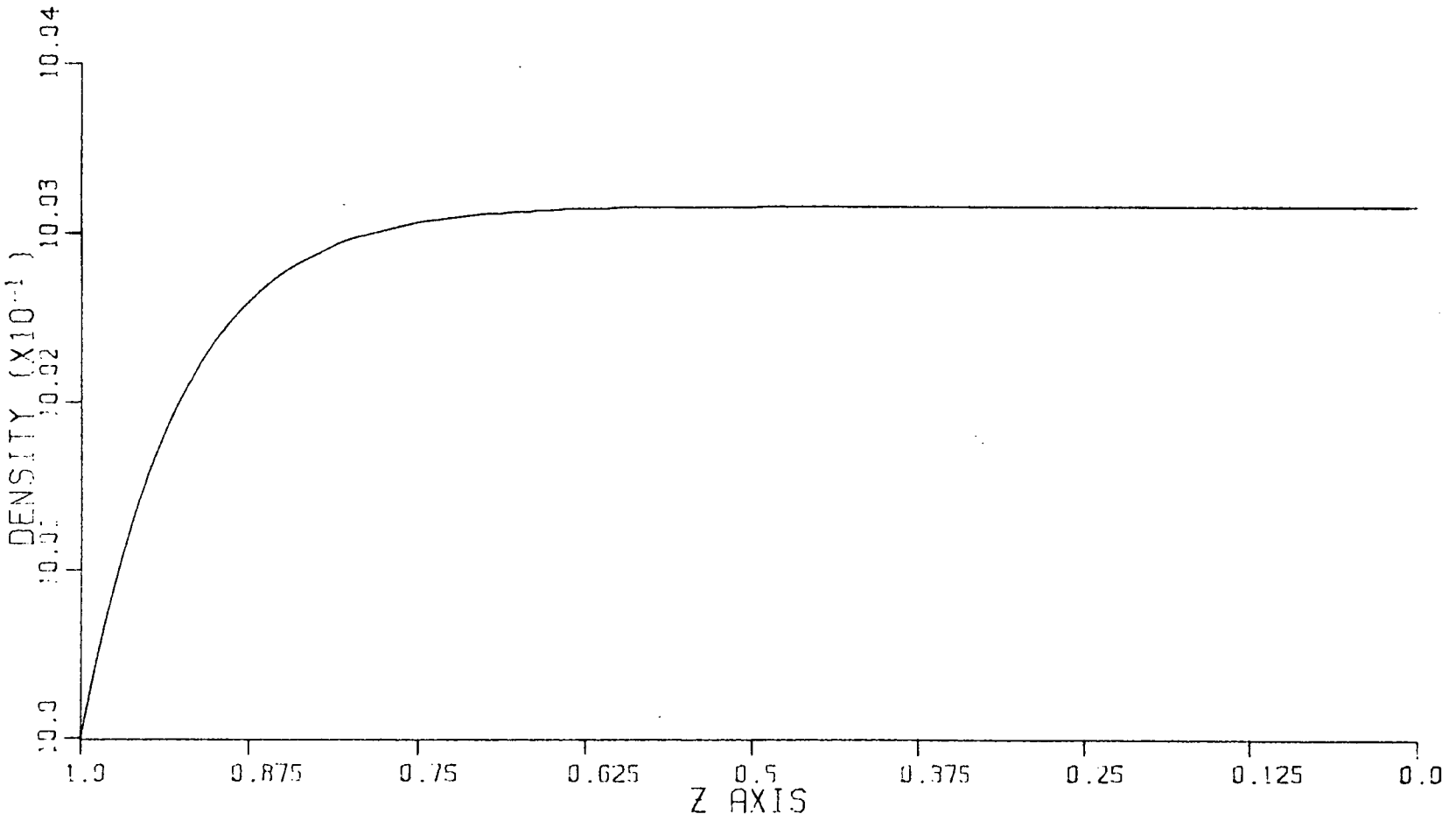

Figure 4 - Mean state density profile

Figure 5 - Contour plot of modelled topography

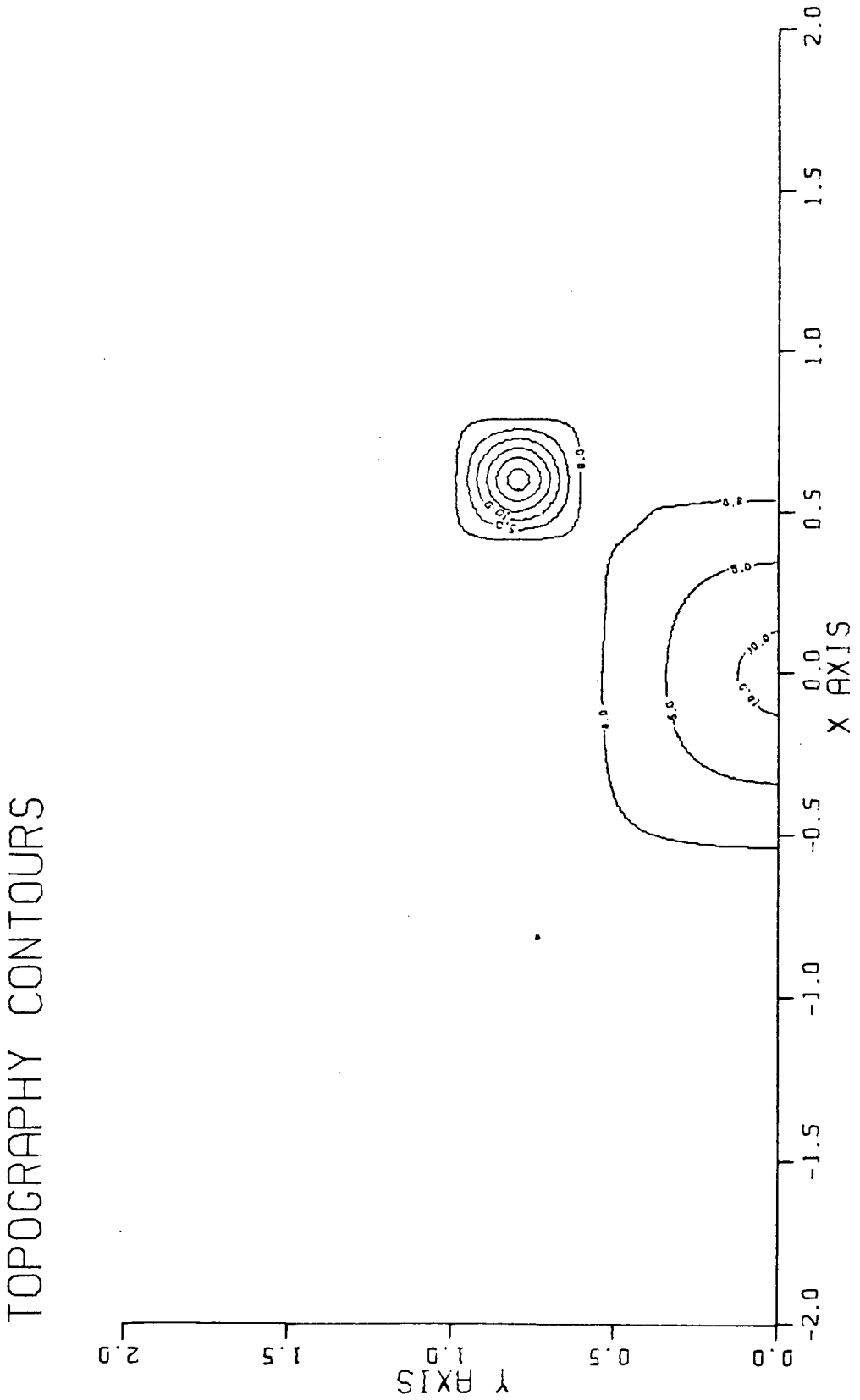

III. SOLUTION OF THE FIELD EQUATIONS

The linearity of the boundary value problem 2.15 through 2.21 is exploited by constructing a solution in the form

$$p^{(0)} = a^{-1}[\exp(-ay) - 1]Z(z) + p(x,y,z).$$

Substituting this expression into 2.15 through 2.19 implies that p(x,y,z) must solve:

$$[\nabla^2 + \partial_3(S^{-1}\partial_3) + \kappa]p = 0 \qquad 3.1$$

subject to the boundary conditions,

$$\partial_1 p = 0 \quad \text{on } y=0 \text{ and } y=2 \qquad 3.2$$

$$Z\partial_3 p - pD_3 Z = 0 \quad \text{on } z=1 \qquad 3.3$$

$$Z\partial_3 p - pD_3 Z = -ZSh \quad \text{on } z=0 \qquad 3.4$$

$$p \to 0 \quad \text{as } |x| \to \infty, \qquad 3.5$$

with Z(z) the solution of 2.20 and 2.21.

The boundary conditions 3.2 and 3.5 imply that p=0 on y=0 and y=2. This is because the boundary planes y=0 and y=2 are parallel to the x-axis and the boundary condition 3.2 implies that the gradient of p in the x direction vanishes on these

planes. Since $p \to 0$ as $|x| \to \infty$ then $p=0$ indentically on $y=0$ and $y=2$. The physical implication is that no net down channel transport can be created from topographic mean flow interaction. The function p is the $O(1)$ effect of the topography on the far field stream function. No restriction is made on the order of magnitude of $p(x,y,z)$. In fact $p \simeq O(a^{-1}\{\exp[-ay] - 1\}Z)$ if flow reversal is to occur.

The function $p(x,y,z)$ is solved for via the following normal mode decomposition (Chao et al.; 1980)

$$p = \sum_{n=0}^{\infty} P_n(x,y)G_n(z) \qquad 3.6$$

with $G_n(z)$ the 'n'th orthonormal eigenfunction solution of:

$$D_3(S^{-1}D_3G_n) + \lambda_n G_n = 0 \qquad 3.7$$

subject to the boundary conditions,

$$ZD_3G_n - G_n D_3Z = 0 \quad \text{on } z=0 \text{ and } z=1 \qquad 3.8$$

$$\int_0^1 G_n(z)G_m(z)dz = \delta_{nm}, \qquad 3.9$$

where δ_{nm} is the Kronecker delta function between n and m.

The governing equations for the cross stream functions $P_n(x,y)$ are obtained by multiplying 3.7 by $p(x,y,z)$ and integrating from 0 to 1 with respect to z ie.,

$$\int_0^1 D_3[S^{-1}D_3G_n]p\,dz + \lambda_n \int_0^1 G_n p\,dz = 0.$$

Integrating the first integrand by parts twice and utilizing 3.1, 3.3 and 3.4 it follows that:

$$(\nabla^2 + \kappa - \lambda_n) \int_0^1 G_n p\,dz = -G_n(0)h(x,y).$$

Since the function p is a linear combination of the eigenfunctions the above equation implies that for each n

$$(\nabla^2 + \kappa - \lambda_n)P_n = -G_n(0)h(x,y) \qquad 3.10$$

subject to the boundary conditions

$$P_n = 0 \quad \text{on } y=0 \text{ and } y=2 \qquad 3.11$$

$$P_n \to 0 \quad \text{as } |x| \to \infty. \qquad 3.12$$

The normal mode solution 3.6 has the property that $\partial_3(p/Z)$ is discontinuous at $z=0$. The boundary condition 3.4 can be rewritten in the form $\partial_3(p/Z) = -S(z)h(x,y)/Z(z)$ on $z=0$ and $\sum_{n=0}^{\infty} P_n$ (3.8) can be written in the form $\partial_3(p/Z) = 0$ on $z=0$. Assuming that $Z(z)$ assumes its boundary condition at $z=0$ smoothly it follows that $\partial_3 p(z=0^+) - \partial_3 p(z=0) = -S(0)h(x,y)$. Consequently $u^{(0)}$, $v^{(0)}$ and $p^{(0)}$ are continuous at $z=0$ while $\rho^{(0)}$ and $w^{(0)}$, which depend on $\partial_3 p$ are not. The order of magnitude of the discontinuity in $\partial_3 p$ is about $30 \cdot e^{-14}$ resulting in a numerically insignificant correction to the $\rho^{(0)}$ and $w^{(0)}$ fields at $z = 0$.

In the remainder of this chapter the solutions for $P_n(x,y)$, $G_n(z)$ and $Z(z)$ are derived. In section one the solution of 3.10, 3.11 and 3.12 is obtained. In section two the problem 2.20 and 2.21 is solved. In section three the problem 3.7, 3.8 and 3.9 is solved. In section four the formulae for the O(1) pressure, velocity, mass transport and density fields are computed.

3.1 Horizontal Amplitude Functions

In this section the 'n'th cross stream, or the horizontal amplitude function P_n is obtained. These functions are the solution of the two dimensional inhomogeneous Helmholtz problem 3.10, 3.11 and 3.12. The inhomogeneity or in other words the forcing term, corresponds to the excitement of the 'n'th eigenmode by the topography. In the absence of topography it is

expected that the interaction pressure field p(x,y,z) vanishes.

Consider the following reformulation of 3.12. For every $\epsilon > 0$ there exists $\delta < \infty$ such that for every $|x| > \delta$ the maximum over $y\epsilon[0,2]$ of $|P_n(x,y)|$ satisfies $|P_n(x,y)| < \epsilon$. It is shown later in this section that $\lambda_0 = a^2 + \kappa$, hence $\lambda_n - \kappa > 0$ for all n. In order to avoid difficulties with the semi-infinite domain consider the problem of solving 3.10, with $h(x,y) = 0$, in the domain given by $\{(x,y): |x| < \delta \text{ and } 0 < y < 2\}$, subject to 3.11 and the reformulated 3.12 for a given ϵ. Applying the maximum principle to this problem it is clear that the maximum of $|P_n|$ must occur on $|x| = \delta$. However this can be made arbitrarily small, by $\epsilon \to 0$ and $\delta \to \infty$.

Linearity and uniqueness therefore imply that the related homogeneous problem has only the trivial solution. This fact in turn implies that there exists a unique Green's function for the horizontal amplitude equations.

The solution of 3.10, 3.11 and 3.12 is constructed from the Green's function, defined as $g(x,y|x_0,y_0)$. The Green's function satisfies:

$$(\nabla^2 + \kappa - \lambda_n)g = -G_n(0)\delta(x-x_0)\delta(y-y_0), \qquad 3.13$$

with $\delta(x-x_0)$ and $\delta(y-y_0)$ the Dirac delta functions centered at $x = x_0$ and $y = y_0$ respectively.

Let F(g) be the Fourier transform with respect to x of

$g(x,y|x_0,y_0)$, ie.

$$F(g) = \int_{-\infty}^{\infty} g(x,y|x_0,y_0)\exp(ikx)dx,$$

where $i^2=-1$ and k is the transform variable. Taking the Fourier transform of 3.13 and 3.11 with respect to x yields,

$$(\partial_{22} + \kappa - \lambda_n - k^2)[F(g)] = -G_n(0)\delta(y-y_0)\exp(ix_0k) \qquad 3.14$$

subject to the boundary conditions:

$$F(g) = 0 \quad \text{on } y=0 \quad \text{and} \quad y=2. \qquad 3.15$$

The Fourier transform of the Green's function is obtained in the form:

$$F(g) = \sum_{m=1}^{\infty} A_{nm}(x_0,y_0,k)\sin(m\pi y/2). \qquad 3.16$$

Modelling the domain as a channel finds its full expression in 3.16. Since 3.14 is defined on a bounded y interval, it is possible to express the solution of 3.14 and 3.15 as a linear combination of a complete set of basis functions. The orthogonal basis functions $\sin(m\pi y/2)$ are such a set which trivially satisfy the boundary conditions.

Substitution of 3.16 into 3.14 implies that:

$$\sum_{m=1}^{\infty} \{(\kappa - \lambda_n - k^2 - (\pi m/2)^2)A_{nm} \sin(m\pi y/2)\} =$$

$$-G_n(0)\exp(ix_0k)\delta(y-y_0).$$

The orthogonality of the cross stream basis functions implies that the coefficient functions $A_{nm}(x_0,y_0,k)$ in 3.16 are given by

$$A_{nm} = 2G_n(0)\sin(m\pi y_0/2)\exp(ix_0k)[(m\pi/2)^2 + k^2 + \lambda_n - \kappa]^{-1}.$$

The Green's function is related to its Fourier transform via

$$g(x,y|x_0,y_0) = (2\pi)^{-1} \int_{-\infty}^{\infty} F(g)\exp(-ixk)dk.$$

Substituting 3.16 into this expression yields,

$$g = \sum_{m=1}^{\infty} \{\pi^{-1}\sin(m\pi y/2)\sin(m\pi y_0/2)G_n(0)\cdot$$

$$\int_{-\infty}^{\infty} [(m\pi/2)^2 + k^2 + \lambda_n - \kappa]^{-1}\exp[-i(x-x_0)k]dk\}.$$

There are no poles in the above integral since $\lambda_0 = a^2 + \kappa$. To see this consider the following argument. Define a function $\Phi_n(z)$ such that $G_n(z) = \Phi_n(z)Z(z)$. Substituting this form of G_n into 3.7, 3.8 and 3.9, utilizing 2.20, results in

$$D_3[Z^2(D_3\Phi_n)/S] + Z^2[\lambda_n - (a^2 + \kappa)]\Phi_n = 0,$$

$$D_3\Phi_n = 0 \quad \text{on } z = 0 \quad \text{and} \quad z = 1,$$

$$\int_0^1 Z^2\Phi_n\Phi_m\,dz = \delta_{nm}.$$

It follows that for each n

$$\lambda_n = a^2 + \kappa + \int_0^1 Z^2S^{-1}(D_3\Phi_n)^2dz.$$

The minimum eigenvalue λ_0 is obtained by minimizing the above integral over the set of Φ_n's for which $D_3\Phi_n = 0$ on $z = 0$ and $z = 1$. Since the integral is positive definite $(S(z) > 0)$ then its minimum is certainly achieved if it vanishes. It vanishes for constant Φ_n. The only constant Φ_n that can satisfy the orthonormalization condition is $[\int_0^1 Z^2dz]^{-1/2}$. It follows

therefore that $G_0(z) = Z(z)[\int_0^1 Z^2 dz]^{-1/2}$ and $\lambda_0 = a^2 + \kappa$.

Evaluating the above Green's function integral in the absence of any poles therefore yields:

$$g = \sum_{m=1}^{\infty} \{G_n(0)[(m\pi/2)^2 + \lambda_n - \kappa]^{-1}\sin(m\pi y/2)\sin(m\pi y_0/2)\cdot$$

$$\exp[-|x-x_0|((m\pi/2)^2 + \lambda_n - \kappa)^{1/2}]\}. \qquad 3.17$$

The 'n'th horizontal amplitude function is related to its Green's function by,

$$P_n(x,y) = \int_{-\infty}^{\infty} \int_0^2 g(x,y|x_0,y_0)h(x_0,y_0)dy_0dx_0. \qquad 3.18$$

Substituting into this equation h(x,y) given by 2.12, 2.13 and 2.14 yields,

$$P_n(x,y) = h_1 \int_0^{.5} \int_{-.5}^{.5} g(x,y|x_0,y_0)\cos(\pi x_0)\cos(\pi y_0)dx_0dy_0 -$$

$$h_2 \int_{.625}^{.875} \int_{.475}^{.725} g(x,y|x_0,y_0)\cos[4\pi(x_0-.6)]\cos(4\pi y_0)dx_0dy_0. \qquad 3.19$$

Equation 3.19 is the horizontal amplitude function associated with 'n'th vertical mode eigenfunction $G_n(z)$. These functions describe the cross channel structure of the topographically

induced pressure field.

3.2 Far Field Vertical Current Structure

In this section the solution for the vertical structure of the far field or upstream current is obtained. The method of solution for 2.20 and 2.21 is similiar to that used by Bryan and Ripa(1978) in their analysis of vertical temperature structure in the north east Pacific Ocean.

Let $V(z)$ be that function defined as $D_3V(z) = Z(z)$. Substituting this definition into 2.20 for $Z(z)$ allows that equation to be integrated once to yield,

$$D_{33}V + (\kappa + a^2)S(z)V(z) = cS(z), \qquad 3.20$$

with c a constant of integration. The solution of 3.20 is, of course, the sum of the homogeneous solution and a particular solution. The particular solution can be written as $c/(\kappa + a^2)$. Since $Z(z)=D_3V(z)$ there is no contribution from the particular solution to the function $Z(z)$. With no loss of generality the constant in 3.20 can therefore be set identically equal to zero. It turns out that the critical parameter in the qualitative description of $Z(z)$ is the sign of $(\kappa + a^2)$.

Considered now is the case when $(\kappa + a^2) > 0$. A new independent variable t is defined so that

$$t = 2\gamma^{-1}[(\kappa + a^2)S(z)]^{1/2}$$

$$V(t) = V[z(t)].$$

This transformation results in 3.20 being recast into the form:

$$t^2V'' + tV' + t^2V = 0, \qquad 3.21$$

where V' and V'' are the first and second derivatives of $V(t)$ with respect to t, respectively. Equation 3.21 is Bessel's equation of order zero. The general solution of 3.21 is therefore given by

$$V(t) = c_1J_0(t) + c_2Y_0(t), \qquad 3.22$$

where J_0 and Y_0 are Bessel functions of the first and second kind of order zero respectively, and where c_1 and c_2 are constants of integration. Taking the derivative of 3.22 respect to z implies that $Z(z)$ can be written:

$$Z(z) = \exp(\gamma z/2)\{C_1J_1[\lambda\exp(\gamma z/2)] + C_2Y_1[\lambda\exp(\gamma z/2)]\}, \qquad 3.23$$

where J_1 and Y_1 are Bessel functions of the first and second kind of order one respectively, and C_1 and C_2 are constants determined by boundary conditions, and finally where

$$\lambda = (2/\gamma)[s_0(\kappa + \alpha^2)\exp(-\gamma)]^{1/2}. \qquad 3.24$$

Application of the boundary conditions 2.21 implies:

$$C_1 = C_0\{bY_1[\lambda\exp(\gamma/2)] - aY_1[\lambda]\exp(-\gamma/2)\} \qquad 3.25$$

$$C_2 = C_0\{aJ_1[\lambda]\exp(-\gamma/2) - bJ_1[\lambda\exp(\gamma/2)]\} \qquad 3.26$$

where

$$C_0 = \{J_1[\lambda]Y_1[\lambda\exp(\gamma/2)] - J_1[\lambda\exp(\gamma/2)]Y_1[\lambda]\}^{-1}. \qquad 3.27$$

In the case when $\kappa + a^2 < 0$ then the solution is written in terms I_1 and K_1, the modified Bessel functions of the first and second kind of order one respectively. Specifically, the solutions are given by 3.23, 3.25, 3.26 and 3.27 with the changes

$$J_1 \rightarrow I_1 \quad \text{and} \quad Y_1 \rightarrow K_1$$

$$\lambda = (2/\gamma)[s_0|\kappa + a^2|\exp(-\gamma)]^{1/2}.$$

In the case when $\kappa + a^2 = 0$ the baroclinic solution to 2.20 and 2.21 is easily computed to be:

$$Z(z) = C_1\exp(\gamma z) + C_2 \qquad 3.28$$

$$C_1 = (b - a)C_0 \qquad 3.29$$

$$C_2 = [a - b\exp(\gamma)]C_0 \qquad 3.30$$

$$C_0 = [1 - \exp(\gamma)]^{-1}. \qquad 3.31$$

The above solution has as a special case the situation where the upstream current is barotropic. In such a situation, $Z(z) = c$ with $a = b = c$ will imply that $C_1 = 0$ and $C_2 = c$. In fact, assuming the upstream current to be barotropic implies that $\kappa = -a^2$. This can be seen by examining 2.20. If $Z(z) = c$ then $D_3 Z = 0$. The only way 2.20 can be satisfied is if $c = 0$ (which is uninteresting) or if $\kappa + a^2 = 0$.

Numerical calculations show that the qualitative shape of $Z(z)$ changes little with either of the first two cases. Typical parameter values for the north east Pacific Ocean suggest that $\kappa + a^2 > 0$. Consequently further analysis is restricted to that case.

Figure 6 is a graph of $Z(z)$ vs. z for the case $\kappa + a^2 > 0$, with $a = .1$ and $b = .01$. In the region where $S(z) \simeq 0$ it is expected that $Z(z) \simeq$ constant because, roughly speaking, in this regime $V(z)$, the solution of 3.20, must be nearly linear in z implying that $Z(z)$ is constant. The physical interpetation for $Z(z)$ being approximately constant in this region is that in this regime the fluid is virtually homogeneous implying that the horizontal velocity field is nearly barotropic. Rapid changes in $Z(z)$ are therefore constrained to a region of nonzero Brunt-Vaisala frequency. Figure 6 illustrates this with the shapest gradient in $Z(z)$ occuring in the upper ocean.

3.3 Vertical Mode Eigenfunctions And Eigenvalues

The orthonormal eigenfunctions are the solutions of 3.7, 3.8 and 3.9. These equations are solved using the same technique used to obtain the upstream vertical current structure functions. First the function $V_n(z)$ is defined so that $D_3V_n(z) = G_n(z)$. Substituting this definition into 3.7 implies that solving 3.7 reduces to solving,

$$D_{33}V_n(z) + \lambda_n S(z)V_n(z) = 0. \qquad 3.32$$

The transformation

$$t = (2/\gamma)[\lambda_n S(z)]^{1/2}$$

$$V_n(t) = V_n[z(t)],$$

allows 3.32 to be rewritten

$$t^2(V_n)'' + t(V_n)' + t^2V_n = 0,$$

where, as before, $(V_n)''$ and $(V_n)'$ are the first and second derivatives of $V_n(t)$ with respect to t, respectively. This is, of course, Bessel's equation of order zero. Therefore the general solution for $V_n(t)$ is given by,

$$V_n(t) = c_1 J_0(t) + c_2 Y_0(t),$$

which in turn implies that $G_n(z)$ is given by:

$$G_n(z) = \exp(\gamma z/2)\{A_n J_1[c_n \exp(\gamma z/2)] + B_n Y_1[c_n \exp(\gamma z/2)]\}, \quad 3.33$$

$$c_n = (2/\gamma)[\lambda_n s_0 \exp(-\gamma)]^{1/2}. \quad 3.34$$

Here J_0, J_1 and Y_0, Y_1 are Bessel functions of the first and second kind of order zero and one respectively.

The requirement that the G_n's be orthonormal (ie. 3.9) implies that

$$1 = (A_n)^2 \int_0^1 \exp(\gamma z)\{J_0[c_n \exp(\gamma z/2)]\}^2 dz +$$

$$(B_n)^2 \int_0^1 \exp(\gamma z)\{Y_0[c_n \exp(\gamma z/2)]\}^2 dz. \quad 3.35$$

These integrals are easily evaluated by introducing the change of variable $x = c_n \exp(\gamma z/2)$. Let a_n and b_n be the numbers defined as

$$a_n = 2[(c_n)^2 \gamma]^{-1} \int_{c_n}^{c_n \exp(\gamma/2)} x\{J_1(x)\}^2 dx$$

$$b_n = 2[(c_n)^2\gamma]^{-1} \int_{c_n}^{c_n \exp(\gamma/2)} x\{Y_1(x)\}^2 dx$$

which can be integrated exactly to give,

$$a_n = \{(c_n)^2\gamma\}^{-1}[\{xJ_0(x)\}^2 - 2J_0(x)J_1(x) + \{xJ_1(x)\}^2]_{c_n}^{c_n \exp(\gamma/2)} \quad 3.36$$

$$b_n = \{(c_n)^2\gamma\}^{-1}[\{xY_0(x)\}^2 - 2Y_0(x)Y_1(x) + \{xJ_1(x)\}^2]_{c_n}^{c_n \exp(\gamma/2)} . \quad 3.37$$

With the aid of 3.36 and 3.37 the orthonormal condition 3.35 can be succinctly rewritten as

$$(A_n)^2 a_n + (B_n)^2 b_n = 1. \quad 3.38$$

The boundary conditions 3.8 implies that at z=0

$$A_n \{(c_n \gamma/2)J_0(c_n) - [Z'(0)/Z(0)]J_1(c_n)\} +$$
$$B_n \{(c_n \gamma/2)Y_0(c_n) - [Z'(0)/Z(0)]Y_1(c_n)\} = 0, \quad 3.39$$

and that at z=1

$$A_n \{(c_n \gamma/2)\exp(\gamma/2)J_0[c_n \exp(\gamma/2)] -$$
$$[Z'(1)/Z(1)]J_1[c_n \exp(\gamma/2)]\} +$$

$$B_n\{(c_n\gamma/2)\exp(\gamma/2)Y_0[c_n\exp(\gamma/2)] -$$

$$[Z'(1)/Z(1)]Y_1[c_n\exp(\gamma/2)]\} = 0. \qquad 3.40$$

Viewing 3.39 and 3.40 as a system of two equations in the unknowns A_n and B_n, the condition that there exist nontrivial solutions for A_n and B_n is that the determinant of the coefficients must vanish ie.

$$\{(c_n\gamma/2)\exp(\gamma/2)Y_0[c_n\exp(\gamma/2)] - [Z'(1)/Z(1)]Y_1[c_n\exp(\gamma/2)]\}\cdot$$

$$\{(c_n\gamma/2)J_0(c_n) - [Z'(0)/Z(0)]J_1(c_n)\} =$$

$$\{(c_n\gamma/2)\exp(\gamma/2)J_0[c_n\exp(\gamma/2)] - [Z'(1)/Z(1)]J_1[c_n\exp(\gamma/2)]\}\cdot$$

$$\{(c_n\gamma/2)Y_0(c_n) - [Z'(0)/Z(0)]Y_1(c_n)\}. \qquad 3.41$$

Equation 3.41 forms a transcendental equation for the parameter c_n. The allowed c_n's form a discrete denumerable set of real numbers, with the eigenvalue λ_n related to c_n by inverting 3.34 to obtain

$$\lambda_n = [\gamma c_n/2]^2(s_0)^{-1}\exp(\gamma). \qquad 3.42$$

The constants A_n and B_n are obtained from the normalization

condition 3.38 and either 3.39 or 3.40. This calculation implies that:

$$A_n = \{(c_n \gamma/2)Y_0(c_n) - [Z'(0)/Z(0)]Y_1(c_n)\}/C_n \quad , \qquad 3.43$$

$$B_n = -\{(c_n \gamma/2)J_0(c_n) - [Z'(0)/Z(0)]J_1(c_n)\}/C_n \quad , \qquad 3.44$$

with

$$C_n = \{b_n [(c_n \gamma/2)J_0(c_n) - [Z'(0)/Z(0)]J_1(c_n)]^2 + a_n [(c_n \gamma/2)Y_0(c_n) - [Z'(0)/Z(\theta)]Y_1(c_n)]^2\}^{1/2}. \qquad 3.45$$

To summarize, the vertical eigenfunctions are given by 3.33 where A_n and B_n are given by 3.43 and 3.44 respectively, and where the eigenvalues λ_n are the solutions of 3.41 and 3.42.

Figures 7, 8 and 9 are graphs of $G_0(z)$, $G_1(z)$ and $G_2(z)$ vs. z, respectively for a = .1 and b = .01. The qualitative comments made in the last section about the structure of Z(z) are also valid for the eigenfunctions. In the region where $S(z) \simeq 0$ it is expected that $G_n(z)$ should vary slowly. Consequently the zeros of the eigenfunctions concomitant with oscillatory behaviour should occur in the upper ocean. This can be seen in $G_1(z)$ with a zero at z = .9 and in $G_2(z)$ with its two zeros at approximately .95 and .7. Graphs computed of the higher modes also have this feature.

3.4 Formulae For The Pressure, Velocity, Density And Mass Transport Fields

With the solution for the interaction stream function obtained in the previous sections, it is now possible to describe the physical variables: pressure, velocity, density and mass transport. Recall that the O(1) pressure field is given by;

$$p^{(0)} = a^{-1}[\exp(-ay) - 1]Z(z) + \sum_{n=0}^{\infty} P_n(x,y)G_n(z), \qquad 3.46$$

where the functions $Z(z)$, $G_n(z)$ and $P_n(x,y)$ have been obtained in the three previous sections. The remaining calculation required for the stream function is the evaluation of the integral 3.19, which yields:

$$P_n = h_1 G_n(0)\sin(\pi y)R_{n2}(x)[2\pi(\pi^2 + \lambda_n - \kappa)(2\pi^2 + \lambda_n - \kappa)]^{-1} +$$

$$\sum_{\substack{m=1 \\ m\neq 2}}^{\infty} h_1 G_n(0)\sin(m\pi y/2)R_{nm}(x)[m/2 - \sin(m\pi/4)]\cdot$$

$$[\pi(m^2/4 - 1)((m\pi/2)^2 + \lambda_n - \kappa)((m\pi/2)^2 + \pi^2 + \lambda_n - \kappa)]^{-1} -$$

$$\sum_{\substack{m=1 \\ m\neq 2}}^{\infty} 4h_2 G_n(0)\sin(m\pi y/2)S_{nm}(x)[\sin(7\pi m/16) + \sin(5\pi m/16)]\cdot$$

$$[\pi(m^2/4 - 1)((m\pi/2)^2 + \lambda_n - \kappa)(16\pi^2 + (m\pi/2)^2 + \lambda_n - \kappa)]^{-1},$$

where the functions R_{nm} and S_{nm} are given by

$$R_{nm}(x) = 2\pi\exp[-|x|((m\pi/2)^2 + \lambda_n - \kappa)^{1/2}].$$

$$\cosh[((m\pi/2)^2 + \lambda_n - \kappa)^{1/2}/2] \qquad \text{if } |x| > .5$$

$$R_{nm}(x) = 2((m\pi/2)^2 + \lambda_n - \kappa)^{1/2}\cos(\pi x) +$$

$$2\pi\exp[-((m\pi/2)^2 + \lambda_n - \kappa)^{1/2}/2].$$

$$\cosh[x((m\pi/2)^2 + \lambda_n - \kappa)^{1/2}] \qquad \text{if } |x| < .5$$

$$S_{nm}(x) = 8\pi\exp[-|x-.6|((m\pi/2)^2 + \lambda_n - \kappa)^{1/2}.$$

$$\cosh[((m\pi/2)^2 + \lambda_n - \kappa)^{1/2}/8] \qquad \text{if } |x-.6| > 1/8$$

$$S_{nm}(x) = 2((m\pi/4)^2 + \lambda_n - \kappa)^{1/2}\cos[4\pi(x-.6)] +$$

$$8\pi\exp[-((m\pi/2)^2 + \lambda_n - \kappa)^{1/2}/8].$$

$$\cosh[(x-.6)((m\pi/2)^2 + \lambda_n - \kappa)^{1/2}] \qquad \text{if } |x-.6| < 1/8.$$

The O(1) alongshore velocity $u^{(0)}$ is given by 2.2 and 3.46, implying;

$$u^{(0)} = Z(z)\exp(-ay) - \sum_{n=0}^{\infty} \partial_2 P_n G_n , \qquad 3.47$$

where $\partial_2 P_n$ is given by:

$$\partial_2 P_n = h_1 G_n(0)\cos(\pi y) R_{n2} [2(\pi^2 + \lambda_n - \kappa)(2\pi^2 + \lambda_n - \kappa)]^{-1} +$$

$$\sum_{\substack{m=1 \\ m\neq 2}}^{\infty} h_1 m G_n(0)\cos(m\pi y/2) R_{nm} [m/2 - \sin(m\pi/4)] \cdot$$

$$[2((m\pi/2)^2 + \lambda_n - \kappa)(m^2/4 - 1)((m\pi/2)^2 + \pi^2 + \lambda_n - \kappa)]^{-1} -$$

$$\sum_{\substack{m=1 \\ m\neq 2}}^{\infty} 2h_2 m G_n(0)\cos(m\pi y/2) S_{nm} [\sin(7\pi m/16) + \sin(5m\pi/16)] \cdot$$

$$[(m^2/4 - 16)((m\pi/2)^2 + \lambda_n - \kappa)((m\pi/2)^2 + 16\pi^2 + \lambda_n - \kappa)]^{-1} .$$

The O(1) cross channel velocity $v^{(0)}$ is given by 2.1 and 3.46, implying;

$$v^{(0)} = \sum_{n=0}^{\infty} \partial_1 P_n G_n , \qquad 3.48$$

where $\partial_1 P_n$ is given by:

$$\partial_1 P_n = h_1 G_n(0)\sin(\pi y) D_1 R_{n2} [2\pi(\pi^2 + \lambda_n - \kappa)(2\pi^2 + \lambda_n - \kappa)]^{-1} +$$

$$\sum_{\substack{m=1 \\ m\neq 2}}^{\infty} h_1 G_n(0)\sin(m\pi y/2) D_1 R_{nm}[m/2 - \sin(m\pi/4)]\cdot$$

$$[\pi(m^2/4 - 1)((m\pi/2)^2 + \lambda_n - \kappa)((m\pi/2)^2 + \pi^2 + \lambda_n - \kappa)]^{-1} -$$

$$\sum_{\substack{m=1 \\ m\neq 2}}^{\infty} 4h_2 G_n(0)\sin(m\pi y/2) D_1 S_{nm}[\sin(7\pi m/16) + \sin(5\pi m/16)]\cdot$$

$$[\pi(m^2/4 - 1)((m\pi/2)^2 + \lambda_n - \kappa)(16\pi^2 + (m\pi/2)^2 + \lambda_n - \kappa)]^{-1},$$

where the derivatives of R_{nm} and S_{nm} with respect to x are given by;

$$D_1 R_{nm}(x) = -2\pi((m\pi/2)^2 + \lambda_n - \kappa)^{1/2}\cdot$$

$$\operatorname{sgn}(x)\exp[-|x|((m\pi/2)^2 + \lambda_n - \kappa)^{1/2}]\cdot$$

$$\cosh[((m\pi/2)^2 + \lambda_n - \kappa)^{1/2}/2] \qquad \text{if } |x| > .5$$

$$D_1 R_{nm}(x) = -2\pi((m\pi/2)^2 + \lambda_n - \kappa)^{1/2}(\sin(\pi x) -$$

$$\exp[-((m\pi/2)^2 + \lambda_n - \kappa)^{1/2}/2]\cdot$$

$$\sinh[x((m\pi/2)^2 + \lambda_n - \kappa)^{1/2}]) \qquad \text{if } |x| < .5$$

$$D_1 S_{nm}(x) = -8\pi((m\pi/2)^2 + \lambda_n - \kappa)^{1/2}\cdot$$

$$\operatorname{sgn}(x-.6)\exp[-|x-.6|((m\pi/2)^2 + \lambda_n - \kappa)^{1/2}\cdot$$

$$\cosh[((m\pi/2)^2 + \lambda_n - \kappa)^{1/2}/8] \qquad \text{if } |x-.6| > 1/8$$

$$D_1 S_{nm}(x) = -8\pi((m\pi/4)^2 + \lambda_n - \kappa)^{1/2}(\sin[4\pi(x-.6)] -$$

$$\exp[-((m\pi/2)^2 + \lambda_n - \kappa)^{1/2}/8]\cdot$$

$$\sinh[(x-.6)((m\pi/2)^2 + \lambda_n - \kappa)^{1/2}]) \qquad \text{if } |x-.6| < 1/8,$$

with sgn(x) being the sign of the variable x.

The 0(1) density field $\rho^{(0)}$ is obtained from 2.3 and 3.36, implying that;

$$\rho^{(0)} = a^{-1}[1 - \exp(-ay)]D_3Z - \sum_{n=0}^{\infty} P_n D_3G_n \qquad 3.49$$

where $D_3Z(z)$ and $D_3G_n(z)$ are given by

$$D_3G_n(z) = (c_n\gamma/2)\exp(\gamma z)(A_n J_0[c_n \exp(\gamma z/2)] + B_n Y_0[c_n \exp(\gamma z/2)]),$$

$$D_3Z(z) = (\lambda\gamma/2)\exp(\gamma z)(C_1 J_0[\lambda\exp(\gamma z/2)] + C_2 Y_0[\lambda\exp(\gamma z/2)]),$$

with the constants A_n, B_n, C_1 and C_2 defined by 3.43, 3.44, 3.25 and 3.26 respectively.

The 0(1) vertical velocity $w^{(0)}$ given by 2.5 and 3.46, can be rewritten in the form;

$$w^{(0)} = [S(z)]^{-1}J[p^{(0)},\rho^{(0)}] \qquad 3.50$$

with $\rho^{(0)}$ given by 3.49.

The vector valued nondimensional 0(1) mass transport is defined as $M = (m_1,m_2)$, with the components m_1 and m_2 given by;

$$m_1 = \int_0^1 u^{(0)}dz \qquad 3.51$$

$$m_2 = \int_0^1 v^{(0)}dz. \qquad 3.52$$

These integrals can be evaluated to yield

$$m_1 = (\lambda\gamma/2)^{-1}\exp(-ay)[C_1J_0(x) + C_2Y_0(x)]^{c_n}_{c_n\exp(\gamma/2)} - \sum_{n=0}^{\infty} \partial_2 P_n (c_n\gamma/2)^{-1}[A_n J_0(x) + B_n Y_0(x)]^{c_n}_{c_n\exp(\gamma/2)},$$

$$m_2 = \sum_{n=0}^{\infty} \partial_1 P_n (c_n\gamma/2)^{-1}[A_n J_0(x) + B_n Y_0(x)]^{c_n}_{c_n\exp(\gamma/2)},$$

with x the dummy integration variable.

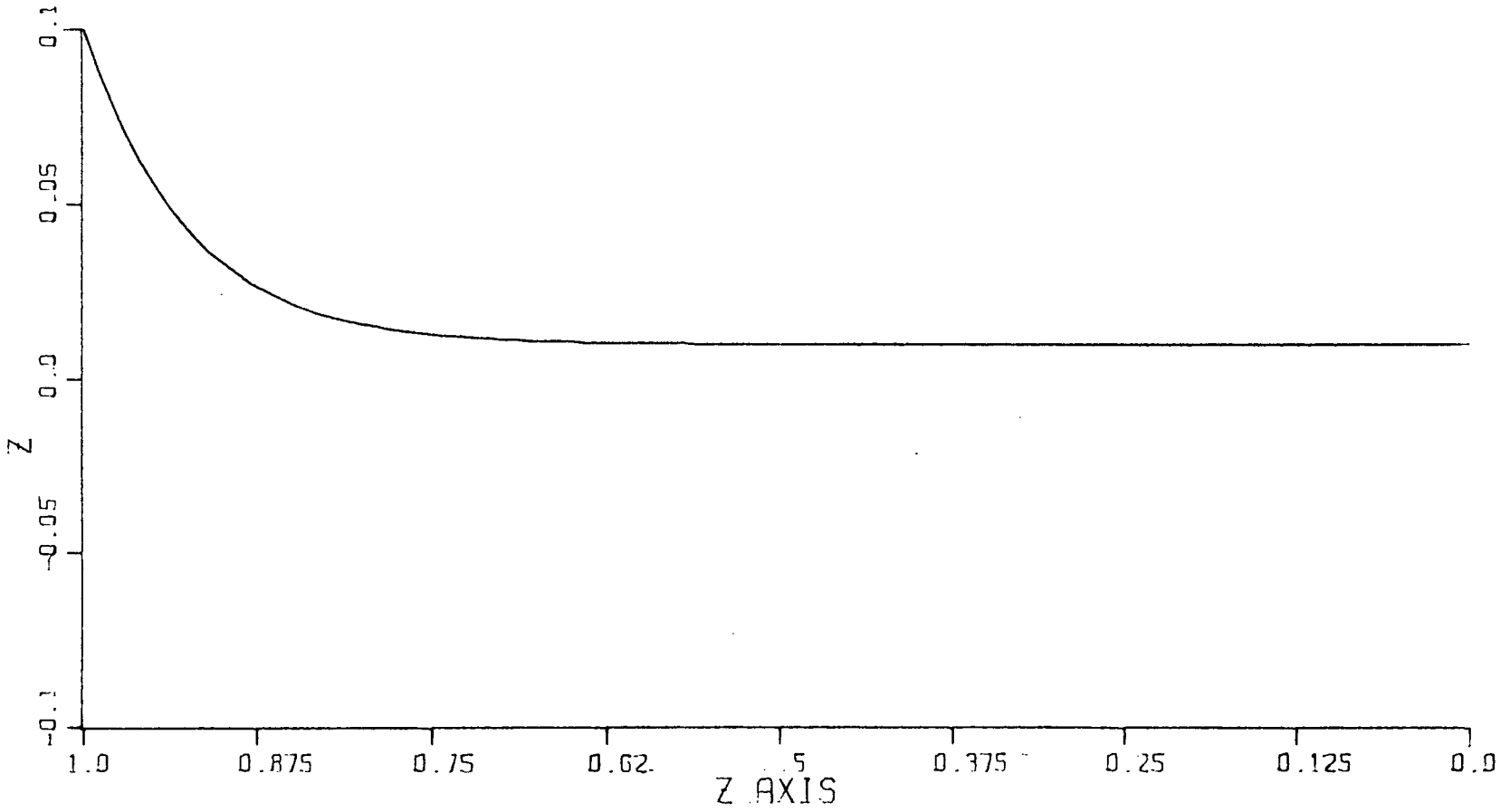

Figure 6 - Far field vertical current structure

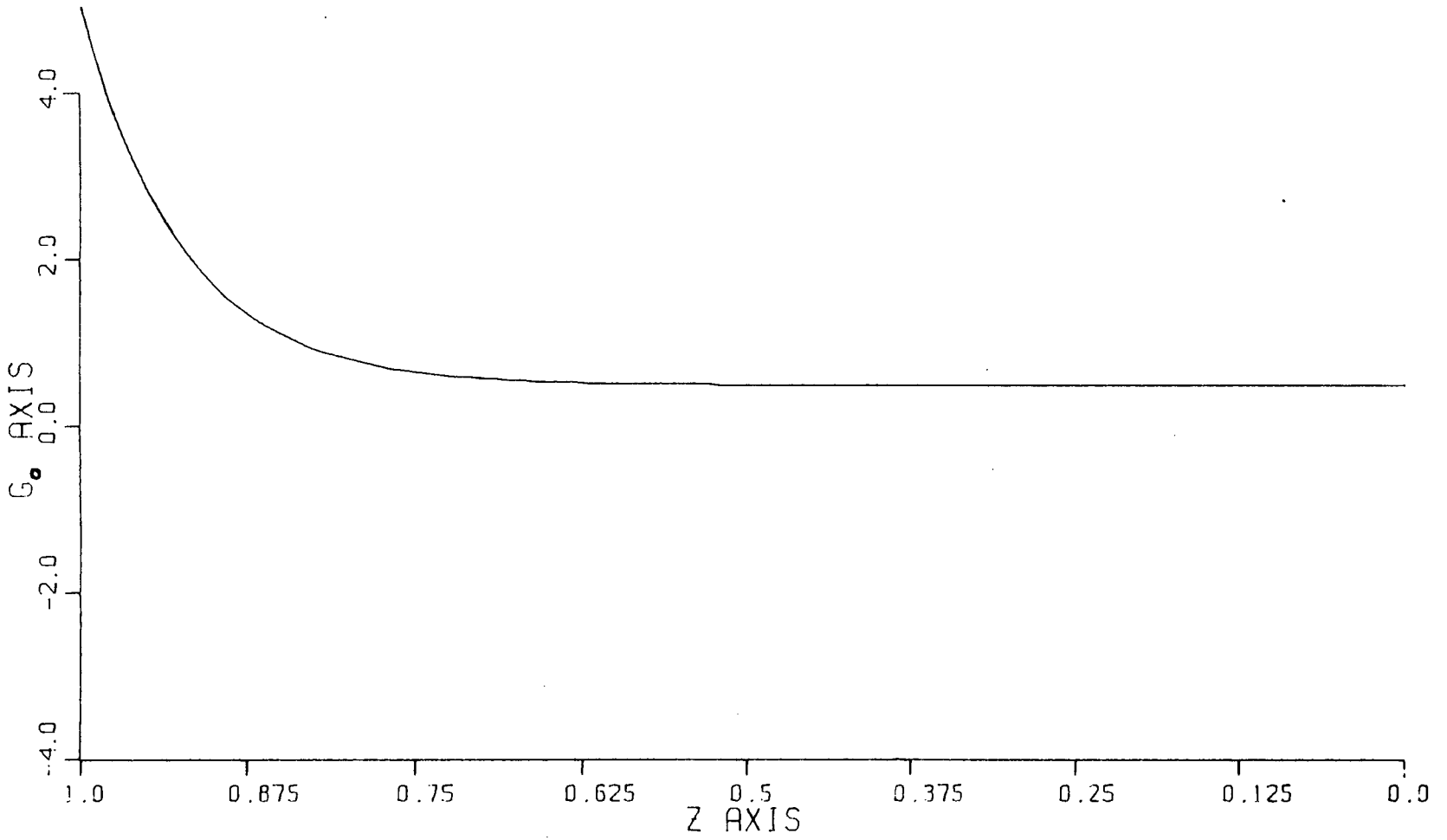

Figure 7 - Graph of $G_0(z)$ vs. z

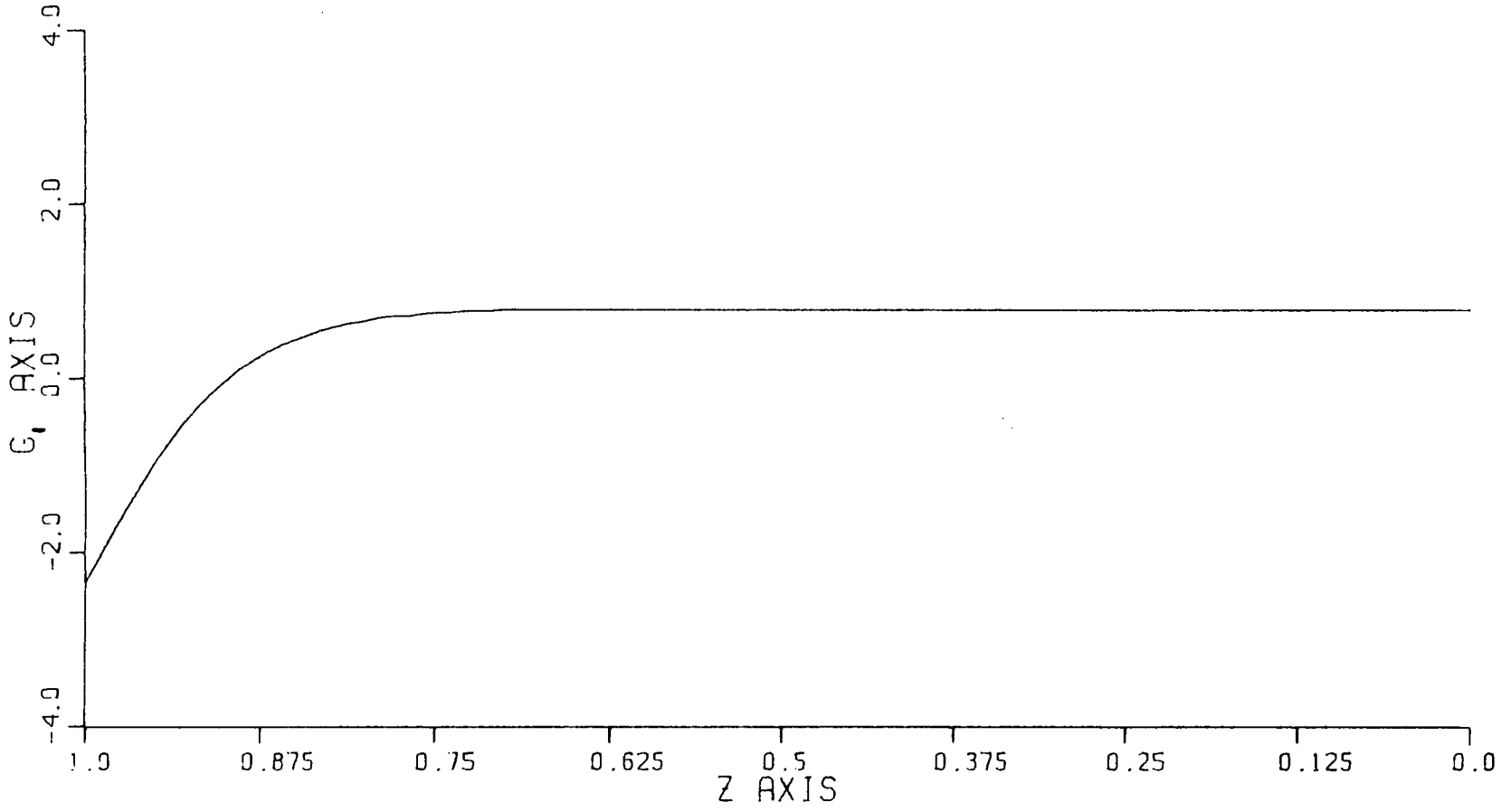

Figure 8 - Graph of $G_1(z)$ vs. z

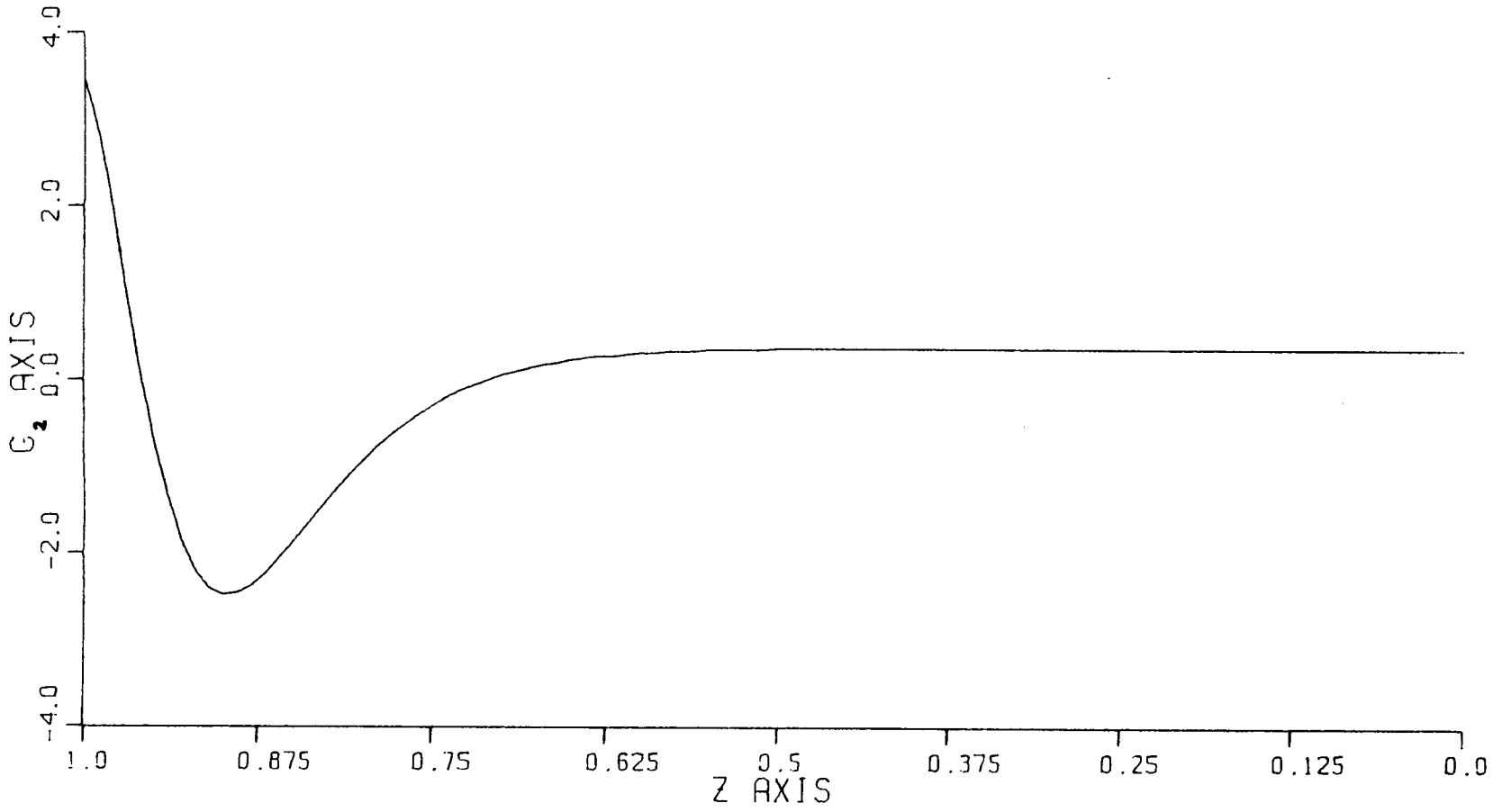

Figure 9 - Graph of $G_2(z)$ vs. z

IV. PARAMETER SENSITIVITY ANALYSIS

The intent of this chapter is two fold. First, a description of the solutions obtained last chapter is given based on parameter values obtained from examining the avaliable data for the north east Pacific Ocean. Second, this chapter discusses the effect of variations in the parameters on the structure of the previously obtained solutions. In particular five tables of parameter calculations representing 97 numerical simulations of the entire solution were preformed. These calculations were preformed on the University of British Columbia's Amdol 470 using double precision Watfiv.

Numerical values for the nondimensional observables were computed at grid locations denoted (i,j,k) located in the domain at $(-2+i\delta x, j\delta y, k\delta z)$ with $(\delta x, \delta y, \delta z) = (.2,.1,.1)$ and i,j,k taking on the integer ranges $0 \leq i \leq 20$, $0 \leq j \leq 20$ and $0 \leq k \leq 10$. The number of cross channel modes used to compute 3.16 was 20 and the number of vertical eigenmodes used to compute 3.6 was 6. Adding additional modes had absolutely no effect on the computed observables to double precision accuracy. In addition to numerical values the 0(1) stream function and density fields were contoured and stick diagrams of the 0(1) velocity and mass transport fields were computed to provide a graphical representation of the resulting flow field.

The five parameter pair groups examined, in order of their discussion, are: the far field horizontal current shear and the Rossby number (α, ϵ), the topographic parameters (h_1, h_2), the

Brunt-Vaisala frequency parameters (N_0,γ^*), the far field horizontal current shear and the far field surface current (a,a) and finally the far field horizontal current shear and the far field bottom current (a,b).

In each parameter pair analysis the other parameters were held fixed. The standard values assumed were based on the topographic and oceanographic observations contained in Bennett(1959), Tabata(1982), Emery et al. (1983) and Willmott and Mysak(1980) of the north east Pacific Ocean, discussed in section 2.1.

The scaling parameters H, L and U were held fixed at 3500 m, 400 km and 1 m s^{-1} respectively, resulting in a Rossby number ϵ of $2.1 \cdot 10^{-2}$. The standard set of values for the parameters N_0, $(\gamma^*)^{-1}$, a, b, a, κ, h_1 and h_2 were .011045 s^{-1}, 254.51 m, 0.1, 0.01, 5.0, 0.0, 10.9 and 34.1 respectively. This set of parameters yield numerical values of the first six eigenvalues of: $\lambda_0 = 25$, $\lambda_1 = 382.86$, $\lambda_2 = 2219.01$, $\lambda_3 = 5584.99$, $\lambda_4 = 10394.55$ and $\lambda_5 = 16642.86$.

In the standard set of parameters the upstream vorticity constant κ has been set identically equal to zero. A brief comment is necessary to outline the reasons for this choice.

The parameter κ cannot be set equal to zero if the upstream current is barotropic. In Section 3.2 it was shown that $\kappa = -a^2$ if Z(z) is given by a constant. However, examining Figure 2, it is obvious that the current profiles in the north east Pacific are baroclinic.

The parameter κ effects a baroclinic upstream current

through the quantity $a^2 + \kappa$ in 2.20. Numerical values for a based on the observations described in Tabata(1892) and Bennett(1959) suggest that $a \simeq 5$, so that the e-folding distance in the horizontally sheared far field current is about 80 km. Numerical calculations of the far field current show that the vertical current structure varies little for different values of κ provided $|\kappa| << a^2$.

The principle mechanism by which κ effects the topographically induced flow field is in the denominator of the Green's function $g(x,y|x_0,y_0)$ given by 3.17. It was shown in Chapter III that $\lambda_0 = a^2 + \kappa$ and that $G_0(z) = Z(z)[\int_0^1 Z^2(z)dz]^{-1/2}$.

For a given (x,x_0,y,y_0) the magnitude of the Green's function $|g(x,y|x_0,y_0)|$ will be maximized when the denominator in 3.17 is minimized, occuring for n = 0. This is consistent with the physical intuition that the principle response of the upstream flow to the topographic forcing will the gravest (n=0) mode. When n = 0 the denominator of 3.17 will satisfy $(m\pi/2)^2 + \lambda_0 - \kappa \geq a^2$. Consequently the gravest mode response of the ocean to the topography is virtually unaffected by κ. Rigorously speaking the parameter κ does effect the n = 0 eigenmode by way of its effect on the far field current and consequently on $G_0(z)$.

The effect of κ on the higher modes is equally insignificant since the eigenvalues form an increasing sequence and $\lambda_0/\lambda_1 << 1$. Typically this ratio is on the order of .07

implying that $\lambda_1 \simeq 10\lambda_0$. Therefore the parameter κ has only minor effect on the higher modes which themselves make a progressively smaller contribution to the flow field. The lack of any significant effect on the flow field for nonzero $0(1)$ κ provided $|a^2 + \kappa| >> 0$ suggests that there is no loss of applicability of the mathematical model to the north east Pacific Ocean if $\kappa = 0$.

The highly non-trivial way that the parameters appear in the solutions derived last chapter makes an analytical investigation of the effect of their variation extremely difficult. Indeed such an examination would not serve to illuminate the essential dynamics in the problem. Of more utility is to argue the effect of variations in the parameters on the solution based on the physics and geometry of the problem. However while the following discussion is qualitative rather than quantitative, it will be extensive consisting of examining several vertical and horizontal sections in the pressure, density and velocity fields. With this philosophy in mind the exact numerical values of all the variables is not so important as the orders of magnitudes and qualitative features of the calculated flow field.

This chapter begins with a description of the flow field for the standard set of parameters. This discussion will concentrate on giving a qualitative but complete description of the resulting flow field. The solution described in this section will be the standard to which the solutions for the varied parameters will be compared. In the sections concerned

with the structure of the solution for the varied parameters, the discussion is two fold. First a qualitative analysis is given describing the effect of variations based on vorticity arguments, and second one or two examples are described illustrating these arguments.

4.1 The Solution For The Observed Parameters

Horizontal sections of solution for the observed parameters were taken at depth intervals of .1 (350 metres). Vertical profiles were computed at the ten locations given by (x,y) coordinates (-2,.1), (-.75,.1), (-.4,.1), (0,.1), (0,.75), (.4,.1), (.6,1.2), (.75,.1), (.75,.75) and (2,.1). These ten locations are plotted in Figure 10 showing their location relative to the topography. In addition vertical sections parallel to the coastline were contoured of $\rho^{(0)}$ and $p^{(0)}$ for y ranging from 0 to 2 in increments of .2.

The discussion proceeds as follows. First, a desription is given of the horizontal structure of the flow field for z = 1, .9, .8, .7 and .6. The order of the discussion of the observables is: $p^{(0)}$, $(u^{(0)},v^{(0)})$, (m_1,m_2), and $\rho^{(0)}$. Following the description of the horizontal variation the focus of this section is shifted to describing the vertical variation of the flow field at various fixed (x,y) coordinates.

Figures 11, 12, 13, 14 and 15 are contour plots of the stream function $p^{(0)}$ at z = 1, .9, .8, .7 and .6 respectively. The contours were plotted at intervals of + or - .01, relative to the zerc streamline.

The zero streamline, in Figure 11, bifurcates at the

upstream stagnation point situated approximately at (-.6,0). One branch remains on the coastline while the other turns into the interior of the domain rejoining the coastline at the downstream stagnation point at approximately (-.65,0). The stagnation points are not symmetric about x = 0 because h(x,y) is not symmetric about x = 0.

The zero streamline forms the outer boundary of a region of closed streamlines. The interior region in Figure 11 forms the surface expression of a baroclinic eddy, with an approximate diamater of 1 (400 km). The stream function in the interior of this region is positive, suggesting that the inward radial gradient of the stream function is positive implying clockwise or anticyclonic circulation.

The structure of the streamlines in the interior of the eddy is somewhat complicated. Over the seamount and shelf protrusion are two well developed anticyclonic eddies. In the region between these two eddies, in the neighbourhood of (.4,.4), it follows that a strong current shear exists. Areas of significant current shear are generally associated with regions of high biological activity.

Figure 11 also pictures streamlines radially inward of the zero streamline which encircle the two local anticyclonic eddies. Thus in addition to the local eddies there is a larger scale anticyclonic circulation. This flow corresponds to the topographic steering of the upstream coastal current by the shelf protrusion out to a region where it can be topographically steered by the seamount. The return coastal flow is

concentrated in a narrow band of width approximately .15 (60 km) near x = 0. In the immediate region of this return flow the currents have the local appearance as bands of alternating currents.

The maximum value of $p^{(0)}$ occurs on z = 1 over the seamount with an approximate value of .1. This maximum occurs over the seamount rather than over the shelf protrusion because $p^{(0)}$ is proportional to h_1 and h_2 and $h_2 > h_1$. There is, however, a local maximum over the continental shelf bump at about (0,.25) with an approximate value between .07 and .08. In addition there must exist a saddle point in the stream function field in the immediate vincinty of (.4,.4), associated with the fluid trajectories in that area.

Figures 12, 13, 14 and 15 are horizontal sections of the stream function field at z = .9, .8, .7 and .6. This sequence of figures shows that the eddy decays rapidly with depth. The decay is most rapid between z = 1 and z = .9 with the pressure field over the seamount decaying from its maximum of .1 on z = 1 to about .035 on z = .9. The vertical decay continues until about z = .6 where the decay becomes negligible and the remaining eddy structure continues more or less uniformly down to the bottom at z = 0. The vertical structure of the decay will be completely described later in this section.

The horizontal gradients in the pressure field on z = 1 are the largest in the return coastal flow. Consequently, the particle velocities will be largest in that region. The relatively large speeds in this area are the result of the

crowding of the coastal streamlines together by the existence of the anticyclonic eddy over the shelf protrusion and the coastal boundary.

The horizontal gradients in the pressure field are larger in the local eddy over the seamount than in the local eddy over the shelf protrusion. The reason is that in this region the velocity field is related to the pressure field through the gradients of $p^{(0)}$, and these in turn will be proportional to $\nabla h(x,y)$. Figure 5 which is a contour map of the function $h(x,y)$ clearly shows that $\nabla h(x,y)$ is largest over the seamont. The weakening of the gradients in the $p^{(0)}$ field with depth is illustrated in Figures 11 through 15 by the fact that as the depth increases the number of contours decrease. Consequently, the angular speed of the eddy decreases with depth.

Figures 16, 17, 18, 19 and 20 are vertical sections of $p^{(0)}$ taken at y = .2, .4, .6, .8 and 1 parallel to the coastline. On each section the pressure field was contoured at intervals of + or - .01 relative to the 0 pressure contour. For this series of graphs the function $p^{(0)}$ is best described as the 0(1) pressure than as the stream function. The latter terminology suggests that the fluid trajectories lie along lines of constant pressure. In the vertical sections described here this interpetation is incorrect, whereas for the horizontal sections previously described it is correct.

Comparing Figure 16 with Figure 11, the vertical section along y = .2 is seen to pass through the seaward region of the return coastal flow and through the interior of the local eddy

produced by the shelf protrusion. The horizontal boundaries of the large scale anticyclonic circulation is formed by the 0 pressure contour. Along $y = .2$ this occurs at $x \simeq -.6$ and $x \simeq .7$.

Figure 16 through 20 show this contour to be vertically straight, which is a consequence of the fact that to lead order there is no vertical velocity. In the interior of the region bounded by the 0 pressure contour the pressure is everywhere postive. Calculations show that for every z the inward radial gradient of $p^{(0)}$ in the interior is positive, implying that the entire interior region rotates anticyclonically.

In line with the observation made for the horizontal sections, Figures 16 through 20 show that the large scale anticylonic circulation is essentially surface trapped. In Figure 16, the flow field is only slightly effected by the seamount since the pressure contours are roughly symmetric about $x = 0$.

The vertical section taken on $y = .4$ passes just seaward of the local eddy formed over the shelf protrusion and cuts through the coastward extreme of the local eddy produced by the seamount. The increasing influence of the seamount is seen in Figure 17 with the pressure contours becoming somewhat asymmetric about $x = 0$. In this intermediate region the vertical extent of the eddy, as manifested in $p^{(0)}$, has shallowed. Along $y = .2$ the .01 contour reaches a maximum depth of about .7 (1000 metres), wheras along $y = .4$ this is reduced to about .2 (800 metres). Examining Figure 5 shows that along

y = .4 the slope height is about 1 (70 metres) resulting in slight topographic forcing at this point.

In the Figures 18 and 19 the influence of the seamount becomes the denominate feature in the forcing of the flow. In Figure 18, taken along y = .6 the vertical extent has increased back down to a depth of 0f .25 (900 metres). The horizontal boundaries of the eddy has shifted toward positive x with the circulation contained between $x \simeq -.4$ and $x \simeq 1$. The vertical extent of the eddy is substantially increased along y = .8, shown in Figure 19. For the first time the .01 pressure contour is not closed and in fact reaches the bottom. Consequently the horizontal gradients for $p^{(0)}$ are much stronger and extend deeper down over the seamount than elsewhere. As argued earlier this is a consequence of the increased height and larger gradients associated with the seamount compared to the slope protrusion. The final vertical section shown of $p^{(0)}$, Figure 20, along y = 1 shows the rapid decay of the pressure field as the distance to the support of h(x,y) increases.

Figures 21, 22, 23, 24 and 25 are stick plots of the horizontal velocity field on z = 1, .9, .8, .7 and .6 respectively. Each stick represents a horizontal velocity vector. The velocity was calculated at (x,y) coordinates $(-2+i\delta x, j\delta y)$ with i, j, δx and δy given earlier in this chapter. The tail of each stick or velocity vector sits on one of these points. The scaling of the vectors is done so that a stick length of one inch equals fifty centimetres per second. By comparing the stick plots to the associated stream function plot

the direction of flow becomes clear.

In the far field upstream region, say along the line $x = -2$, the current is unaffected by the topography and is given by $u^{(0)} = \exp(-ay)Z(z)$ $v^{(0)} = 0$ as described in Chapter II. On the surface ($z=1$) the current along $x = -2$, shown in Figure 21 is a maximum at the coast with a magnitude of .1 (10 cm s^{-1}). The current exponentially decays away from the coast with an e-folding length of a^{-1} (80 km). Figure 21 shows that the particle speeds increase as the upstream current interacts with the topography. It is possible to see the two interior anticyclonic eddies in Figure 21 by comparing that figure with Figure 11.

Numerical calculations show that typical speeds at the exterior of the eddy in Figure 21 (corresponding to the offshore 0 streamline in Figure 11) are about .2 (20 cm s^{-1}), representing about a 700% increase in particle speeds. Immediately over the seamount the typical surface speeds are on the order of .4 (40 cm s^{-1}) . Typical speeds calculated over the continental shelf bump are on the order of .2 (20 cm s^{-1}), consistent with those speeds calculated for the larger encircling anticyclonic circulation. The narrow coastal band of return flow has the largest speeds with the calculations showing that at on the surface at (x,y) coordinate (0,0) the speeds are in excess of .50 (50 cm s^{-1}) decaying to about .3 (30 cm s^{-1}) at (0,.1).

Figure 21 also clearly shows that the topographically induced flow decays rapidly as the horizontal distance from the

support of h(x,y) increases. If the center of the eddy is chosen as (x,y) coordinate (.25,.5) then at the center the surface speeds are typically on the order of .2 (20 cm s^{-1}). Further out from the center say at (.2,.6) the speed is about .15 (15 cm s^{-1}). The distance between these two points is about 40 km. At (.2,1), about 250 km from the center, the surface speed is on the order of .05 (5 cm s^{-1}). However as Figure 21 illustrates the eddy produced from the combined interaction of the coastal topography and the seamount does not produce a symmetric eddy. Consequently from the view point of an observer moving Northwestward, toward the seamount, from the center (.2,.6) the particle speeds would seem to increase as the seamount induced flow is encountered.

Figures 22, 23, 24 and 25 are stick plots of the horizontal velocity field at z = .9, .8, .7 and .6 respectively. These figures show the vertical decay of the horizontal velocity as the depth increases. The most significant decay occurs between the surface z = 1 and z = .9. In general the particle speeds at z = .9 are half those at the surface. For example in the near coastal return flow associated with the large anticyclonic circulation the speeds at z = .9 are on the order of .2 (20 cm s^{-1}) compared to the 50 cm s^{-1} computed for the surface. Over the seamount current speeds are reduced from 40 cm s^{-1} on z = 1 to about 21 cm s^{-1} on z = .9. The speeds over the continental shelf protrusion are reduced from a surface maximum of about 25 cm s^{-1} to about 12 cm s^{-1} on z = .9.

The horizontal decay of the velocity field is independent

of depth as a consequence of the vertical mode solution technique. The vertical decay of the velocity field continues until about z = .6 where the horizontal velocity field becomes virtually depth independent.

The depth associated with z = .6 is about 1400 metres. Below this depth the flow appears depth independent and therefore barotropic. Based on the computations of this section, using a level of no motion on the order of 1500 to 2500 metres, the vertical extent of the eddy would be on the order of 1000+ metres.

Typical speeds computed for the deep interior of the water column (z<.5) over the seamount are about .01 (1 cm s^{-1}). Over the continental shelf bump, typical speeds are on the order of .02 (2 cm s^{-1}). The coastal return flow has speeds on the order of .1 (10 cm s^{-1}). Currents in the seaward exterior region of the eddy, associated with the 0 streamline, have magnitudes on the order of .005 (.5 cm s^{-1}). Thus while the eddy decays rapidly in the vertical direction the model calculations predict continued anticyclonic flow even in the deep interior of the water column.

Figure 26 is a stick plot of the mass transport vector (m_1,m_2) given by 3.51 and 3.52. The scaling of the stick lengths is such that 1 inch of stick length corresponds to about $7 \cdot 10^6$ kg m^{-1} s^{-1}, based on an average density of 1025 kg m^{-3}. To convert to volume transport units (ie. Sverdrups; 1 Sv = 10^6 m^3 s^{-1}) m_1 and m_2 are integrated over a horizontal distance of .25 (100 km). Thus a constant nondimensional

transport of one corresponds to a volume transport of 350 Sv which in turn would be represented by a stick length of 2 inches.

In the far field the transport is parallel to the coast, decaying exponentially away from the coast with the nondimensional e-folding length of α^{-1}. On y=0 $m_1 \simeq .02$ (7 Sv) and $m_2 = 0$.

The transport increases as the flow interacts with the topography. Over the seamount the magnitude of the transport is about .06 (20 Sv). The near coastal return flow has a transport on the order of .06 (20 Sv). The continental shelf bump induces a typical transport of .04 (14 Sv). The outer exterior of the eddy has a typical transport magnitude of .01 (4 Sv). The horizontal decay of the transport field is qualitatively the same as the the horizontal decay of the velocity field. Consequently the topographically induced mass transport quickly decays away to zero as the distance increases from the support of h(x,y).

Figures 27, 28 and 29 are contoured plots of horizontal sections of the 0(1) density field $\rho^{(0)}$ for z = 1, .9, .8 respectively. The contouring increment is + or - .1 relative to the 0 density contour.

Figure 27, in which $\rho^{(0)}$ is contoured for z = 1, clearly shows that the density contours closely follow the stream function contours of Figure 11. In the far field, say along x = -2 or +2, the 0(1) density increases as the distance from the coast increases. Along the coastline $\rho^{(0)} = 0$, owing to the

fact that $p^{(0)} = 0$ along $y = 0$ and that $\rho^{(0)} = -\partial_3 p^{(0)}$. It follows from the thermal wind relation $\partial_3 u^{(0)} = \partial_2 \rho^{(0)}$ that the 0(1) far field density should increase as y increases since the magnitude of the 0(1) alongshore velocity $u^{(0)}$ decreases with increasing depth.

The topography begins to effect the density field around x = -1. There is a bifurcation of the 0 density contour at about x = -.6, similiar to the bifurcation in the 0 pressure contour, rejoining the coastline downstream at about x = .65. This 0 density contour is another indicator of the horizontal extent of the eddy circulation on z = 1. The 0(1) density radially inward of this contour is negative, indicative of the downward deflection of the isopycnals associated with an anticyclonic circulation that decays with increasing depth.

In the interior of the region bounded by the 0 density contour, the density contours clearly mark out the two smaller anticyclonic eddies over the seamount and continental shelf protrusion. The minimum in the 0(1) density field occurs over the seamount with a value of about -1.2 . Recall that the flow related density field was scaled by $\epsilon F \rho_0 \simeq 2$ kg m^{-3}, hence the minimum in the surface 0(1) density field corresponds to a change in the total density of about -2.5 kg m^{-3}. There is another local minimum in the 0(1) surface density field located over the continental slope protrusion at about (x,y) coordinate (0,.25), with value approximately -.9 (-1.8 kg m^{-3}). Corresponding to the saddle point in the stream function field in the neighbourhood of (.4,.4) there is a local maximum in the

0(1) surface density field of about -.4 (-.8 kg m^{-3}).

Concomitant with the increasing uniformity of the stream function as the depth increases, Figures 28 and 29 picture the horizontal variation in $\rho^{(0)}$ flatting out. Figure 29 which maps the contours $\rho^{(0)}$ on z = .8 (700 m depth) shows that the density gradients decay rapidly with depth. In fact at this depth the density variations are bounded by + or - .1 (.2 kg m^{-3}), since only the 0 contour is mapped.

The vertical deflection of the isopcynals is shown in Figures 30, 31, 32, 33 and 34. These figures are vertical sections of the 0(1) density field taken parallel to the coastline at y = .2, .4, .6, .8 and 1, respectively. By comparing Figure 30 to Figure 27, the vertical slice along y = .2 is seen to pass through both the return coastal flow and the flow associated with the anticyclonic eddy over the continental shelf bump. Thus the deflections shown in Figure 30 are largely due to the slope topography and coastal return flow rather than the seamount.

The external boundary of the eddy circulation is marked by the 0 density contour. It extends down to the bottom because the anticyclonic circulation does so as well. However in the deep interior of the water column (z<.6) the deflection of the isopycnals, related to the vertical shear in the pressure field becomes quite small (<.2 kg m^{-3}) due to the uniformity with respect to depth of the stream function $p^{(0)}$.

Figures 31, 32 and 33 show the progressive influence of the seamount on the vertical deflection of the isopcynals. Along

y = .8, shown in Figure 33, there is only a minimal contribution of the slope protrusion to the flow as manifested in the O(1) density field. Figure 34, taken on y = 1, shows the gradual decay of the deflections of the ispcynals as the distance from the support of h(x,y) increases. Computations for y > 1.2 contain virtually no isopycnal deflection.

The series of Figures 30 through to 34 support the conclusion that the anticyclonic circulation produced by the the topography is essentially surface trapped. The maximum downward penetration of the eddy takes place over the seamount, consistent with the extrema observed in the O(1) pressure, density, velocity and mass transport fields over this region. Based on Figure 33 the sharpest vertical gradients in the density field take place in approximately the top 30% of ocean. Roughly speaking the vertical extent of the eddy can be associated with sharpest vertical gradients, resulting in the depth to which the anticyclonic circulation occurs on the order of 1000 metres.

Described now is the change in the vertical profile of the upstream flow field as it interacts with the support of h(x,y). The previously given has shown that the flow field along x = -2 is unaffected by the topography. Figures 35, 36, 37, 38 and 39 are the vertical profiles at (x,y) = (-2,.1) of $p^{(0)}$, $\rho^{(0)}$, $u^{(0)}$, $v^{(0)}$ and $w^{(0)}$ respectively.

The lack of any interaction between the topography and the upstream flow at this location implies that $v^{(0)} = w^{(0)} = 0$ throughout the water column as shown in Figures 38 and 39. The

upstream down channel velocity $u^{(0)}$, shown in Figure 37, decays with increasing depth. At $(x,y,z) = (-2,.1,1)$, $u^{(0)} = \exp(-.2)/10 \simeq .06$ (6 cm s^{-1}). The upstream current is essentially surface trapped with virtually no current (< .1 cm s^{-1}) for $z < .85$ (deeper than about 500 metres).

The pressure field profile shown in Figure 35 is a minimum at the surface and increases with increasing depth. At the surface $p^{(0)} \simeq -.01$, increasing to approximately -.001 at the bottom. This is a consequence of the fact that the current decays with increasing depth implying that the crosschannel gradient in $p^{(0)}$ decays with depth, which in turn implies that $p^{(0)}$ increases with increasing depth.

The 0(1) density $\rho^{(0)}$, shown in Figure 36, satisfies $\partial_3\rho^{(0)} > 0$. This is a consequence of the thermal wind relation $\partial_3 u^{(0)} = \partial_2\rho^{(0)}$. Since the vertical gradient in the along channel velocity component is positve it follows that the cross channel gradient in $\rho^{(0)}$ is also positive. The vertical gradient in $u^{(0)}$ decreases with increasing depth so that $\rho^{(0)}$ is more positive at the surface than deeper in the water column and hence the shape of $\rho^{(0)}$ in Figure 36.

This fact does not imply that the water is unstably stratified. From Chapter II the nondimensional in situ density field will be given by $\bar{\rho} + \epsilon F\rho^{(0)} + 0(\epsilon^3)$. Numerical calculations confirm that $\partial_3(\bar{\rho} + \epsilon F\rho^{(0)}) < 0$ so that the water column is stably stratified.

Figures 40, 41, 42, 43 and 44 are the vertical profiles of

$p^{(0)}$, $\rho^{(0)}$, $u^{(0)}$, $v^{(0)}$ and $w^{(0)}$ computed at (x,y) = (-.4,.1). This point is about .4 units (64 km) away from the centre (.2,.6) of the entire anticyclonic circulation. Examining Figure 10 the coordinates (-.4,.1) are seen to be located slightly downstream from the upstream edge of the coastal protrusion. The height of the slope protrusion at this location is about 2.5 (175 metres). Figure 11 shows that this vertical profile is situated in the boundary region between the coastal return flow and the local anticyclonic eddy produced by the slope protrusion.

Figure 40 of the 0(1) pressure field is an typical example of $p^{(0)}$ in the interior of the region bounded by the 0 streamline. At the surface the 0(1) pressure is positive which decays as the depth increases. The surface pressure is approximately .02 at this location decaying to about .004 at z = .8.

The 0(1) density is negative throughout the water column with its minimum at z = 1 of about -.27 increasing as the depth increases. As argued earlier the interior density field must be negative as consequence of the thermal wind relation which has that the density must increase as the distance to the centre of the eddy increases because the vertical gradient in the velocity field is positive.

Figures 42 and 43 are the vertical profiles of the horizontal velocity components $u^{(0)}$ and $v^{(0)}$ respectively. Consistent with Figure 11 these figures show $u^{(0)} < 0$ and $v^{(0)} > 0$ at this location. At the surface the speed

$[(u^{(0)})^2 + (v^{(0)})^2]^{1/2}$ is about .2 (20 cm s^{-1}) decaying to about .04 (4 cm s^{-1}) at z = .8 (700 metres deep).

The vertical profile of the vertical velocity $w^{(0)}$ at (-.4,.1) is shown in Figure 44. The vertical velocity is negative everywhere in the water column because the horizontal coordinates are situated in a region where the flow is down the coastal slope protrusion. The velocity is zero at the surface as a consequence of the rigid lid approximation. The minimum in $w^{(0)}$ occurs at approximately .75 (900 metres deep).

The extrema in $w^{(0)}$ is expected to occur in the upper region of the water column since in this region the Brunt-Vaisala frequency has its largest gradients. In the deep interior of the water column $S(z) \simeq 0$ meaning that the water column is approximately homogeneous. In this region the vertical velocity is therefore quite small. Figure 44 suggests a value of about .005 (10^{-4} cm s^{-1}) at z = .25 (2600 metres deep). Futhermore in the deep interior where $S(z) \simeq 0$, $w^{(0)}$ is approximately linear, consistent with the remarks made in Chapter III about Z(z) and $G_n(z)$ in this region.

Figure 44 confirms the qualitative assertion that the dicontinuity in $\partial_3 p^{(0)}$ at z = 0 is not significant numerically. The vertical velocity is given by $w^{(0)} = J[p^{(0)}, \rho^{(0)}/S(z)]$. In Chapter III it was shown that the vertical mode decomposition of the interaction pressure field induces a discontinuity in $\partial_3 p^{(0)}$ of order $30 \cdot e^{-14} \simeq 2 \cdot 10^{-5}$ at z = 0 for (x,y) coordinates in the support of h(x,y). Since $\rho^{(0)} = -\partial_3 p^{(0)}$, it follows that $w^{(0)}$ will be discontinuous at z = 0 with a discontinuity

$0(10^{-5})$. However since $w^{(0)} \simeq 0(10^{-2})$, then the discontinuity is three orders of magnitude smaller than the typical values $w^{(0)}$ assumes in the water column. Therefore a continuously differentiable stream function would probably only marginally differ from the solution obtained here, and then only so near the bottom. Since one objective of this thesis is to characterize the middle to upper ocean predictions of this model, in a desire to understand a portion of the dynamics of the Sitka eddy, this mathematical property is only a formal difficulty and is not an essential weakness in the mathematical model.

Figures 45, 46, 47, 48 and 49 are the vertical profiles of $p^{(0)}$, $\rho^{(0)}$, $u^{(0)}$, $v^{(0)}$ and $w^{(0)}$ taken at (x,y) = (0,.1). These profiles are representative of the outer region flow of the larger anticyclonic circulation that encloses the two smaller eddies. Examining Figure 11 it is seen that in this region the horizontal gradients in the stream function are smaller than in the narrow coastal return flow. It follows that since the vertical shear in the observables is independent of horizontal position the vertical profiles will be flatter at this location. Figures 45 through 49 have this property.

The relatively weak horizontal gradients in $p^{(0)}$ at this location result in a surface speed of about .1 (10 cm s^{-1}). The speed decays quickly to about .02 (2 cm s^{-1}) at z = .8 (700 metres deep). There is a negligible vertical velocity in the water column at this point because this horizontal location is not in the support of h(x,y). This fact also implies that

$w^{(0)}$ and $\rho^{(0)}$ are continuous at z = 0.

The final set of vertical profiles examined are those for (x,y) = (.75,.75). Figures 50, 51, 52, 53 and 54 are the graphs of the vertical profiles of $p^{(0)}$, $\rho^{(0)}$, $u^{(0)}$, $v^{(0)}$ and $w^{(0)}$ respectively computed at (.75,.75). This location is on the upstream edge of the seamount, as can be seen in Figure 10. The height of the seamount at this location is about 5 (350 metres).

Figure 50, of $p^{(0)}$ shows over the seamount a region of intense high pressure is formed, on account of the fact that $h_2 > h_1$. The fact that the vertical extent of the eddy is deeper here than over the slope protrusion can be seen by comparing Figure 50 to Figure 40. Associated with the higher pressure is a corresponding increases in the vertical deflection of the isopycnals. This is deduced by comparing Figure 51 with Figure 41 and Figure 46. The increase in the magnitude of $\rho^{(0)}$ means that the density observed at a particular in Figures 41 and 46 will occur at a deeper location in Figure 51.

Figure 52 of $u^{(0)}$ shows that there is virtually no down channel flow at this location. Comparing Figure 11 to Figure 10 it is seen that at this location the streamlines appear to be parallel to the topographic contours, which are oriented in the cross channel direction. At the surface $u^{(0)} \simeq .02$ (2 cm s^{-1}) and $v^{(0)} \simeq -.4$ (-40 cm s^{-1}). The vertical extent of the eddy in this location can be observed in the vertical profile of $v^{(0)}$ which increases from its surface minimum of -40 cm s^{-1} to -5 cm s^{-1} at z = .25 (900 metres deep).

Figure 54 of $w^{(0)}$ shows that the vertical velocity is small

at this location. Throughout the water column $w^{(0)} \simeq 0(2 \cdot 10^{-3})$ $(4 \cdot 10^{-5}$ cm $s^{-1})$. The extrema in $w^{(0)}$ occurs at about 350 metres with magnitude about 10^{-4} cm s^{-1}. The vertical velocity is negative since at this location the flow is passed the maximum height and is now flowing down the back of the seamount.

The four sets of vertical profiles just examined effectively characterize the flow field. The flow field at (.4,.1) is similiar to that at (-.4,.1). In this region however the currents are not as strong as those computed at (-.4,.1), with a surface current on the order of 18 cm s^{-1}. The flow field at (.75,1.2) is similiar that that of (0,.75), however here again the flow is weaker with a surface speed about 2 cm s^{-1}.

In summary the following physical description emerges of the interaction between the topography and the upstream current. The baroclinic coastal current begins to interact with the topography in the vinicity of x = -.75. The topography forces the current to upwell. The upwelling is constrained by the rigid lid so that the vortex tubes are then compressed. The compression of the vortex tubes coupled with the conservation of potental vorticity implies that the angular momentum of the vortex tube must decrease.

This is accomplished with an increased anticyclonic circulation, since for clockwise circulation $\partial_1 v^{(0)} - \partial_2 u^{(0)} < 0$. Hence the fluid trajectories are forced out into the channel. For some of the streamlines the strong gradients in the coastal protrusion topographically trap them so a local

anticyclonic eddy is set up. For streamlines outside of some critical gradient of h(x,y) the slope protrusion cannot trap them and they continue out into the channel where some of them are trapped by the seamount and others outside some critical radius continue down stream.

The seamount again induces an upwelling of the water column with the concomitant increased anticyclonic rotation of the vortex tubes. Thus the flow is directed back toward the coastline where it is either trapped by the slope protrusion or is forced by the coastline in the downstream direction. The return flow trapped by the slope protrusion is again upwelled, decreasing its angular momentum where upon it turns clockwise and proceeds on the above circuit again.

The surface intensification of the flow has a similiar simple explanation in the conservation of potential vorticity. In the absence of any stratification the topography would induce a vertically uniform decrease in the angular momentum of the vortex tubes. This is the situation in the lower region of the water column.

In the deep interior of the water column the relative homogeneity of the mean density field implies that the fluid cannot sustain significant vertical gradients. Thus in this region of the water column there is, practically speaking, no baroclinic vortex tube compression. The absence of any significant stratification in the lower water column has the mathematical implication that the topography forces the vorticity term $\partial_3(S^{-1}\partial_3 p^{(0)})$ to be positive but small. The

conservation of potential vorticity implies that in the lower water column there will be a corresponding decrease in the angular velocity of the vortex tubes.

Near the surface, where the mean density gradient is the largest, the upwelling of the water column results in a larger baroclinic compression of the vortex tubes than in the interior of the water column. Consequently the angular momentum of the vortex tubes is strongly reduced in this region resulting in an increased clockwise circulation of the fluid particles, relative to the interior.

4.2 Horizontal Current Shear And Rossby Number

The Rossby number [$\epsilon = U(fL)^{-1}$] and the parameter governing the far field current shear a are two of the more important parameters controlling the qualitative structure of the flow field. The solutions obtained in Chapter III were computed for a taking on the range of values 10, 5, 2, 1 and .1, corresponding to e-folding lengths of 40, 80, 200, 400 and 4000 km, respectively. The Rossby number assumed the values .01, .05, .1 and .5. For each value of the Rossby number the effect of the five different e-folding lengths was examined. Thus, in total 20 numerical experiments were preformed testing the effect of variations in a and ϵ.

The Rossby number has two main effects on the flow field. Obviously, without $0(\epsilon) << 1$ the entire asymptotic analysis has no validity. The property which is most germain to our discussion, however, is the relationship between ϵ and the topographic parameters h_1 and h_2. The nondimensional heights of

the slope protrusion h_1 and the seamount h_2 have been obtained as $h_0(H\epsilon)^{-1}$ with the term h_0 defined as the maximum height of the slope protrusion for h_1 and as the maximum height of the Pratt seamount for h_2.

Increasing the Rossby number will therefore have the effect of reducing the magnitude of h_1 and h_2. The reduction of these two parameters will result in reducing the order of magnitude of the topographic forcing term in 3.10 and consequently will affect the horizontal amplitude functions $P_n(x,y)$.

The affect of increasing the Rossby number on the flow field is not, however, uniform. Huppert(1975) has provided a necessary condition for the formation of a stratified Taylor column over an order Rossby number topography. Simply stated, Huppert's condition is that the parameter $h_0(H\epsilon)^{-1}$ must be greater than some critical 0(1) value based on the topographic geometry, flow and domain geometry.

The critical value is obtained by examining the conditions under which a stagnation point can occur in the flow, ie. under what conditions can $\nabla p^{(0)} = (0,0)$ somwhere in the domain. This analysis was attempted for the present problem, however the topography, domain and upstream flow conspired to make this an unproductive exercise. Huppert's analysis assumed an axisymmetric topography in a horizontally unbounded fluid with a barotropic upstream current.

Nevertheless, one qualitative fact remains clear. The continental slope protrusion and the seamount would have critical values for h_1 and h_2, respectively for which local

eddies would form. Since there is no reason to assume that the critical values would be the same for each individual topographic feature, it follows that increasing the Rossby number will result in a nonuniform change in the flow as one or the other of h_1 and h_2 nears its critical value.

Consequently, there could be physically realistic Rossby numbers for which an eddy forms over one of the topographic features but not the other. In fact, depending on the value of the other parameters, increasing the Rossby number to about 0.1 prevents an eddy from forming over the slope protrusion, but allows an eddy to form over the seamount. In the situation where ϵ decreases the topographic parameters increase so that the interaction between the flow and the support of h(x,y) should intensify.

The effect of the Rossby number on the interaction between the upstream current and the support of h(x,y) has a simple physical interpetation. For a fixed length scale and latitude increasing ϵ is equivalent to increasing the speed scale of the flow. Intuitively, if the upstream flow is sped up it is possible to think of the upstream current has having a reduced sense of the bottom topography. In other words, by the time a fluid parcel can respond to variations in the bottom its speed has forced it to shoot past the support of h(x,y).

The Rossby number can also be increased for fixed speed scale and latitude by decreasing the length scale. (Recall that the length scale is chosen as the distance from the coastline to the Pratt seamount.) Decreasing the length scale intuitively

leads to the expectation that the upstream current experiences topographic changes over too short an interval to induce closed streamline circulation.

The parameter a determines the upstream horizontal current shear. If a increases than the current assumes the shape of a narrow coastal baroclinic jet. Decreasing a creates a broader coastal flow. The dimensional equivalent of a is given by $aL^{-1}\ m^{-1}$. Choosing $L = 400$ km implies that $a = 5$ corresponds to a current with a horizontal e-folding distance of $La^{-1} = 80$ km.

The main mathematical mechanism by which a effects the flow is its existence in the denominator of the Green's function $g(x,y|x_0,y_0)$ in 3.17. Since $\lambda_0 = a^2 + \kappa$ the denominator of 3.17 satisfies $(m\pi/2)^2 + \lambda_n - \kappa \geq (m\pi/2)^2 + a^2$. Therefore reducing a should result in intensifying the interaction between the upstream flow and the topography. Increasing a will decrease the denominator and consequently reduce the order of magnitude of the interaction stream function $p(x,y,z)$. The increased interaction, ie. greater anticyclonic motion in the water column, for decreased a has the following physical interpetation.

The physics behind the response of the eddy flow field to variations in a is obtained by examining the potential vorticity. The relative vorticity of the upstream current is given by $-\partial_2 u_0 = a\exp(-ay)Z(z)$, which is positive for the a and $Z(z)$ considered in this thesis. The portion of the far field current which is within an e-folding distance ($y<a^{-1}$) of the

coastline (y=0) experiences decreasing relative vorticity for decreasing a. The far field current outside this region (ie. $y>a^{-1}$) experiences increased relative vorticity for decreasing a.

Variations in a, however have no effect on the mean state density profile. Hence the change in vorticity associated with the compression of the mean state isopcynals, as the flow encounters the topography, can be viewed as a fixed positive number.

For those upstream streamlines for which $y < a^{-1}$, conservation of potential vorticity therefore implies that the relative vorticity of the eddy field decreases for decreasing a. In the region $y > a^{-1}$ the relative vorticity of the eddy field will increase as a decreases. In other words, decreasing a forces the along coastline current to increase its anticyclonic motion but forces the more horizontally interior flow to decrease its anticyclonic motion during interaction with h(x,y).

The decrease of the relative vorticity of the near coastline current is achieved by the turing of the streamlines further out into the horizontal interior of the domain. This tendency is mitigated against by the reduced tendency of the more interior streamlines to change their relative vorticity. The subsequent crowding together of streamlines increases the horizontal gradients in the pressure field resulting in the increased anticyclonic rotation of the eddy interior.

Figures 55, 56, 57 and 58 are contour plots of $p^{(0)}$ on $z = 1$ for the (a,ϵ) pairs (10,.1), (10,.01), (1,.1) and (1,.01)

respectively. Figures 55 and 56 illustrate the effect of increasing a from its standard value of 5 to 10, for an increased ϵ of .1 and a decreased ϵ of .01 from its standard value of .02. Figures 57 and 58 depict the effect of decreasing a from 4 to 1 for the same set of Rossby numbers.

In this series of calculations the order of magnitude of $p^{(0)}$ varied substantially. Therefore the contouring intervals have been altered for each particular case. In Figure 55 the contouring intervals are + or - .001 relative to the 0 contour. In Figures 56 and 58 the intervals are + or - .01 relative to the 0 contour. In Figure 57 the contour intervals are + or - .1 relative to the 0 pressure contour.

Figure 55, the contour plot of $p^{(0)}$ for $(a,\epsilon) = (10,.1)$ on $z = 1$, shows the effects of increasing the shear in the upstream current and the Rossby number. Based on the physics of the problem it is expected that for this parameter regime the size and strength of the eddy produced should be smaller than the that calculated for the standard parameters. Comparing Figure 55 to Figure 11 this is clearly seen to be the case.

Several changes to the flow field are apparent. Increasing the Rossby number to 0.1 has decreased the topographic parameters h_1 and h_2 to 2.2 and 7.1, respectively. For this set of (a,ϵ) the parameter h_1 is less than its (Huppert) critical value since no eddy has formed over the slope protrusion. The failure to generate closed streamlines over the slope protrusion results in the eddy (centered over the seamount) having a small regional extent, with an radius of order .25 (100 km).

The magnitude of the interaction pressure field $p(x,y,z)$ has been sharply reduced for $(a,\epsilon) = (10,.1)$. In fact the interaction is weakened to the degree that $p^{(0)} < 0$ everywhere in the domain in Figure 55. Typical values for the magnitude of $p^{(0)}$ over the seamount are -.003 in Figure 55, whereas in Figure 11 $p^{(0)}$ was typically +.1 in the same region.

Corresponding to the sharp decline in the horizontal gradients in $p^{(0)}$ for $(a,\epsilon) = (10,.1)$, the magnitudes of the topographically induced velocities have been reduced. Over the slope protrusion the speeds are on the order of .05 (5 cm s^{-1}) compared to 20 cm s^{-1} in Figure 11. The seamount induces speeds on the order of .02 (2 cm s^{-1}) in Figure 55 compared to 40 cm s^{-1} for $(a,\epsilon) = (10,.1)$.

The transports have similiarly decreased for this choice of a and ϵ. Defining the transport magnitude as $|M| = [(m_1)^2 + (m_2)^2]^{1/2}$, typical transports in Figure 55 are about .006 (2 Sv) at $(x,y) = (0,.1)$ compared to 20 Sv for $(a,\epsilon) = (5,.02)$. Over the seamount the transport magnitude $|M| \simeq .007$ (2.5 Sv) compared to 20 Sv for the standard parameters.

In Figure 56 $(a,\epsilon) = (10,.01)$, reducing the Rossby number for fixed current shear has intensified the interaction between the flow and the topography. The topographic parameters h_1 and h_2 have been increased to 22.8 and 71.4, respectively. The parameter h_2 is close to becoming $0(\epsilon^{-1})$ implying that the seamount for $\epsilon = .01$ is not $0(\epsilon H)$.

Examining Figure 56 the local anticyclonic eddy over the

slope protrusion has reappeared. Associated with the slope eddy is the reappearance of the upstream and downstream stagnation points. Although the contours in Figure 56 do not indicate it, there is an anticyclonic flow which encompasses both local eddies, located just radially inward of the 0 streamline.

The magnitude of the interaction between the topograpghy and the upstream flow has intensified. Over the seamount $p^{(0)} \simeq .05$ and over the slope protrusion $p^{(0)} \simeq .04$. Concomitant with the increased interaction are the larger horizontal gradients in $p^{(0)}$ as manifested in the computed velocity field.

Current speeds over the seamount are on the order of .3 (30 cm s^{-1}). The surface speeds over the slope protrusion have increased to about .25 (25 cm s^{-1}). Typical transports over the seamount are on the order of .07 (25 Sv) and over the slope protrusion .01 (3.5 Sv).

The vertical structure of the eddies in Figures 55 and 56 is consistent with the vertical structure of the standard parameter solution described last section. By this it is meant that the qualitative properties of the decay of the eddies with increasing depth remains more or less invariant for the (a,ϵ) parameter pairs of Figures 56 and 57. That being the case it suffices to say that the eddies are surface trapped, with the horizontal velocity field decaying to about half its surface value at z = .9 (350 metres depth).

Comparing Figure 55 to 56 a couple of points should be made. For a = 10, increasing the Rossby number from .01 to .1

decreases h_1 to below its (Huppert) critical value and thus an eddy fails to form over the slope protrusion. Second for a relatively narrow coastal current (a=10 implies an e-folding length of 40 km) the qualitative appearance of the induced flow over the support of h(x,y) looks more like two separate eddies, than the large scale flow interaction seen in Figure 11. It is not surprising to conclude, therefore, that as the current becomes broader the disturbances produced by the slope protrusion and the seamount progressively interact with each other and produce a more coherent large scale eddy circulation.

In Figures 57 and 58 the parameter a = 1 and ϵ takes on the values .1 and .01 respectively. Having a = 1 implies that the upstream current has a horizontal e-folding length of 400 km. These two figures clearly illustrate that decreasing a increases the size and strength of the eddy.

Caution must be applied though when arguing any application of these two figures to the north east Pacific Ocean. Numerical calculations suggest that in Figure 57 the no normal flow boundary condition along y = 2 is begining to affect the structure of the flow field over the support of h(x,y). Calculations show that in Figure 58 the interior flow has been definitely altered by the seaward channel wall.

In both Figures 57 and 58 there is no local eddy production over the slope protrusion. Numerical experiments were unable to distingush between whether the increased interaction of the seamount on the flow simply dominated any local effect of the slope protrusion, or whether the for this choice of a the

(Huppert) critical value of h_1 was so large that no reasonably small values of the Rossby number could generate a local eddy over the slope protrusion.

The maximum value of $p^{(0)}$ occured over the seamount in both calculations. In Figure 57, $p^{(0)} \simeq .1$ and in Figure 58 $p^{(0)} \simeq 1$ over the seamount. Typical speeds for $(a,\epsilon) = (1,.1)$ were on the order .2 (20 cm s^{-1}) over the seamount. In the return coastal flow the speeds increased to about .25 (25 cm s^{-1}). For the parameter pair $(a,\epsilon) = (1,.01)$ typical speeds were about 2 (2 m s^{-1}) over the seamount and about 4 (4 m s^{-1}) in the return coastal flow.

The computed transports varied substantially as well. For $(a,\epsilon) = (1,.1)$ the transport magnitude was about .1 (35 Sv) over the seamount and about .3 (100 Sv) in the return coastal flow. With $(a,\epsilon) = (1,.01)$ the transport magnitude increased to about 1.2 (400 Sv) over the seamount and to about 2 (700 Sv) in the return coastal flow.

Decreasing the shear in the upstream current increases the horizontal extent of the eddy. While Figures 55 and 56 almost gives the impression of two separate flow distortions over the seamount and the slope protrusion. Figures 57 and 58 suggest a single large scale eddy. In Figure 57 the eddy has a typical radius of about 300 km and in Figure 58 a radius of 400 km.

It was argued earlier the calculations for Figures 57 and 58 suggest that for this a the seaward boundary is significantly affecting the structure of the interior flow field. This means that as the size of the eddy increases and the affects of the

boundary become important to the interior, the eddy must elongate itself and begin to penetrate deeper in the water column. This elongation begins to occur in Figure 57 and is quite apparent in Figure 58.

Associated with the broadening of the eddy for decreasing a is a related deeping in the vertical extent of the eddy. Figures 59 and 60 are along coastline vertical sections of $p^{(0)}$ at $y = .6$ for $(a,\epsilon) = (1,.1)$ and $(1,.01)$, respectively. Comparing these two figures with Figure 18, the corresponding figure for the standard set of parameters, a couple of observations can be made.

The deepening of the eddy is apparent from the fact that in Figure 18 the .01 $p^{(0)}$ does not reach the bottom, whereas in Figure 59 it does. In Figure 60 the contouring intervals are + or - .1, with the .1 contour reaching the bottom, implying that the .01 does as well. Thus the horizontal gradients of the $p^{(0)}$ field remain higher deeper, indicating that the vertical structure protrudes further into the water column. Finally, Figures 59 and 60 show the increased horizontal extent of the eddy corresponding to the 0 pressure contour displaced outward from $x = 0$.

4.3 Topographic Parameters

Varying the topographic parameters h_1 and h_2 directly is the simplest way to investigate the contribution to the total eddy field of each individual topographic feature. From Chapter II and last section, the topographic parameters h_1, h_2 are given by the maximum height of the slope protrusion and the Pratt

seamount height respectively, divided by ϵH. The topographic parameters are required to be 0(1) if the Taylor expansion of the boundary condition $w = (u,v)\cdot\nabla h(x,y)$ on $z = \epsilon h(x,y)$ about $z = 0$ is to be formally justified.

The maximum heights of the Pratt seamount and the slope protrusion are estimated to be 2500 metres and 800 metres respectively from Figure 1. With $\epsilon \simeq .02$ and $H \simeq 3500$ this means that h_1 and h_2 are approximately 11 and 34, respectively. This calculation implies that h_1 and h_1 are situated in the intermediate region between 0(1) and $0(\epsilon^{-1})$. Thus the Taylor expansion is appropiate, if only marginally justified.

Numerical simulations of the solutions were computed for h_1 taking on the range of values 0, 5, 10 and 15 and h_2 taking on the range of values 0, 10, 20, 30, 35. This means 20 different numerical experiments were preformed varying the topographic parameters.

Figures 61 and 62 are contour plot of $p^{(0)}$ for $(h_1,h_2) = (10.9,0)$ and $(0,34.1)$, respectively. The contouring interval was + or - .01 relative to the 0 stream line. These two simulations correspond to computing the flow field for the standard set of parameters in the absence of the seamount (Figure 61) or in the absence of the slope protrusion (Figure 62).

Comparing Figures 61 and 62 with Figure 11 the relative contribution of each topographic feature to the total topographic mean flow interaction can be seen. The interior structure of the local eddy (contours of value greater than

+.03) over the slope protrusion is laregly unaffected by the existence of the seamount. The exterior region, given by those contours of value less than about +.03 are significantly affected by the seamount since the fluid parcels associated with with these streamlines are topographically steered out to the seamount.

The effect of the slope protrusion on the local eddy formed over the seamount is more intense. Figures 11 and 62 suggest that the size and intensity of the local seamount eddy are decreased by the slope protrusion. This makes sense since most of the near coastal flow is directed into an eddy by the slope protrusion. Since the far upstream flow decreases as the distance to the coastline increases it follows that the slope protrusion interacts with the component of the flow which accounts for the most significant interaction.

The magnitude of $p^{(0)}$ over the seamount in Figure 62 is about .11 compared to about .1 in Figure 11. Thus the pressure field over the seamount is about 10% to 20% higher in Figure 62 than it is in Figure 11. The change in surface speeds over the seamount is similiar. In Figure 11 the speeds are are about 30 cm s^{-1} at (x,y) = (.6,.6) and in Figure 62 typical speeds are about 34 cm s^{-1}.

All the numerical experiments performed suggest that if a local eddy is to occur over the slope protrusion the stagnation points associated with eddy must occur on the x - axis, implying that stagnation streamline is the 0 pressure contour. This is a consequence of the conservation of potential vorticity.

Suppose that a local eddy is produced over the slope protrusion but that its stagnation points are in the interior of the domain. For all those streamlines coastward of the stagnation streamline the following two facts are most relevant. First, they are bounded seaward by the stagnation streamline, and second h(x,y) monotonically decreases with increasing distance to the coastline. The second fact implies that compression of the isopcynals is increased coastward of the stagnation streamline, where upon the first fact will imply that the fluid parcels cannot sufficiently decrease their relative vorticity in order to conserve potential vorticity. This contradiction of the basic physics of the model therefore implies that if a local eddy exists over the slope protrusion the stagnation points must occur on the 0 pressure contour lying on the coastline.

This is not necessarily the case for the local eddy formed over the seamount since the support of h(x,y) does not extend to the coastline for $h_1 = 0$. Thus in the absence of the slope protrusion the stagnation points for the eddy over the seamount can occur in the interior of the domain, as it does in Figure 62. Numerical experiments varying the values of h_1 with $h_2 = 0$ and h_2 with $h_1 = 0$ suggest that the (Huppert) critical value of h_1 is about 4 and for h_2 is about 9.

4.4 Brunt-Vaisala Frequency

The parameters N_0^2 and $(\gamma^*)^{-1}$ correspond to the maximum value (at z=1) and the vertical attenuation of the dimensionalized Brunt-Vaisala frequency $[N^*(z^*)]^2$ given in section 2.1. Their physical importance resides in controlling the contribution to the potential vorticity of the angular momentum associated with baroclinic vortex tube stretching.

Recall that the nondimensional Brunt-Vaisala frequency was given by $S(z) = s_0 \exp[\gamma(z-1)]$ with the Burger number $s_0 = [N_0 H/(fL)]^2$ and $\gamma = \gamma^* H$. Holding γ fixed and decreasing N_0 will decrease the Burger number s_0, the maximum amplitude of S(z). Physically, decreasing N_0 is equivalent to reducing the vertical shear in the mean state density field, thereby assuming a more homogeneous ocean.

Consider the consequences of reducing N_0. The increased homogeneity of the ocean results in reducing the degree of compression that can occur to the isopcynals. Thus, as the upstream flow encounters the support of h(x,y), baroclinic vortex tube compression is reduced. The conservation of potential vorticity will imply that the magnitude of the associated change in the relative vorticity will be equivalently reduced. However, since isopcynal compression occure primarily near the surface the principle effect of decreasing N_0 will be to decrease the degree of surface intensification in the eddy flow field.

Increasing N_0 should have the opposite effect. The surface intensification will increase as the vertical gradients in the

mean state density field surface sharpen. Increasing N_0 also as the possibility of deepening the depth to which the eddy penetrates, since changes in N_0 uniformily effect S(z) throughout the water column. If N_0 is sufficiently increased then appreciable baroclinic vortex tube compression can occur in intermediate regions of the water column. This will result in a decreased relative vorticity in this region and consequently in an apparent deepening of the eddy motion.

In the extreme case in which $N_0 = 0$ the interaction stream function p(x,y,z) is independent of z and a Taylor column will form over the region where $h(x,y) \neq 0$. The circulation around the Taylor column will be anticyclonic and will extend uniformly to the surface. However if $N_0 \neq 0$ then a stratified Taylor column will appear over the region $h(x,y) \neq 0$, with a more complicated vertical structure than in the homogeneous case.

The vertical shear in S(z) is governed by $\gamma = \gamma^* H$. Increasing γ^* will result in decreasing the e-folding distance required for S(z) to decay to $s_0 e^{-1}$. Thus increasing γ^* will imply that the most significant vertical changes in the mean state density field occur closer to the surface. Near the surface, therefore, the compression of the isopcynals increases as γ^* increases. This results in an increased surface intensification of the eddy trapped closer to the surface. Decreasing γ^* should have the opposite effect. The surface intensification should decrease somewhat as the gradients in the mean state density field are smoothed out.

The compilation by Emery et al. (1983) of typically

observed North Pacific Ocean Brunt-Vaisala frequencies suggests that the parameter N_0 lies between 10^{-1} s^{-1} and $2 \cdot 10^{-1}$ s^{-1}. The data presented in Emery et al. (1983) also suggests that the attenuation of the Brunt-Vaisala frequency with depth is more or less geographically invariant in the Northeast Pacific. It remains, however, desirable to investigate the effects of variable vertical shear of the Brunt-Vaisala frequency on the flow field.

The least squares fit of the parameter $(\gamma^*)^{-1}$ by Willmott and Mysak(1980) gave a value of 254.51 m, so this parameter was varied between 225 and 300 metres. Varying $(\gamma^*)^{-1}$ outside this range was numerically impossible since at certain stages in the calculations some of the variables exceeded the ability of the computer to handle, ie. they were too large.

The parameter N_0 was varied between 0.01 s^{-1} and 0.02 s^{-1}. Specifically, the solutions obtained in Chapter II were computed for N_0 taking on the values 0.01 s^{-1}, 0.015 s^{-1} and 0.02 s^{-1} and $(\gamma^*)^{-1}$ taking on 225 m, 250 m, 275 m and 300 m, giving 12 parameter pair calculations.

Figure 63 is a contour plot of a vertical section of $p^{(0)}$ computed along $y = .8$ for $(\gamma^*, N_0) = (300^{-1}m^{-1}, .01\ s^{-1})$. This value of $(\gamma^*)^{-1}$ corresponds to a change of about +12% from its standard value. The contour intervals are + or - .01 relative to the 0 pressure contour. Comparing Figure 63 with Figure 19 illustrates the main features argued previously that are associated with decreasing γ^* from its standard value.

In Figure 19 the $p^{(0)}$ field has a surface maximum of about

+.1 over the seamount. In Figure 63, $p^{(0)} \simeq .08$ on $z = 1$ over the seamount, representing about a 20% decrease. It is also possible to see that the eddy flow field in Figure 63 is less intense than in Figure 19 by the fact that the width of the eddy (in this section) is about 1 (400 km) in Figure 19 and about .75 (350 km) in Figure 63.

The surface speeds in Figure 63 at $(x,y) = (.8,.8)$ are about 26 cm s^{-1} compared to about 29 cm s^{-1} in Figure 19, so that there is slightly more than a 10% reduction in the speeds. The transports at this (x,y) coordinate in Figure 63 is about .05 (18 Sv) which is about 5% smaller than the 19 Sv calculated in Figure 19.

Figures 64 and 65 are contoured vertical sections of $p^{(0)}$ along $y = .2$ and $y = .8$ respectively for $(\gamma^*,N_0) = (225^{-1}m^{-1},.02\ s^{-1})$. Based on previously made arguments, increasing N_0 should result in an increased surface intensification and an increased vertical penetration of the eddy. Decreasing $(\gamma^*)^{-1}$ from its standard value to 225 metres should increase the surface response and decrease the depth to which the eddy extends. It is not surprising, however, that Figures 64 and 65 show, in addition to an intensified surface response, an increased depth penetration of the eddy. The changes in $(\gamma^*)^{-1}$ and N_0 from their standard values for these figures are 12% and 90% respectively. Therefore effect of variations in N_0 can be reasonably expected to dominate those created by varying γ^*.

Comparing Figure 64 to Figure 16 the dramatic increase in

the vertical extent in the eddy can be seen. In Figure 16 the +.01 contour extends to about z = .6 (1400 metres deep), whereas in Figure 64 this contour extends to the bottom. Interestingly the magnitude of $p^{(0)}$ is only slightly increased in Figure 64 compared to Figure 16. The most significant change occurs in the transports. In Figure 64, at (x,y) = (.2,.2) the transport has magnitude about .015 (4 Sv). This represents about a 25% change in the transport (5 Sv) calculated in Figure 16.

The increased vertical extent of the eddy is also seen by comparing Figure 65 with Figures 63 and 19. In Figure 65 the upstream 0 pressure contour occurs at about $x \simeq -.1$ for $y = .8$, whereas in Figure 63 it occurs for $x \simeq 0$. The +.02 contour extends down to about 900 metres in Figure 65 and down to about 600 metres in Figure 63.

The intensity of the eddy is increased in Figure 65 compared to Figure 63. In Figure 65, $p^{(0)} \simeq +.09$ on $z = 1$ compared to about +.08 in Figure 63. The magnitude of $p^{(0)}$ in Figure 65 is about the same as in Figure 19. The surface speeds are increased from about 26 cm s^{-1} in Figure 63 to about 28 cm^{-1} in Figure 65, consistent with those in Figure 19. The transports have increased as well, in line with the deepening of the eddy. In Figure 65 at (x,y) = (.8,.8) the transport is about 21 Sv compared to about 17 Sv in Figures 63 and 19, representing a 20% increase.

Figure 66 is a contour plot of a vertical section for $p^{(0)}$ along $y = .8$ in which both $(\gamma^*)^{-1}$ and N_0 have been increased from their standard values to 300 m and .02 s^{-1} respectively.

The contour intervals are + or - .01 relative to the 0 pressure contour. Figure 66 has the resulting eddy flow extending deeper into the water column and at the same time has the near surface motion decreased.

The magnitude of $p^{(0)}$ on z = 1 is about +.06 in Figure 66 compared to about +.08 in Figure 65, about +.08 in Figure 63 and +.1 for the standard set of parameters in Figure 19. The increased spacing between the surface contours in Figure 66 suggests that the horizontal velocities are reduced. At (x,y) = (.8,.8) the surface speed is about .3 cm s^{-1} in Figure 66 compared to surface speeds in excess of 20 cm s^{-1} in Figures 65, 63 and 19.

The transport is not significantly decreased in Figure 66 compared to Figure 65. In Figure 66 the transport is about 21 Sv which is about the same as in Figure 65. Thus while the surface intensity has decreased due to larger N_0 and smaller γ^*, the larger N_0 has also deepened the eddy so that the integrated effect is to increase the transport.

4.5 Horizontal Current Shear And Surface Current

The principle concern of this section is to describe the effect of variations of the boundary condition Z(1) = a on the qualitative structure of the eddy flow field. Attention is given to the parameter a only in so far as it effects the role played by Z(1). A complete discussion of the response of the flow field to variations in a is given in Section 4.2.

The effect of variations in Z(1) is again best understood within the frame work of vorticity arguments. The upstream

vorticity is given by $-\partial_2 u_0 = \alpha \exp(-\alpha y) Z(z)$. Consequently increasing $Z(1)$, holding α fixed, will increase the relative vorticity of the surface flow. Moreover, since $Z(z)$ smoothly assumes its boundary value at $z = 1$, increasing $Z(1)$ will also tend to increase the vorticity of the near surface flow. Decreasing $Z(1)$ will obviously decrease the relative vorticity of the near surface upstream current.

Consider the effect of increasing $Z(1)$ on the interaction between the upstream current and the topography. The conservation of potential vorticity and the fixed change in the compression of the isopcynals implies that increasing $Z(1)$ will increase the relative vorticity of the eddy field. Consequently the anticyclonic motion in the eddy is reduced.

In fact, for a sufficiently large surface current no eddy is produced. If all other parameters are held to their standard values, numerical experiments suggest that this so-called cutoff speed is about 30 cm s^{-1}. Increasing (decreasing) the horizontal current shear parameter α, decreases (increases) the necessary cutoff speed.

In the extreme situation with $Z(1) = 0$ there is no surface expression of any interaction between the upstream current and the topography. This can be seen by examining the boundary condition 3.3. If $Z(1) = 0$ then 3.3 requires that $pD_3Z = 0$ on $z = 1$. If $D_3Z = 0$ on $z = 1$ then (providing $Z(z)$ is analytic) $Z(z) = 0$ everywhere in the water column. Therefore $Z(1) = 0$ must imply that $p = 0$ on $z = 1$, which has the physical implication that no interaction occurs on the surface.

The existence of a cutoff surface speed and the fact that $Z(1) = 0$ leads to $p^{(0)} = 0$ on $z = 1$ implies the existence of a value of $Z(1)$ for which the surface interaction is maximized. For the standard set of parameters this value is about 5 cm s^{-1}.

Decreasing (increasing) $Z(1)$ below this extremal value will tend to decrease (increase) the surface eddy circulation. Decreasing (increasing) $Z(1)$ above this value will tend to increase (decrease) the surface response.

The solutions obtained in Chapter III were computed for $a = Z(1)$ taking on the range of values 0, .1, .25, .5, and 1.0 corresponding to 0 cm s^{-1}, 10 cm s^{-1}, 25 cm s^{-1}, 50 cm s^{-1} and 1 m s^{-1}. The horizontal current shear was varied as in Section 4.2, thus 25 numerical experiments were preformed varying a and $Z(1)$.

Figure 67 is a contour plot of $p^{(0)}$ on $z = 1$ for the extremal case where $Z(1) = .05$ (5 cm s^{-1}). All other parameters are held to their standard values. Figures 68 and 69 are contour plots of vertical sections of $p^{(0)}$ along $y = .2$ and $y = .8$, respectively. In all three figures the contouring interval is + or - .01 relative to the zero pressure contour.

Comparing Figure 67 with Figure 11 the increased eddy flow features can be seen. The coastal stagnation points in Figure 67 are displaced outward from $x = 0$ compared to Figure 11, implying that the interaction between the topography and the upstream current begins further upstream for $Z(1) = .05$. The area of eddy circulation is also larger in Figure 67 than in Figure 11.

The value of $p^{(0)}$ has increased in the interior of the eddy. Over the seamount, $p^{(0)}$ is on the order of .13 in Figure 67. This represents an increase of about 30% from $p^{(0)} \simeq .1$ calculated in Figure 11. Similiar increases are observed over the slope protrusion with $p^{(0)}$ increasing from about .08 in Figure 11 to about .1 in Figure 67.

The reduced spacing between the streamline contours in Figure 67 compared to Figure 11 manifests itself in an increased clockwise circulation. Over the seamount, the surface speeds computed in Figure 67 are typically on the order of .5 (50 cm s^{-1}). This represents an increase of about 25% over the .4 (40 cm s^{-1}) computed in Figure 11. There is a similiar increase over the slope protrusion. At (x,y) = (0,0), the speeds in Figure 67 are about .75 (75 cm s^{-1}) compared to the .5 (50 cm s^{-1}) in Figure 11. Further out, say at (x,y) = (0,.1), the speeds are about .45 (45 cm s^{-1}) in Figure 67 compared to about .3 (30 cm s^{-1}) in Figure 11.

Comparing Figures 68 and 69 with Figures 16 and 19 respectively, the increased vertical penetration of the eddy flow field can be seen. In Figure 68, the slope protrusion induces a typical current speed of about .05 (5 cm s^{-1}) in the deep interior of the water column, compared to a negligible flow in Figure 16. A similiar situation is found in the section along y = .8. In Figure 69, the deep interior speeds are on the order of .1 (10 cm s^{-1}) compared to about .01 cm s^{-1} in Figure 19.

The increase in the magnitude of the velocity throughout

the water column results in increasing the transports in the eddy. Over the seamount, the transport is about .12 (40 Sv) compared to about the 20 Sv computed for the standard set of parameters. In the return coastal flow the transport has increased from 20 Sv, for the standard parameters, to about 70 Sv with Z(1) = .05.

Figure 70 is a contour plot of $p^{(0)}$ on z = 1 for Z(1) = 1. The contour intervals are + or - .02 relative to the zero pressure contour. This value of Z(1) is well above the numerically determined cutoff value of .3. Consequently, no surface expression of an eddy is expected to occur. There is a seaward deflection of the streamlines over the seamount. Over the slope protrusion there is a less noticeable seaward deflection of the streamlines. Vertical sections of $p^{(0)}$ show that there is no submerged eddy over the slope protrusion or over the seamount.

Figure 71 is a contour map of $p^{(0)}$ on z = 1 with Z(1) = .01. The contour intervals are + or - .01 relative to the zero $p^{(0)}$ contour.

This value of Z(1) is smaller than the extremal value of .05, consequently the eddy circulation shown in Figure 71 is weaker than in Figure 67. Over the seamount, $p^{(0)} \simeq .04$ corresponding to about 70% decrease from that in Figure 67. The $p^{(0)}$ field over the slope protrusion is similiarly reduced, with $p^{(0)} \simeq .03$ in Figure 71 compared to $p^{(0)} \simeq .1$ in Figure 67.

The surface speeds have been reduced as well. Typical speeds over the seamount are about .12 (12 cm s^{-1}) and over the

slope protrusion are about .2 (20 cm s^{-1}), corresponding to about a 75% compared to those in Figure 67.

Figures 72 and 73 are vertical sections of $p^{(0)}$ along y = .2 and y = .8 respectively, for Z(1) = .01. The contouring interval is + or - .01 relative to the zero $P^{(0)}$ contour. These two figures show that, except near the surface, the response is nearly depth independent. Numerical experiments show that this is the case whenever $Z(1) \simeq Z(0)$.

If the boundary conditions on Z(z) are equal then the form of S(z) will imply that Z(z) will only slightly deviate from the constant value Z(0) (=Z(1)). Since $G_0(z)$ is proportional to Z(z), the principle response of the flow to topographic excitment will be only marginally depth dependent. However if Z(z) is truly barotropic then form of the solution shown in Figures 71, 72 and 73 is incorrect. In Section 3.2 it was shown that if Z(z) is barotropic then $\kappa = -a^2$ implying that $\lambda_0 = 0$ which in turn implies that the form of the solution used to compute Figures 71, 72 and 73 is invalid.

4.6 Horizontal Current Shear And Bottom Current

Variations in the bottom boundary condition Z(0) = b have a significant effect on the eddy flow field. Vorticity arguments are again the most physically relevant way to understand the effect of the parameter Z(0).

Figure 6 shows that from z = 0 to $z \simeq .5$ Z(z) is approximately depth independent. This is a consequence of a Brunt-Vaisala frequency which is approximately zero at this depth. Variations in Z(0) will lead to more or less uniform

changes in the value of Z(z) in the lower water column.

Consequently, increasing Z(0) will increase the relative vorticity of the upstream current throughout the lower half of the water column. The conservation of potential vorticity and the compression of the mean state isopcynals as the flow encounters the support of h(x,y) will imply that that the anticyclonic motion over the topography will be reduced for increased Z(0). In fact, for sufficiently large Z(0) no eddy is produced at all. This cutoff value for the bottom boundary current was numerically determined to be about 50 cm s^{-1}, assuming all other parameters are held to their standard values. The above vorticity argument implies that decreasing Z(0) will tend to increase the anticyclonic motion over the topography.

This scenario must be modified by the fact that Z(0) = 0 will result no interaction occuring at all. From 3.18 and 3.19 it is clear that each $P_n(x,y)$ is proportional to $G_n(0)$. However, from 3.8 it follows that if Z(0) = 0 then $G_n(0) = 0$ for each mode. Therefore no bottom current will imply no interaction.

The preceding argument and the previous vorticity argument are compatible if there exists some value of Z(0) for which the interaction field is maximized. For the standard set of parameters this value is Z(0) = .02. Numerical experiments seem to indicate that the eddy circulation is maximized if $5 \cdot Z(0) = Z(1)$, provided the other parameters are held to their standard values. Increasing (decreasing) Z(0) or Z(1) above

this equilibrium relationship will decrease (increase) the magnitude of the interaction flow field. Increasing (decreasing) Z(0) or Z(1) below this equilibrium relationship will increase (decrease) the magnitude of the interaction flow field.

Figure 74 is a contour plot of $p^{(0)}$ on z = 1 for Z(0) = .001. This value of Z(0) corresponds to a upstream coastal bottom current of .1 cm s^{-1}. All other parameters are held at their standard values. The contour interval is + or - .002 relative to the zero streamline.

For this value of Z(0) there is no surface expression of an eddy over the slope protrusion. However, closed streamline circulation does occur over the seamount. The reduction of Z(0) to .001 from its standard value of .01 has a significant effect on the properties of the flow field.

Over the slope protrusion typical velocities were computed to be about .02 (2 cm s^{-1}). Over the seamount the velocities are about .03 (3 cm s^{-1}). Transports are about .001 Sv and .002 Sv over the slope protrusion and seamount respectively.

Figure 75 is a contour plot of a vertical section of $p^{(0)}$ along y = .2. The contour interval is + or - .002 relative to the zero $p^{(0)}$ contour.

The most interesting feature of Figure 75 is the region of positive $p^{(0)}$ bounded by the zero contour and z = 0. This region corresponds to an anticyclonic eddy extending from the ocean floor to about z = .75. The magnitude of the velocity field in its interior is very weak, on the order of .005 cm s^{-1}.

The near surface contours turn upward toward the surface over the submerged eddy as a consequence of the turning of the coastal flow seaward as it encounters the slope protrusion.

Figure 10 - Location of computed vertical profiles relative to the topography

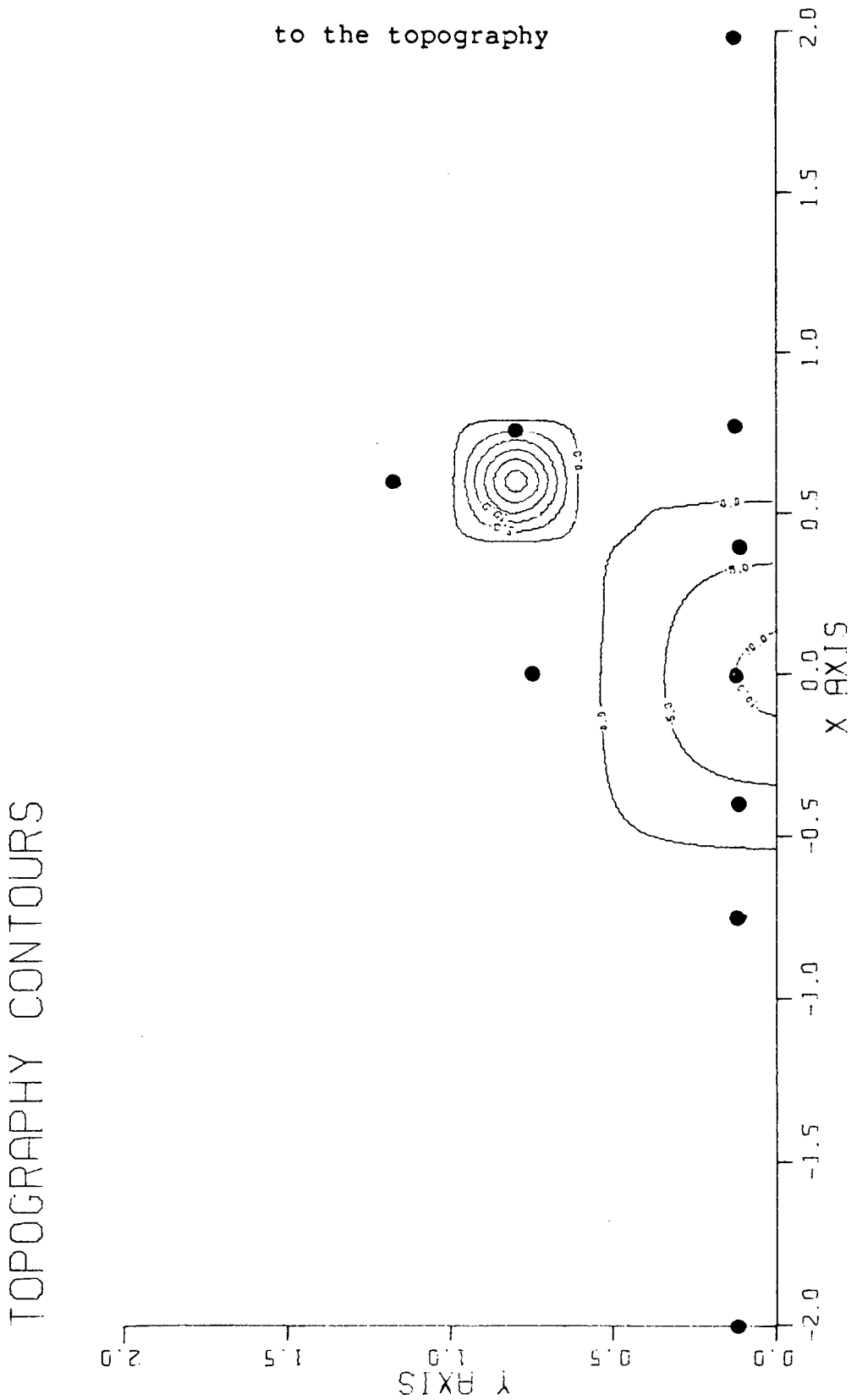

Figure 11 - Horizontal contour plot of the stream function on z = 1

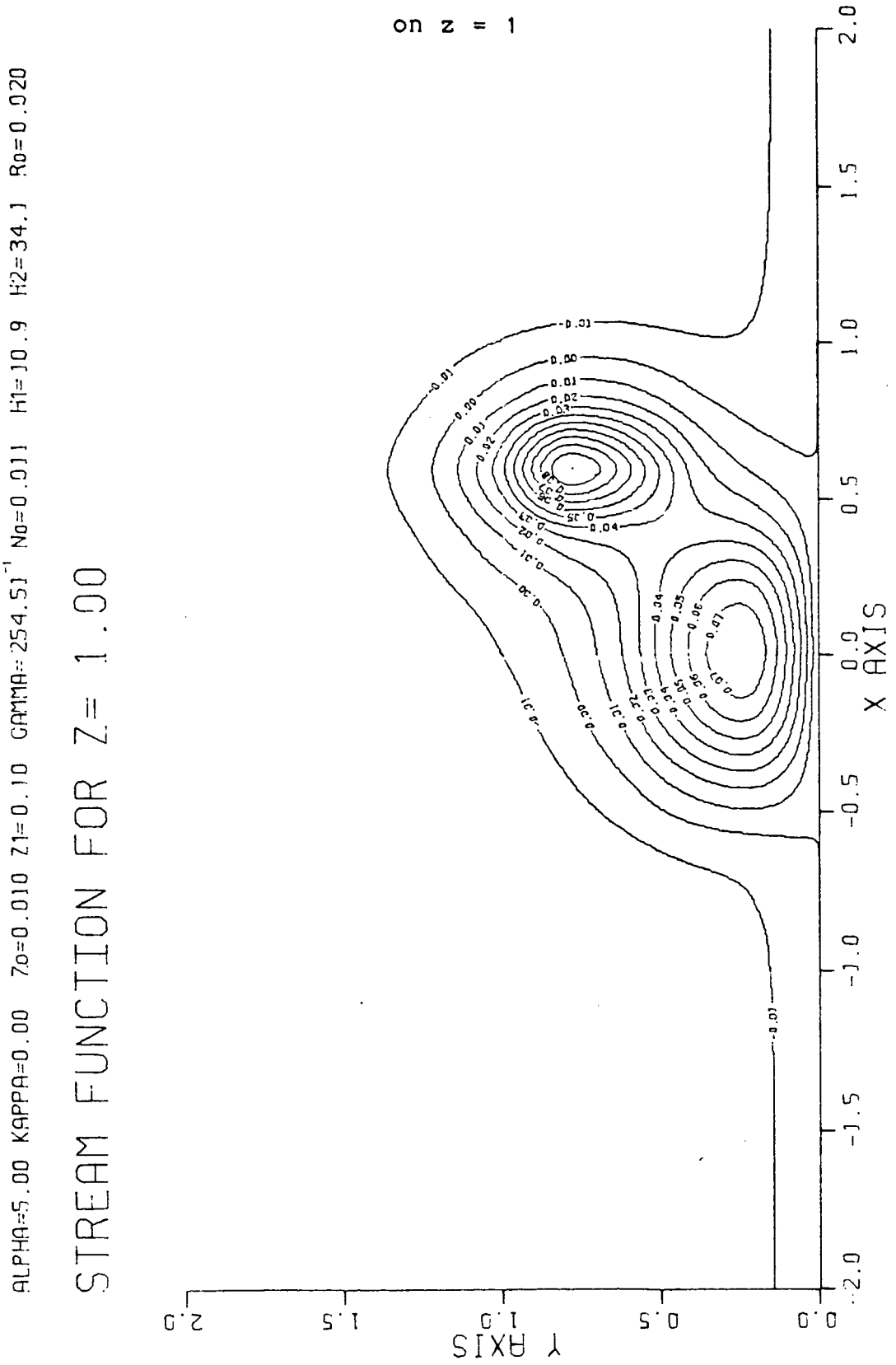

Figure 12 - Horizontal contour plot of the stream function on z = .9

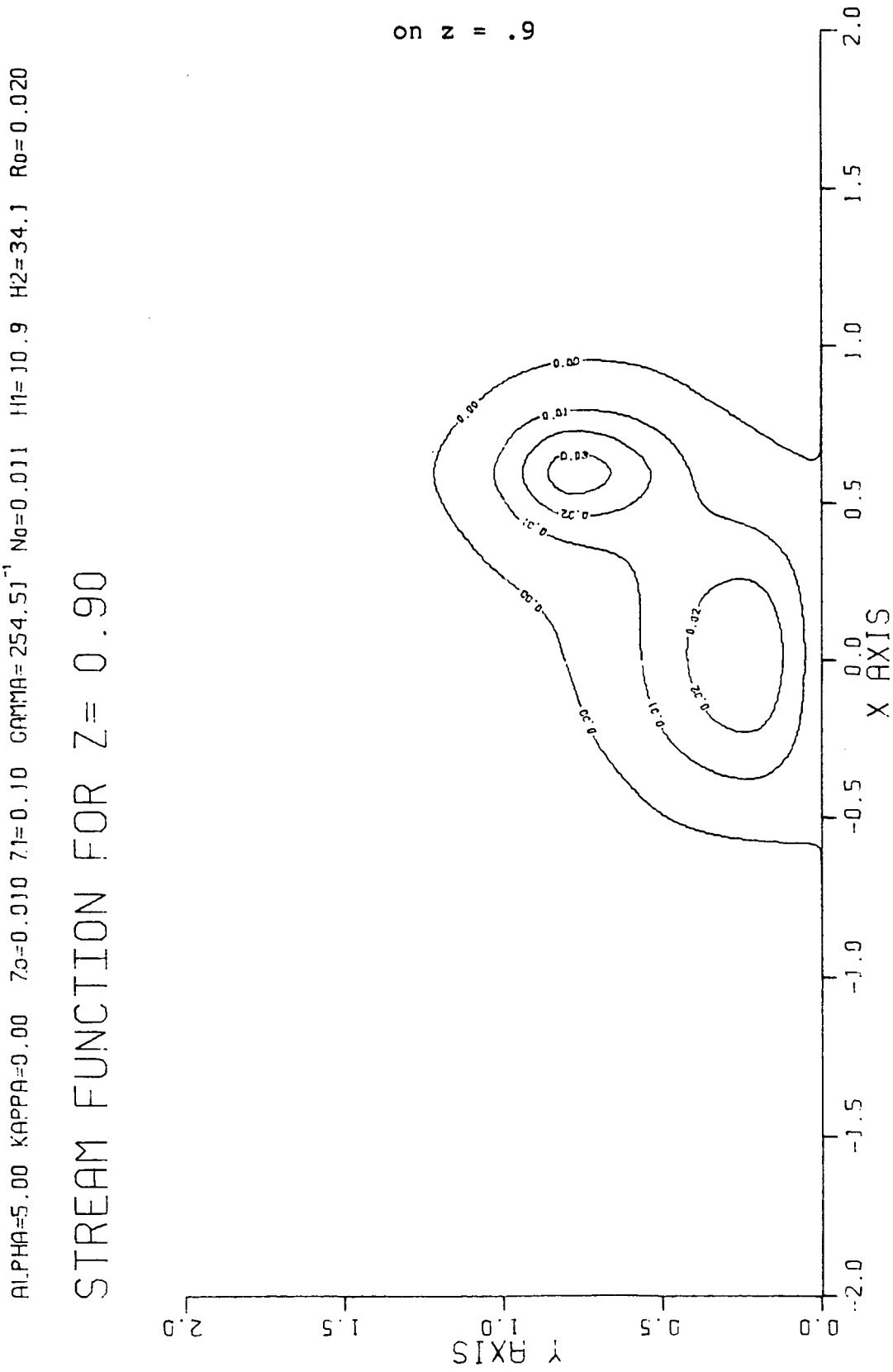

Figure 13 - Horizontal contour plot of the stream function on z = .8

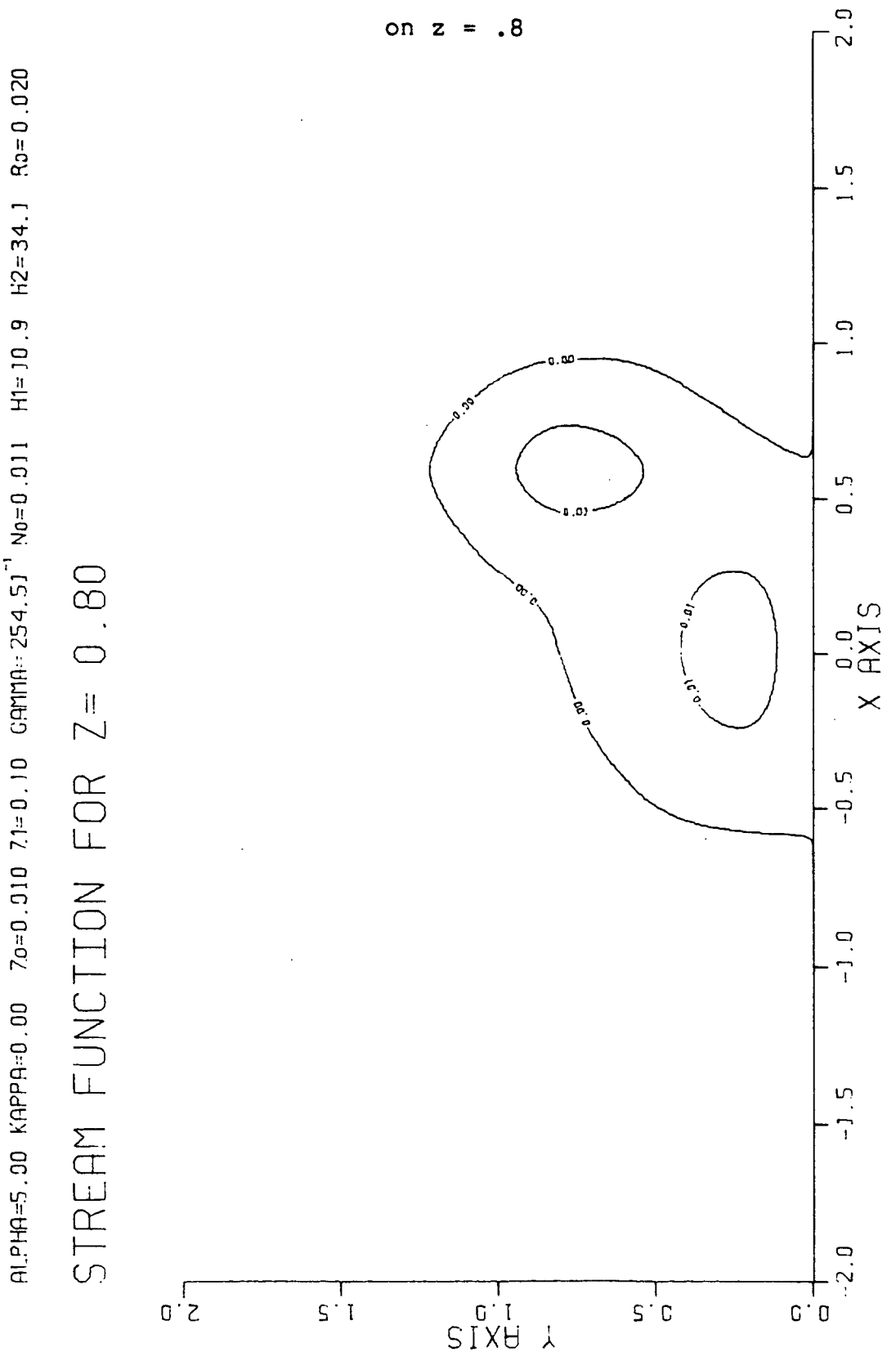

Figure 14 - Horizontal contour plot of the stream function on z = .7

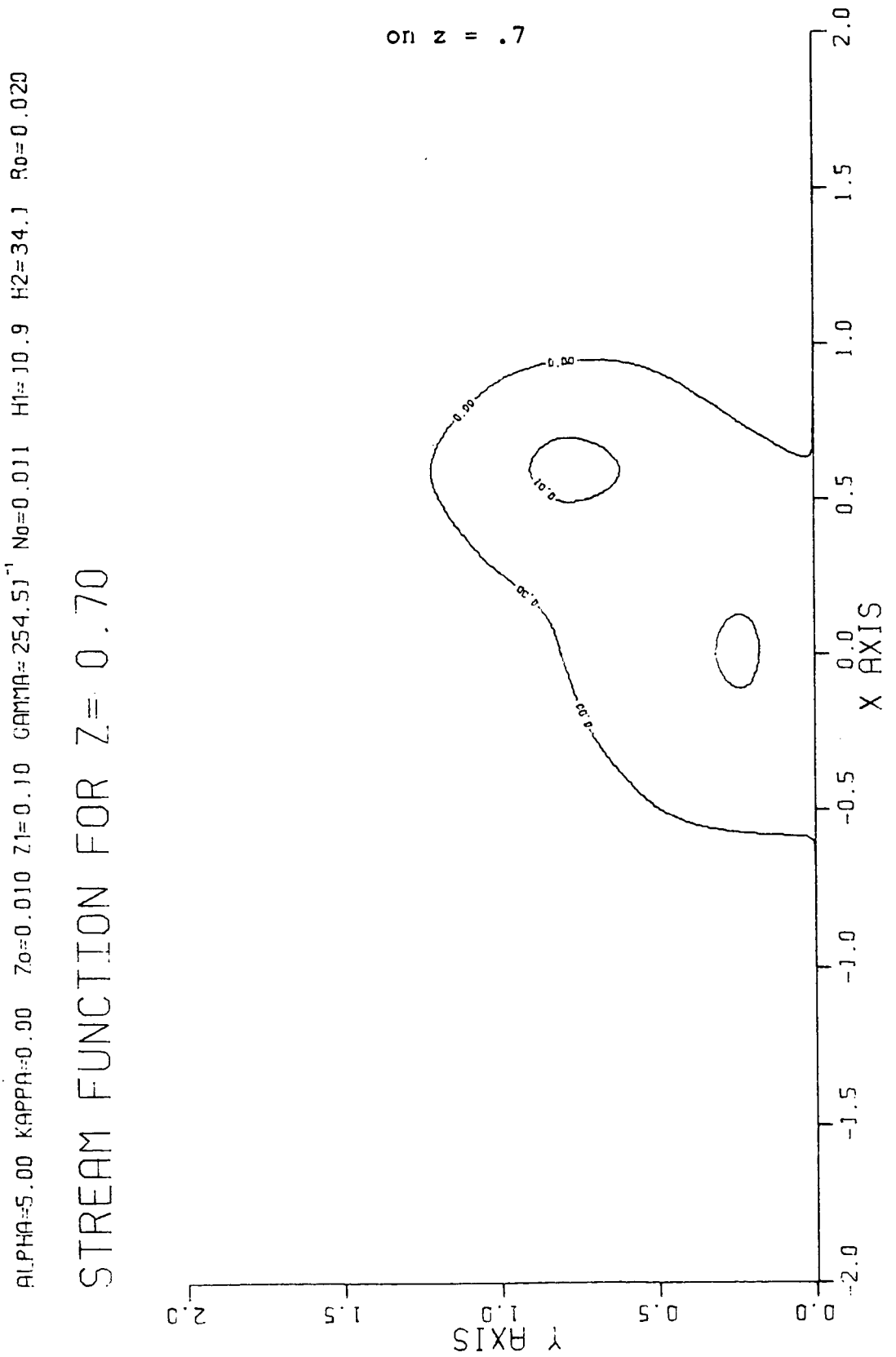

Figure 15 - Horizontal contour plot of the stream function on z = .6

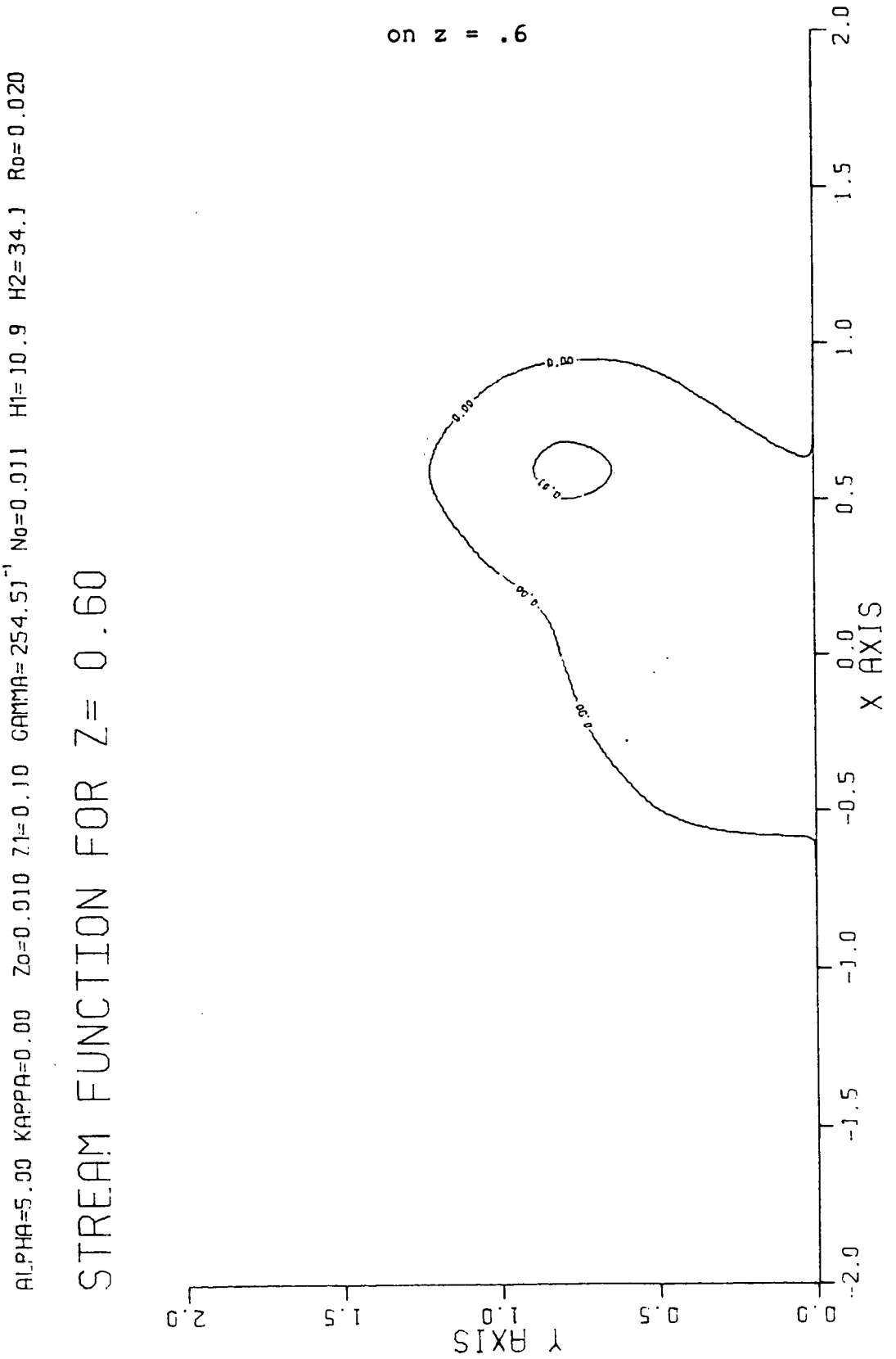

Figure 16 - Vertical contour plot of $p^{(0)}$ on y = .2

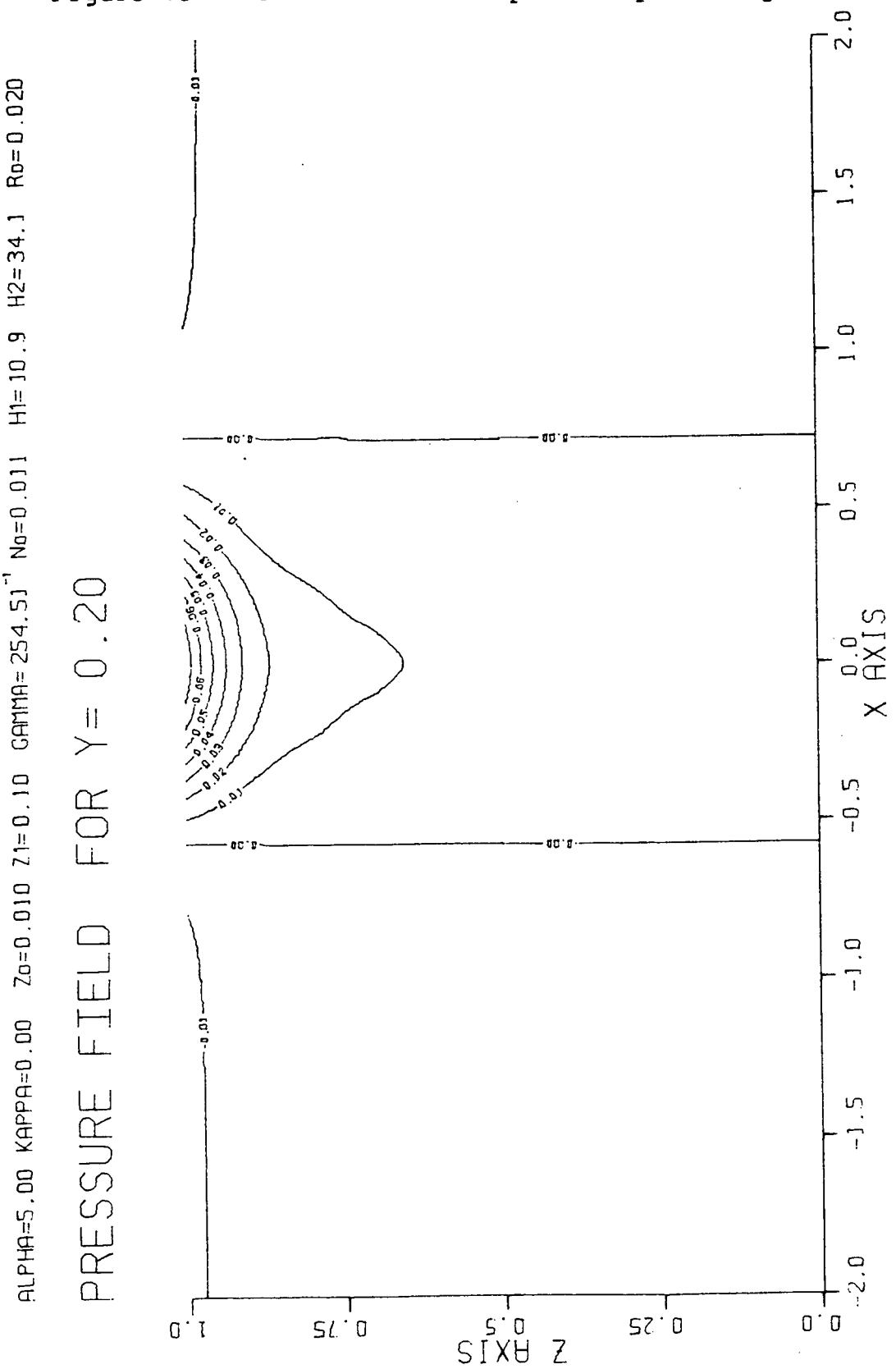

Figure 17 - Vertical contour plot of $p^{(0)}$ on y = .4

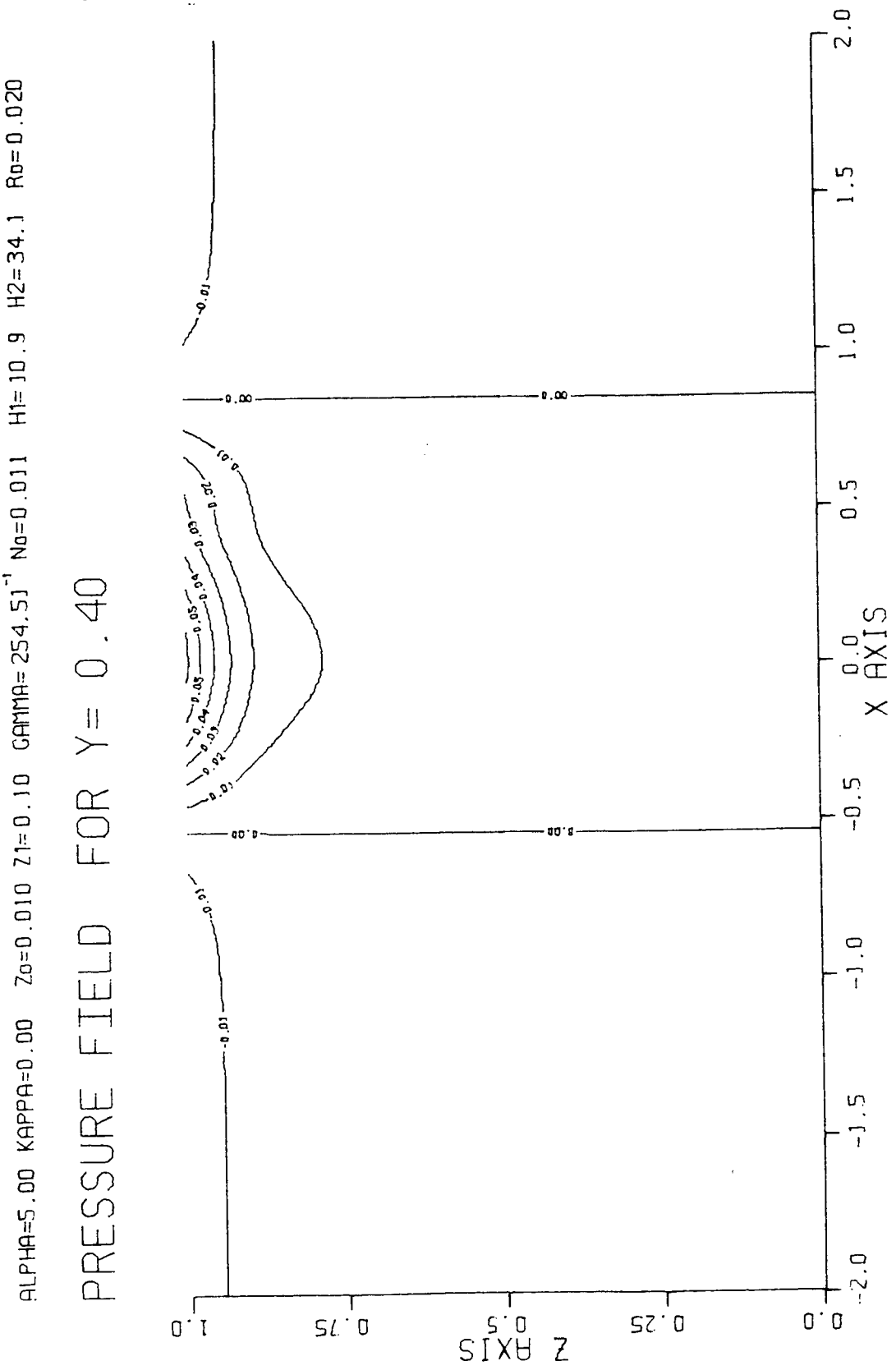

Figure 18 - Vertical contour plot of $p^{(0)}$ on y = .6

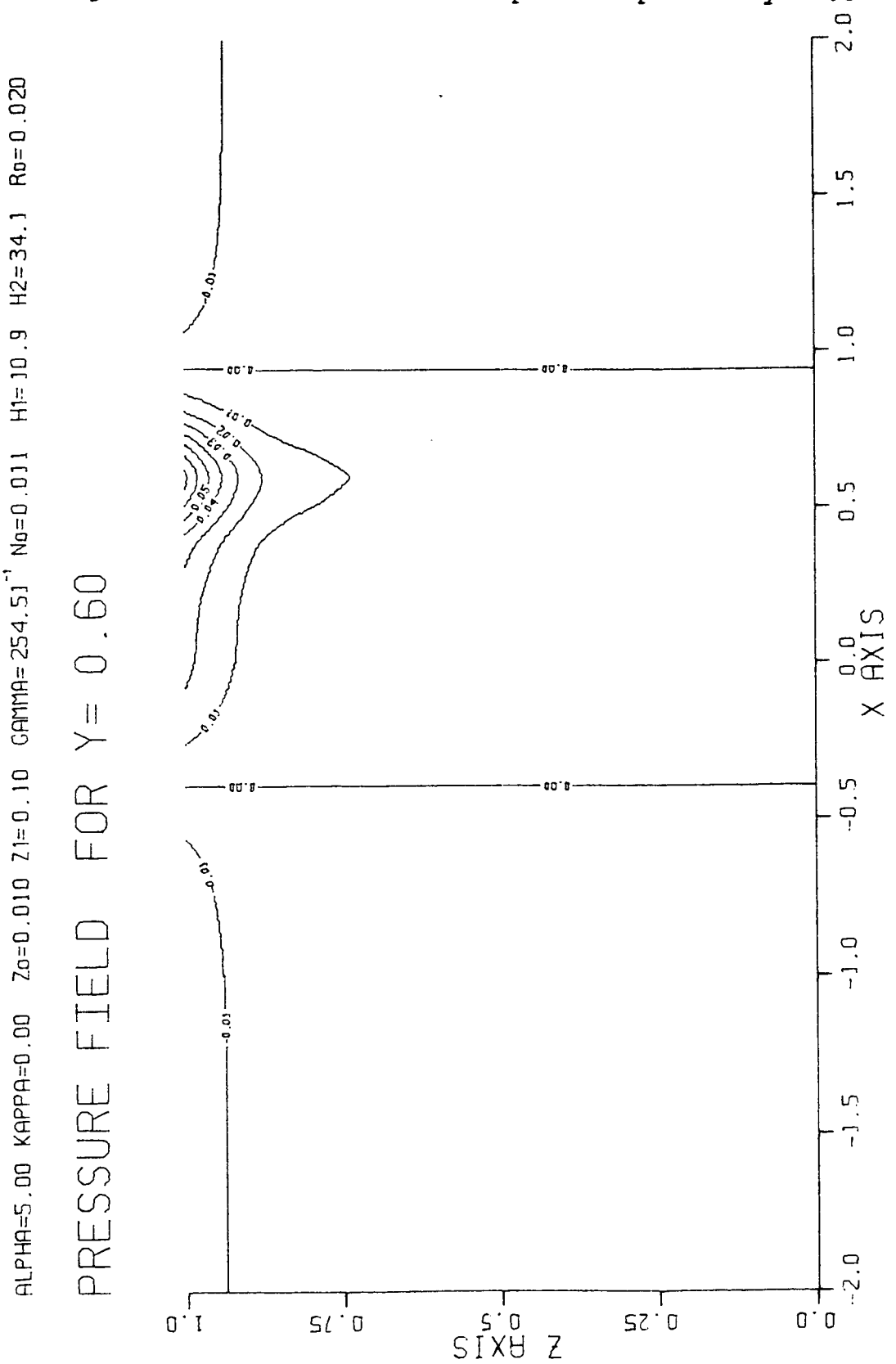

Figure 19 - Vertical contour plot of $p^{(0)}$ on y = .8

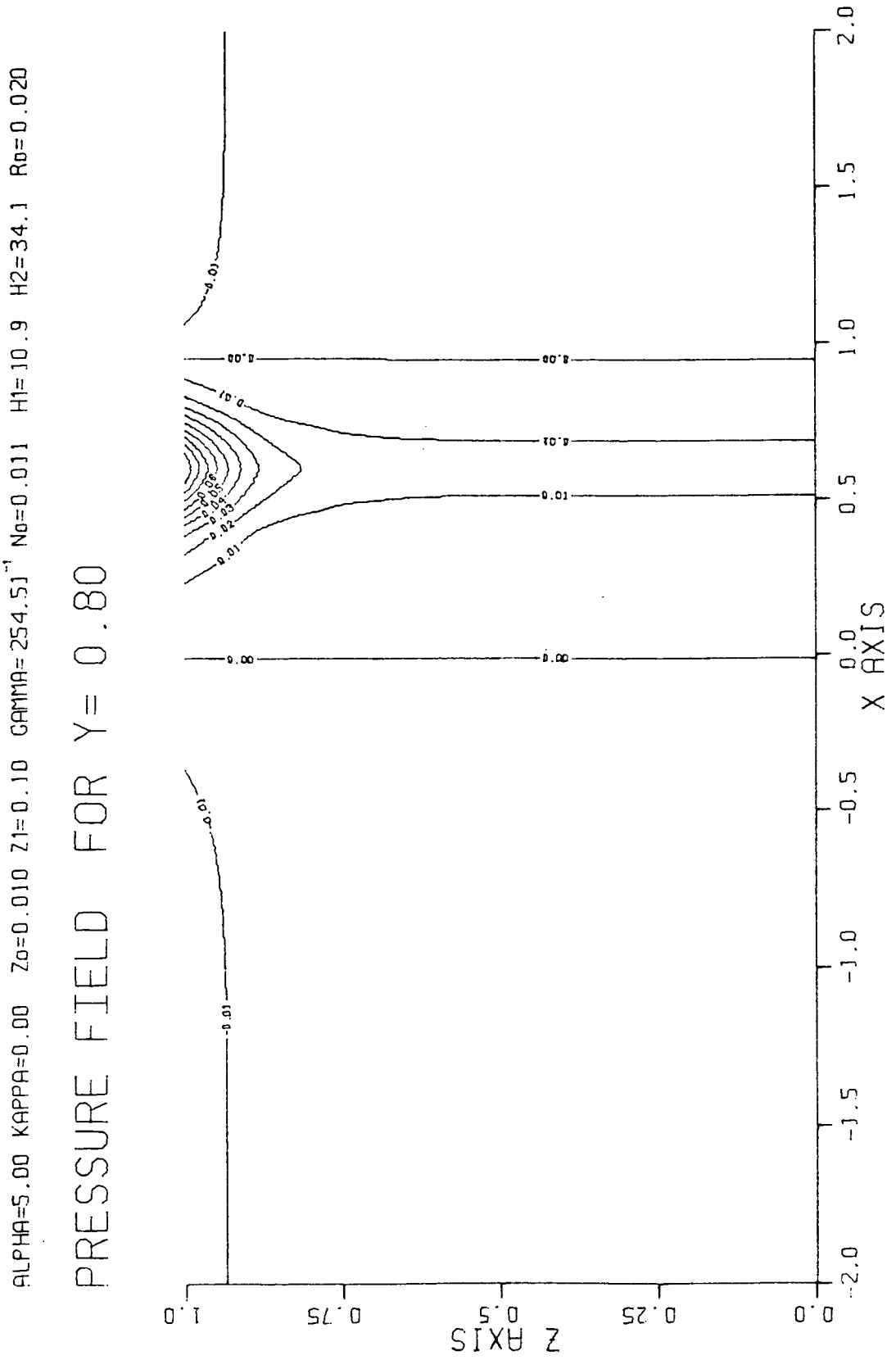

Figure 20 - Vertical contour plot of $p^{(0)}$ on y = 1

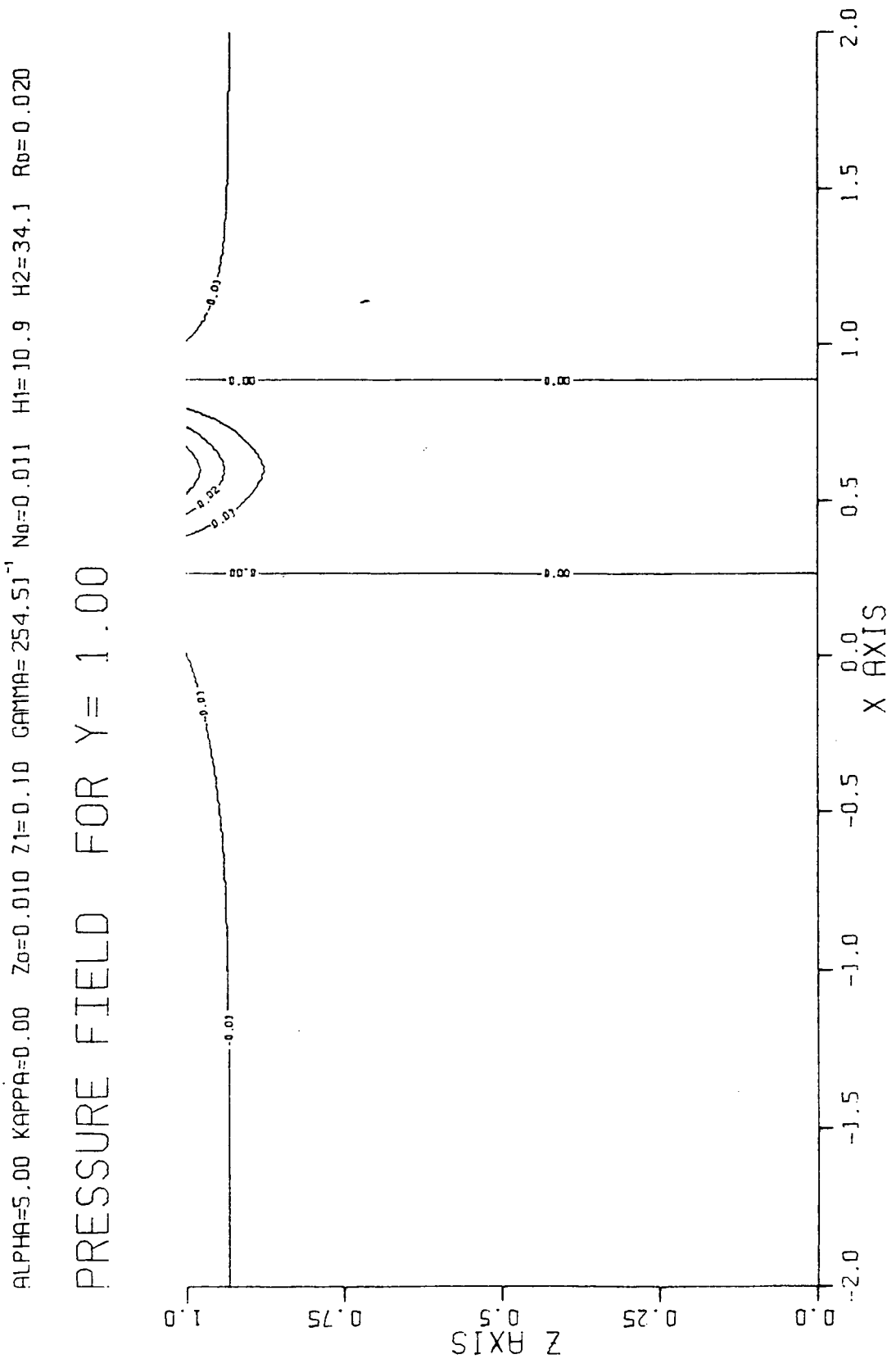

Figure 21 - Stick plot of the horizontal velocity field on

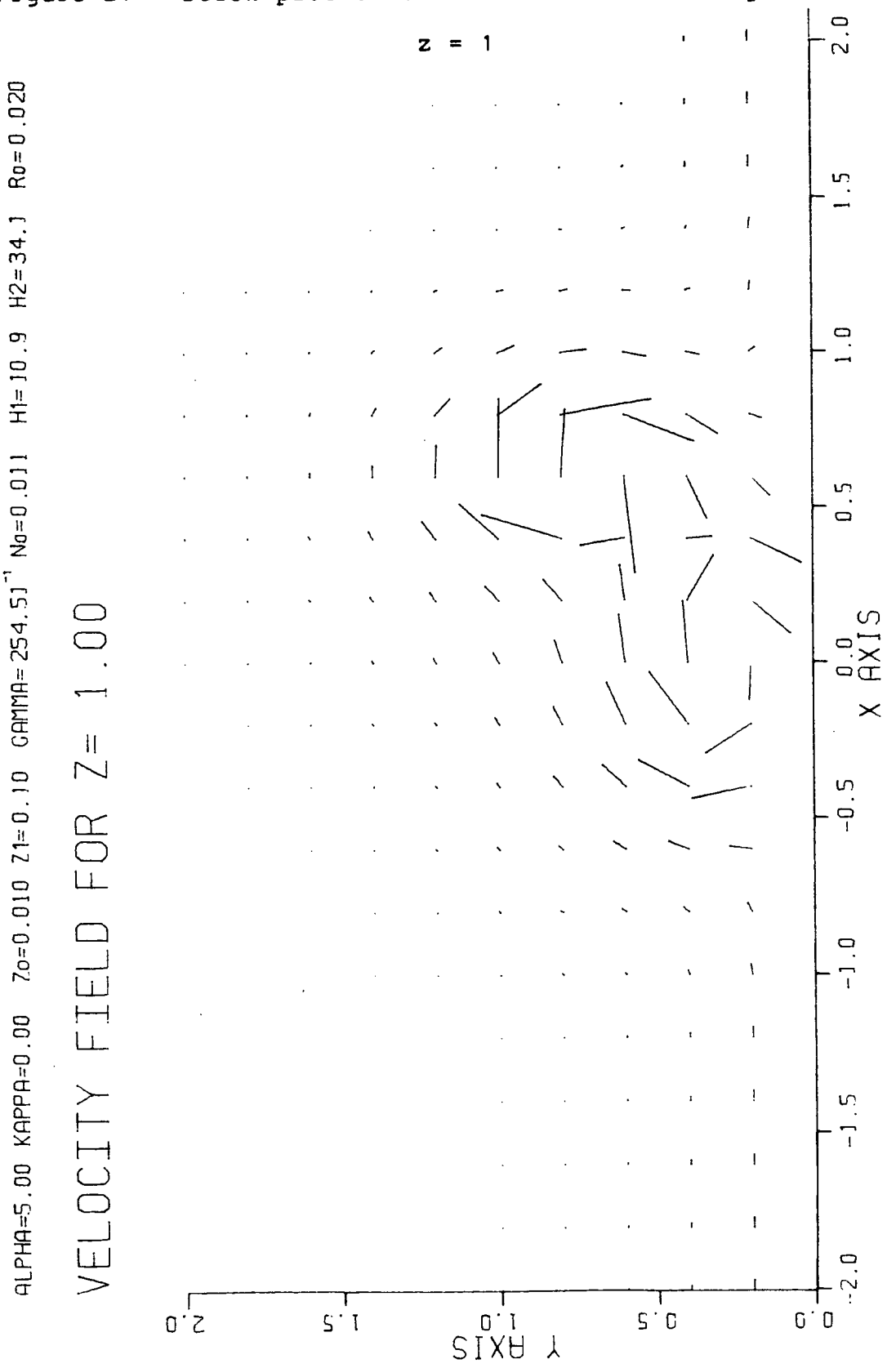

Figure 22 - Stick plot of the horizontal velocity field on $z = .9$

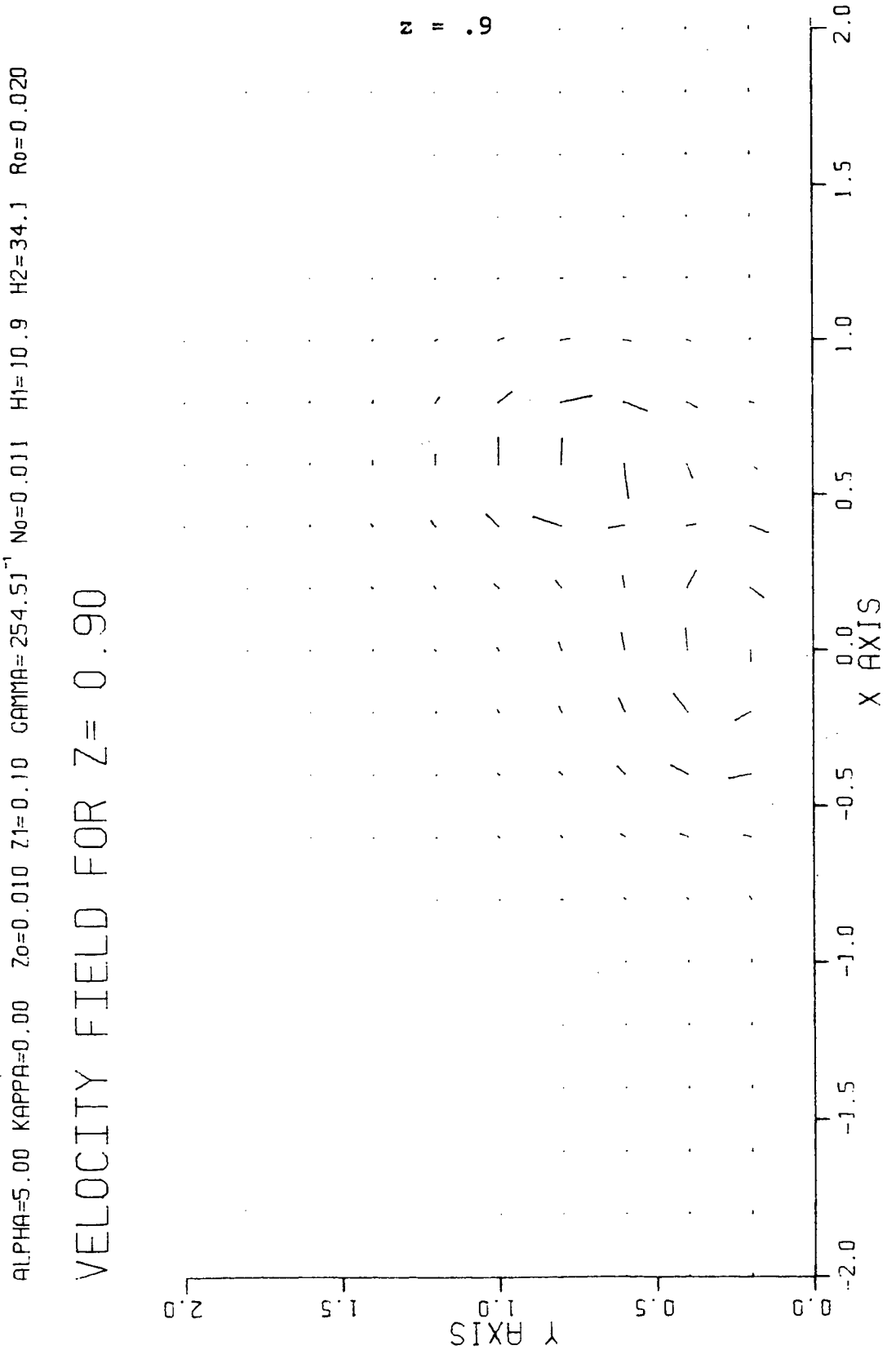

Figure 23 - Stick plot of the horizontal velocity field on z = .8

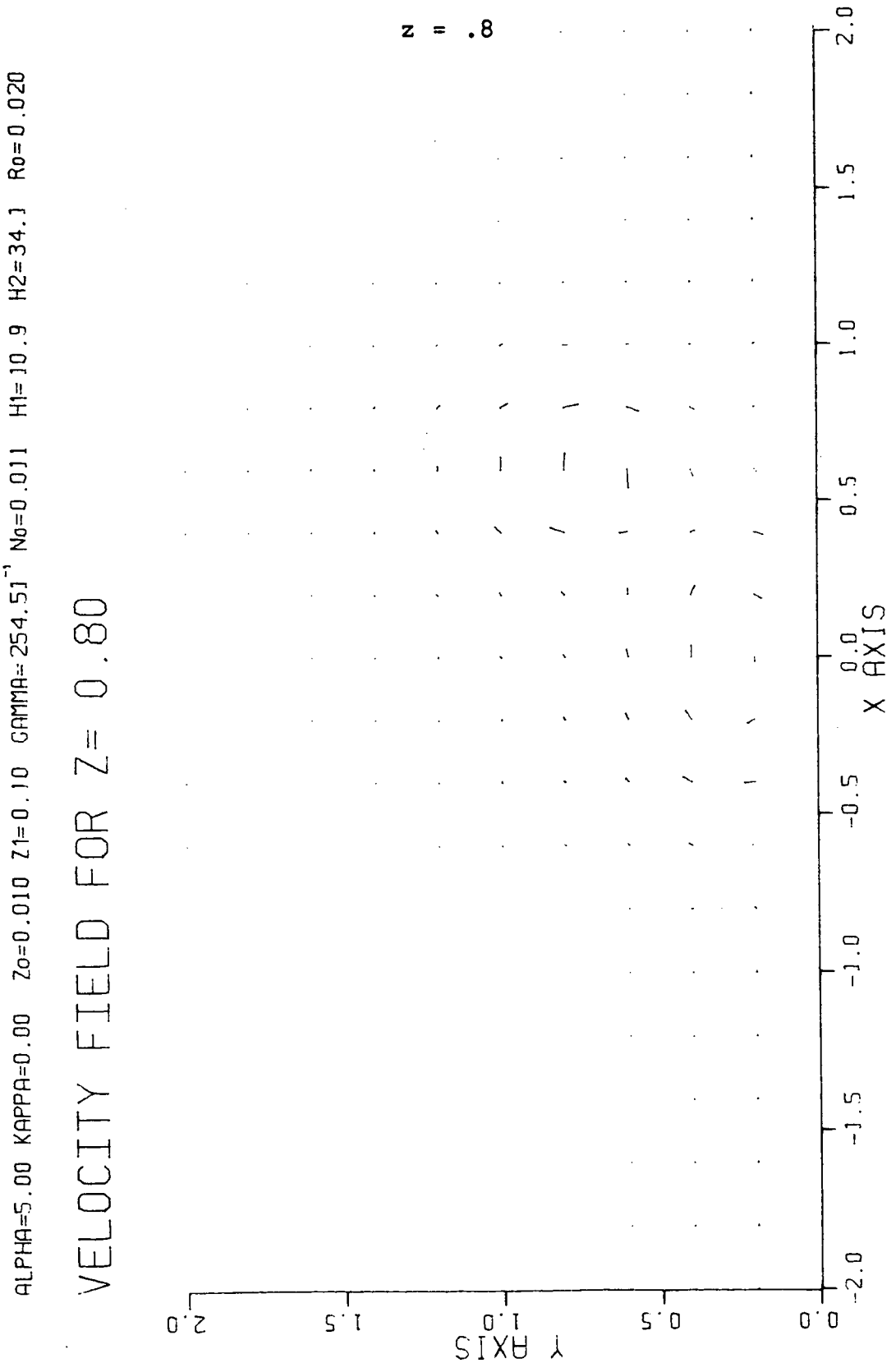

Figure 24 - Stick plot of the horizontal velocity field on z = .7

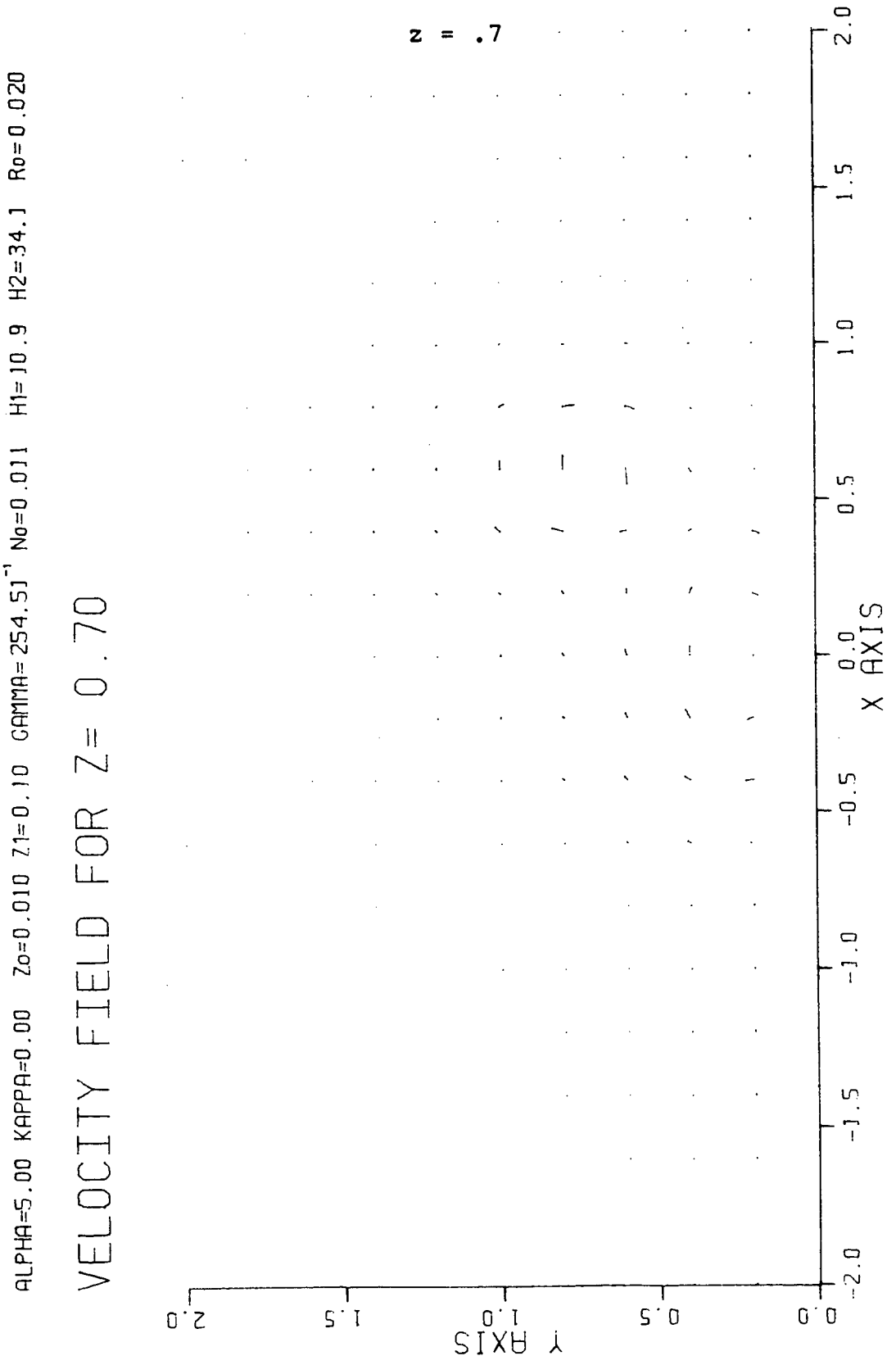

Figure 25 - Stick plot of the horizontal velocity field on $z = .6$

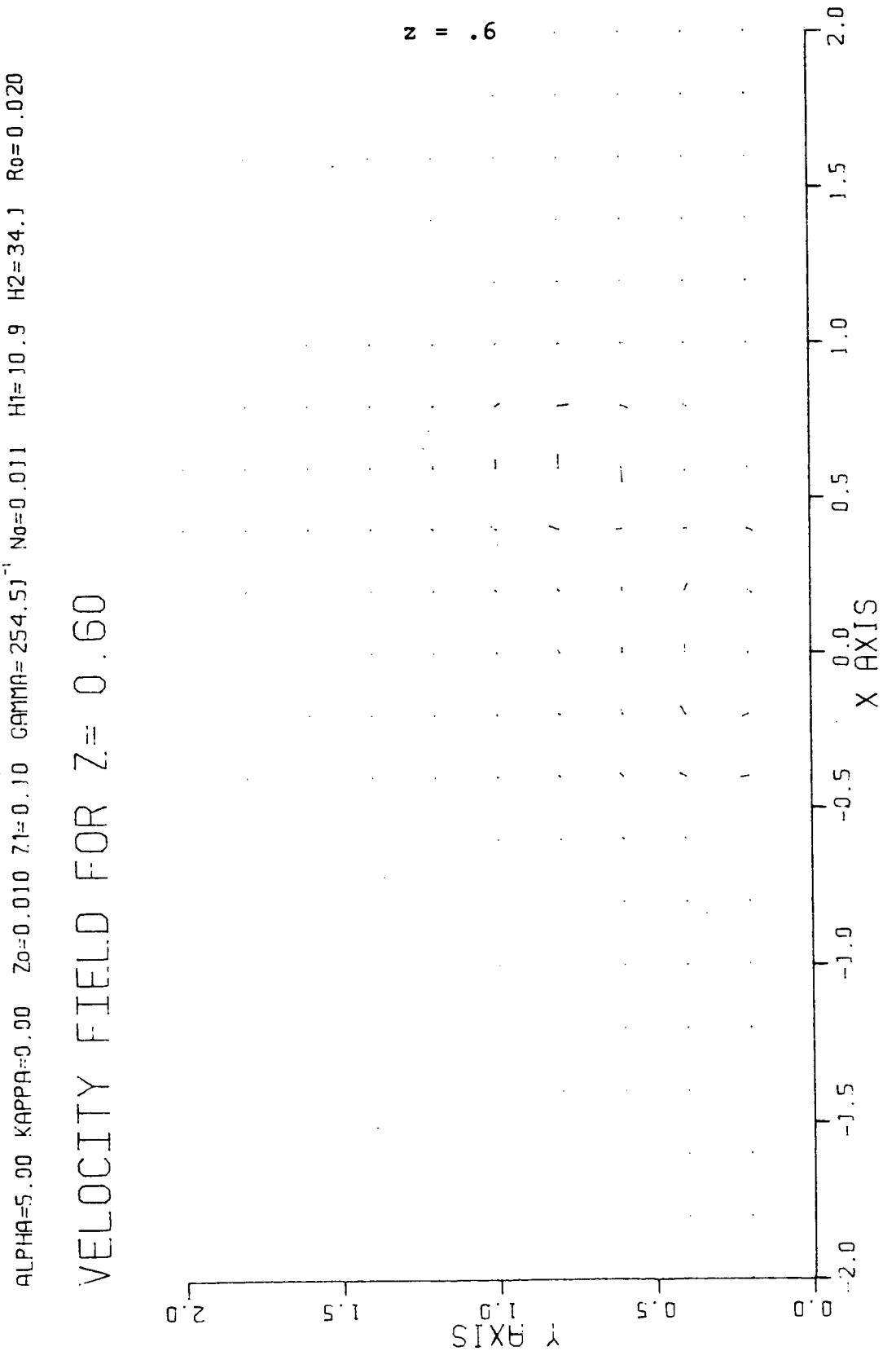

Figure 26 - Stick plot of the mass transport field

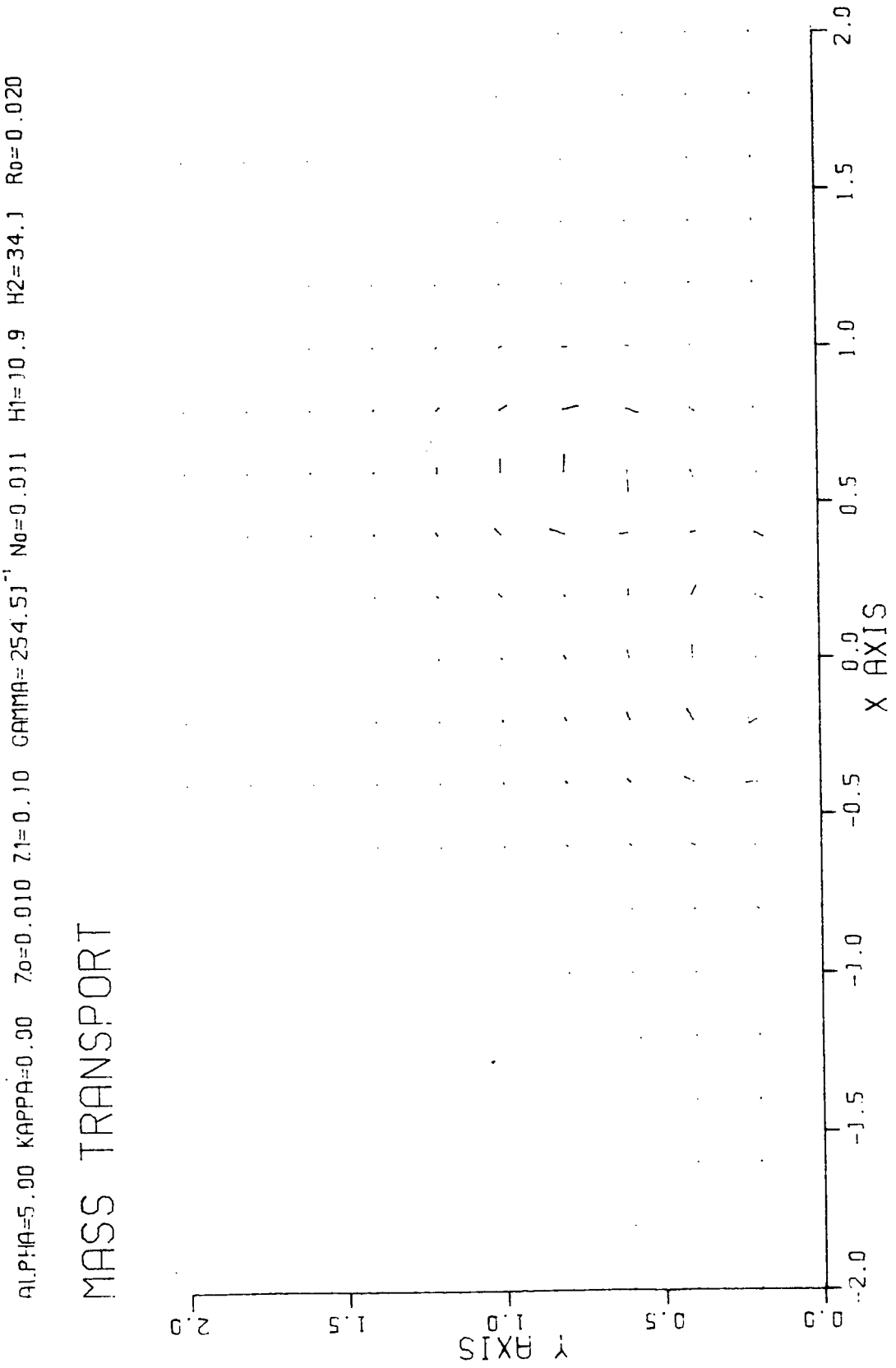

Figure 27 - Horizontal contour plot of $\rho^{(0)}$ on z = 1

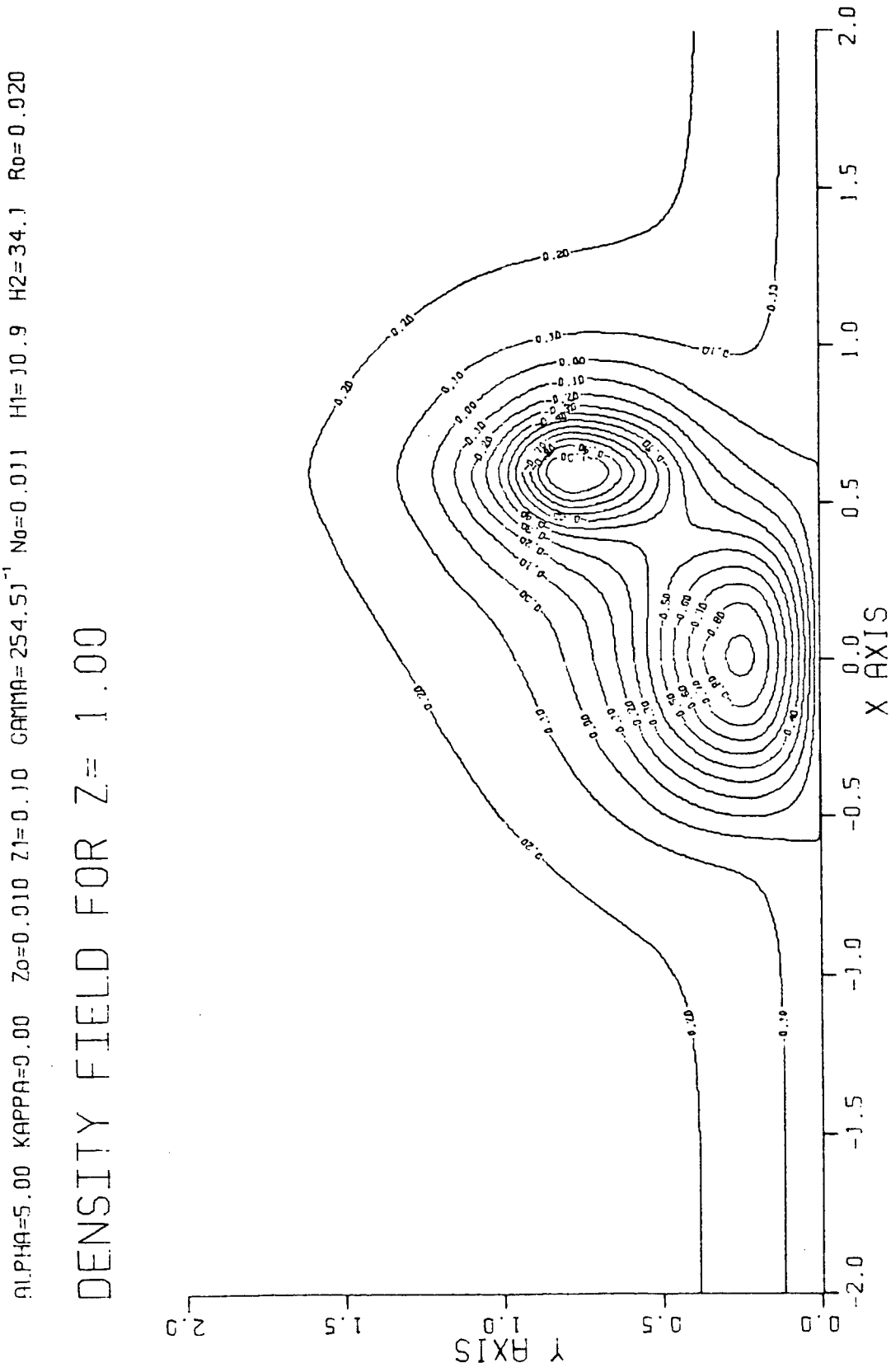

Figure 28 - Horizontal contour plot of $\rho^{(0)}$ on z = .9

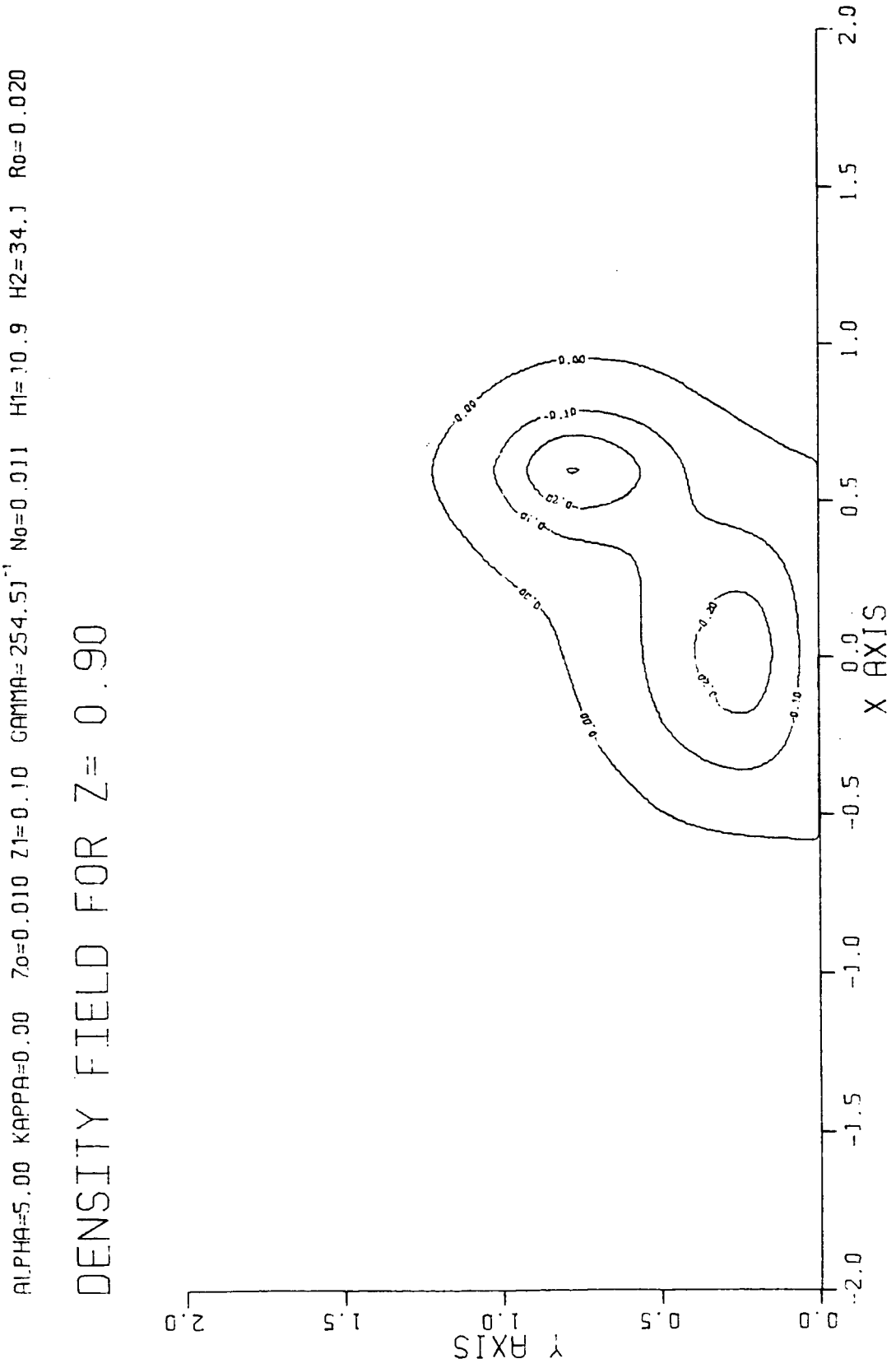

Figure 29 - Horizontal contour plot of $\rho^{(0)}$ on z = .8

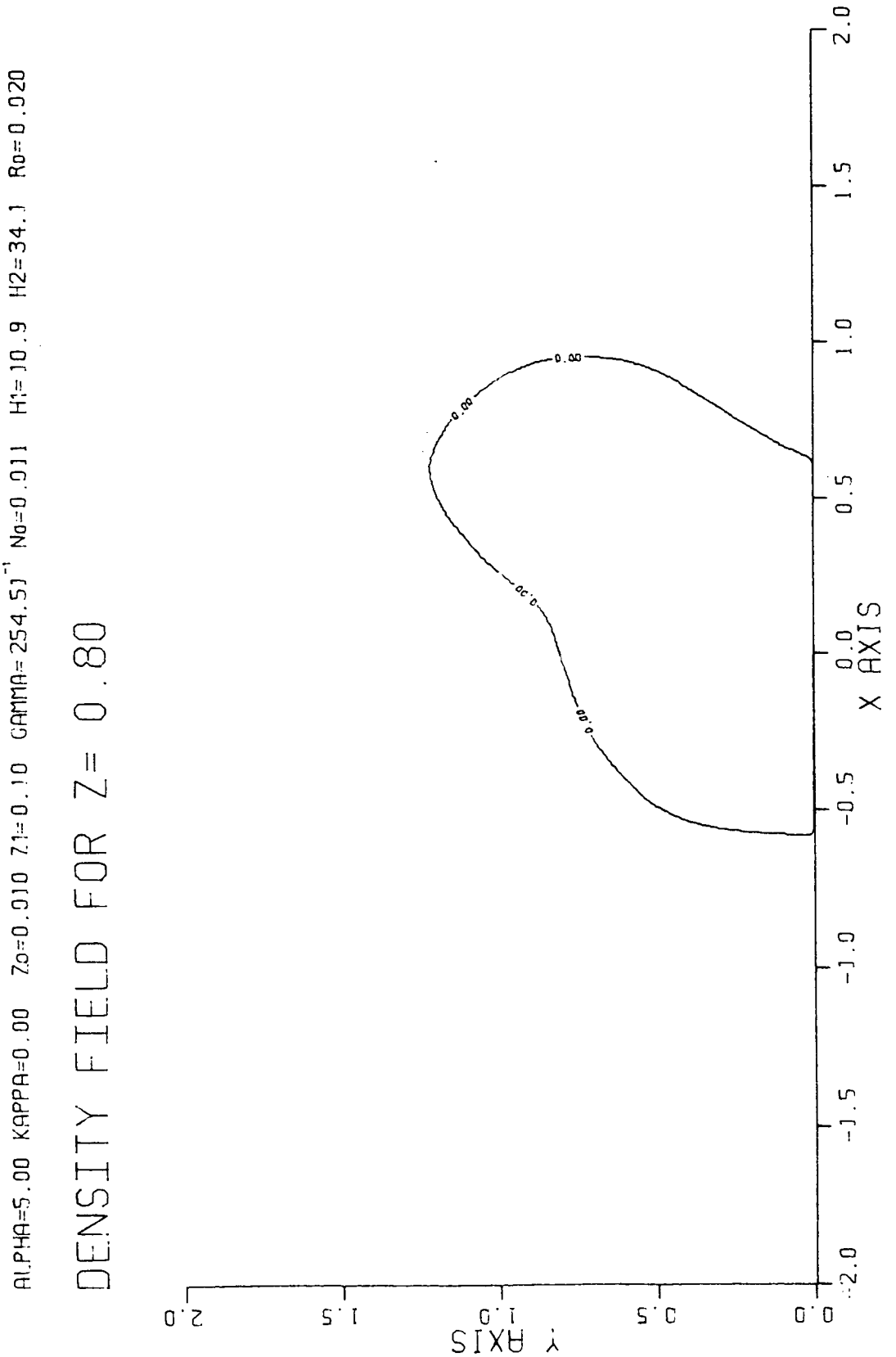

Figure 30 - Vertical contour plot of $\rho^{(0)}$ on y = .2

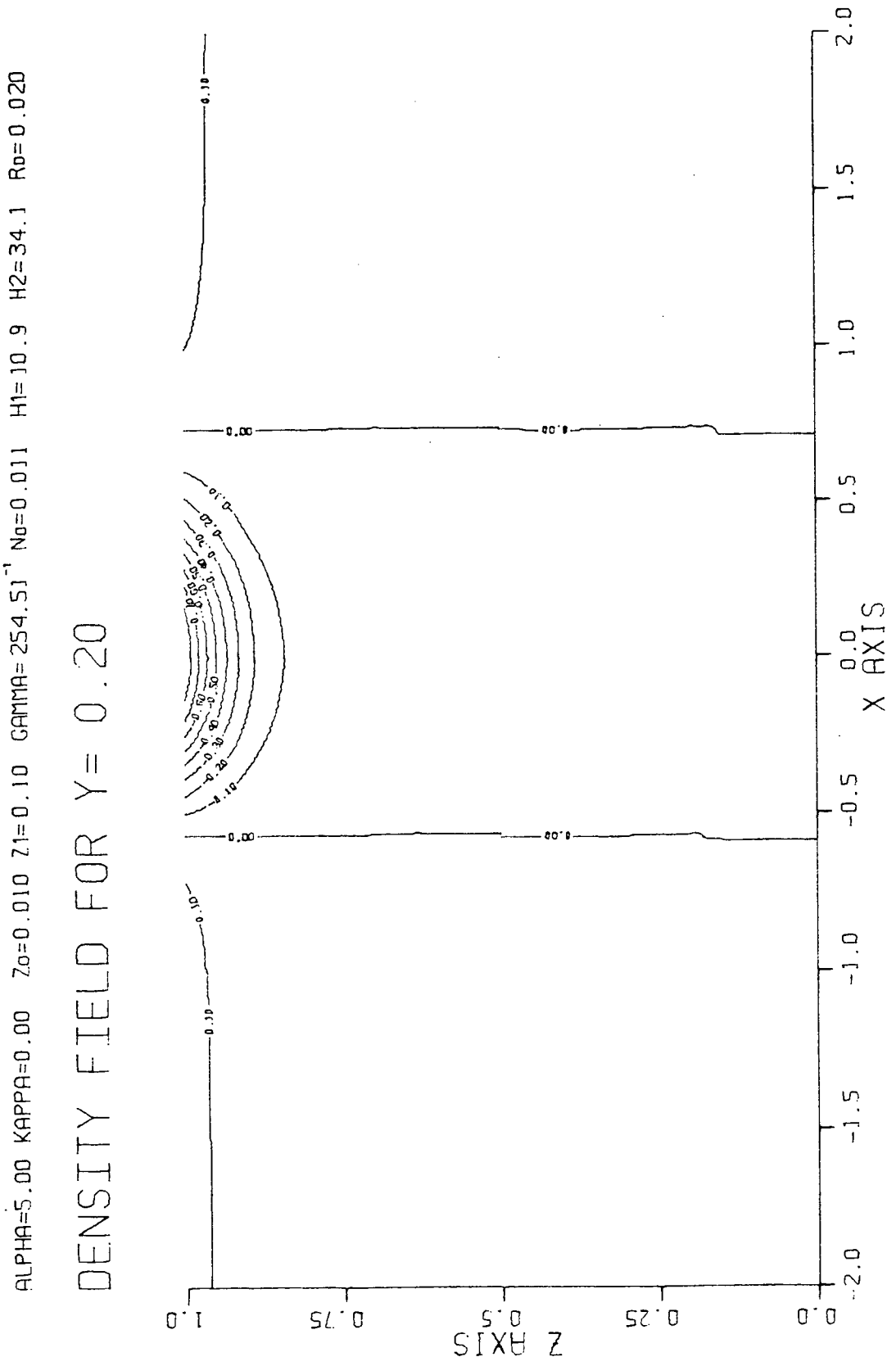

Figure 31 - Vertical contour plot of $\rho^{(0)}$ on y = .4

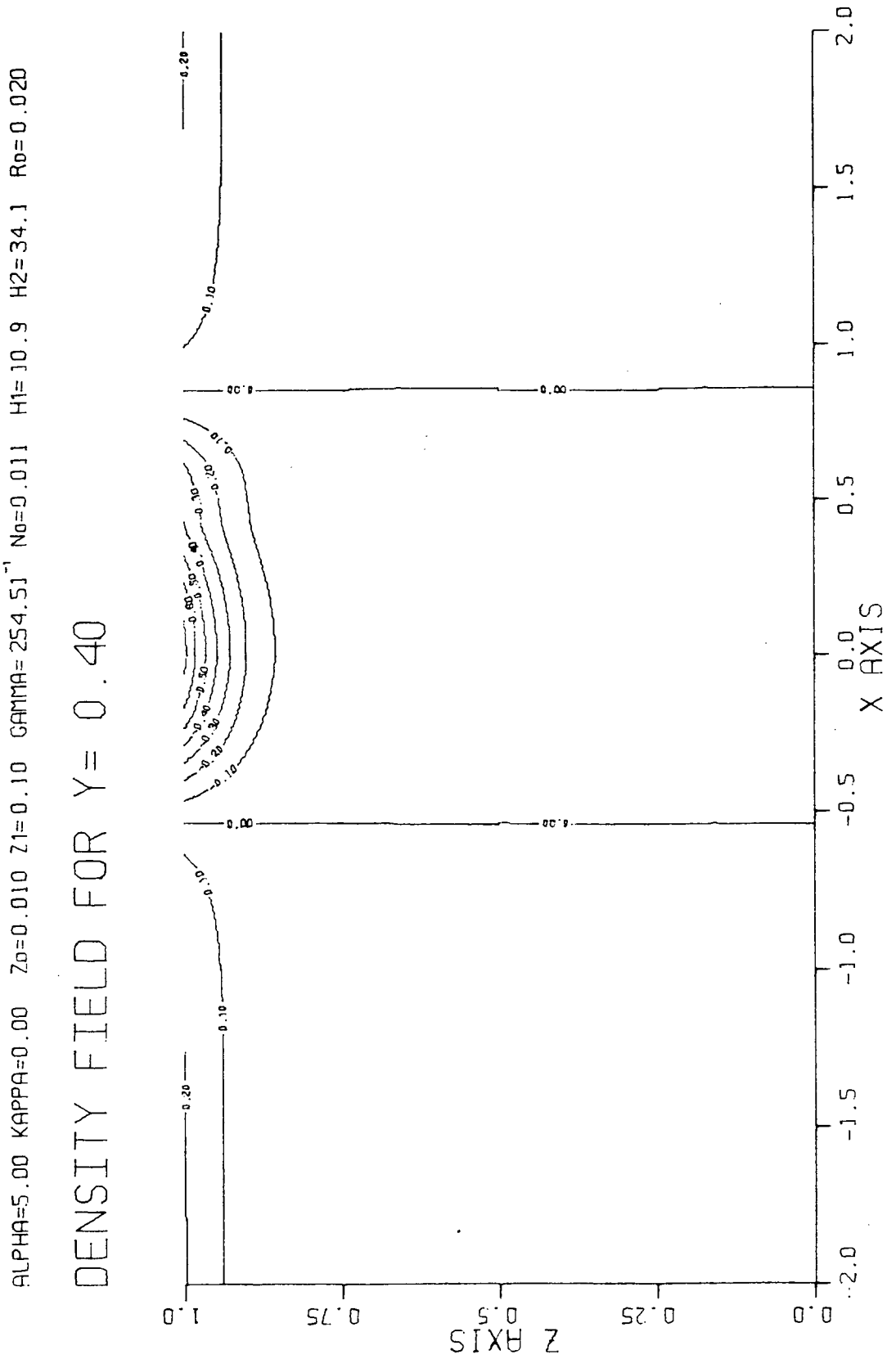

Figure 32 - Vertical contour plot of $\rho^{(0)}$ on y = .6

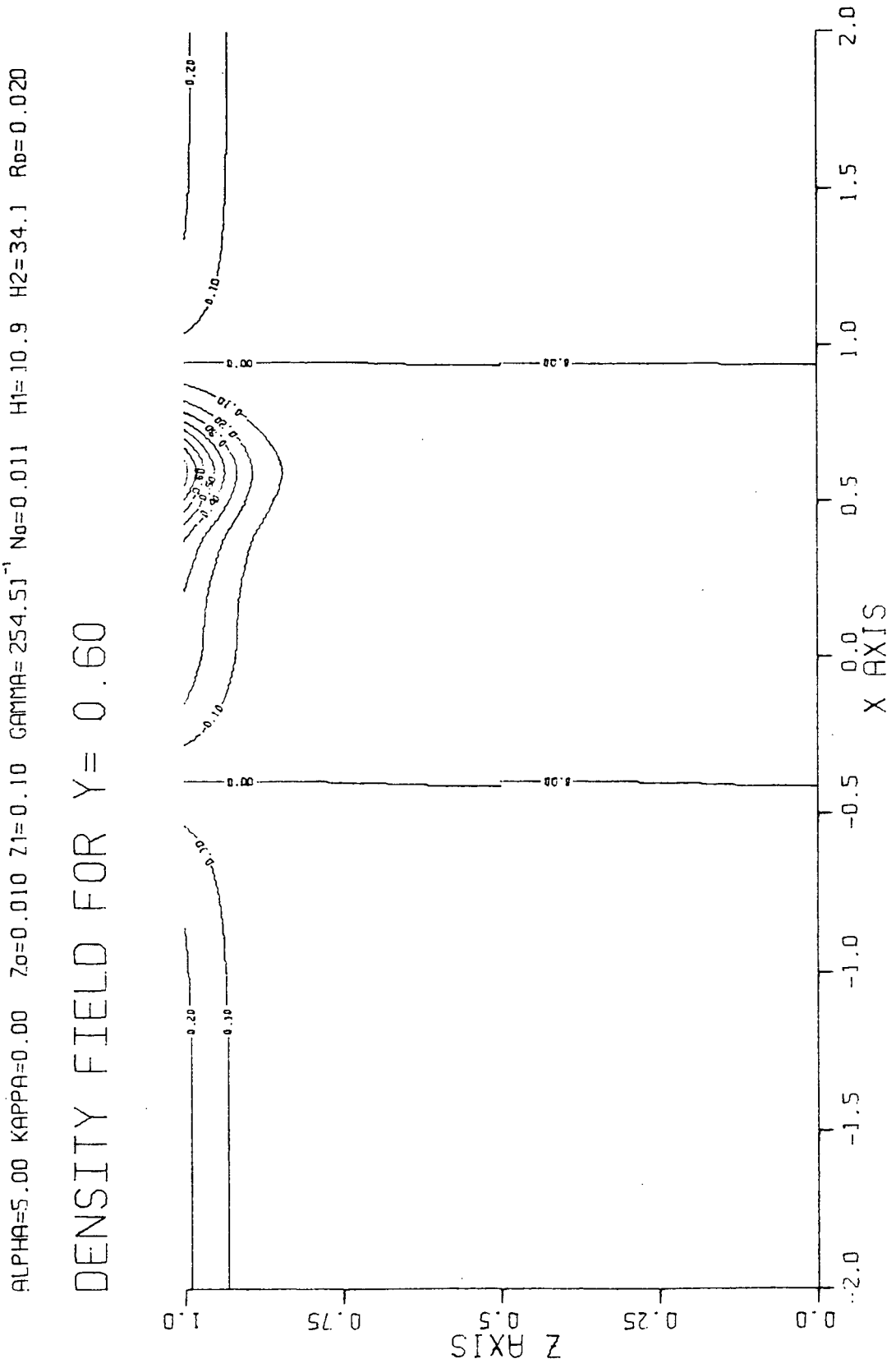

Figure 33 - Vertical contour plot of $\rho^{(0)}$ on y = .8

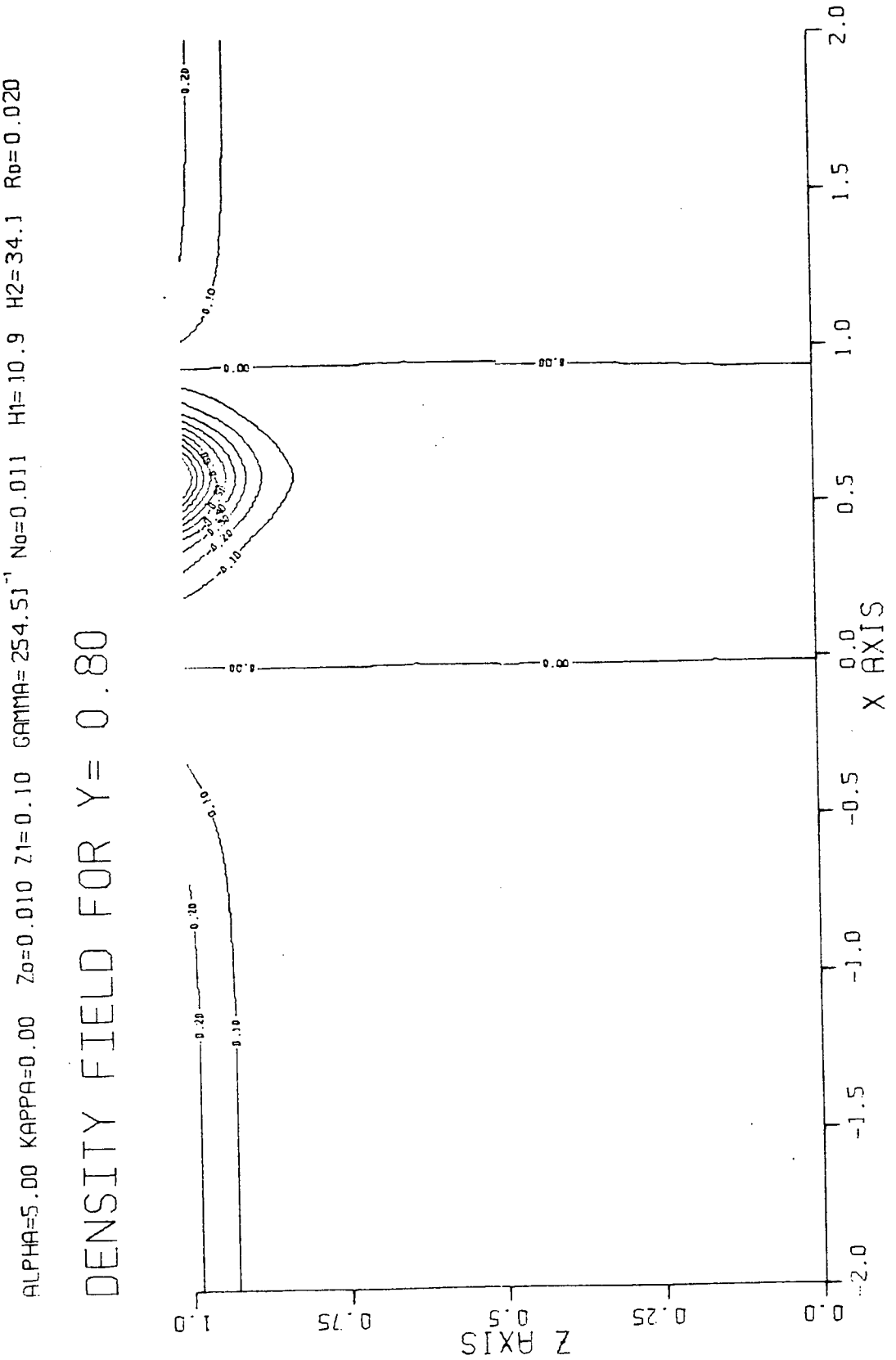

Figure 34 - Vertical contour plot of $\rho^{(0)}$ on y = 1

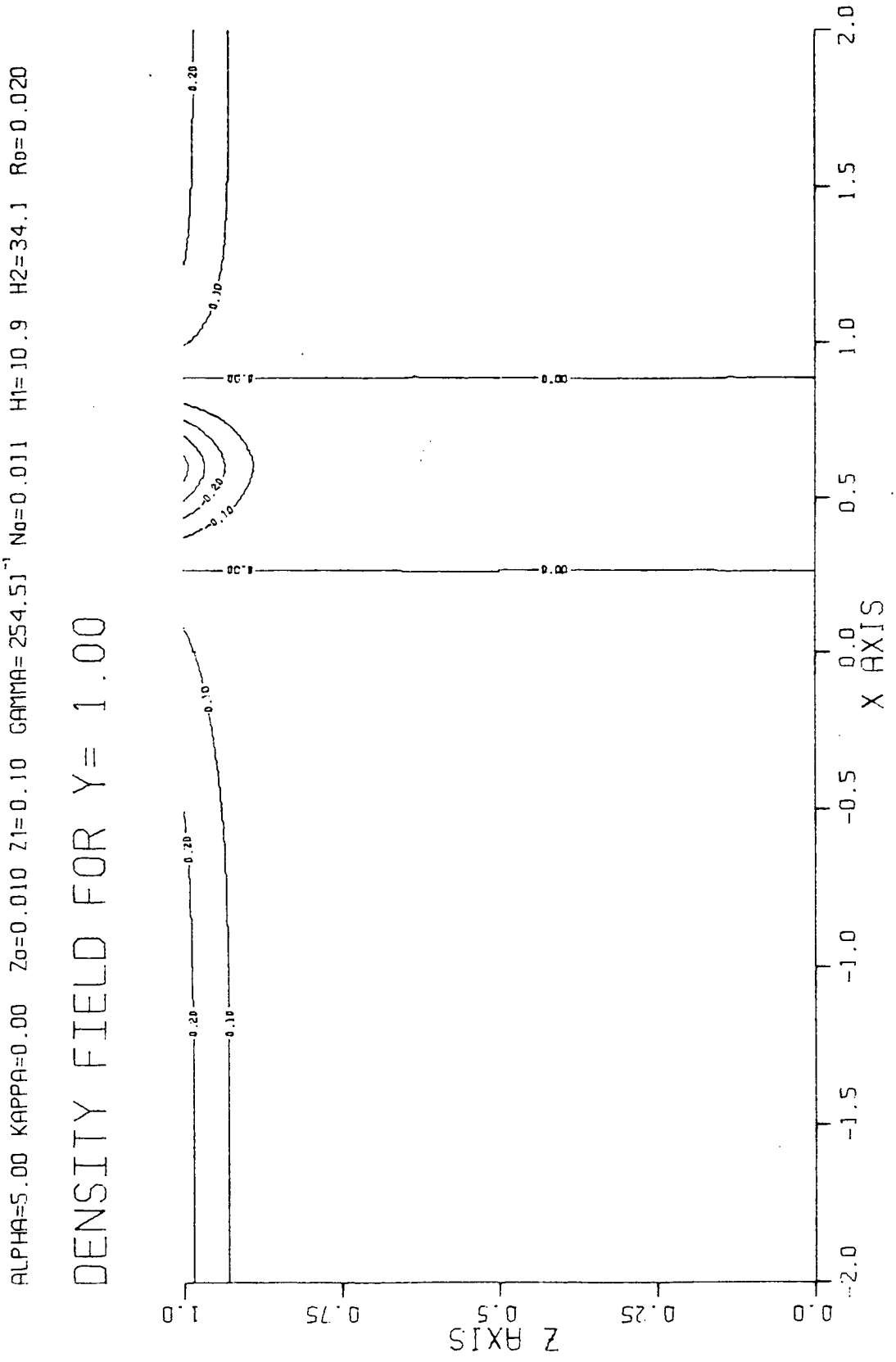

Figure 35 - Vertical profile of $p^{(0)}$ at (x,y) = (-2,.1)

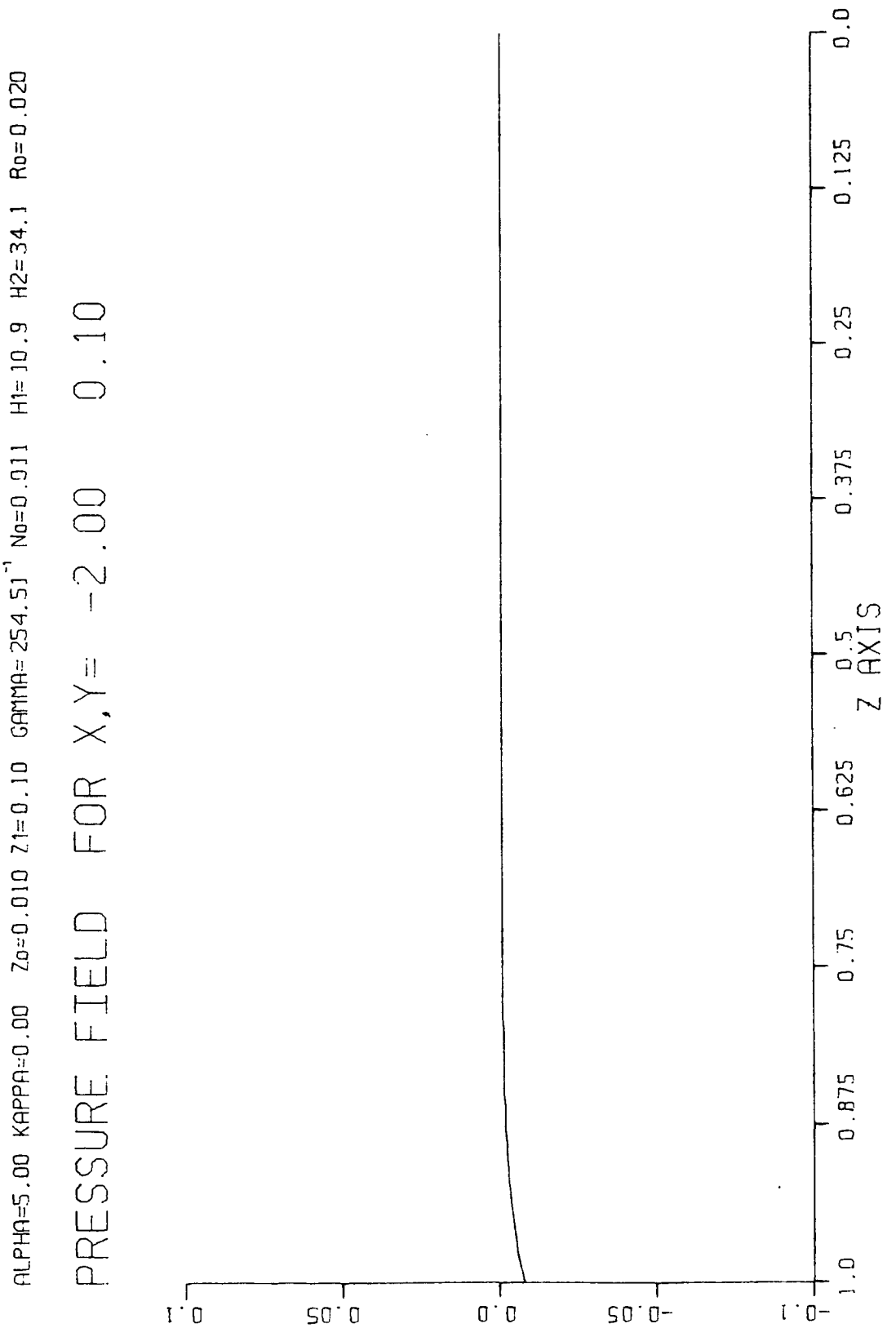

Figure 36 - Vertical profile of $\rho^{(0)}$ at (x,y) = (-2,.1)

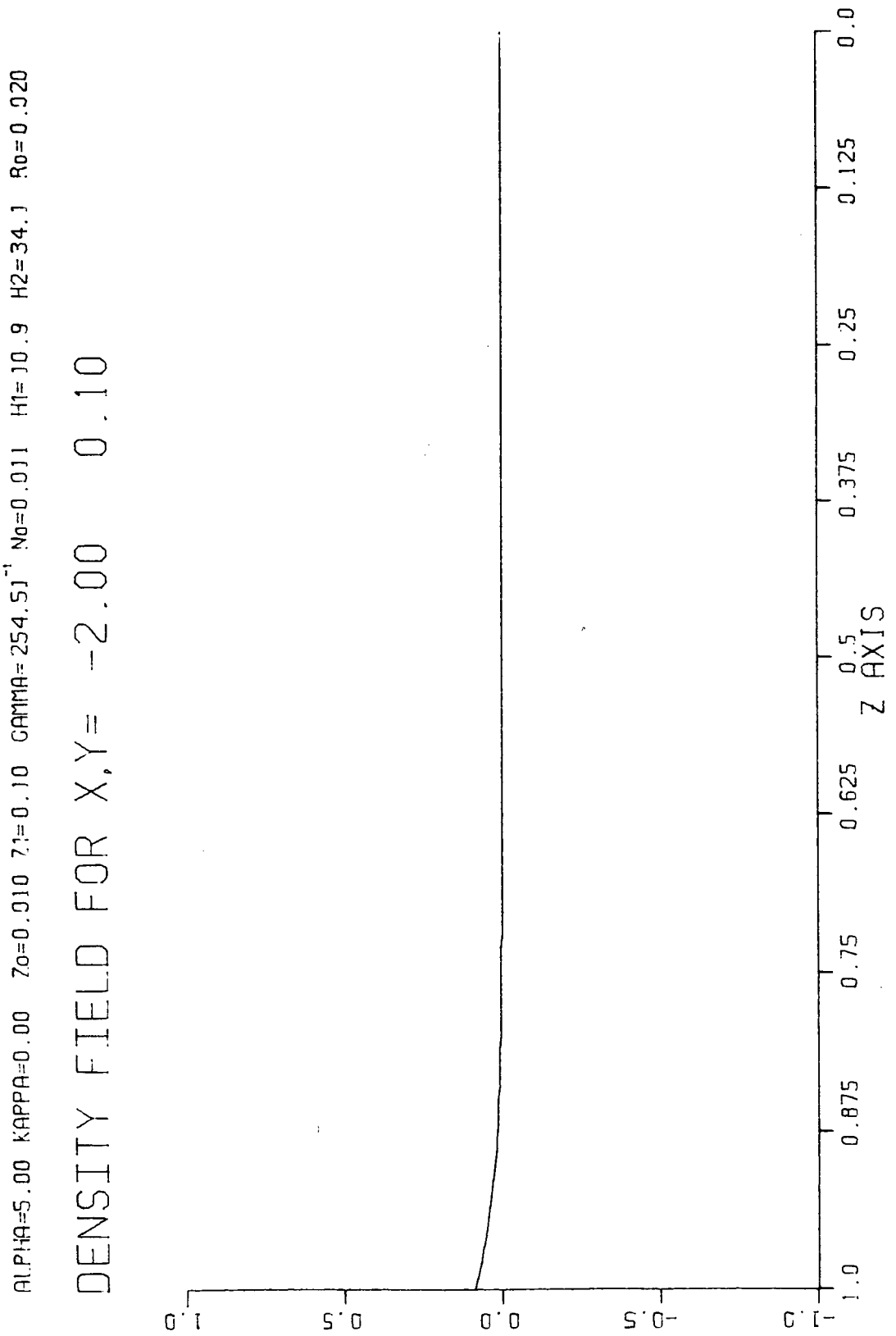

Figure 37 - Vertical profile of $u^{(0)}$ at (x,y) = (-2,.1)

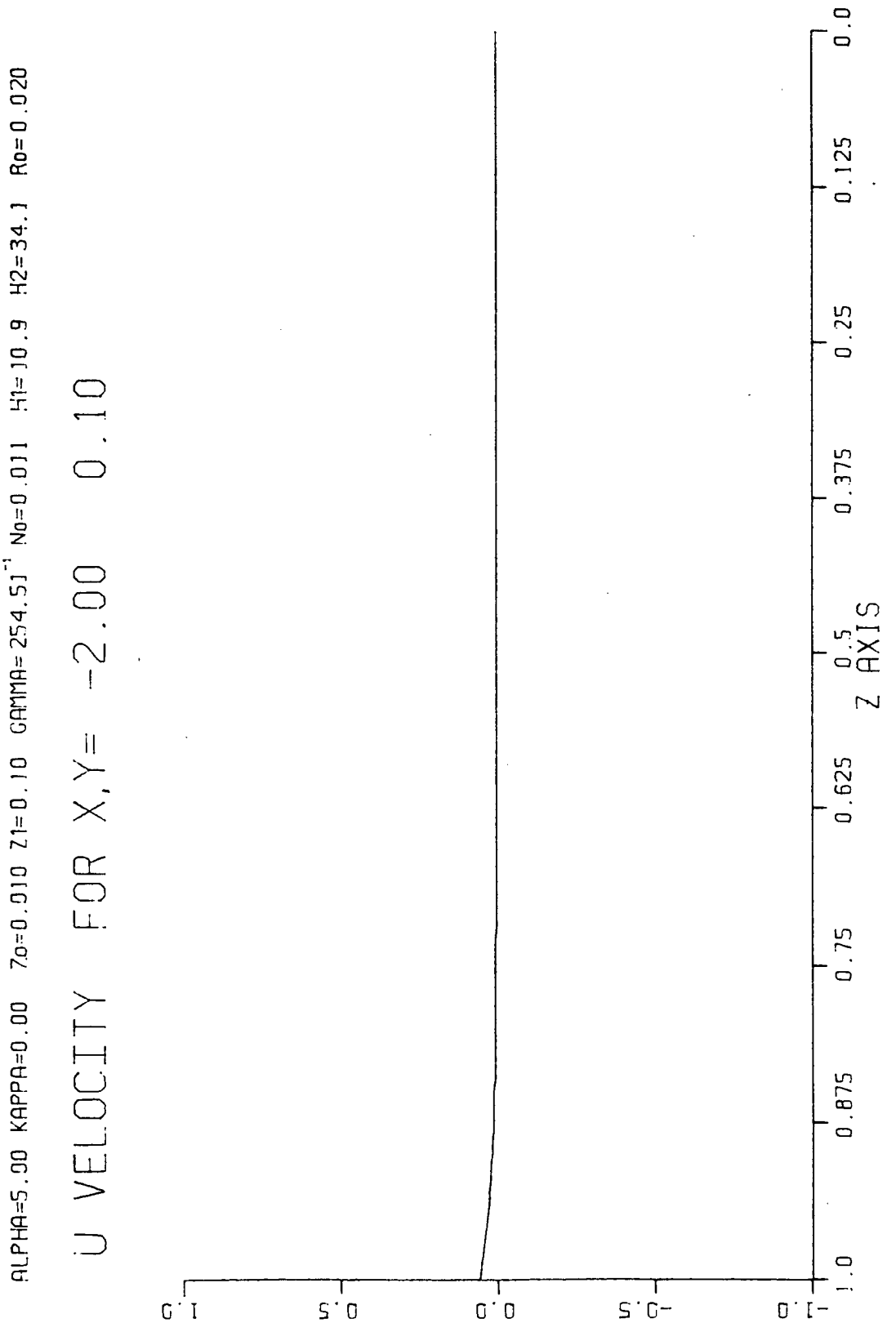

Figure 38 - Vertical profile of $v^{(0)}$ at (x,y) = (-2,.1)

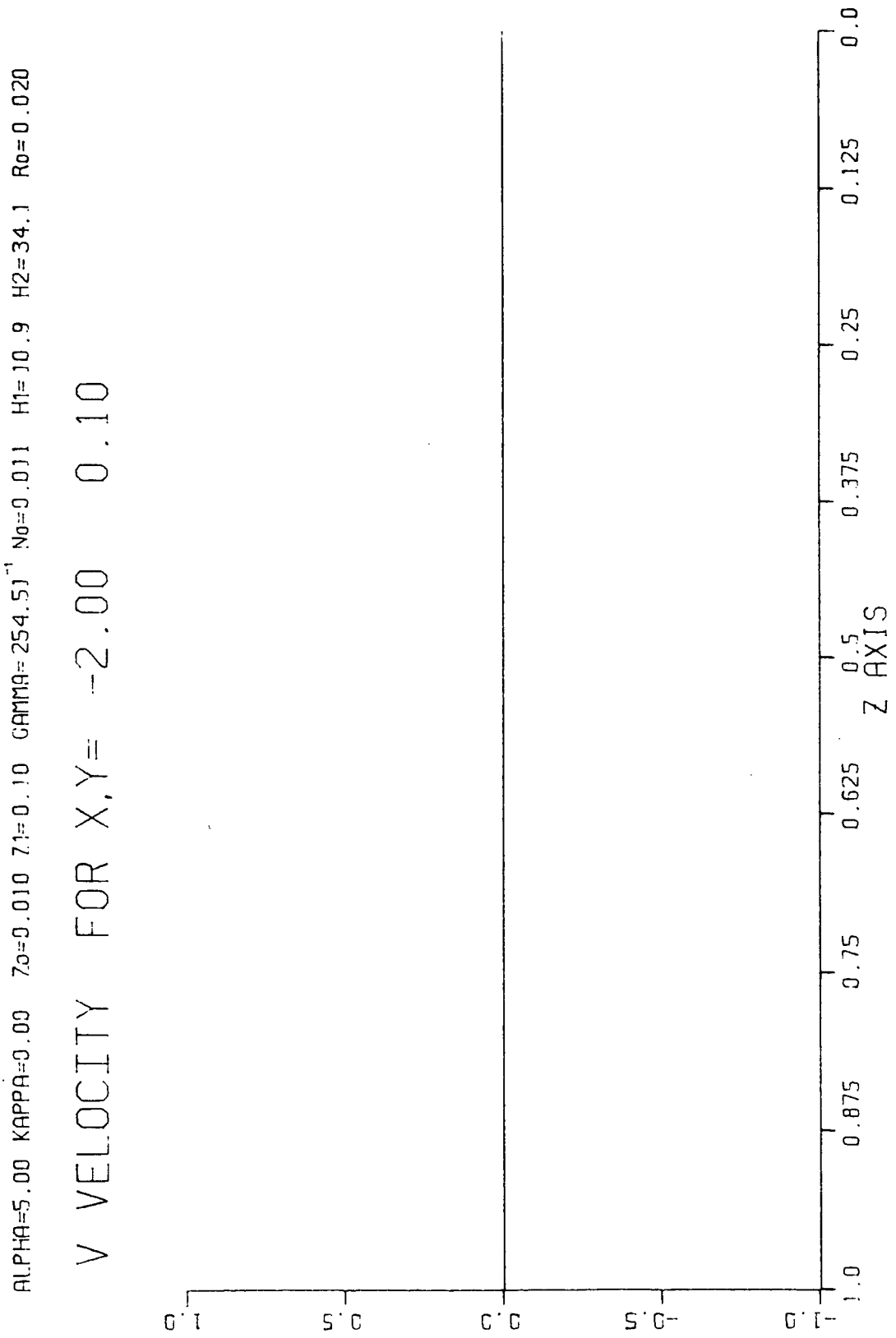

Figure 39 - Vertical profile of $w^{(0)}$ at (x,y) = (-2,.1)

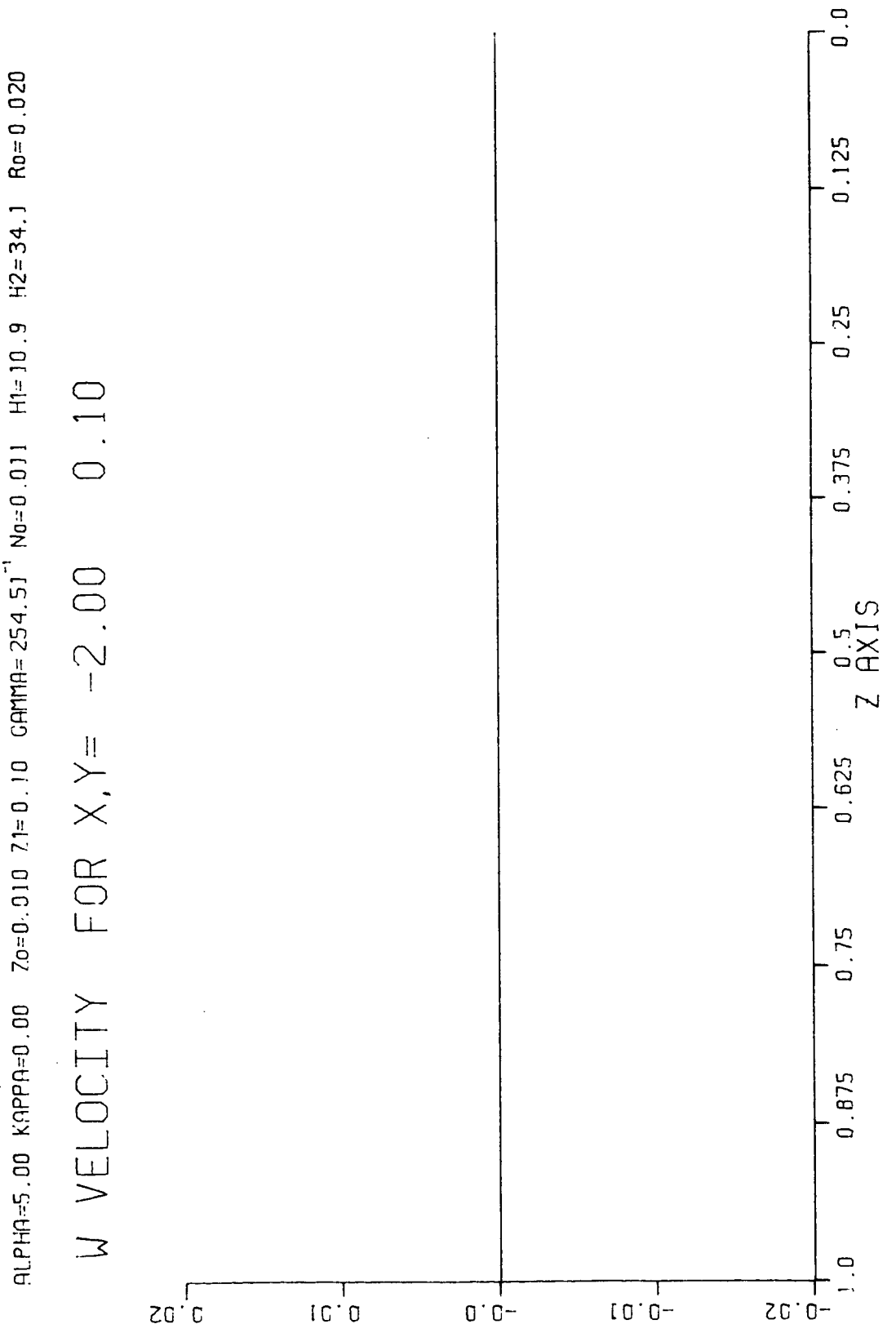

Figure 40 - Vertical profile of $p^{(0)}$ at (x,y) = (-.4,.1)

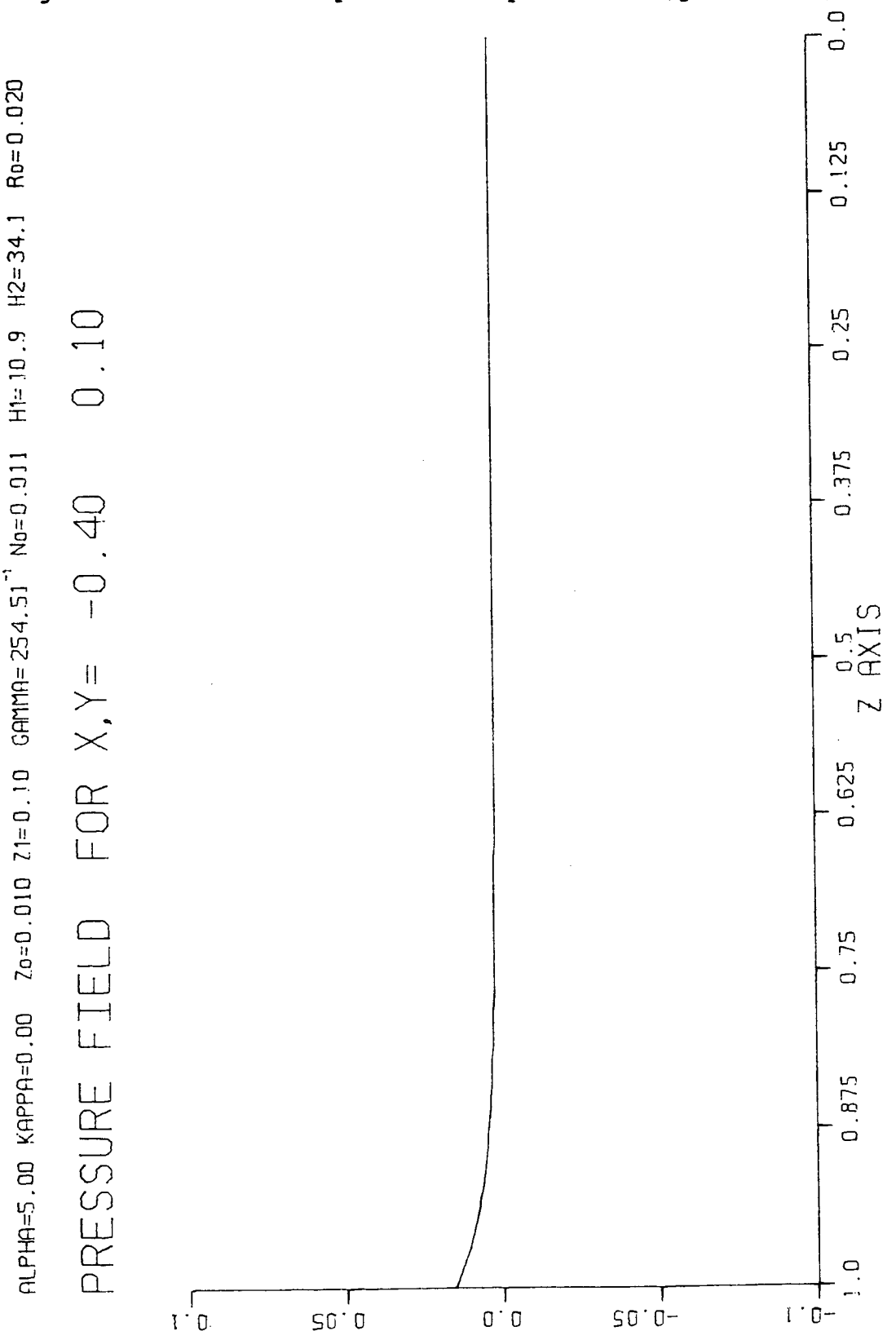

Figure 41 - Vertical profile of $\rho^{(0)}$ at (x,y) = (-.4,.1)

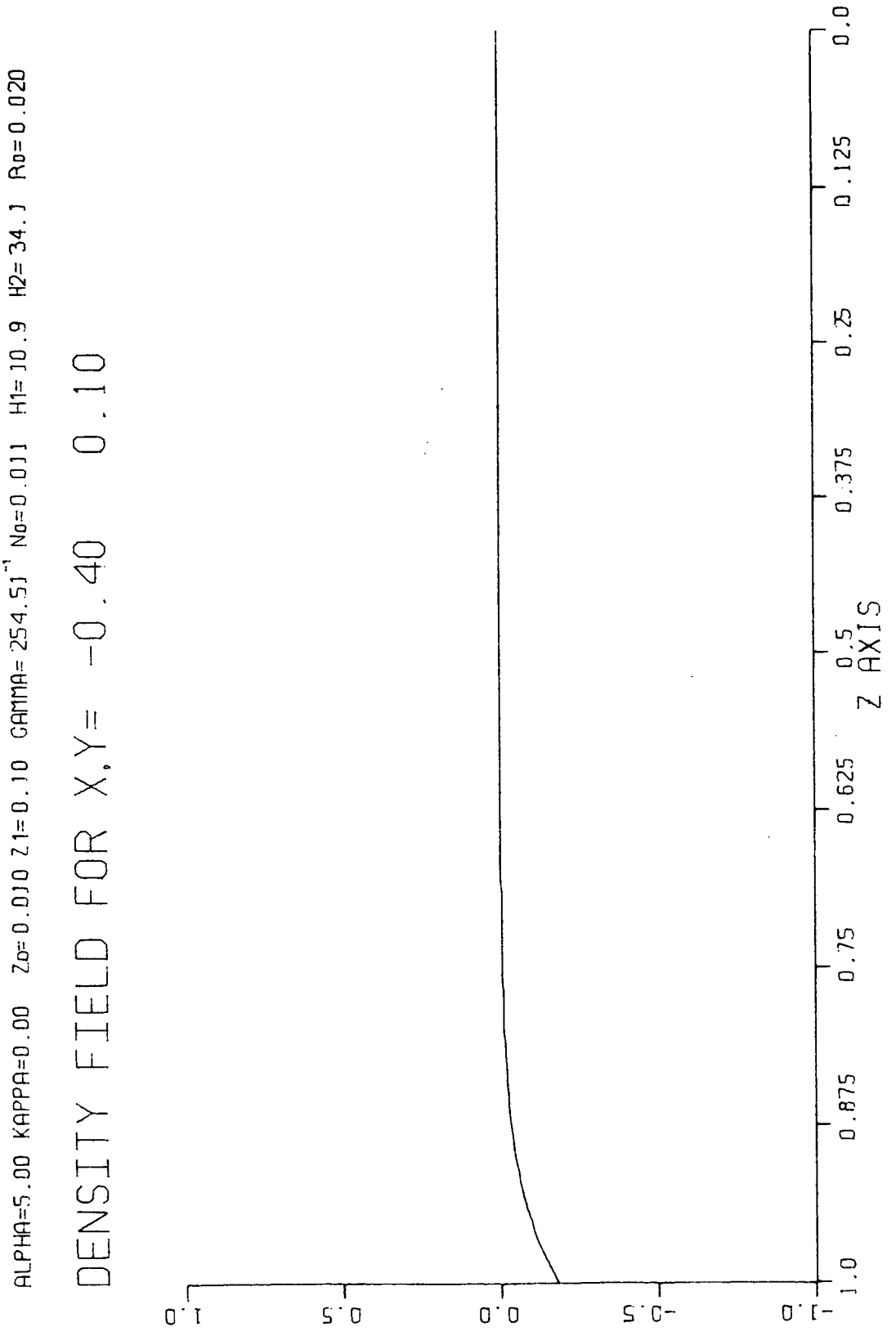

Figure 42 - Vertical profile of $u^{(0)}$ at (x,y) = (-.4,.1)

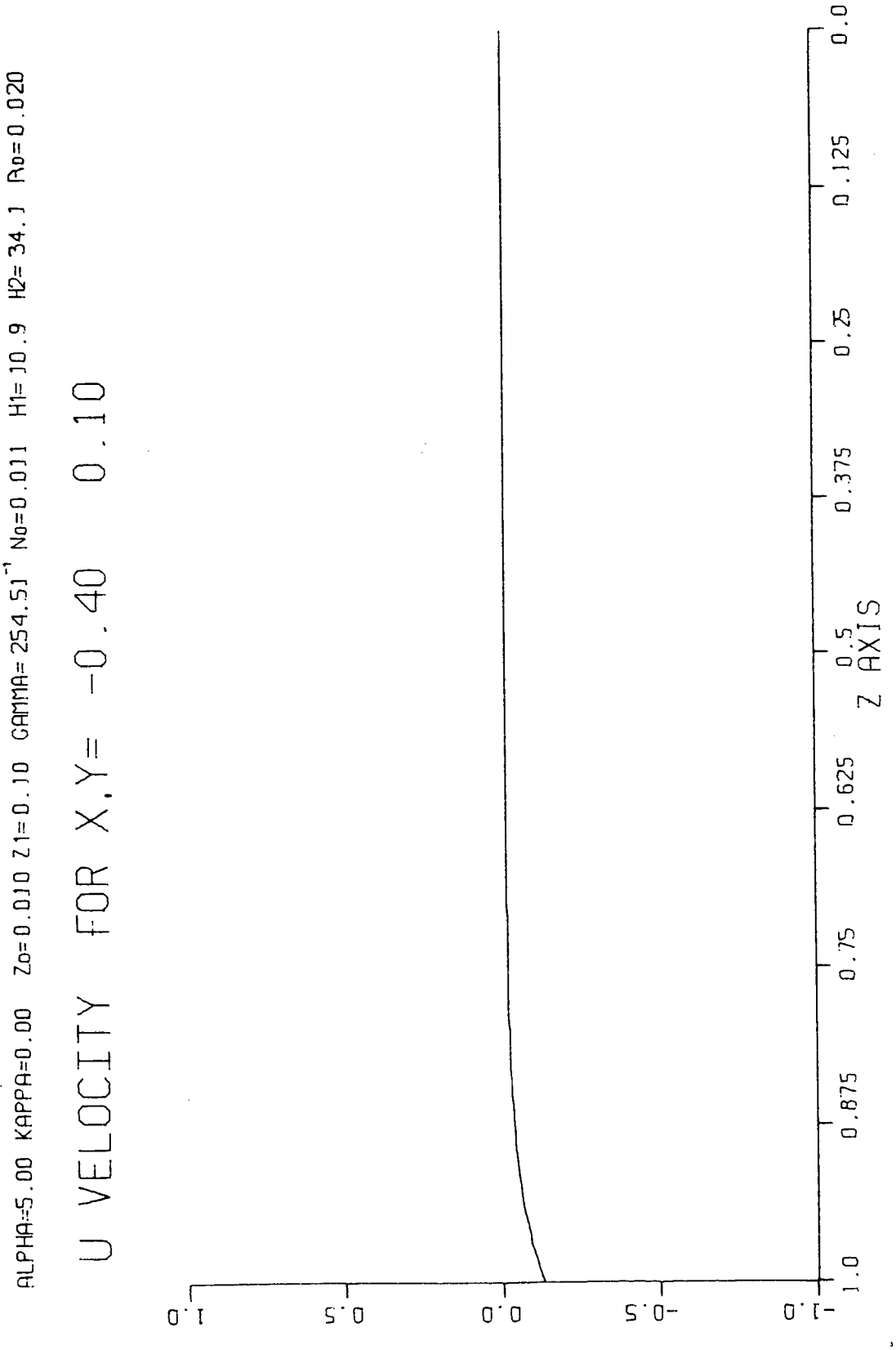

Figure 43 - Vertical profile of $v^{(0)}$ at (x,y) = (-.4,.1)

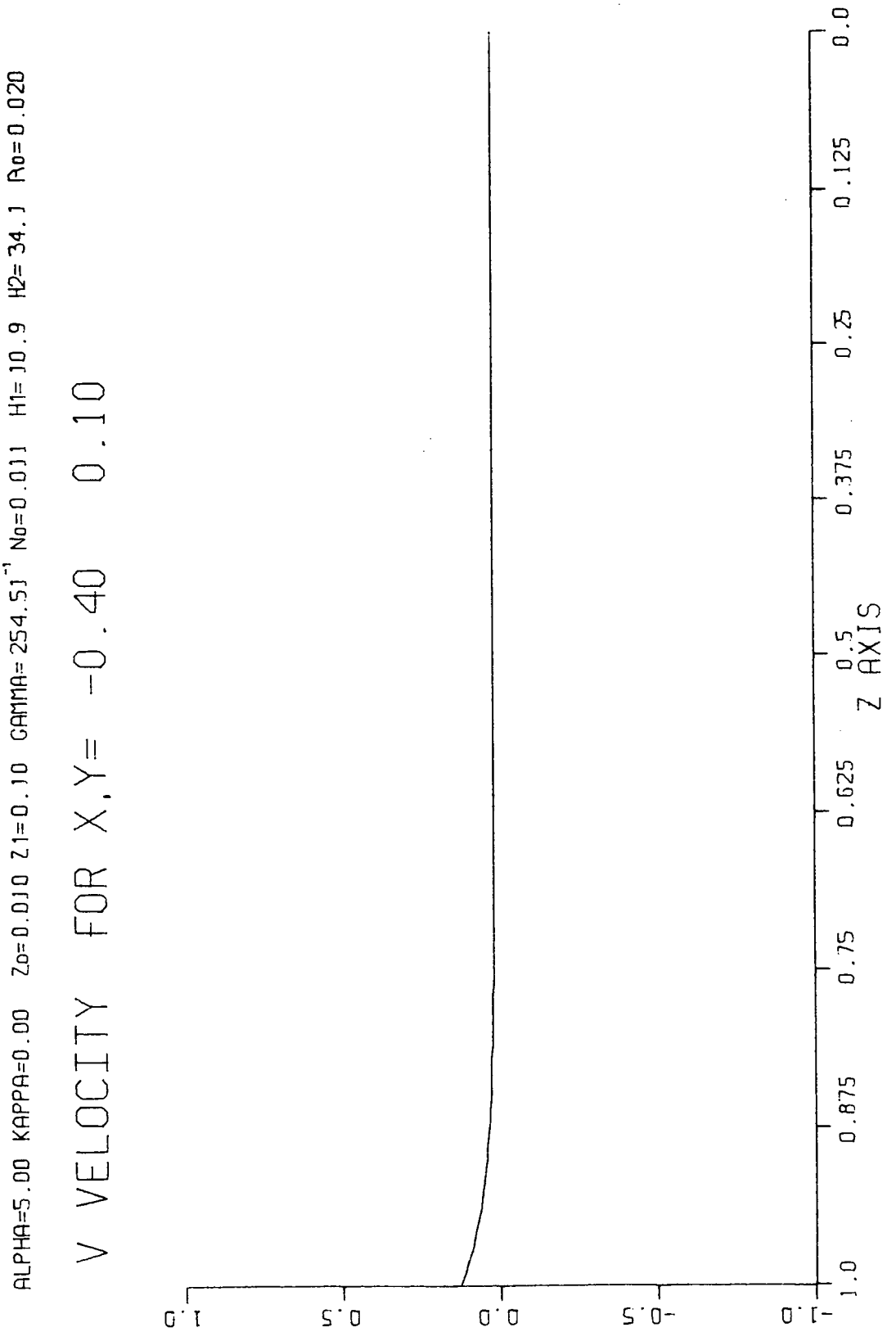

Figure 44 - Vertical profile of $w^{(0)}$ at (x,y) = (-.4,.1)

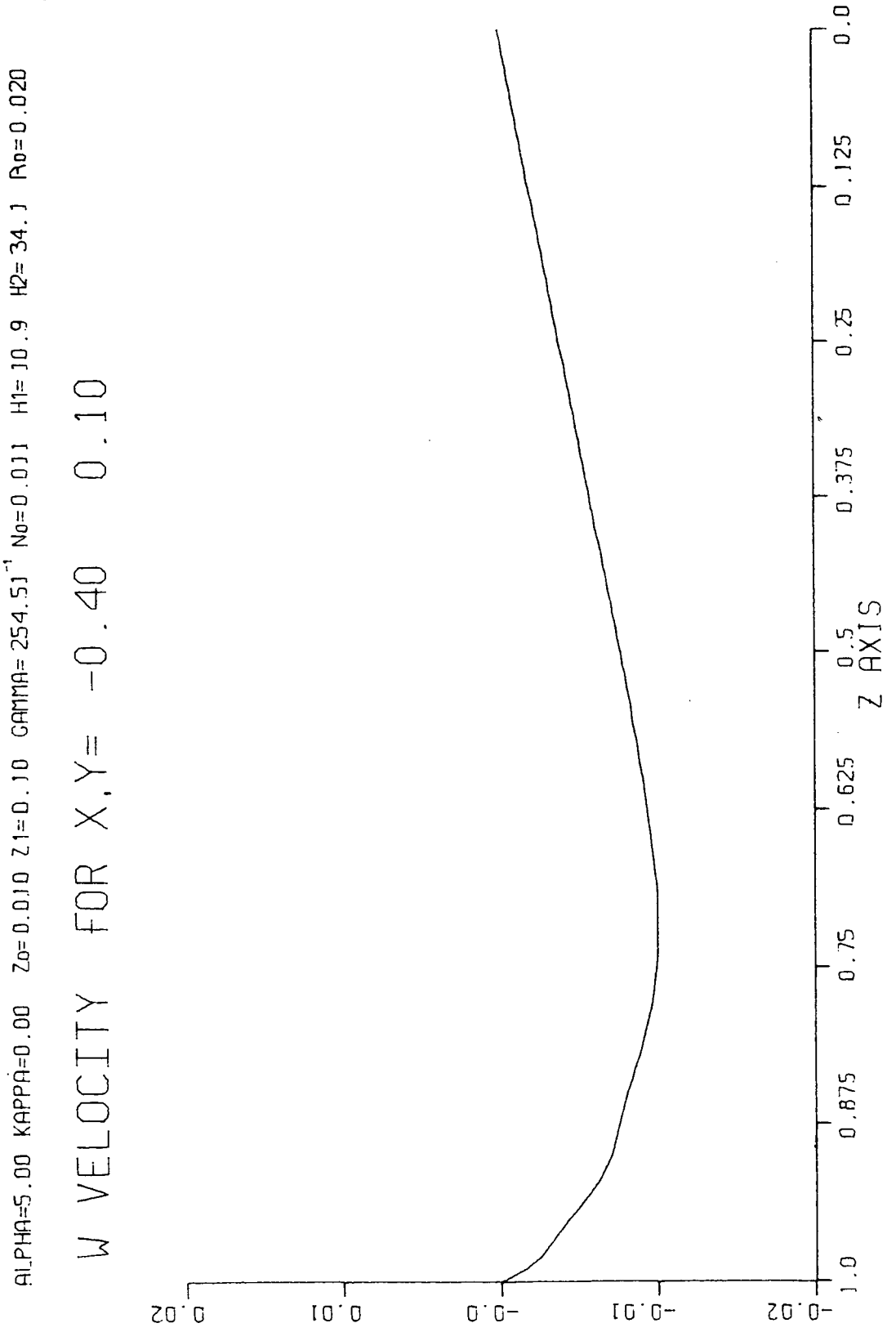

Figure 45 - Vertical profile of $p^{(0)}$ at (x,y) = (0,.75)

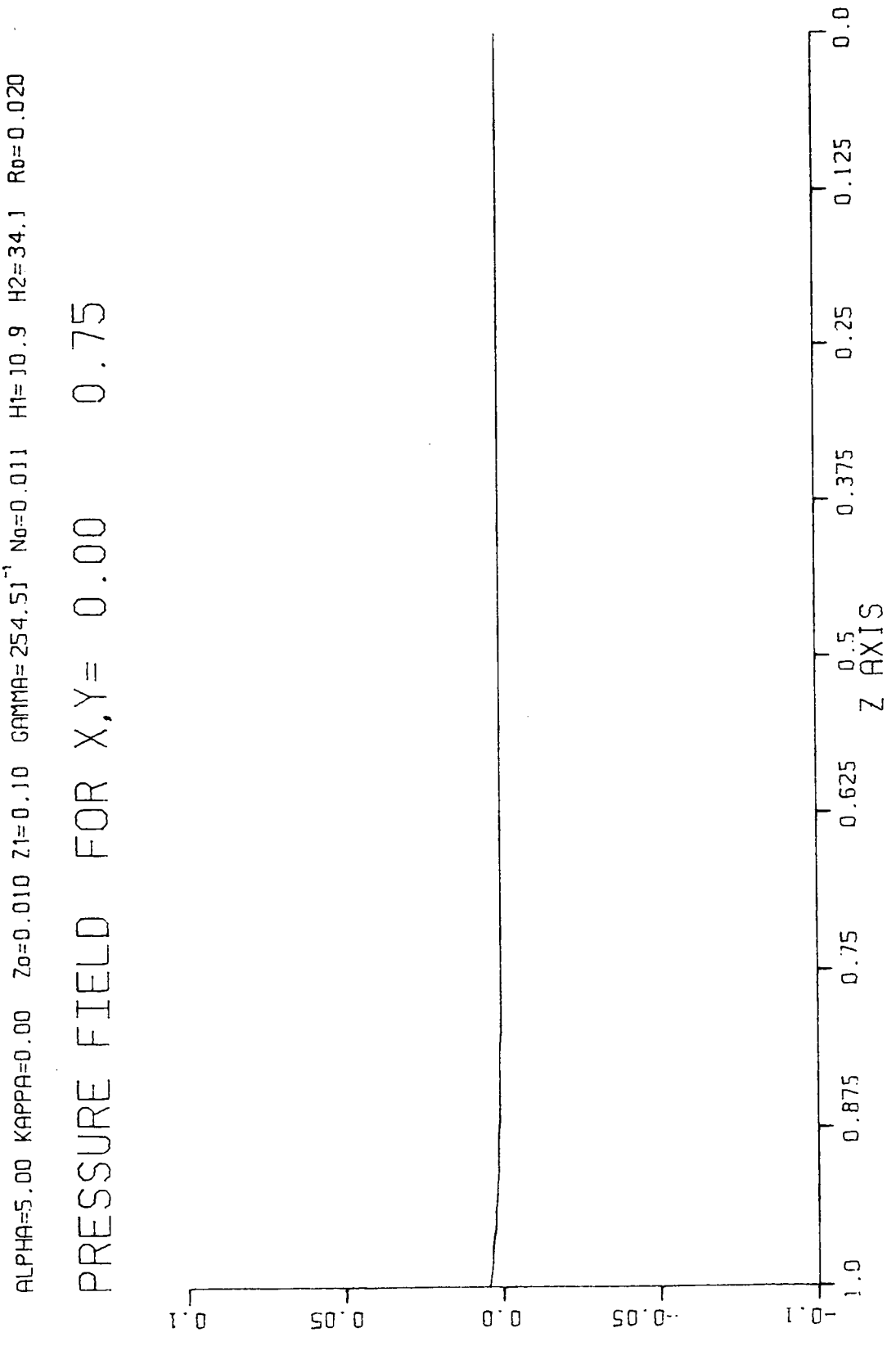

Figure 46 - Vertical profile of $\rho^{(0)}$ at (x,y) = (0,.75)

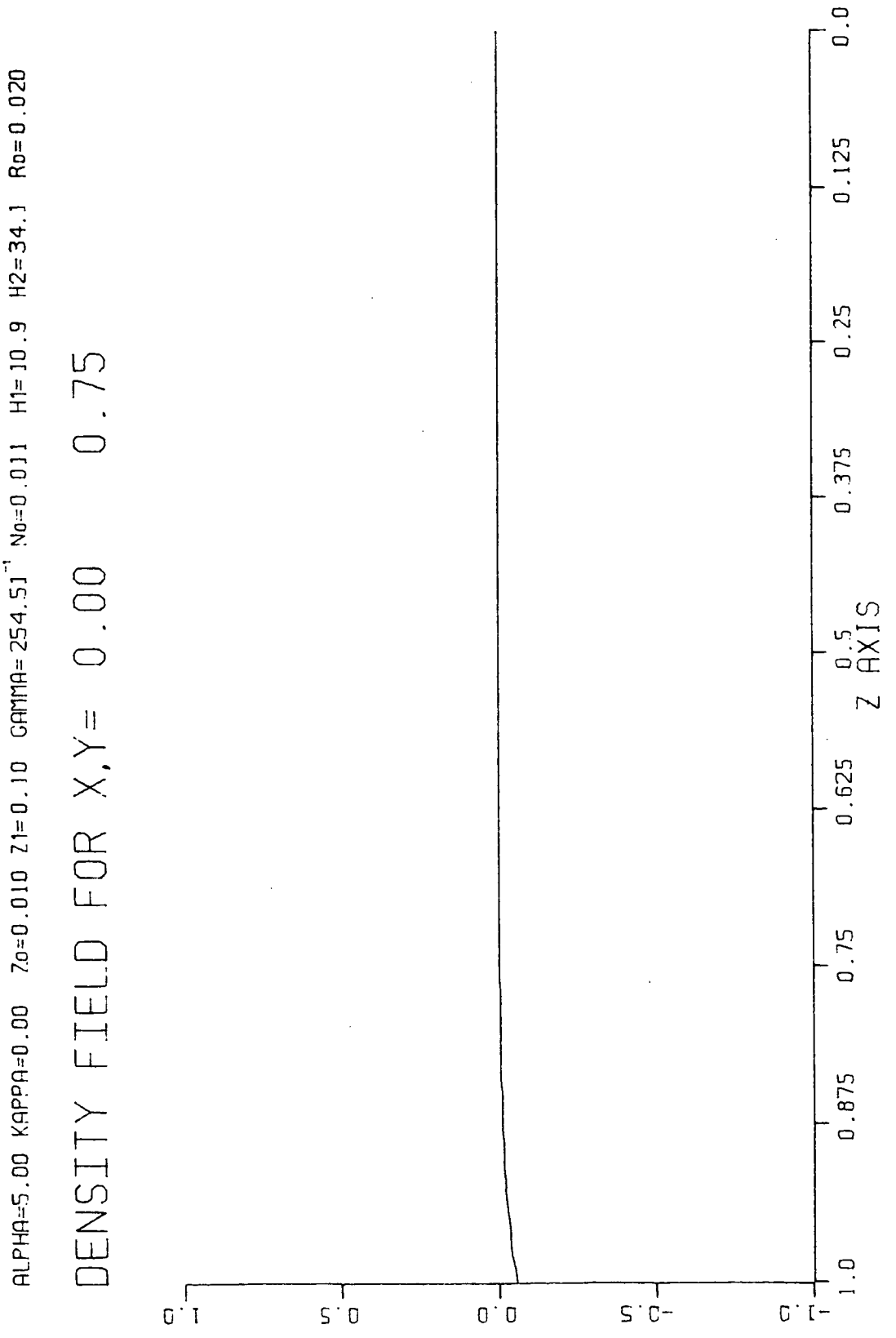

Figure 47 - Vertical profile of $u^{(0)}$ at (x,y) = (0,.75)

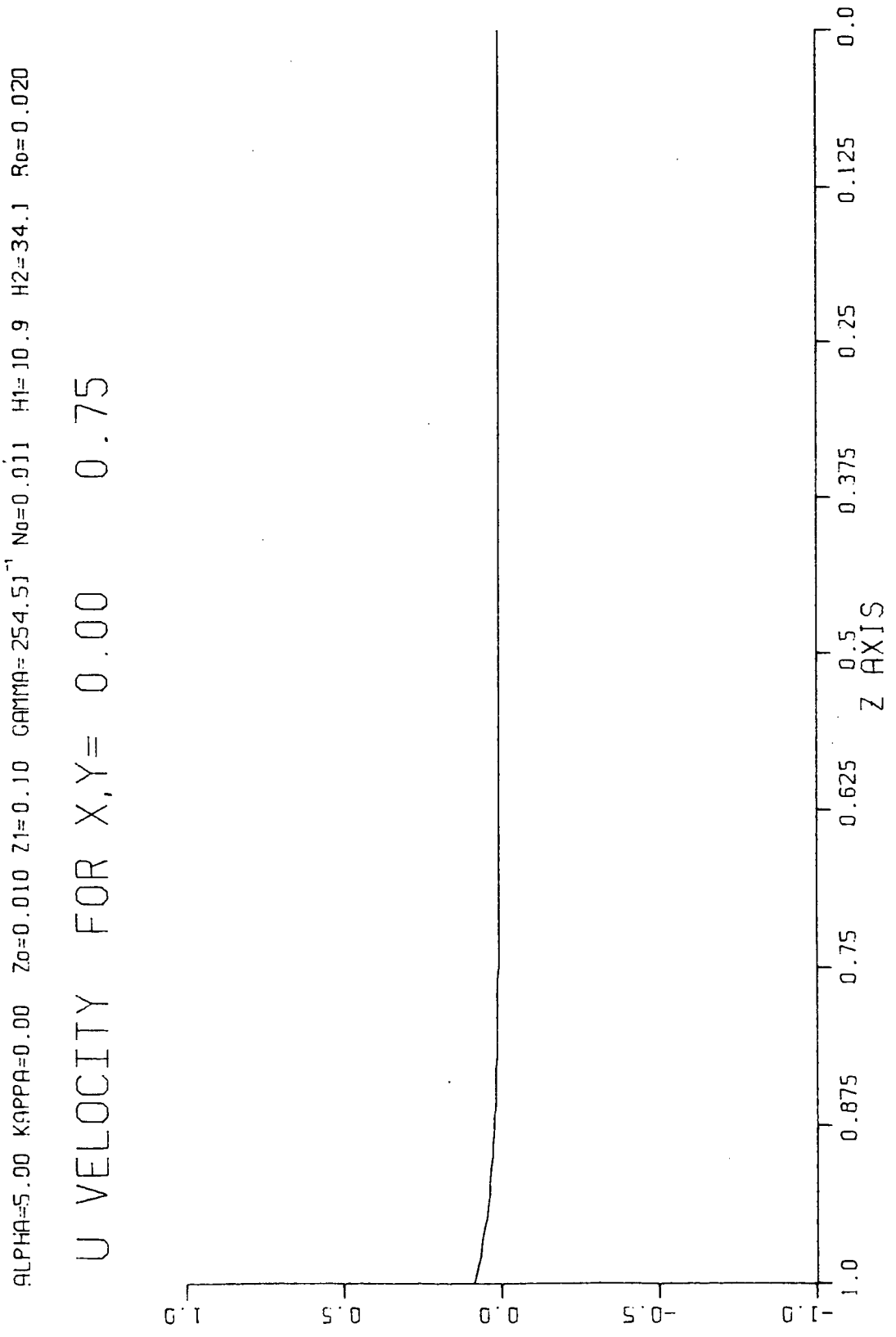

Figure 48 - Vertical profile of $v^{(0)}$ at (x,y) = (0,.75)

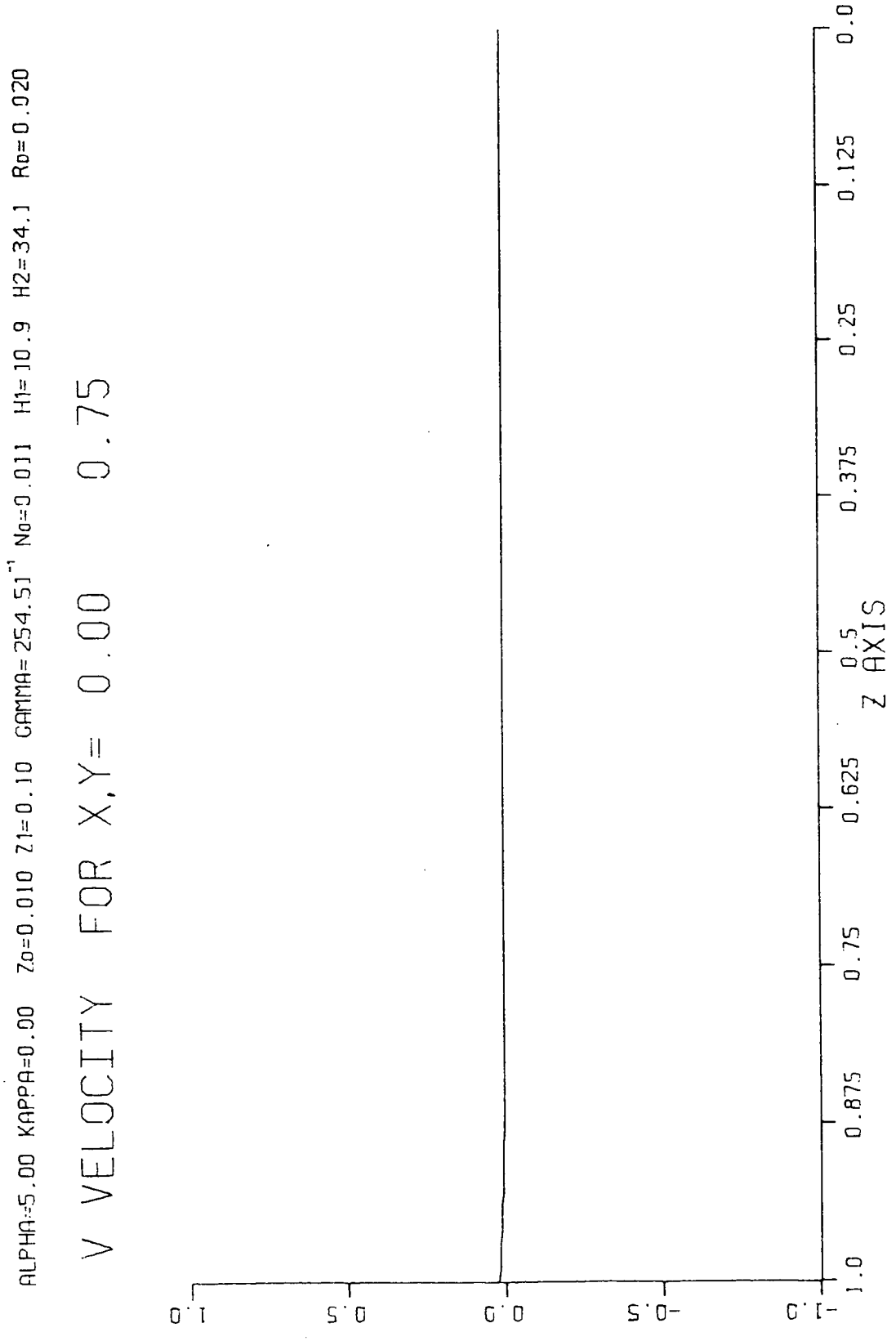

Figure 49 - Vertical profile of $w^{(0)}$ at (x,y) = (0,.75)

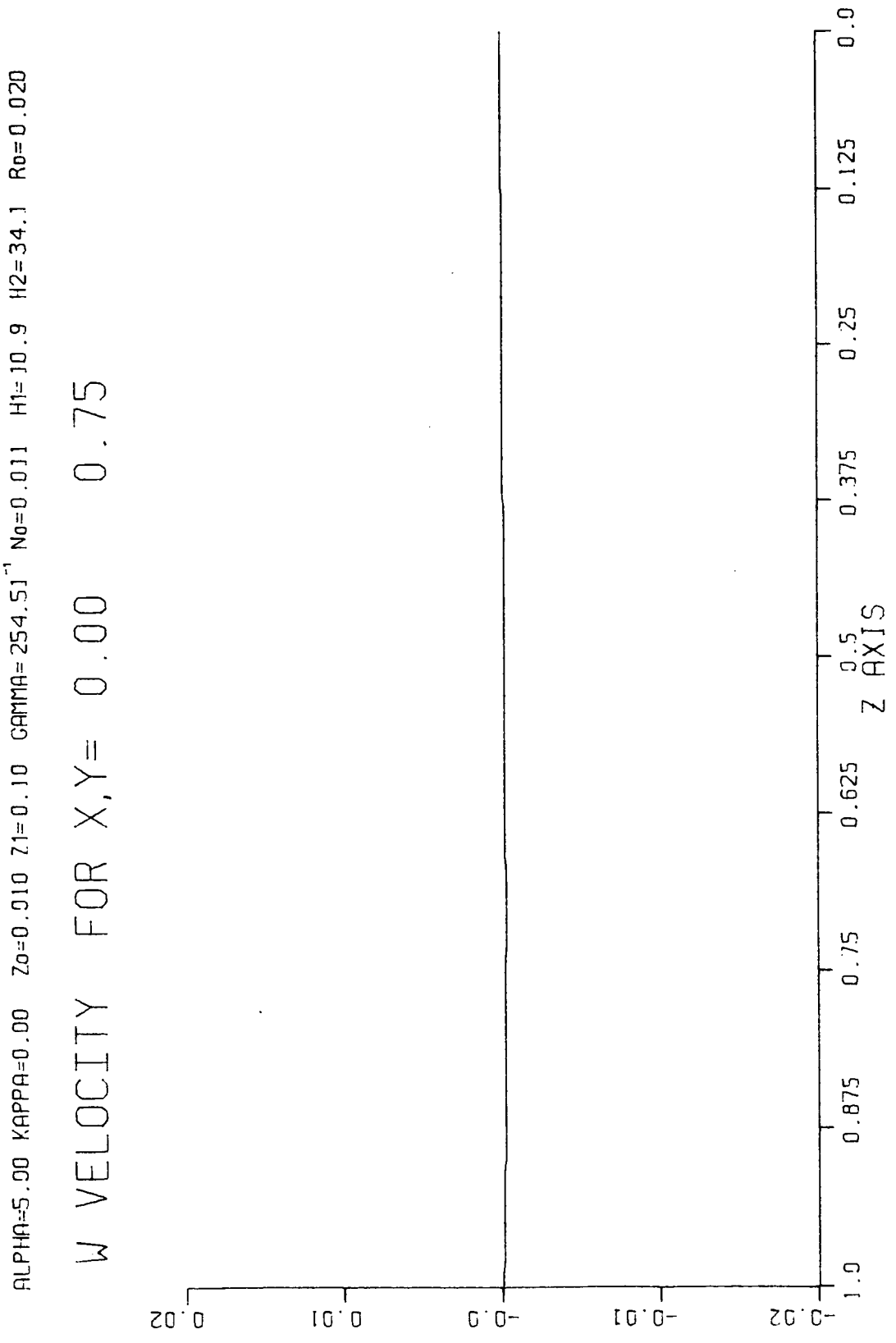

Figure 50 - Vertical profile of $p^{(0)}$ at $(x,y) = (.75,.75)$

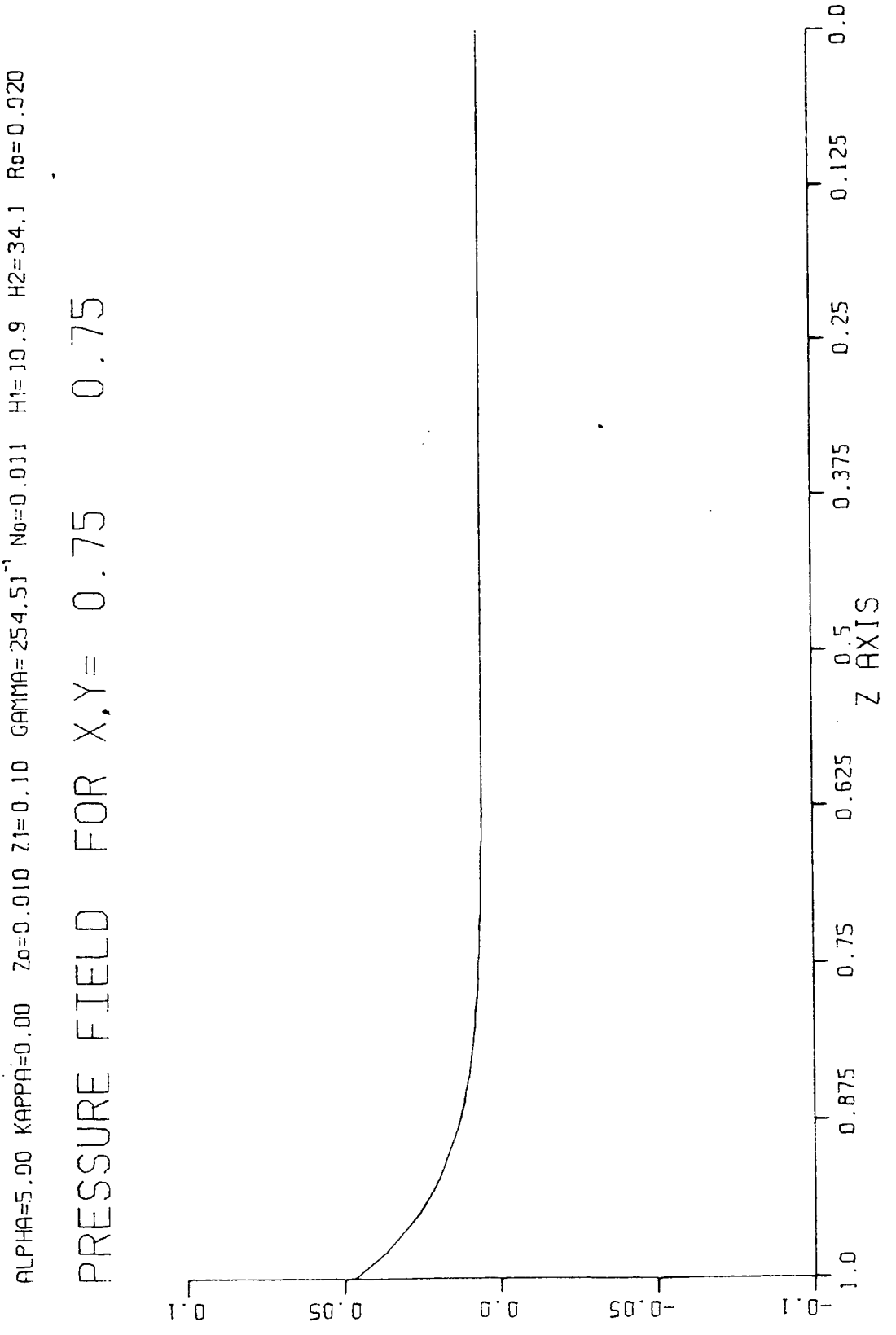

Figure 51 - Vertical profile of $\rho^{(0)}$ at (x,y) = (.75,.75)

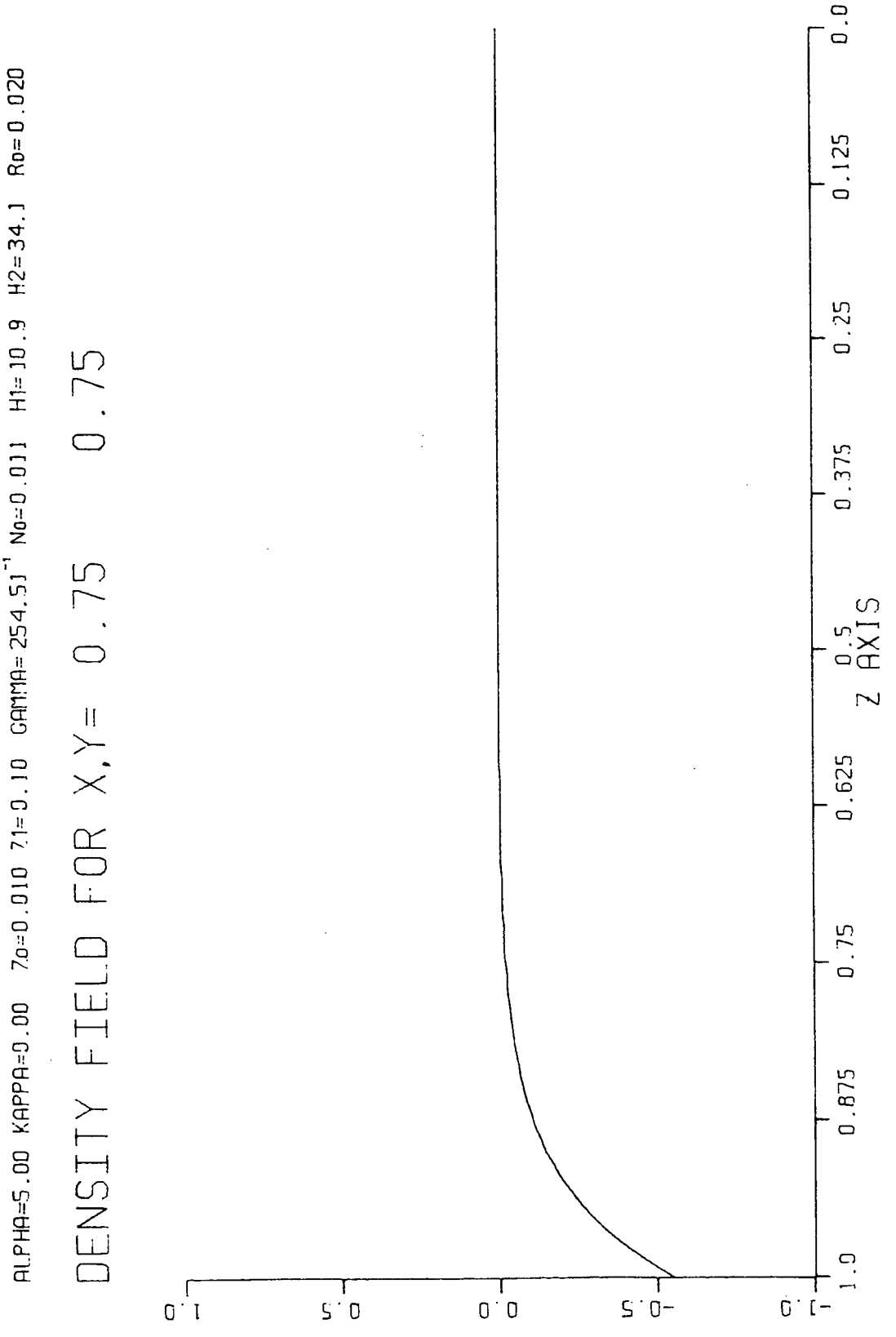

Figure 52 - Vertical profile of $u^{(0)}$ at (x,y) = (.75,.75)

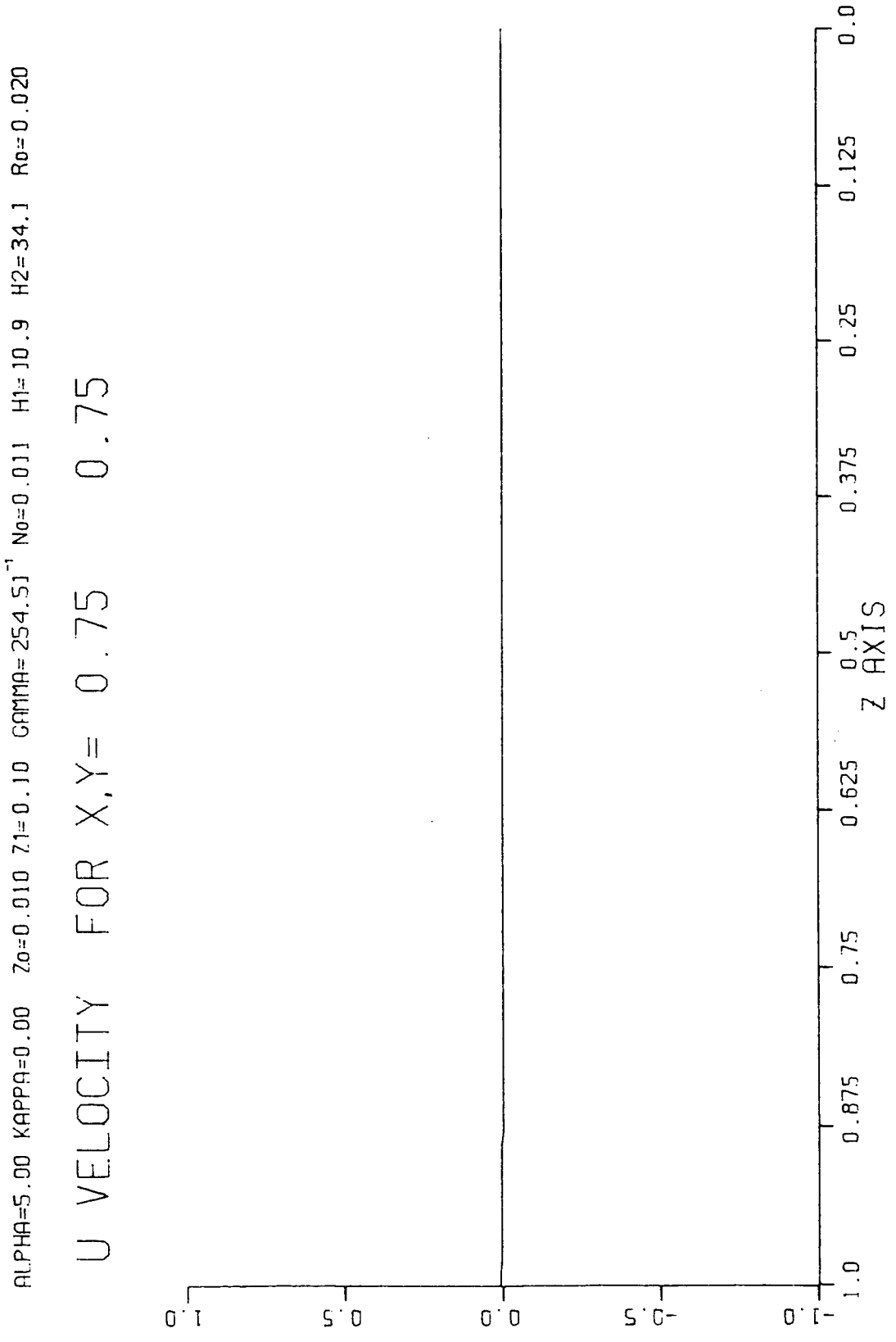

Figure 53 - Vertical profile of $v^{(0)}$ at (x,y) = (.75,.75)

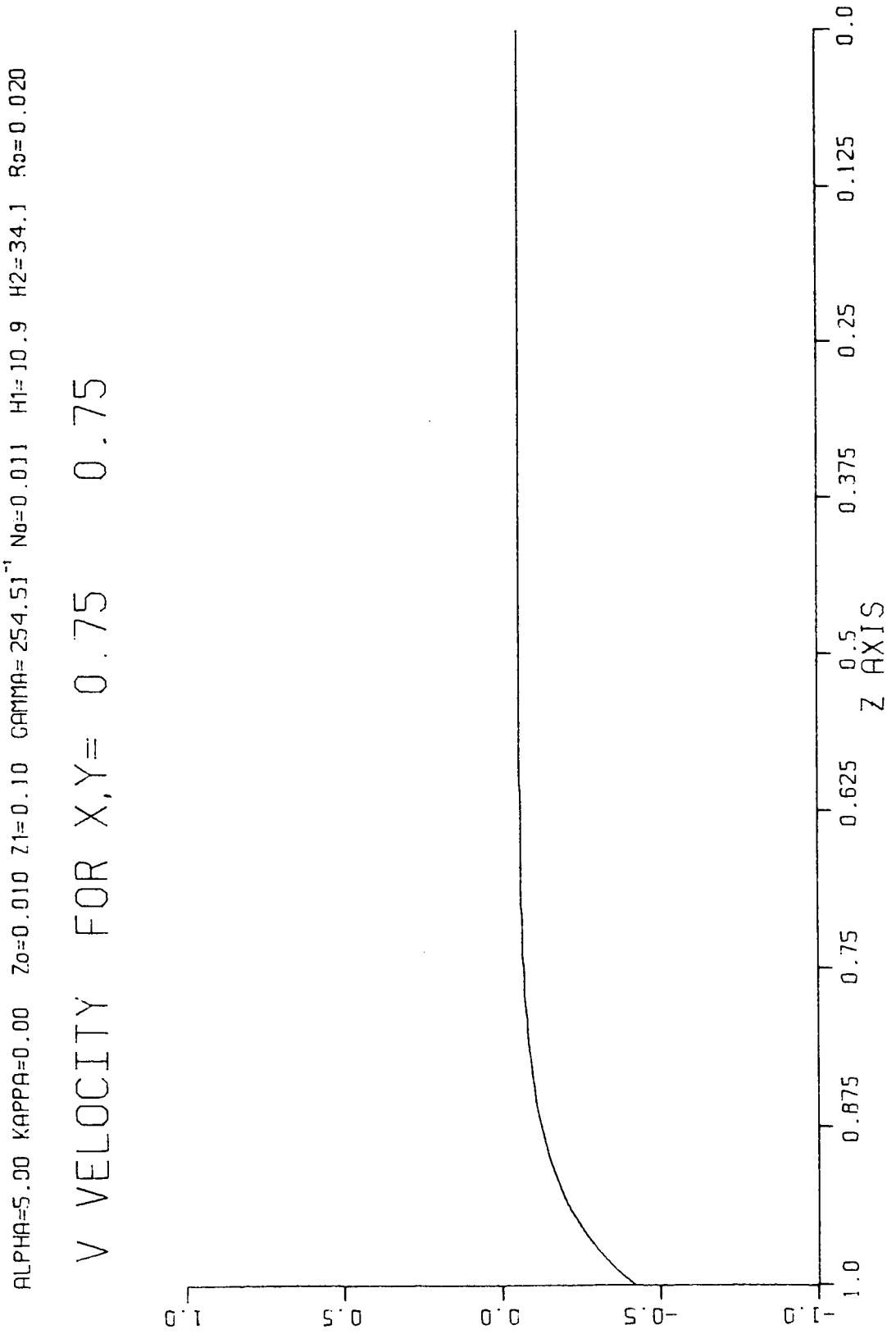

Figure 54 - Vertical profile of $w^{(0)}$ at (x,y) = (.75,.75)

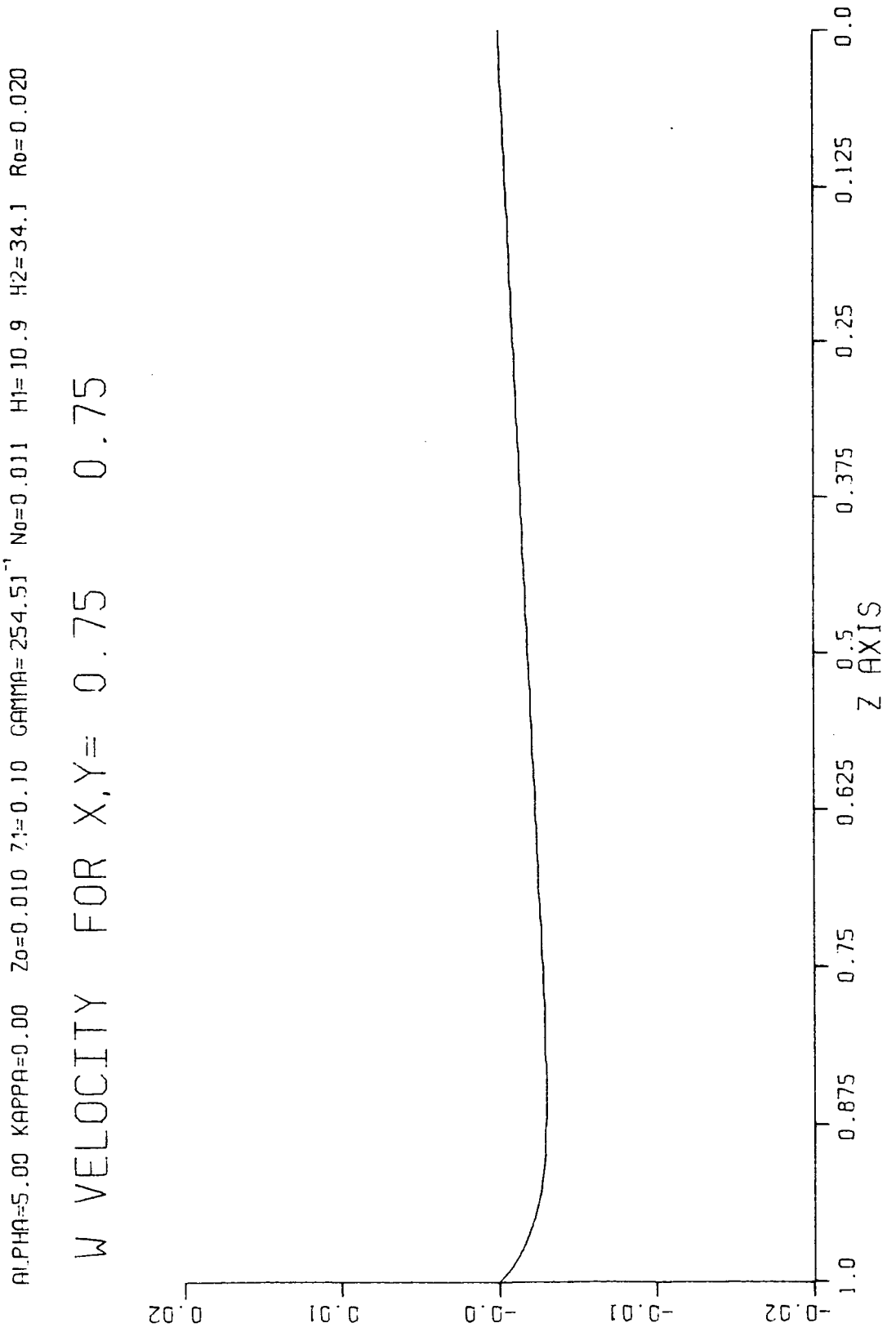

Figure 55 - Horizontal contour plot of the stream function on $z = 1$ with $(a, \epsilon) = (10, .1)$

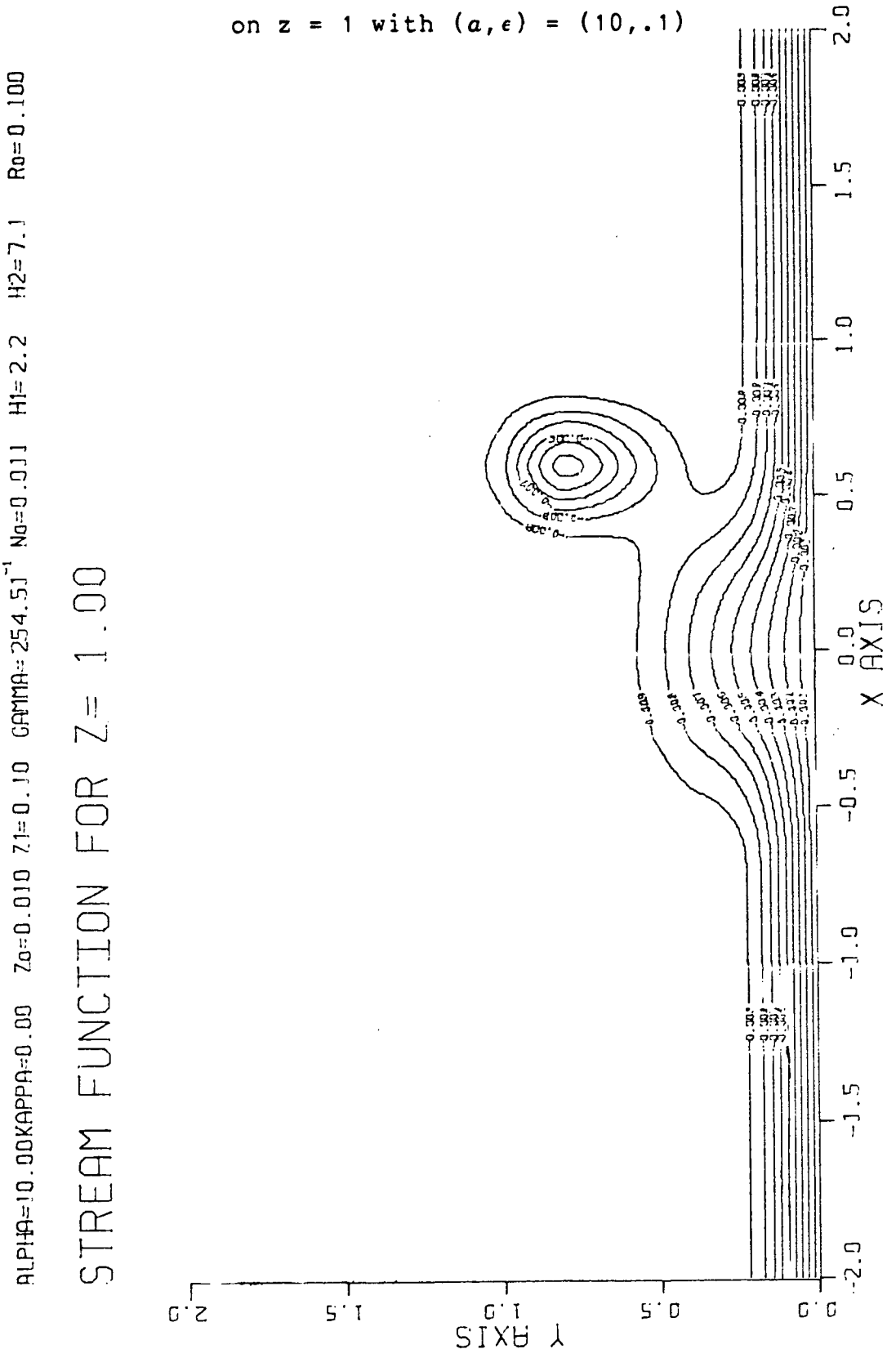

Figure 56 - Horizontal contour plot of the stream function on $z = 1$ with $(a, \epsilon) = (10, .01)$

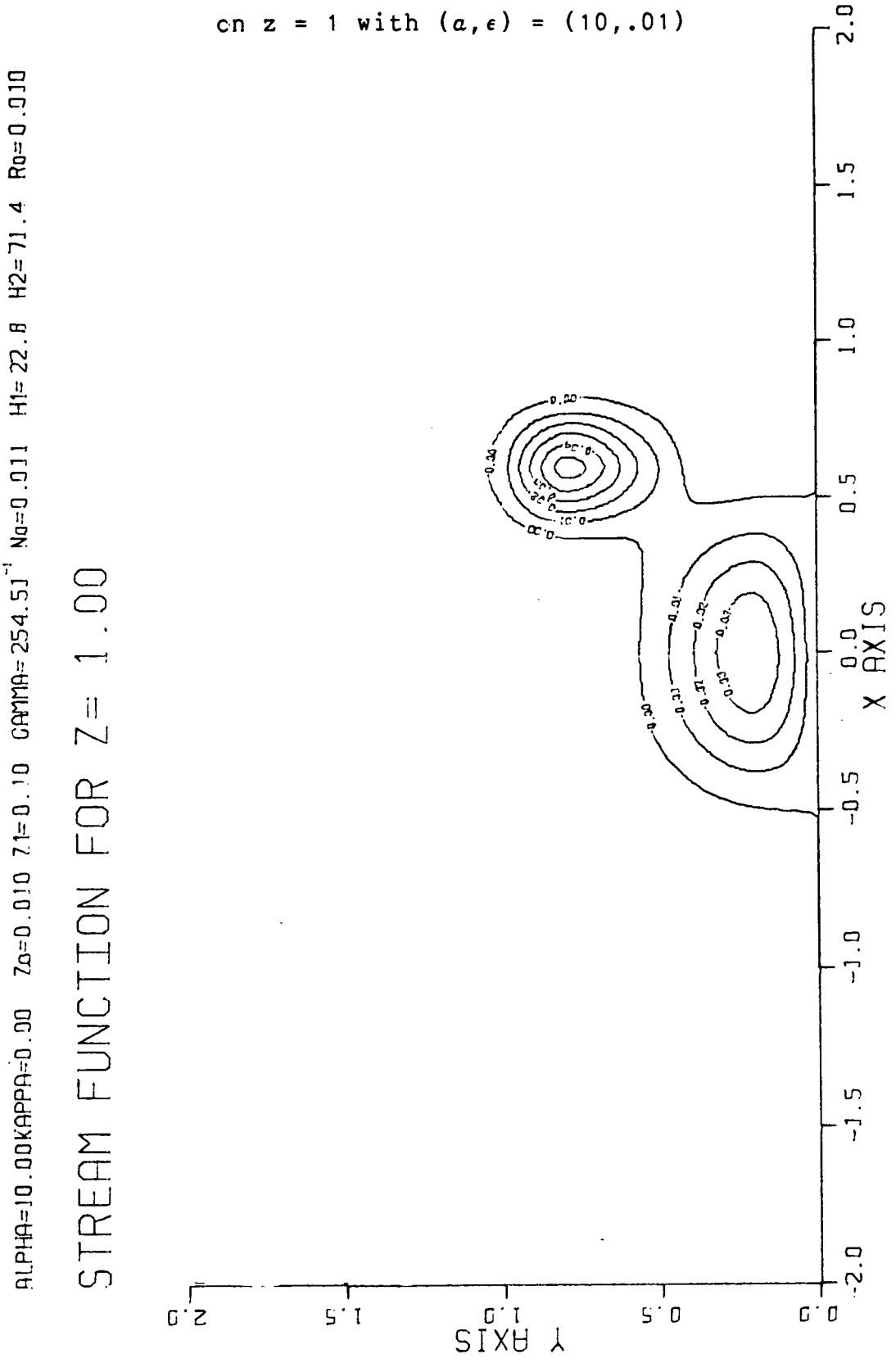

Figure 57 - Horizontal contour plot of the stream function

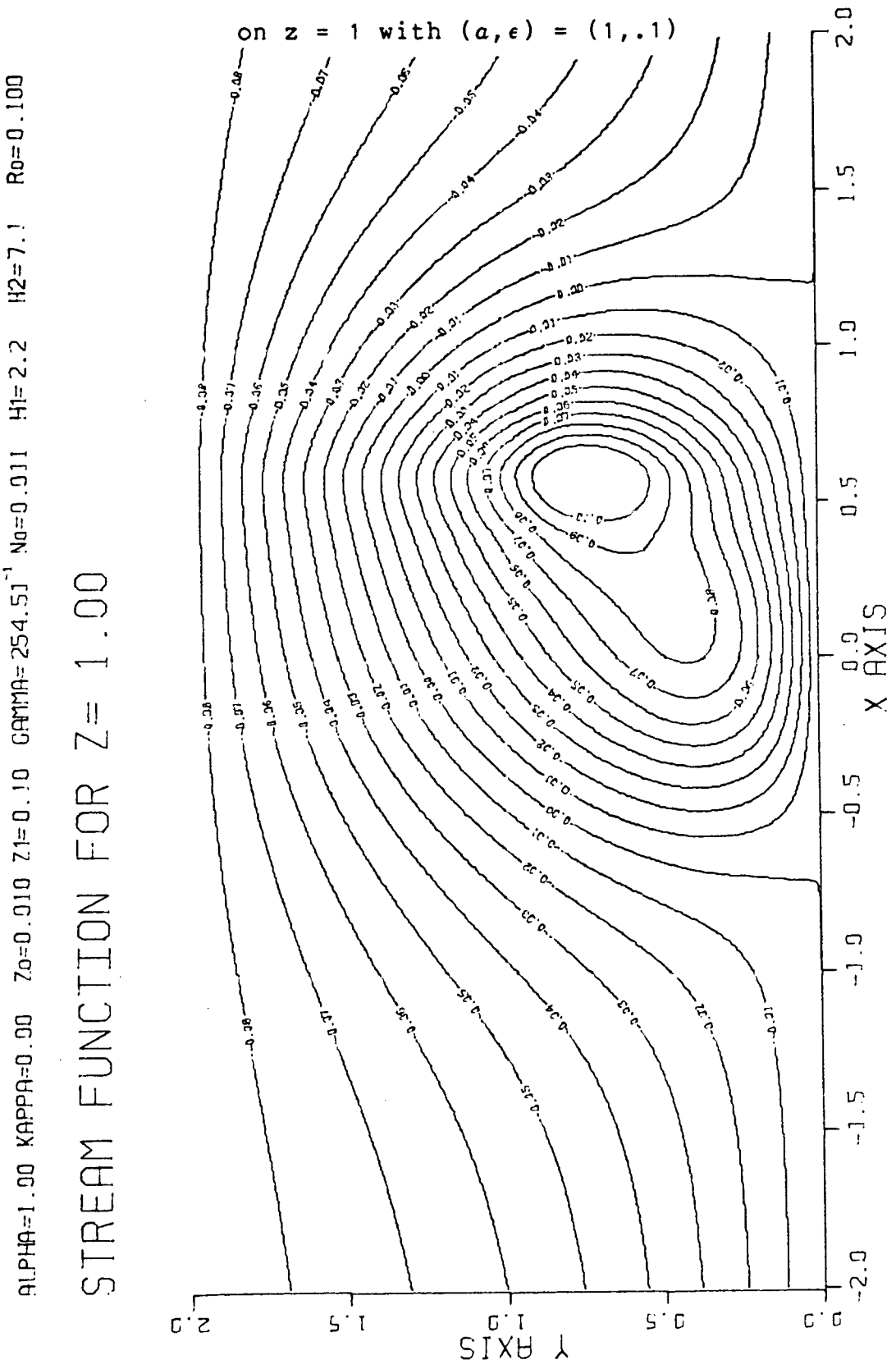

Figure 58 - Horizontal contour plot of the stream function on z = 1 with $(a,\epsilon) = (1,.01)$

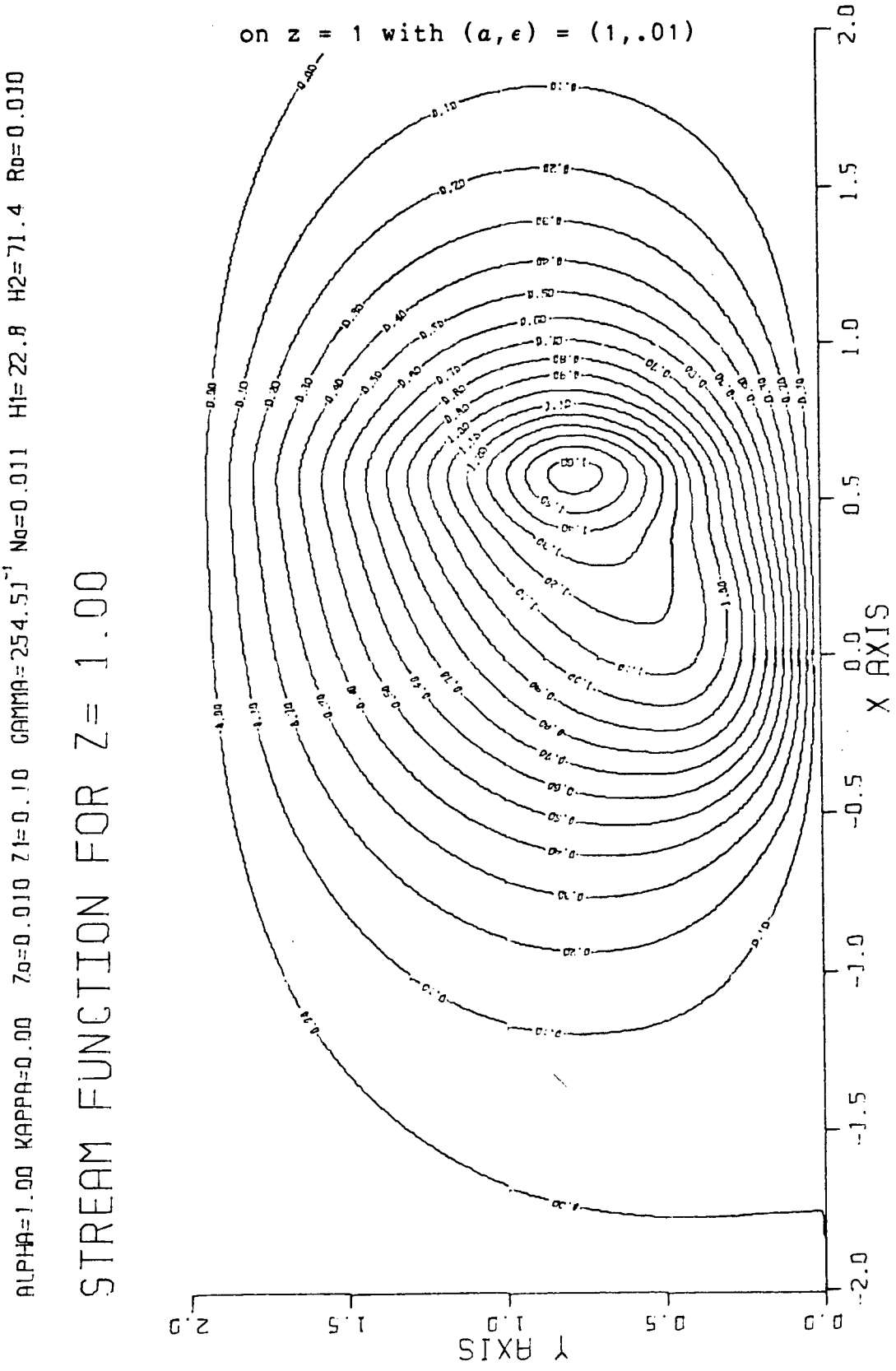

Figure 59 - Vertical contour plot of $p^{(0)}$ on y = .6 with $(a,\epsilon) = (1,.1)$

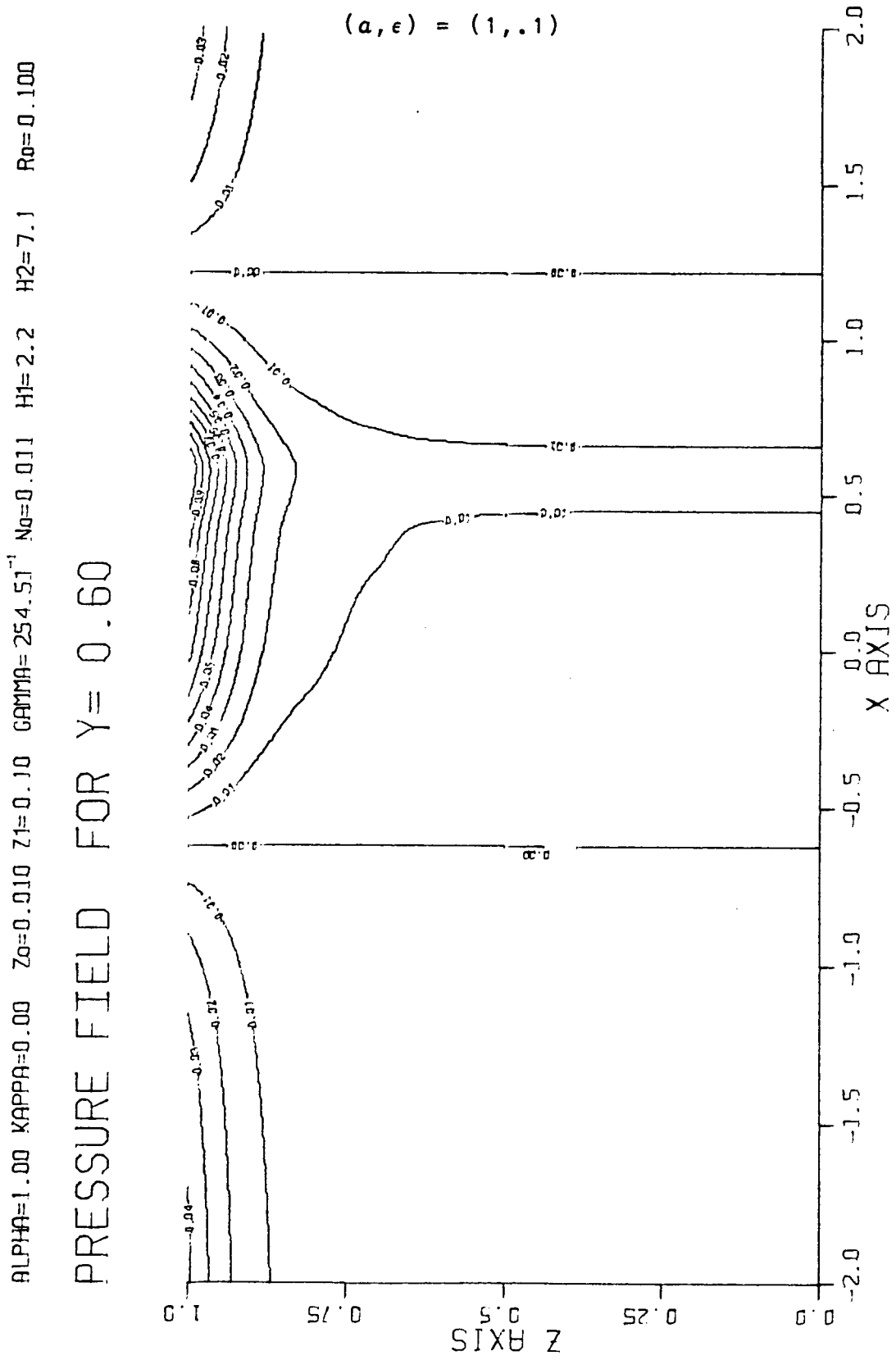

Figure 60 - Vertical contour plot of $p^{(0)}$ on y = .6 with $(a,\epsilon) = (1,.01)$

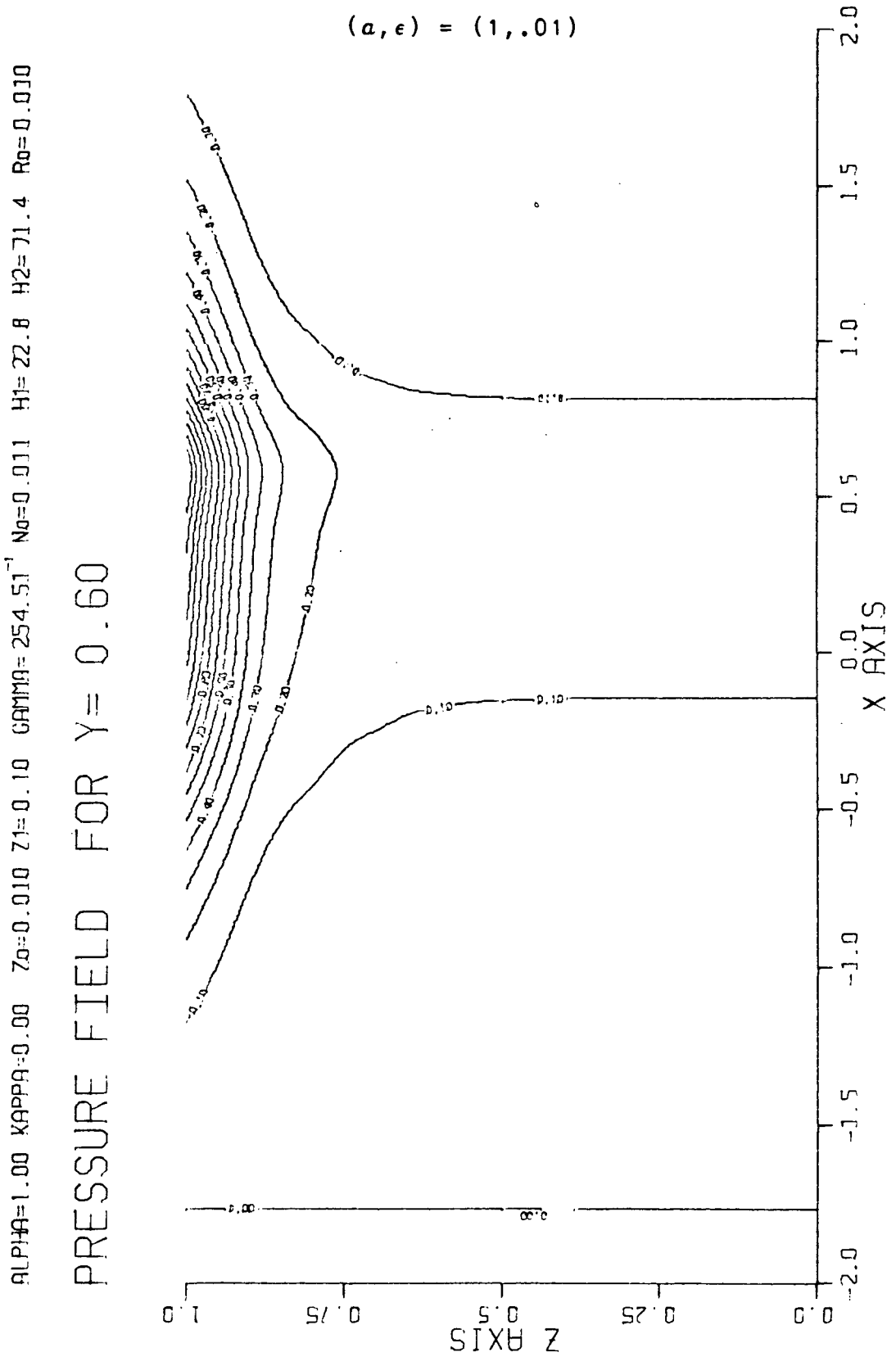

Figure 61 - Horizontal contour plot of the stream function on z = 1 with no seamount

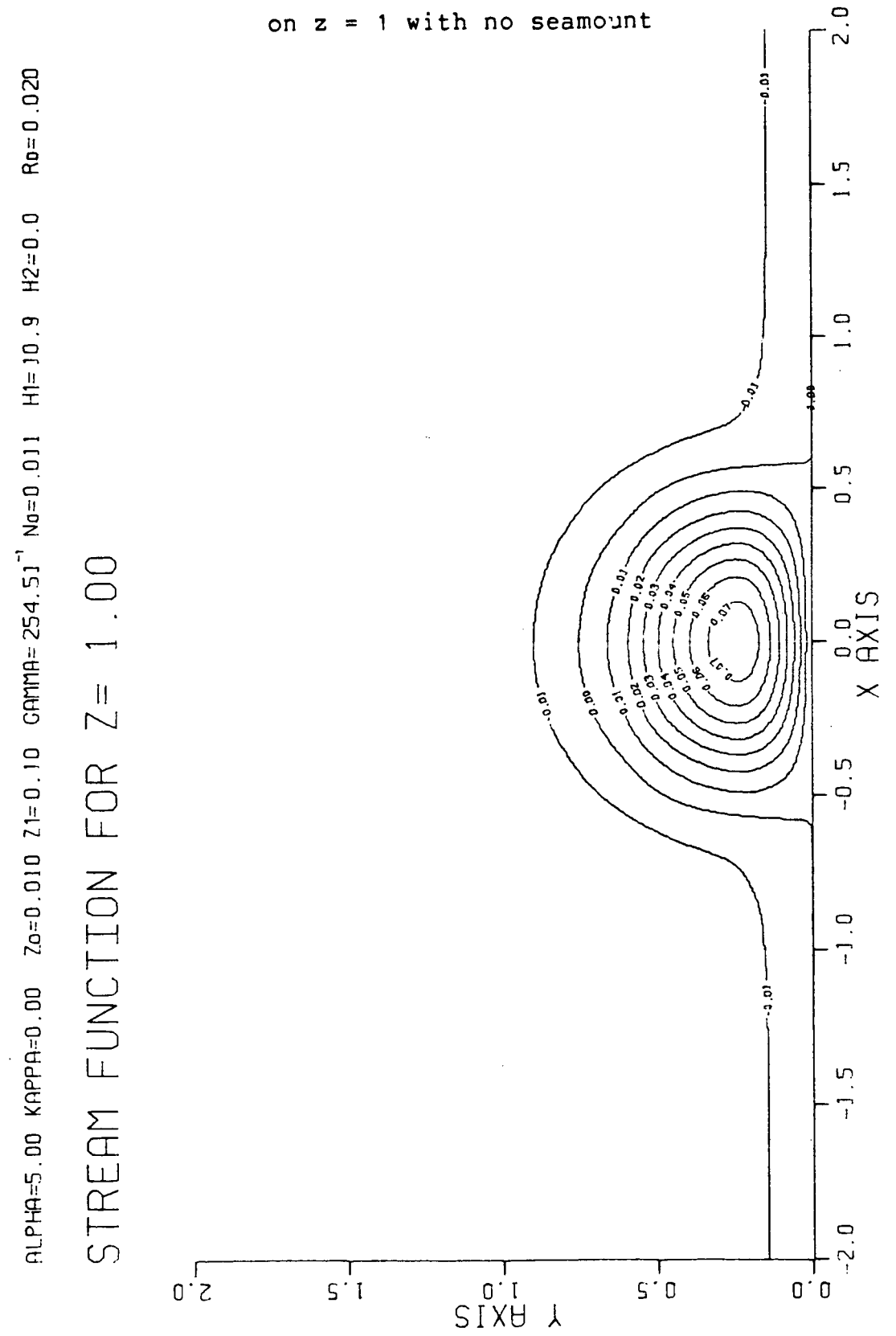

Figure 62 - Horizontal contour plot of the stream function on z = 1 with no slope protrusion

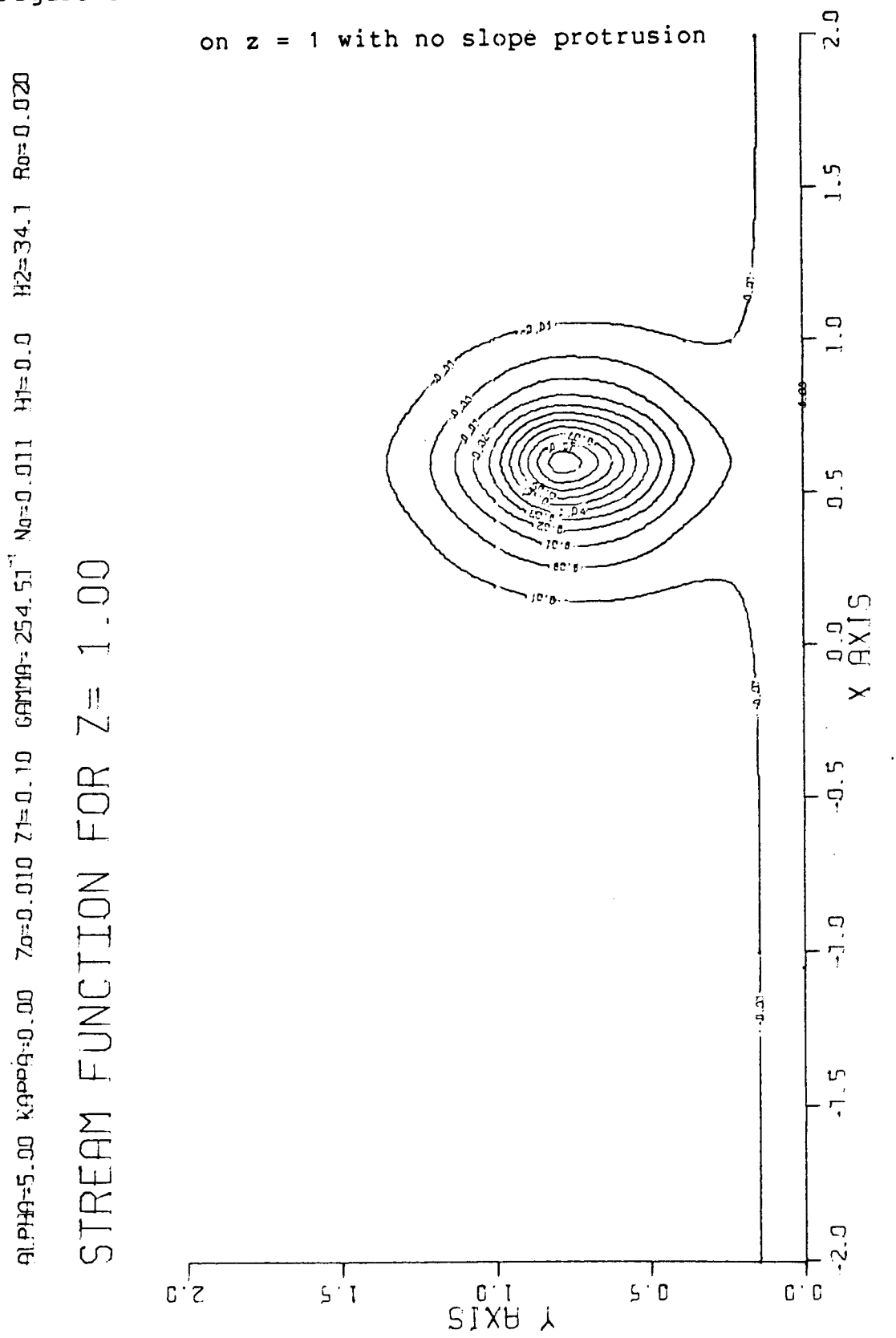

Figure 63 - Vertical contour plot of $p^{(0)}$ on y = .8 with $(N_0, \gamma^*) = (.01s^{-1}, 300^{-1}m^{-1})$

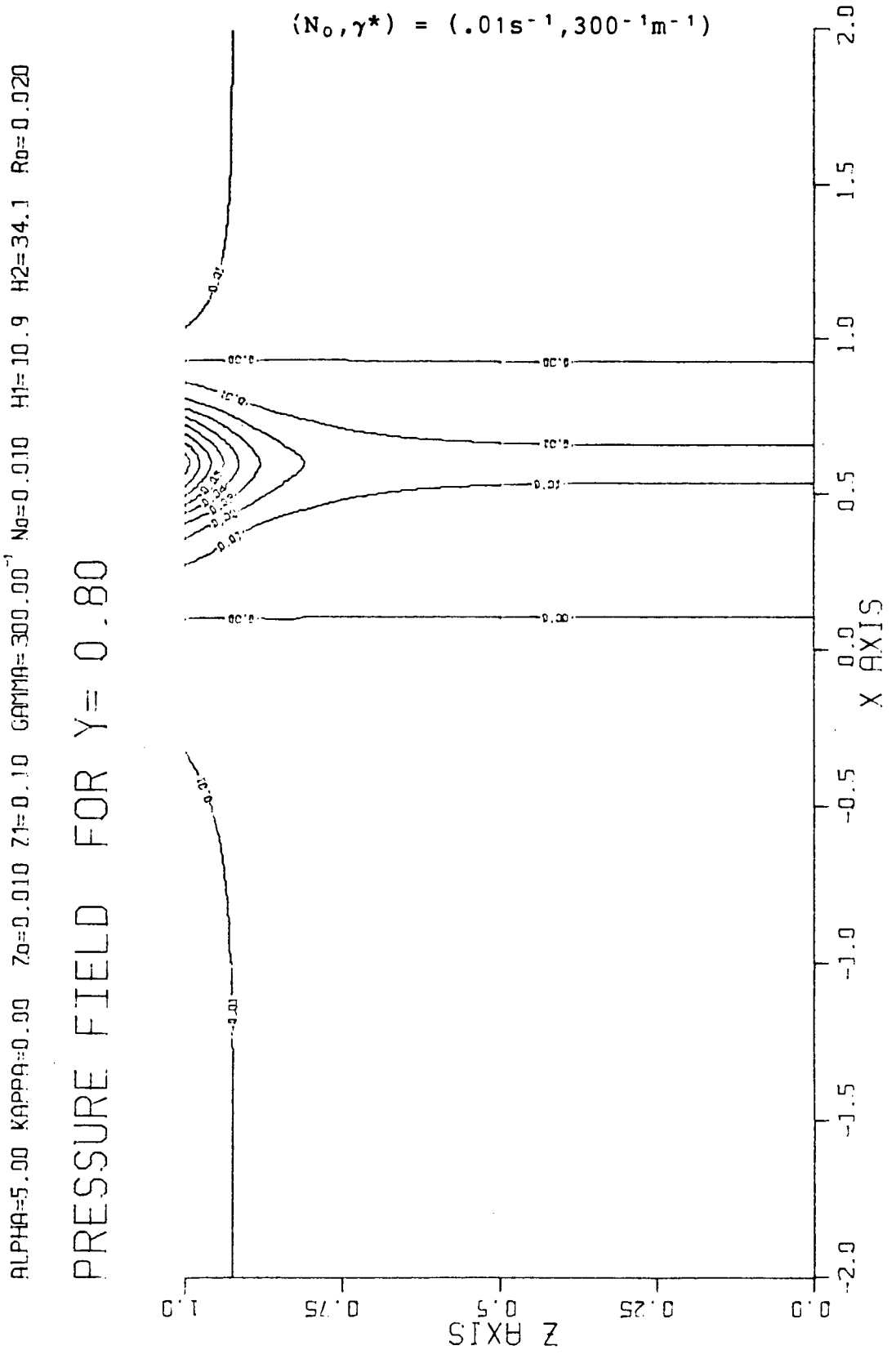

Figure 64 - Vertical contour plot of $p^{(0)}$ on y = .2 with $(N_0, \gamma^*) = (.02s^{-1}, 225^{-1}m^{-1})$

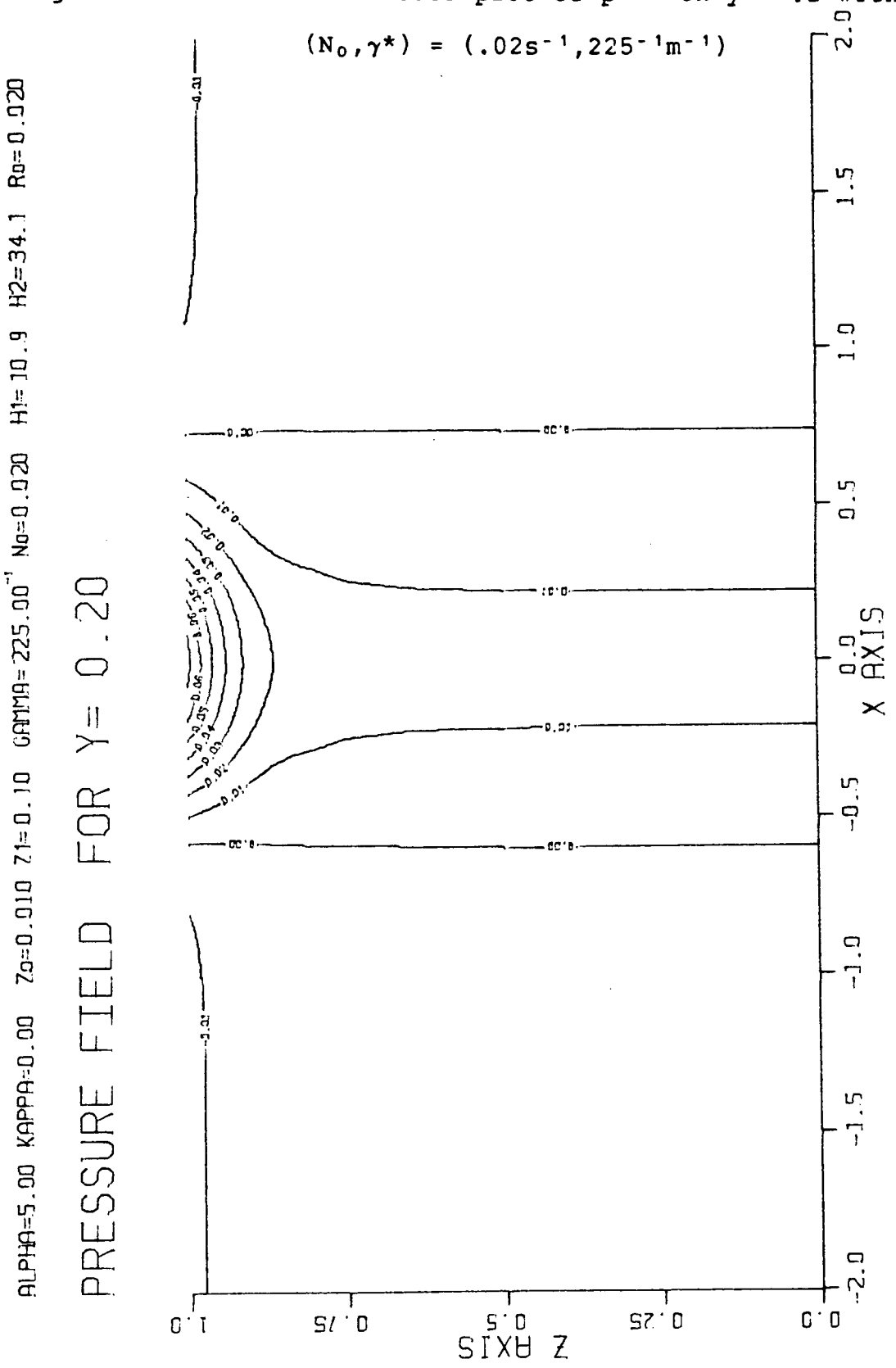

Figure 65 - Vertical contour plot of $p^{(0)}$ on y = .8 with $(N_0, \gamma^*) = (.02s^{-1}, 225^{-1}m^{-1})$

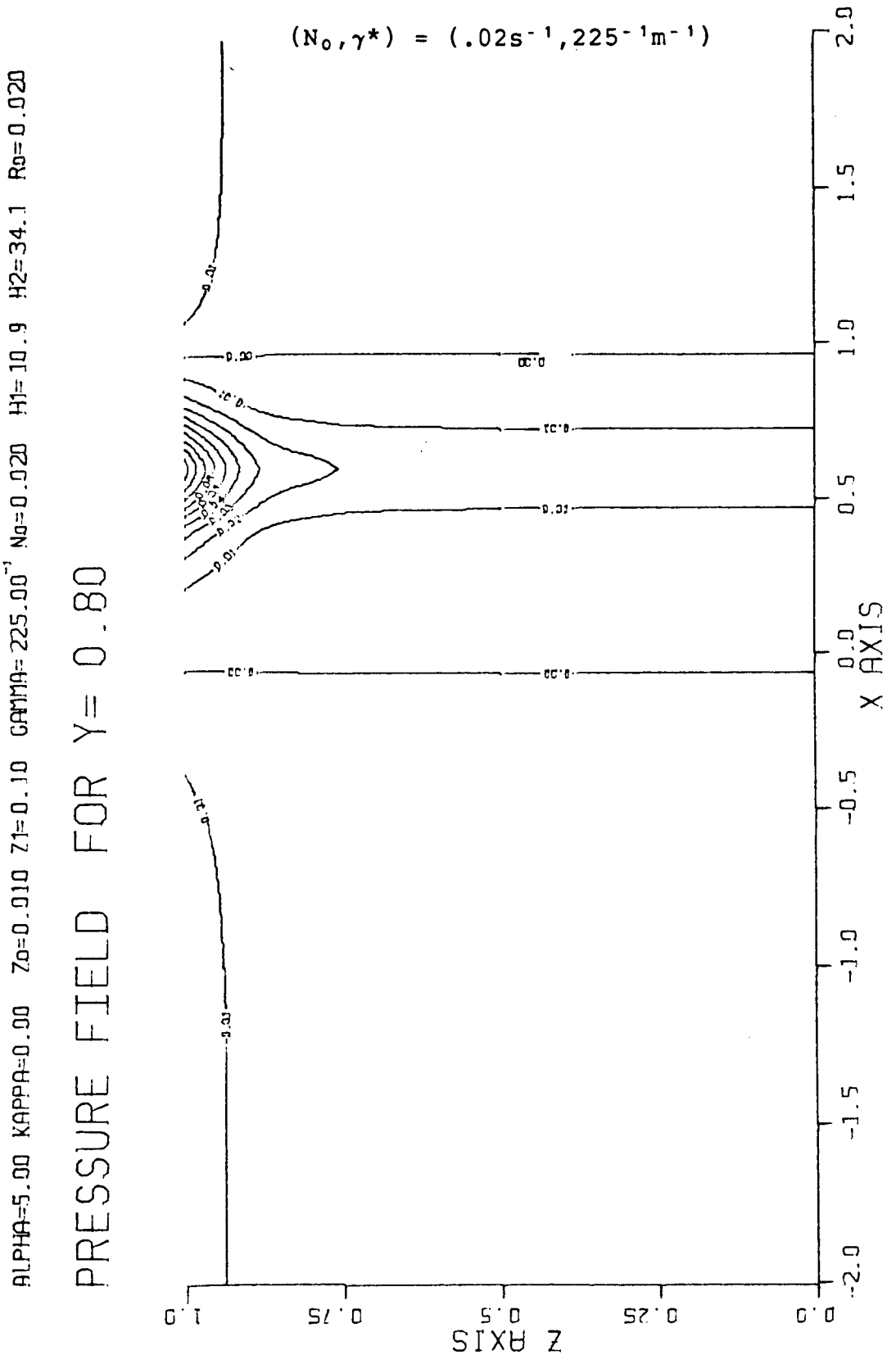

Figure 66 - Vertical contour plot of $p^{(0)}$ on y = .8 with $(N_0, \gamma^*) = (.02s^{-1}, 300^{-1}m^{-1})$

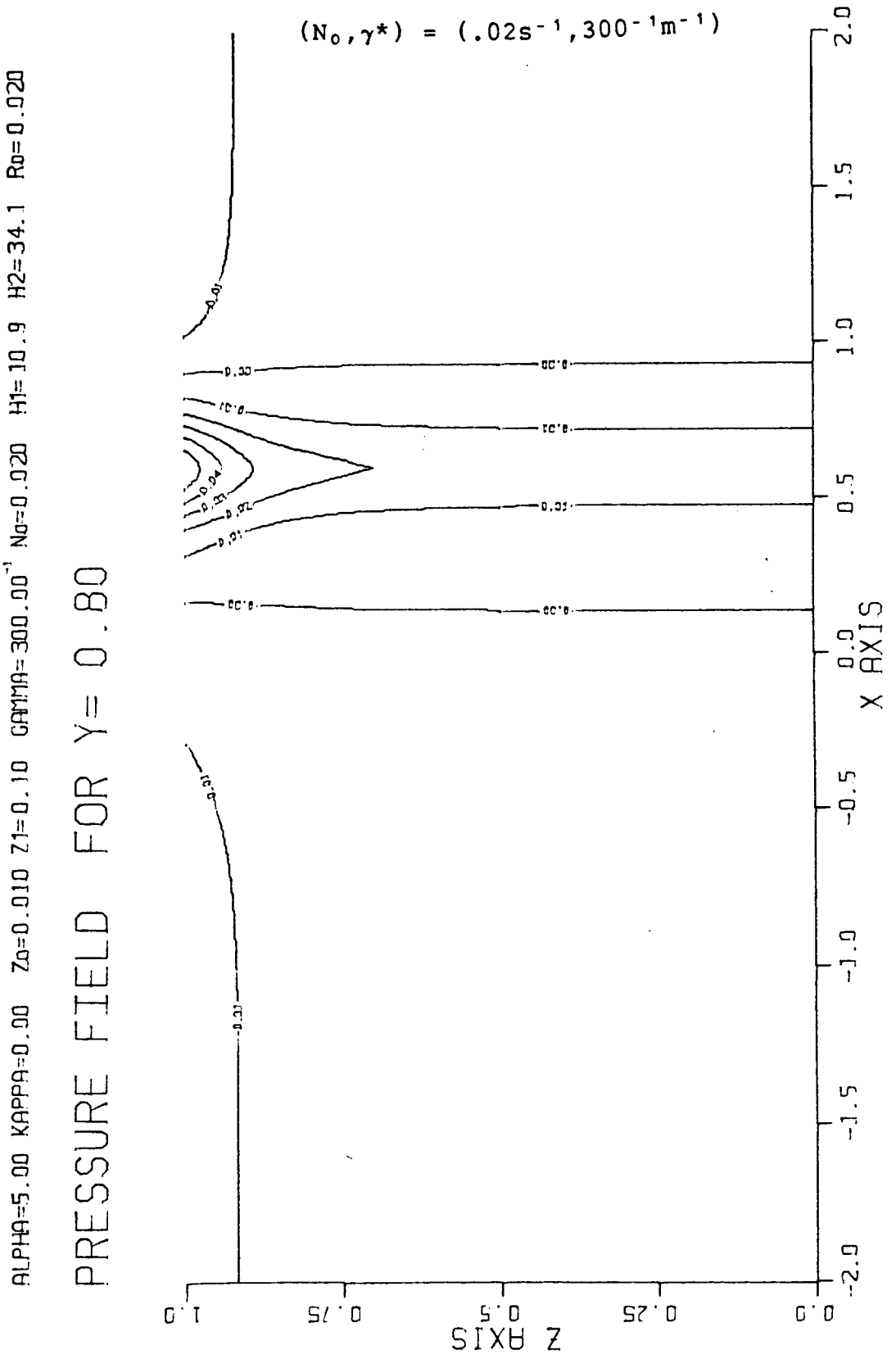

Figure 67 - Horizontal contour plot of the stream function on z = 1 with Z(1) = .05

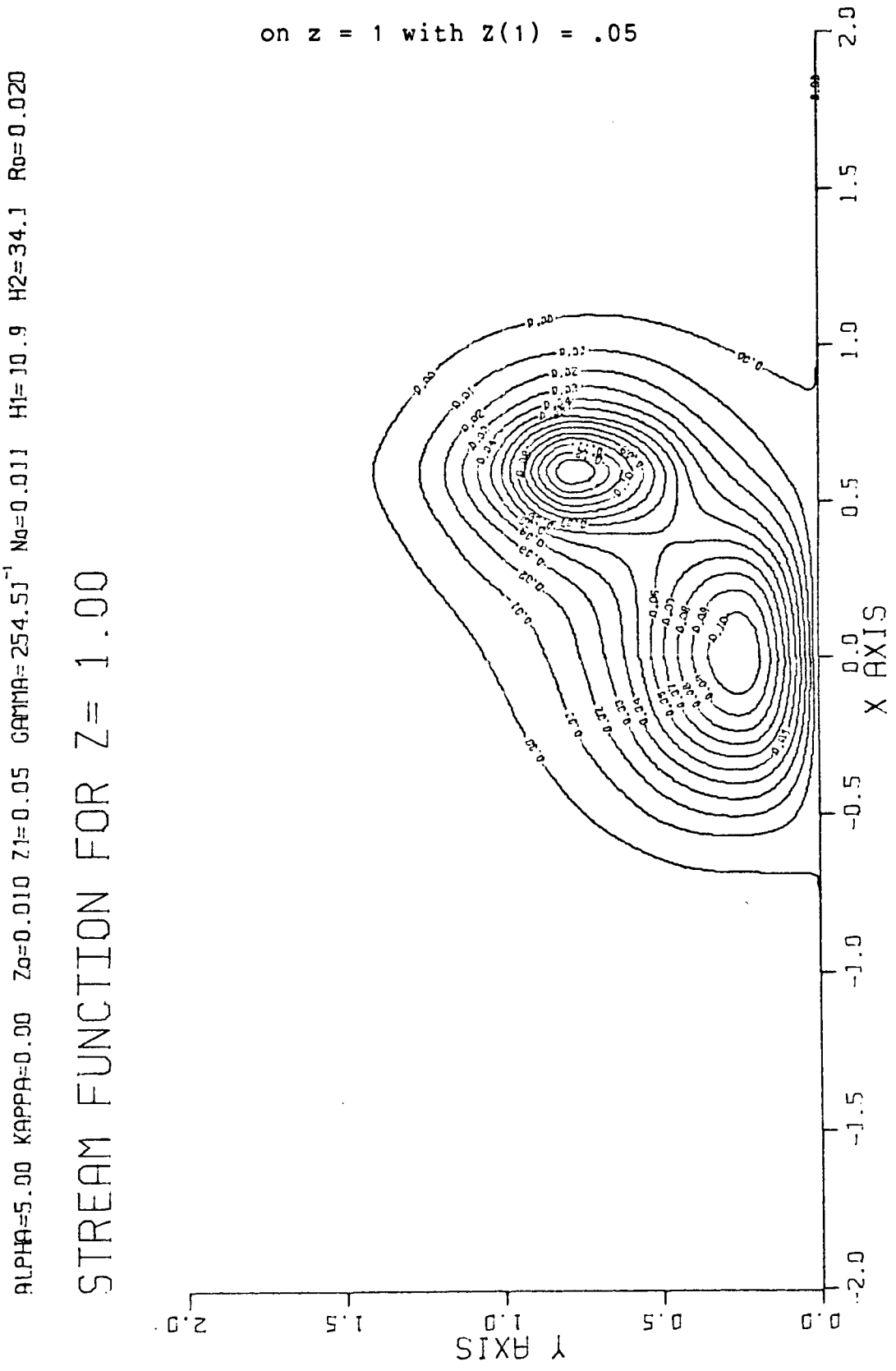

Figure 68 - Vertical contour plot of $p^{(0)}$ on y = .2 with Z(1) = .05

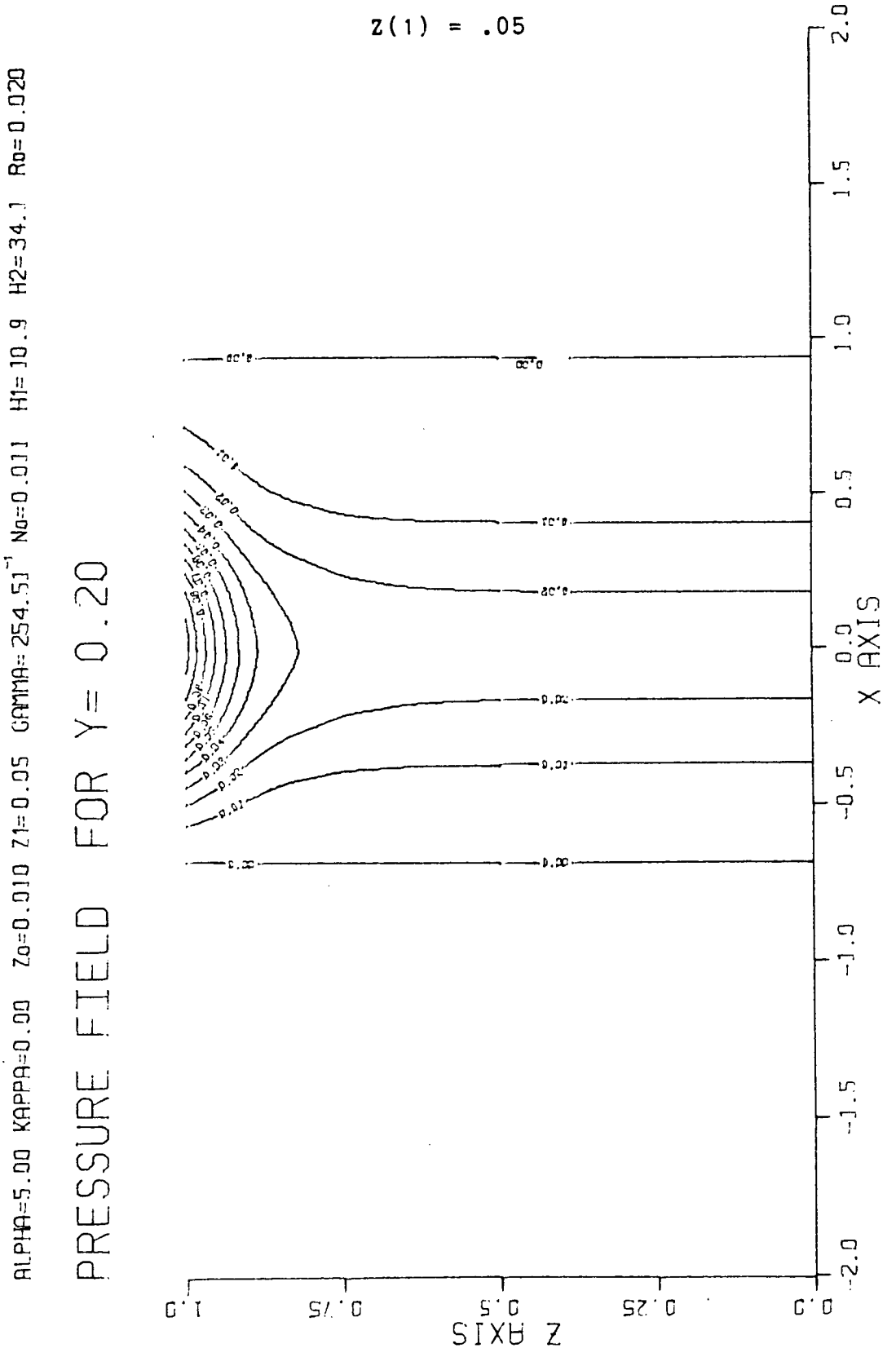

Figure 69 - Vertical contour plot of $p^{(0)}$ on y = .8 with Z(1) = .05

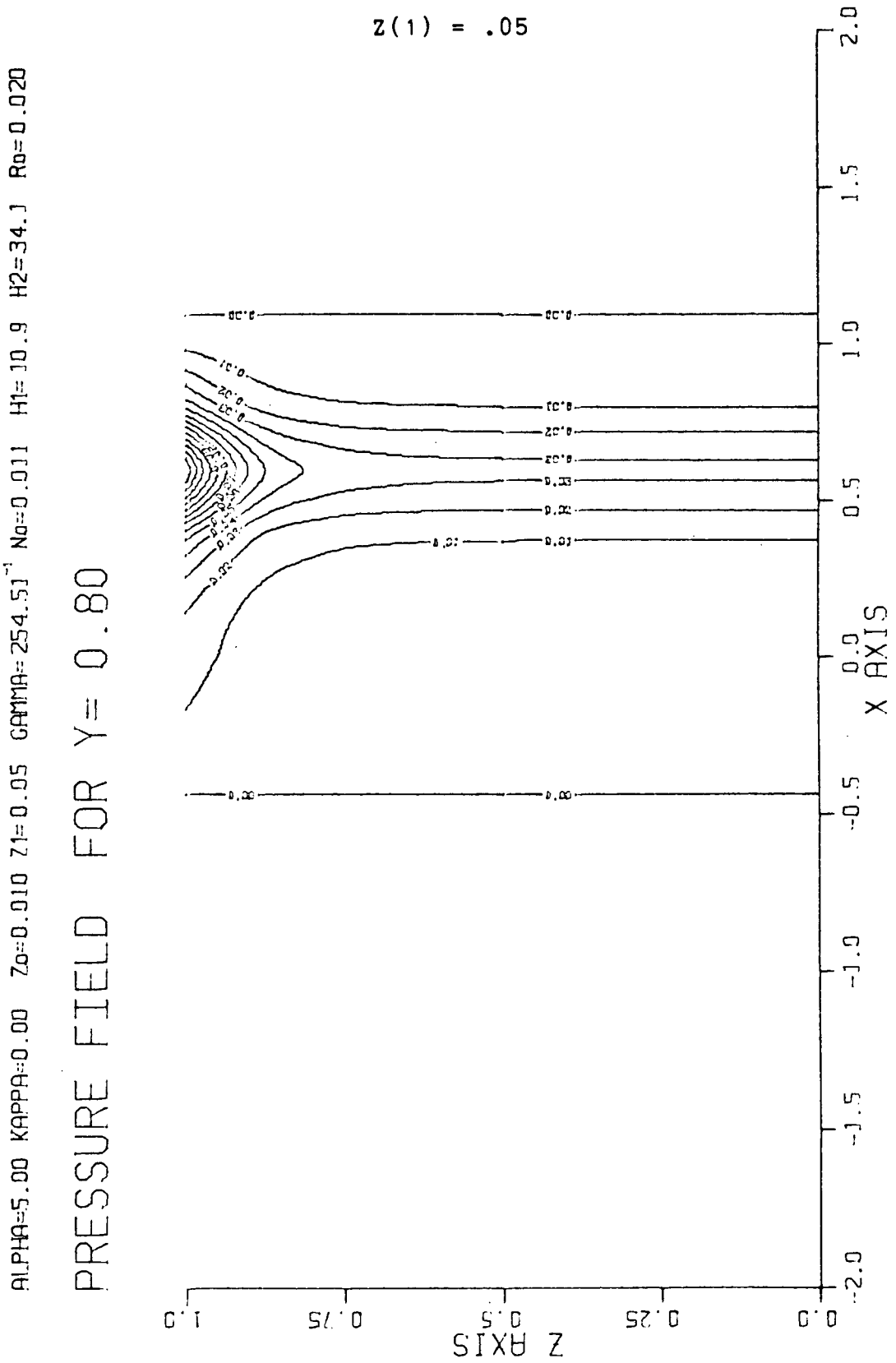

Figure 70 - Horizontal contour plot of the stream function on z = 1 with Z(1) = 1

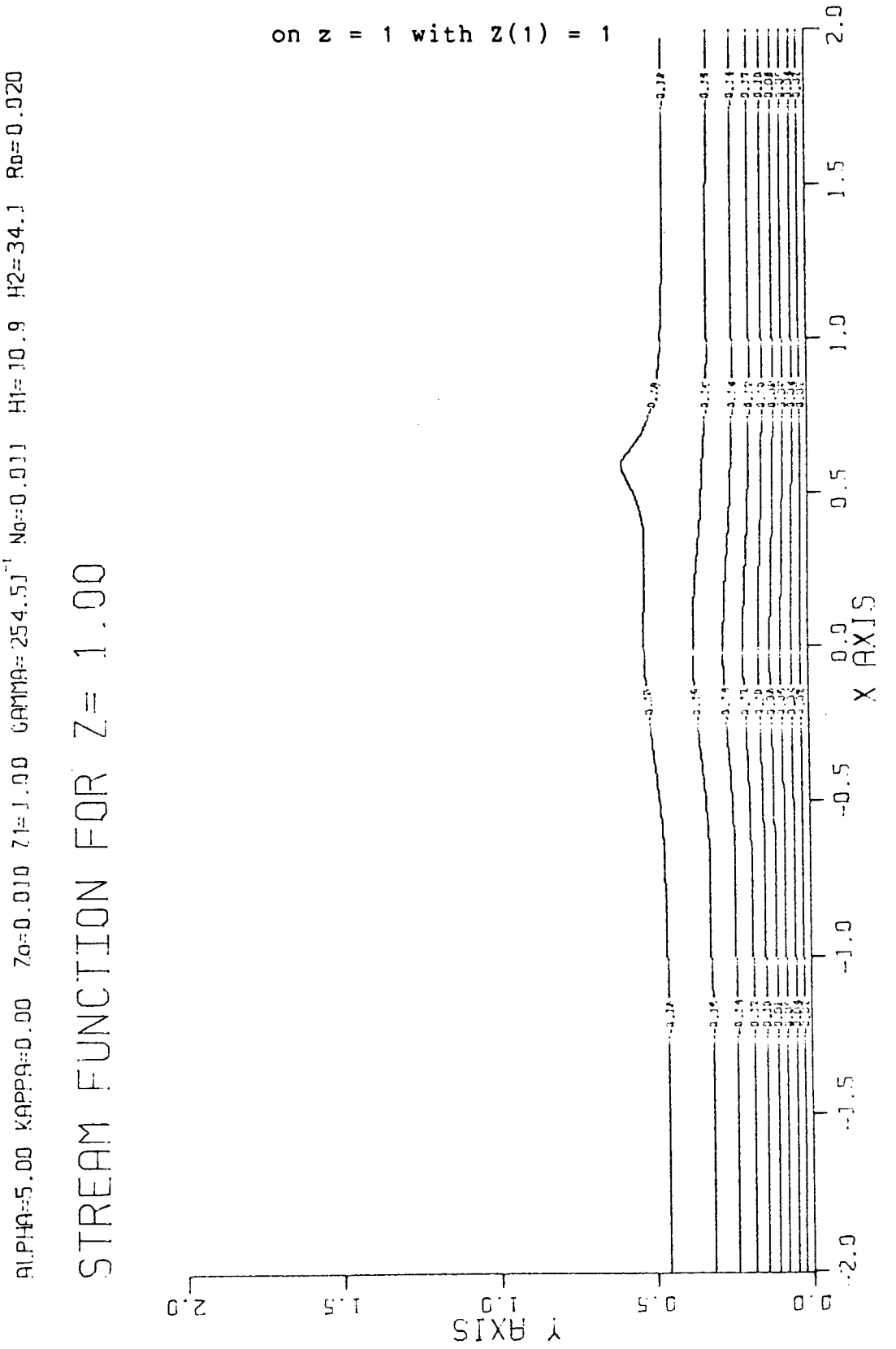

Figure 71 - Horizontal contour plot of the stream function on z = 1 with Z(1) = .01

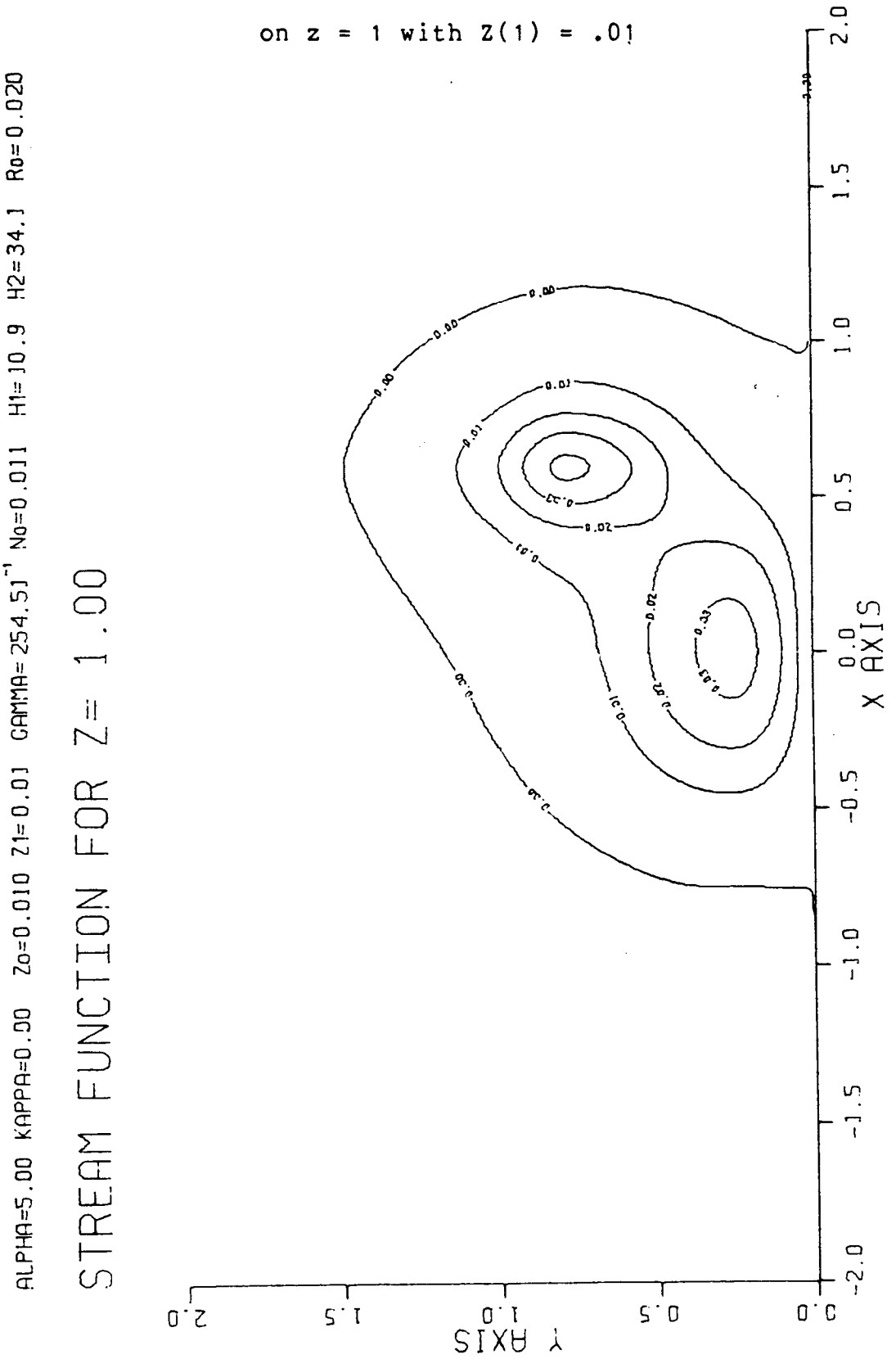

Figure 72 - Vertical contour plot of $p^{(0)}$ on y = .2 with Z(1) = .01

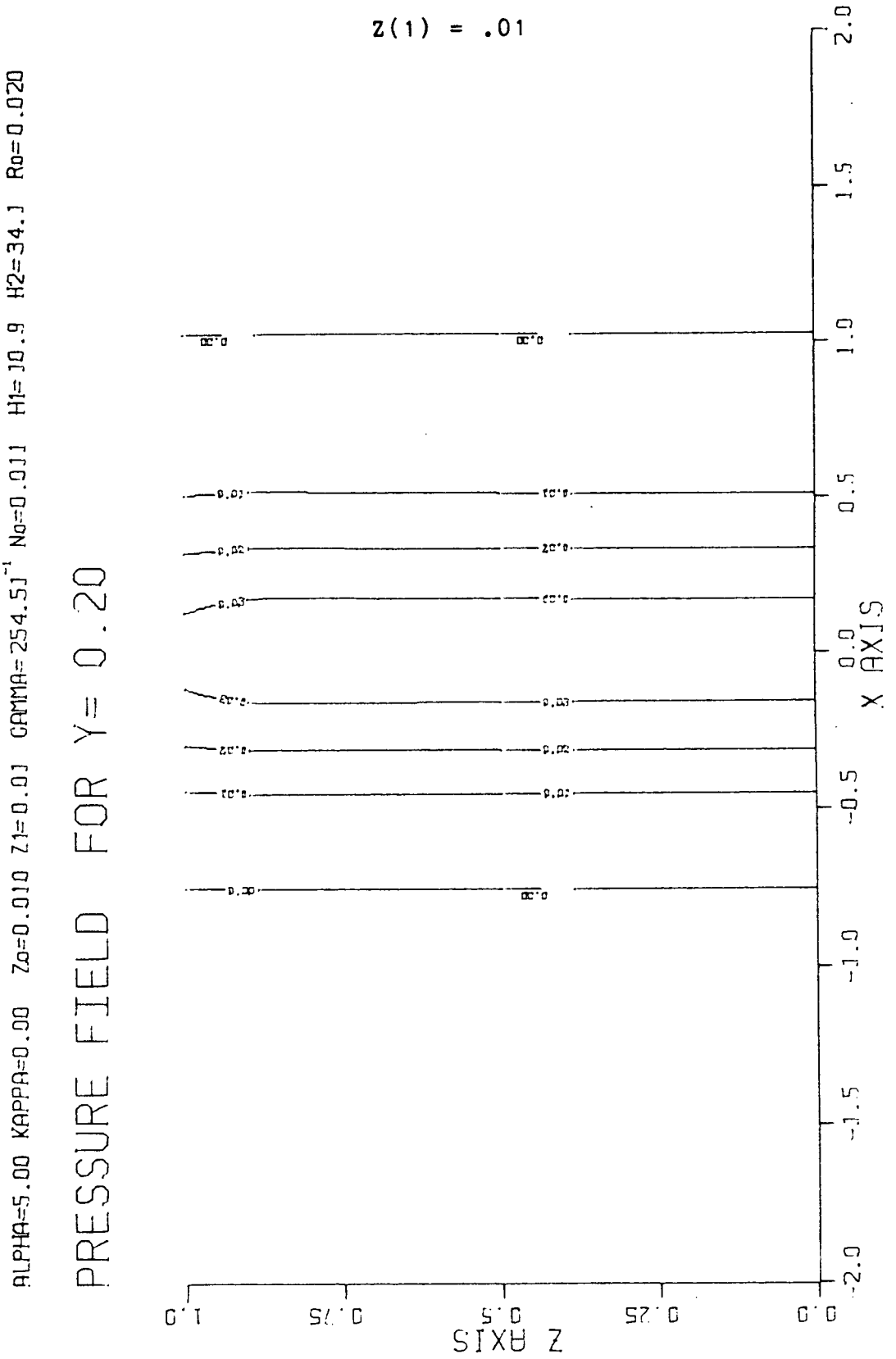

Figure 73 - Vertical contour plot of $p^{(0)}$ on y = .8 with Z(1) = .01

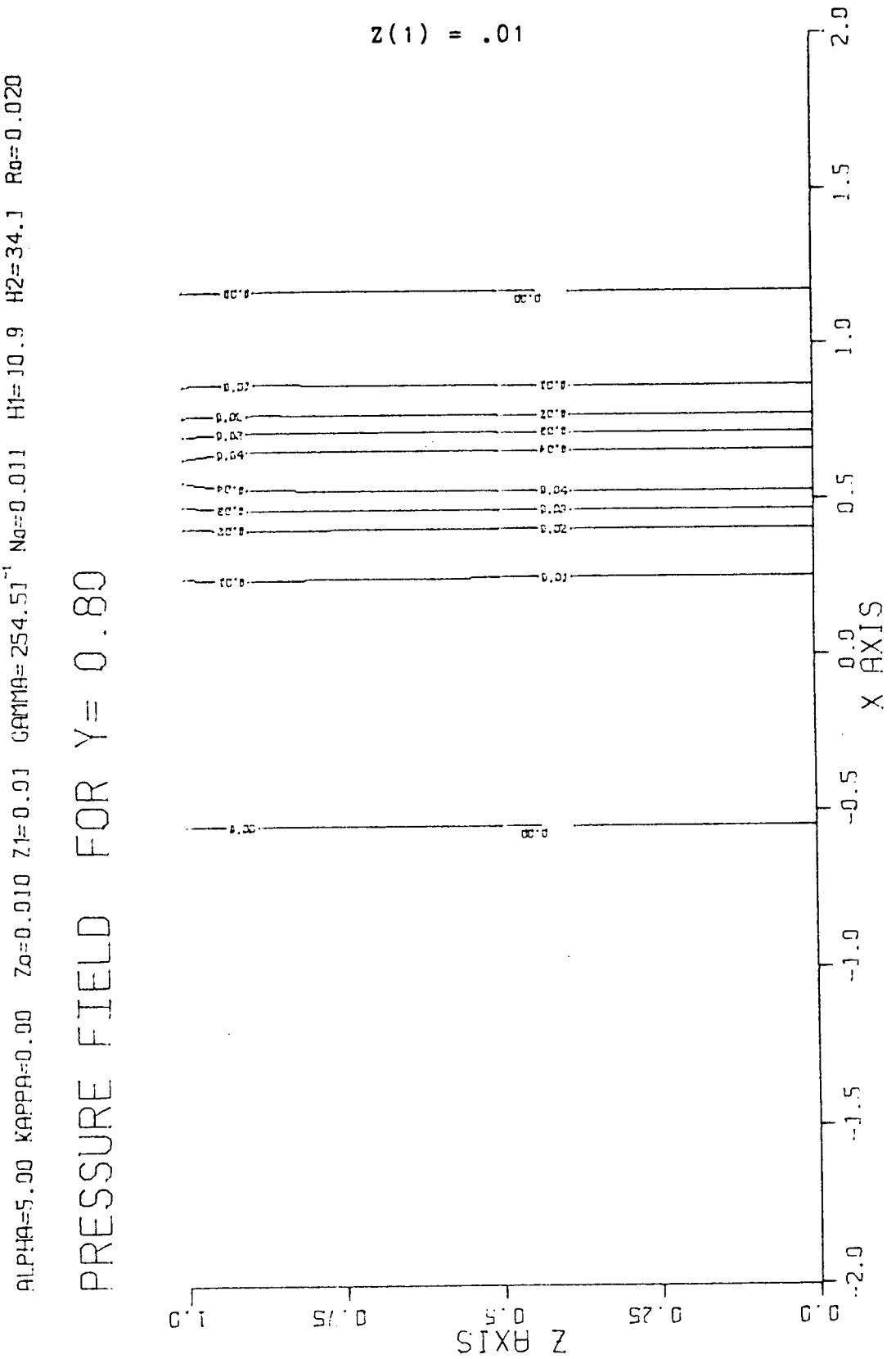

Figure 74 - Horizontal contour plot of the stream function on z = 1 with Z(0) = .001

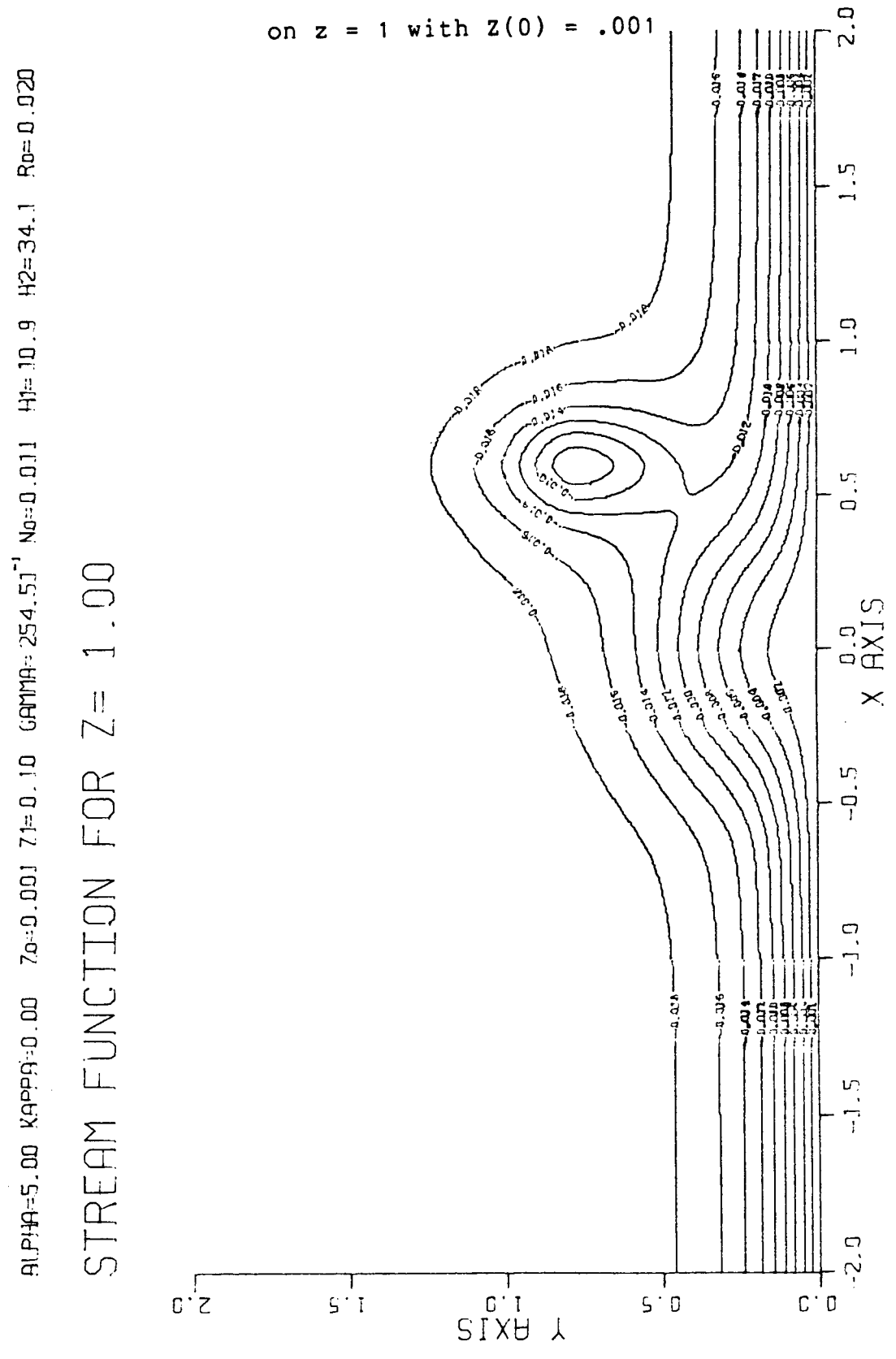

Figure 75 - Vertical contour plot of $p^{(0)}$ on y = .2 with Z(0) = .001

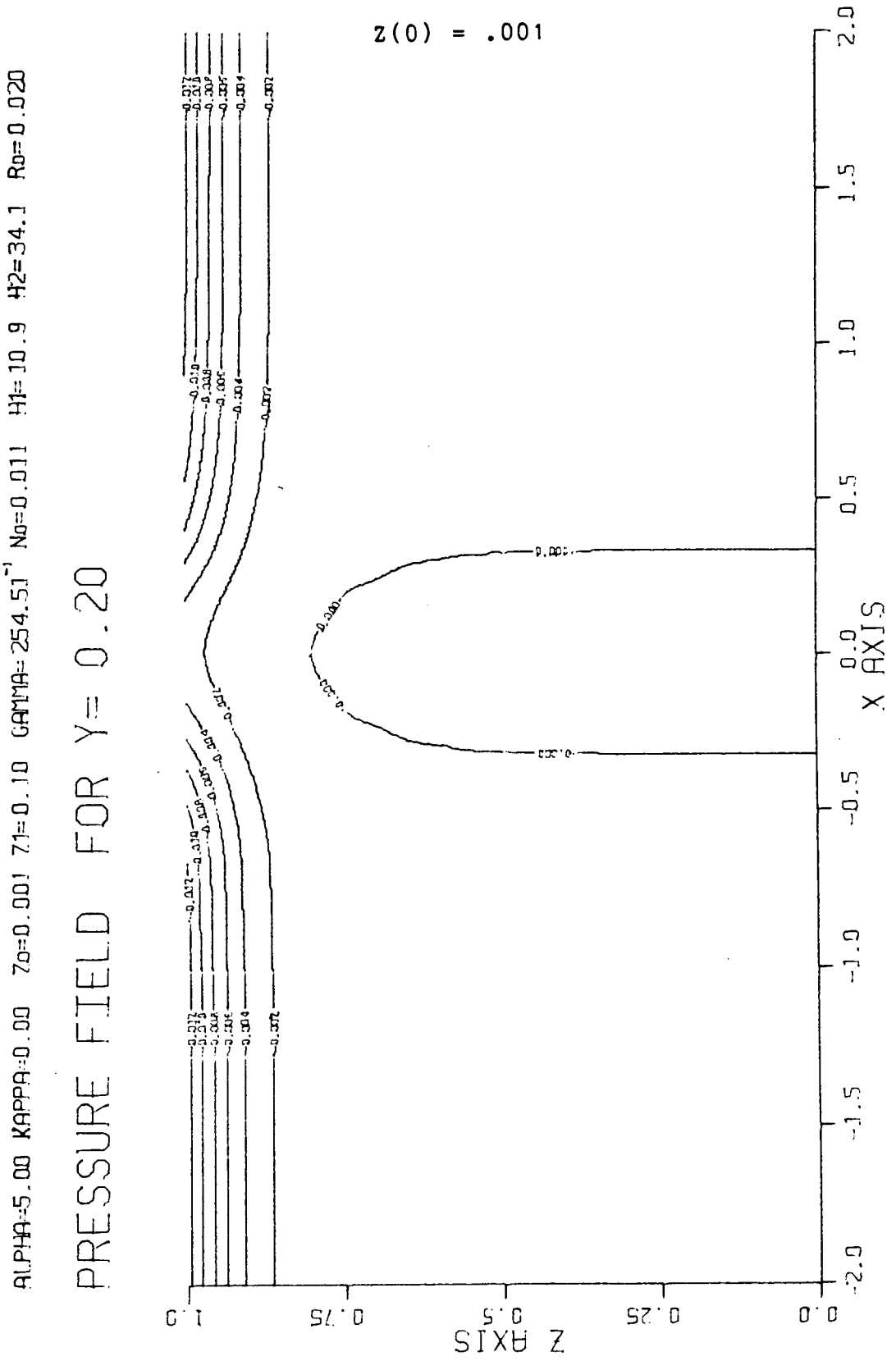

V. APPLICATION TO THE SITKA EDDY

The mathematical model developed in Chapter III illustrates that a baroclinic coastal current forced by topography can generate anticyclonic baroclinic eddies. The model contains a number of parameters. Estimates of these parameters based on the available data record for the north east Pacific Ocean suggests that the prominent regional bathymetry and the local mean flow can interact to produce eddies which are qualitatively similiar to the eddy observed by Tabata(1982). This chapter concerns itself with qualitatively comparing the numerical calculations described in Chapter IV with Tabata's(1982) and Bennett's(1959) observations.

The lateral scale of the calculated large scale anticyclonic circulation agrees favorably with the observed radius of the Sitka eddy. Figure 11, computed for the standard set of parameters, has a large scale anticyclonic circulation with nondimensional radius .5, corresponding to a dimensional radius of 200 km. Tabata's estimate of the eddy radius was on the order of 100 to 150 km. The center of the computed large scale circulation is more or less located at (x,y) coordinates (.25,.5) which when converted to approximate longitude and latitude is consistent with Tabata's location of the Sitka eddy given as 57°N 138°W.

In Section 4.3 the numerical calculations of the resulting flow field in the absence of the seamount (Figure 61) or the slope protrusion (Figure 62) were presented. In either case the

resulting eddy has a radius on the order of 100 km. The location of the Sitka eddy suggests that it is unlikely that the Sitka eddy is simply produced by the individual interaction of the seamount or the slope protrusion on the coastal current.

The calculations of Section 4.3 show that the seaward deflection of the coastal current by the slope protrusion extends out to the vincinty of the seamount. This implies that the effect of the seamount on the flow field cannot be ignored. This suggests that upstream from the Sitka eddy the currents would show a tendency toward the region containing the Pratt seamount. This topographic steering of the coastal current has been detected in the oceanographic data (Tabata; personal communication).

Ignoring the effects of the slope protrusion does not lead to realistic results. Figure 62, in which $h_1 = 0$, has the resulting eddy located substantially seaward of its observed location. Furthermore, the strong seaward deflection of the observed coastal current is absent, as is any significant return coastal flow.

Observations of the isopcynal depression place the vertical extent of the eddy on the order of a kilometer (Tabata; 1982). During March 1958 and January 1960, the deflections of the ispcynals persisted as deep as 2000 metres. Strictly speaking the model predicts anticyclonic motion throughout the entire water column. There are, however, large vertical gradients in $p^{(0)}$, $u^{(0)}$, $v^{(0)}$ and $\rho^{(0)}$ near the surface. Vertical sections of the density field (Figures 30 through 34) suggest that the

sharpest gradients in $\rho^{(o)}$ occur in upper 900 metres of the ocean. Contour plots of the isobars (Figures 16 through 20) show that the significant vertical variation in $p^{(o)}$ is constrained to the upper 1100 metres of ocean. Thus estimates of the vertical extent of the calculated eddy based on the pressure and density fields are on the order of 1000 metres, which is entirely consistent with the observations.

The observed surface currents in the Sitka eddy are also consistent with those computed in the model. Tabata(1982) describes three drifting bouys that in 1977 entered the northwest area of the Sitka eddy. This region would correspond to the area surrounding (x,y) coordinates (.75,1.25) in the horizontal sections contained in this thesis. The average drift rate for these bouys was computed to be 62 cm s^{-1}, 91 cm s^{-1} and 47 cm s^{-1}, with the later average obtained from a drogued bouy. The model computes a surface drift speed in this region, for the standard set of parameters, between 30 and 40 cm s^{-1}. Thus the calculations are consistent with the drogue bouy results but are about 50% of value obtained from the undrogued bouys.

Tabata's estimates of the southward drift rate in the northeast sector of the Sitka eddy is range of values between 48 and 64 cm s^{-1}. Assuming the northeast sector to be in the general neighbourhood of (x,y) coordinates (.5,.25), the model predicts surface speeds on the order of 50 cm s^{-1}.

Current speeds in the interior of the water column in the eddy are consistent with the observations of the Sitka eddy. Relative to the 2500-decibar level, Tabata estimates a

1.5 cm s^{-1} current at the 2000-decibar level. The model computes currents at the 1750 metre depth level as 2 cm s^{-1} over the slope protrusion and 3 cm s^{-1} over the seamount.

The upstream current was effectively modelled as $\exp(-\alpha y)Z(z)$. Bennett's(1959) analysis of the coastal current revealed that the coastal current was significantly sheared, both horizontally and vertically. The assumed horizontal structure of the upstream current, modelled with an exponential function with a distance of 80 km, was an accurate idealization of the actual coastal currents horizontal structure.

The vertical structure of the upstream current was described by the function Z(z). Assuming that the potential vorticity was conserved throughout the flow field forced Z(z) to be formulated in a particular way. The resulting vertical structure of the upstream current is consistent with the profiles shown in Bennett(1959). The montonic decay of the current with increasing depth was obtained.

The upstream alongshore surface current was assumed to be about 10 cm s^{-1} and the current speed in the deep interior of the water column about 1 cm s^{-1}, as described in Bennett(1959). Tabata(1982) reports that the upstream coastal current has a transport on the order of 6 Sv. The modelled upstream current had a transport of 5.9 Sv. This suggests that the linearization of the potential vorticity equation as manifested in 2.10 was an effective and accurate model of the upstream current.

The transports computed in the eddy were in the main consistent with those observed by Tabata(1982). The large scale

anticyclonic circulation (shown in Figure 11 as exterior to the smaller local eddies) has a transport of about 4 Sv. This compares favorably with Tabata's observation of 5 Sv. The local eddies produced over the slope protrusion and the seamount had computed transports on the order of 20 Sv. These estimates are somewhat larger than the the observations. Over the slope protrusion, Tabata estimates a southward transport of about 8 Sv. Tabata estimates the transport over the Pratt seamount as between 5 and 6 Sv.

VI. CONCLUSIONS

This thesis has examined the following conjecture: that bathymetry and the local mean coastal flow of the north east Pacific Ocean can interact to produce baroclinic anticyclonic eddies. A mathematical model was developed to examine this possibility.

This model demonstrates that the regional bathmetry and local mean flow can interact to produce mesoscale anticyclonic eddies. These eddies are generated for parameter values which are obtained from estimates of the geometry, bathymetry and oceanographic data for the north east Pacific Ocean.

The solution of the mathematical model is consistent with the oceanographic data of this region as reported by Bennett(1959) and Tabata(1982). The lateral and vertical scales of the anticyclonic circulation predicted by the model agrees closely with the observations. The eddy is observed and computed to have a radius of about 200 km and to extend at least to 1000 metres in depth. The decay of the velocity field with depth is consistent with the observations. The computed transports are in good agreement with the observations. The solution of the field equations is robust in the sense that for variations in the parameters the basic qualitative structure of the solution varies little.

The mathematical model is derived from the steady, inviscid, incompressible, stratified, f-plane and Boussinesq equations of motion. The ocean is assumed to lowest order to be

at rest and in hydrostatic balance. The Brunt-Vaisala frequency, derived from the mean state density field, is a least squares fit (Willmott and Mysak; 1980) of a typically observed Brunt-Vaisala frequency for the north east Pacific Ocean (Emery et al.; 1983) with an exponential function.

The dynamic pressure and density fields associated with fluid motion are in hydrostatic balance. The horizontal velocity field is geostrophically scaled relative to the dynamic pressure field. This scaling resulted in the nondimensional parameters ϵ, F, and s_0 which are the Rossby number, the squared ratio of the length scale to the external Rossby radius and the Burger number respectively. Estimates of these parameters based on scales obtained from the north east Pacific suggest that $s_0 \simeq 0(1)$, $F \simeq 0(\epsilon)$ and $0(\epsilon) \simeq 10^{-2}$.

These parameters suggest that the motion is primarily geostrophic and therefore horizontal. The smallness of F implies that the vorticity associated with the deformation of the sea surface is an order of magnitude smaller than the relative vorticity. However, since the Burger number is order unity then the baroclinic compression of the isopcynals makes an equal contribution to the vorticity of a vortex tube as does its angular velocity. The smallness of ϵ is exploited by constructing the lead terms for the pressure, density, velocity and mass transport fields in an asymptotic expansion in the parameter ϵ.

The essential physical feature captured in this lead order solution is that the order one dynamics is the result of the

conservation of potential vorticity along streamlines. The potential vorticity is the balance between the relative vorticity and the vorticity induced by the compression of vortex tubes.

The quasi-geostrophic potential vorticity equation (ie. the Jacobian between the stream function and the potential vorticity must vanish) was solved by assuming that the potential vorticity was a linear function of the pressure field. This procedure implied that the upstream vertical current structure was the solution of a second order ordinary differential equation.

The horizontal structure of the upstream current was assumed to exponentially decay away from the coast. The observed upstream current and the modelled upstream current were in very good agreement. The vertical structure of the computed upstream current was in good agreement with the observations contained in Bennett(1959). Tabata(1982) suggests that this current transports about 6 Sv of water northward. The modelled current transported about 5.9 Sv northward.

The topography of the ocean floor in the north east Pacific Ocean was idealized as an abyssal plain with two orographic features. The seamounts in the vincinty of the Pratt seamount were modelled as a smooth orographic feature with the maximum height of the Pratt seamount. In addition, the continental shelf has a prominent horizontal seaward protrusion in the coastal region near the Sitka eddy. This feature was modelled as a smooth cosine-like orographic feature protruding from an

other wise straight channel wall.

Estimates of the heights of the topography suggested that the heights of the seamount and slope protrusion was order Rossby number with respect to the mean depth of the ocean. Thus the no normal boundary condition on the velocity field at the bottom could be expanded in a Taylor series about a state of no topography.

The solution for the order one stream function was obtained as a linear sum of the upstream stream function and an interaction pressure field. The interaction pressure field was obtained via a normal mode analysis described in Chao et al. (1980). The boundary conditions on the interaction pressure field were integrated upstream into the form suggested by Hogg(1980). The vertical modes and upstream vertical structure were obtained using a technique illustrated in Bryan and Ripa(1978) in their analysis of the vertical structure of temperature anomalies in the north east Pacific Ocean. The horizontal amplitude function, associated with the normal mode analysis, were obtained using Green's functions.

The solution obtained in this thesis suggests that Sitka eddy is essentially produced in the following manner. The northward flowing coastal current encounters the southern edge of the slope protrusion. The compression of the isopcynals and the conservation of potential vorticity implies that the relative vorticity must decrease. This decrease in the relative vorticity is obtained by increasing the anticyclonic motion of a vortex tube, implying that the current turns seaward. Some of

the deflected current encounters the Pratt seamount, the rest continuing downstream.

For those streamlines passing over the Pratt seamount the isopcynals are again compressed which induces an anticyclonic rotation toward the coastline. Some of these streamlines subsequently interact with the slope protrusion, others are deflected downstream by the coastline. Those that interact with the slope portrusion are as a consequence of the conservation of potential vorticity turned upstream. The constraint of the coastline and the upstream streamlines therefore sets up a closed anticyclonic circulation. This large scale circulation is centered and has charateristics which agree closely with the observations made of the Sitka eddy contained in Tabata(1982).

BIBLIOGRAPHY

1. Bakun, A., 1978: Monthly Transport Parameters Computed From Monthly Mean Pressure Fields On A 3-degree Grid. Unpublished Manuscript, U. S. Dept. Commerce, N.O.A.A., Nat. Mar. Ser., Pacific Environ. Group, Monterey, Cal., 15 pp.

2. Bennett, E. B., 1959: Some Oceanographic Features Of The Northeast Pacific Ocean During August 1955. J. Fish. Res. Bd. Can., 21, 565-633.

3. Byran, K. and P. Ripa, 1978: The Vertical Structure Of North Pacific Temperature Anomalies. J. Geophys. Res., 83, 2419-2429.

4. Chao, S., L. J. Pietrafesa and G. S. Janowitz, 1980: On The Dynamics Of A Baroclinic Jet Over Shallow Topography. Unpublished Manuscript.

5. Emery, W. J., W. G. Lee and L. Magaard, 1983: Geographic Distributions Of Density, Brunt-Vaisala Frequency And Rossby Radii In The North Atlantic and North Pacific. Submitted to J. Phys. Oceanog..

6. Hogg, N. G., 1980: Effects Of Bottom Topography On Ocean Currents, Orographic Effects In Planetary Flows. Garp Publication Series No. 23., 167-265.

7. Huppert, H. E., 1975: Some Remarks On The Initiation Of Inertial Taylor Columns. J. Fluid Mech., 67, 397-412.

8. LeBlond, P. H. and L. A. Mysak, 1978: Waves In The Ocean. Elsevier, 602 pp.

9. Tabata, S., 1982: The Anticyclonic, Baroclinic Eddy Off Sitka, Alaska, In The Northeast Pacific Ocean. J. Phys. Oceanog., 12, 1260-1282.

10. Thomson, R. E., 1972: On The Alaskan Stream. J. Phys. Oceanog., 2, 363-371.

11. Willmott, A. J. and L. A. Mysak, 1980: Atmospherically Forced Eddies In The Northeast Pacific. J. Phys. Oceanog., 10, 1769-1791.